HgCdTe Auger-Suppressed Infrared Detectors Under Non-Equilibrium Operation

by

Pierre-Yves Emelie

A dissertation submitted in partial fulfillment
of the requirements for the degree of
Doctor of Philosophy
(Electrical Engineering)
in The University of Michigan
2009

Doctoral Committee:

Associate Professor Jamie Dean Phillips, Chair
Professor Fred L. Terry Jr.
Assistant Professor Pei-Cheng Ku
Assisant Professor Kevin Patrick Pipe

Je dédie cette thèse,

A mes parents, Pilar et Mathieu;

A mon frère, Jean-Philippe;

A ma soeur, Marie-Christine.

Acknowledgements

I would like to take this opportunity to thank my advisor Prof. Jamie Phillips. Looking back on those five years, I have really enjoyed doing research in his group. I would like to thank him for his support, and his guidance throughout my thesis work. I also would like to thank him for being very much involved in my research, as well as in the research of everyone else who are, or were part of this group. He has always been available nearly anytime I needed for quick questions, and long discussions. He has also always provided very detailed and thorough feedback when I was preparing presentation slides, journal publications, and this document. I admire his scientific rigor; I hope to have learned from it; I realize how privileged I was to have an advisor who cares so much about the work of his students, and I will surely miss this.

I also would like to thank EPIR Technologies for providing technical and financial support for my thesis. I owe a significant part of what I know about HgCdTe to my internship at EPIR, and to working with EPIR employees during my research work. I would like to thank particularly Dr. Silviu Velicu for all his help during my thesis. I also would like to thank Dr. Siva Sivananthan for giving me the opportunity to work with EPIR, and Dr. Chris Grein for our very useful discussions. Thanks to all EPIR employees I have interacted with, especially Dr. Alok Chatterjee, Dr. Shubhrangshu Mallick, Dr. Rajni Mallick, Ramana Bommena and Craig Lennon. Thanks also to former EPIR employees Dr. Tae-Seok Lee for teaching me everything about HgCdTe device processing, and Dr. An. I also would like to acknowledge the Microphysics Laboratory at the University of Illinois at Chicago where I performed most of the experimental work for this thesis. Thanks to the people from MPL, especially Yesim Anter. I also would like to thank Dr. Wijewarnasuriya from the US Army Research Laboratory for his collaboration in this work.

Next, I would like to thank past and current graduate students from our group: Kaveh Moazzami, Emine Cagin, Willie Bowen, Jeff Siddiqui, and Weiming Wang. Although I would have liked to have more work interactions with you, I have enjoyed our personal interactions. Kaveh has been very helpful and patient to help me get started with my research work. Emine has helped me on so many occasions during my time here that I cannot even count them.

Pour finir, je voudrais aussi remercier mes parents qui ont simplement toujours fait tout pour moi. Je voudrais remercier mon frère Jean-Philippe pour m'avoir guidé, et pour continuer à le faire sans relâche, vers le bonheur et le succès. Je voudrais remercier ma sœur Marie-Christine pour avoir toujours été d'une gentillesse infaillible avec moi. A ses côtés, le quotidien est toujours plus joyeux. Je voudrais remercier ma belle-sœur Helen pour m'avoir aidé avec mon frère pour ma candidature à l'Université du Michigan, et pour m'avoir aidé dans bien d'autres occasions. Je voudrais remercier mon autre moitié, Sonca, sans qui je n'aurais probablement pas trouvé la force de finir cette thèse. Elle m'a toujours soutenu et poussé dans les moments difficiles. L'avoir à mes côtés me permet de croire que tout est possible. Je voudrais enfin remercier tous mes amis du passé et du présent, surtout Julie, Sébastien, et Antoine. J'espère vraiment vous voir plus souvent dans le futur.

Table of Contents

List of Figures

List of Tables

List of Appendices

List of Abbreviations

BLIP	Background-Limited Performance
DLPH	Double-Layer Planar Heterojunction
FOV	Field-of-View
HOT	High Operating Temperature
IR	Infrared
LWIR	Long-Wave Infrared
MBE	Molecular Beam Epitaxy
MWIR	Mid-Wave Infrared
NDR	Negative Differential Resistance
PV	Photovoltaic
SE	Spectroscopic Ellipsometry
SIMS	Secondary Ion Mass Spectroscopy

Abstract

A nearly universal goal for infrared photon detection systems is to increase their operating temperature without sacrificing performance. The limiting factor for cooling requirements is the dark current in the detector devices. The dark current in HgCdTe infrared detectors is limited by Auger processes at near-room temperatures of operation. Device designs based on non-equilibrium operation in HgCdTe devices have been proposed to overcome this. In this work, we study non-equilibrium operation in reverse-biased HgCdTe detectors in order to achieve Auger suppression and decrease the dark current. Finite-difference methods are used to accurately model the devices, including self-consistent, steady-state solutions of Poisson's equation and the carrier continuity equations for carrier densities. It is found that background-limited performance can be achieved in ideal Auger-suppressed HgCdTe devices operated at 180 K for mid-wave infrared detection, opening the possibility to use thermoelectric cooling, and operated at 120 K for long-wave infrared detection. The material structure and doping levels in an HgCdTe detector with cutoff wavelength λ_c=5.5 μm at 200 K are optimized to maximize Auger suppression. The most critical parameters are found to be those of the absorber layer, especially the doping level and concentration of traps. We also present full temperature-dependent device characterization of fabricated HgCdTe photodiodes, designed using our device model, with cutoff wavelength of λ_c=10 μm at 100 K. HgCdTe wafers are grown by molecular beam epitaxy by EPIR Technologies, Inc. Devices are fabricated by the US Army Research Laboratory and the University of Michigan. Clear evidence of Auger suppression is observed in the experimental current-voltage data between 120 K and room temperature with up to 50 % decrease of the dark current as the reverse bias is increased. The measured detectivity D^* with black-body of 500 K, field-of-view of 90°, and chopper frequency of 1 kHz is in the low-10^9 cm.$Hz^{0.5}$/W at

120 K and the mid-10^7 cm.$Hz^{0.5}$/W at 300 K. The electrical characteristics of the devices are fitted using our device model. Leakage current induced by traps and impurities in the material causing Shockley-Read-Hall recombination limits the saturation current after Auger suppression.

Chapter 1

Introduction

1.1 Background and Motivation

Infrared (IR) imaging technology has been significantly improving over the years and is finding new areas of applications as the cost for high sensitivity sensors keeps decreasing. Due to the long wavelengths, optical data can be transmitted without much attenuation. But because of the absorption by earth's atmospheric CO_2 and H_2O, not all wavelengths can be used for free space optical data transmission in the infrared region. Looking at the transmission of air as a function wavelength (Figure 1.1), it is evident that only a few wavelength windows are available for such purpose. Therefore, interest is centered mainly on the wavelengths of the atmospheric windows short-wave infrared (SWIR) from 1-3 μm, mid-wave infrared (MWIR) from 3-5 μm, long-wave infrared (LWIR) from 8-14 μm and very long-wave infrared (VLWIR) higher than 16 μm and not shown here.

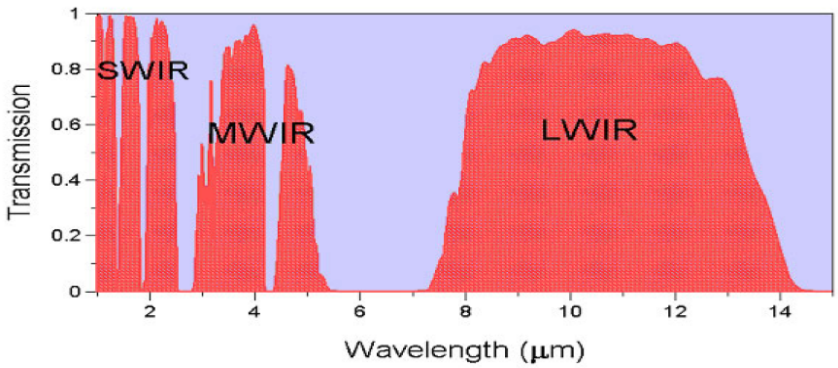

Figure 1.1: Atmospheric transmittance.

Infrared imaging is widely used for both military and civilian applications. Military applications include target acquisition, surveillance, night-vision and tracking to guide defense interceptor seekers. Civilian applications include thermography, short-range wireless communication, spectroscopy, weather forecasting and infrared astronomy. Each application requires a sensor capable of detecting the infrared radiation in one or several of the infrared windows described previously. A wide range of detectors which can be subdivided into different types are now available:

- intrinsic detectors
- extrinsic detectors
- photoemissive detectors
- quantum well and quantum dot intraband detectors
- thermal detectors

Intrinsic detectors are composed by direct band gap semiconductors such as PbSe, InSb, InAs or HgCdTe. Possible devices use the photovoltaic (PV) effect such as in p-n photodiodes or the photoconductive (PC) effect in photoconductors where the change of conductivity in the material is related to the incoming infrared radiation. Extrinsic detectors are composed of indirect band gap semiconductors such as Si or Ge and typically use the photoconductive effect. Photoemissive detectors correspond to metal silicide Schottky barriers such as PtSi or IrSi. Examples of quantum well infrared photodetectors (QWIP) include HgTe/CdTe or InAs/InGaSb superlattices. In thermal detectors such as silicon bolometers or pyroelectric detectors, the change of the material temperature due to the absorption of the incident radiation results in a change in some electrical or optical property which produces an electrical output. Unlike the previous detector types described, the signal of thermal detectors is wavelength-independent.

Low cost thermal detectors such as bolometers are mostly used in applications where high sensitivity and speed are not required such as IR spectrometers. However, they are easy to use and cheap partly because they can be operated near room temperature. High-sensitivity and high-speed infrared detectors can be achieved by PV, PC or QWIP detectors. However, they usually require to be cooled down to cryogenic temperatures, i.e. 77 K or lower. Cryogenic cooling systems such as Joule-Thomson

cryostats add significant cost, power consumption and weight to infrared imaging systems. There is therefore a great interested in achieving high sensitivity infrared imaging at higher temperatures. Although the ultimate goal is to achieve high sensitivity uncooled infrared imaging, "one giant leap" for infrared technology would be to first achieve high sensitivity infrared imaging using thermoelectric (TE) coolers. TE-coolers are relatively light and do not consume a lot of power. They can cool systems down to about 180-200 K.

Regarding state-of-the-art infrared sensors, as we can see in Figure 1.2 [1], ideal PV detectors have a higher detectivity D^* than ideal PC or thermal detectors. Detectivity D^* is the main parameter characterizing normalized signal-to-noise performance of detectors and is defined later in this chapter. Cooled infrared detectors with detectivity close to the theoretical limit are now available. In order to increase the operating temperature of infrared systems up to 180-200 K, we are interested in this work in PV detectors which offer more room for improvement than PC detectors by making use of novel heterostructures. In addition, photodiodes have a faster response than photoconductors and are not affected by many of the trapping effects associated with photoconductors.

Cooled infrared detector based on HgCdTe (mercury-cadmium-telluride) is the only technology providing near theoretical limit D^* in both MWIR and LWIR bands. HgCdTe is the dominant semiconductor for high-performance infrared imaging as we explain in details later. However, HgCdTe infrared photodiodes are also limited at high temperatures. A novel device structure based on HgCdTe is presented in this work in order to achieve high sensitivity infrared imaging at high temperatures.

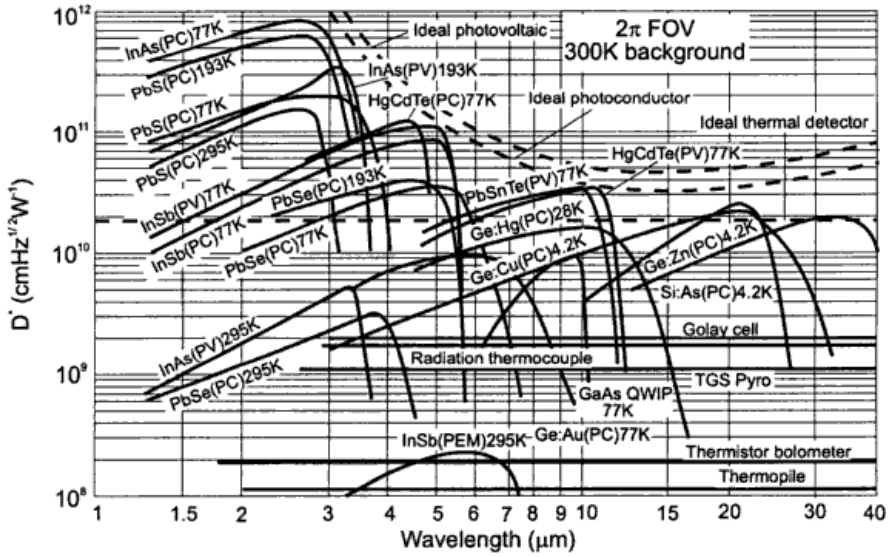

Figure 1.2: Comparison of the detectivity D^* of various commercially available infrared detectors when operated at the indicated temperature. Theoretical curves for D^* for ideal photovoltaic, photoconductive and thermal detectors are also shown.

1.2 P-N Junction Infrared Photodiodes

The operating principles of p-n junction photodiodes are presented in this section. We introduce important figures of merit for infrared photodiodes which are used throughout this work. The fundamental limitations of narrow-gap semiconductor infrared photodiodes are also discussed. Finally, the novel device structure proposed to overcome some of these limitations is presented.

1.2.1 Operating Principles

The photovoltaic effect corresponds to light being converted into an electrical signal. Several structures are possible to observe the PV effect. These include p-n homojunctions or heterojunctions, Schottky barriers, metal-insulator-semiconductor (MIS) photocapacitors. The most common example of an infrared PV detector is the semiconductor p-n junction photodiode. The structure and operation of the p-n photodiode is illustrated in Figure 1.3 [2]. Incoming photons with energy E=hν larger

than the band gap E_G create electron-hole (e-h) pairs in the material on both sides of the junction. By diffusion, the electron and holes generated within a diffusion length from the junction reach the depletion region. Minority electron and holes are then swept to the n- and the p- side of the junction respectively where they become majority carriers. This creates a photocurrent which shifts the current-voltage (I-V) characteristic in the direction of negative current as we can see in Figure 1.4 [2].

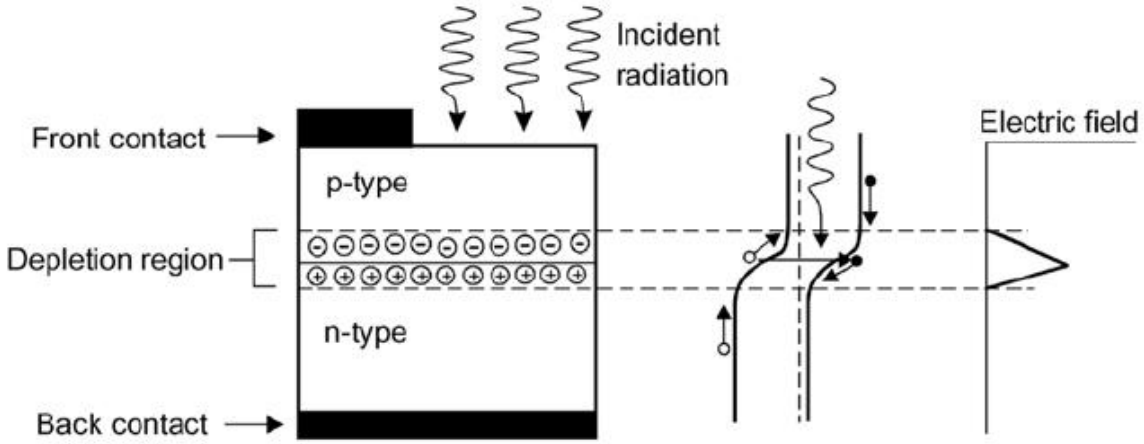

Figure 1.3: a) Structure of a p-n junction photodiode with the corresponding b) energy band diagram taken along a vertical cross-section and c) electric field profile at zero bias.

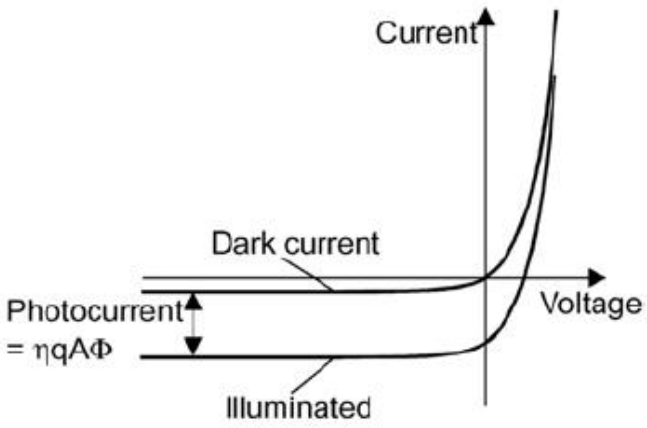

Figure 1.4: I-V characteristic of a p-n junction photodiode.

The minority carrier diffusion length (cm) is given by the following expression:

$$L_{n,p} = \sqrt{D_{n,p}\tau_{n,p}} \tag{1}$$

$$D_{n,p} = \frac{\mu_{n,p} kT}{q} \tag{2}$$

where $D_{n,p}$ is the minority carrier diffusion coefficient ($cm^2.s^{-1}$), $\tau_{n,p}$ is the minority carrier recombination lifetime (s) and $\mu_{n,p}$ is the minority carrier mobility ($cm^2/V.s$). Various mechanisms, both fundamental and technology-related, are related with the generation G and recombination R processes occurring inside the photodiode. Each mechanism k results in a net generation rate $(G - R)_k$ associated with a carrier recombination lifetime τ_k by the following formula:

$$(G - R)_k = -\frac{\Delta n}{\tau_k} \tag{3}$$

where Δn is the excess carrier concentration. More details on generation-recombination and carrier lifetime are provided in the following chapter.

The total current density (A/cm^2) in the p-n junction is usually written as:

$$J(V, \phi) = J_{dark}(V) - J_{ph}(\phi) \tag{4}$$

where the dark current density J_{dark} depends only on the bias voltage V, and the photocurrent density J_{ph} depends only on the flux density ϕ (W/cm^2). In addition to the I-V characteristic, a frequently encountered figure of merit for infrared photodiodes is the zero-bias resistance-area product R_0A (ohms-cm^2) defined as the inverse derivative of the dark current density-voltage characteristic at zero bias:

$$R_0 A = \left(\frac{\partial J}{\partial V} \right)^{-1}_{|V_b = 0} \tag{5}$$

The photodiode dark current and R_0A product are both directly related to the detector noise, as we explain later, and therefore have a direct impact on the photodiode signal-to-noise ratio. The dark current corresponds to the reverse bias current-voltage characteristic of the non-illuminated photodiode and is non-zero due to various leakage mechanisms in the device. High performance infrared photodiodes are characterized by low dark current and high R_0A in order to minimize the detector noise. In many direct applications, the photodiode is operated at zero bias. In this case, the dark current contribution to noise can be ignored and the detector noise is related to the inverse of the

R_0A product. However, operation at a small reverse bias is usually preferred in infrared imaging. A small reverse bias increases the depletion region width and electric field magnitude and therefore high speed can be achieved. In this case, the dark current at the bias of operation contributes to detector noise. Thus, it is important to understand the sources of dark current in infrared photodiodes. Each independent dark current source has an associated R_0A product. R_0A products add like resistances in parallel to give the total R_0A product.

1.2.2 Mechanisms Contributing to Dark Current

Diffusion current is the fundamental current mechanism in a p-n junction photodiode. The dark current-voltage characteristic for an ideal diffusion-limited photodiode is given by:

$$I_{diff} = AJ_{diff} = AJ_s\left[\exp\left(\frac{qV_b}{kT}\right)-1\right] \tag{6}$$

$$J_s = q\left(\frac{n_{p0}D_n}{L_n}+\frac{p_{n0}D_p}{L_p}\right) \tag{7}$$

where A is the photodiode junction area (cm^2), V_b is the applied bias voltage, n_{p0} and p_{n0} are the equilibrium electron and hole concentration (cm^{-3}) on the p- and the n- side of the junction respectively.

Several additional excess mechanisms are involved in determining the photodiode dark current. Between them, we can distinguish:

- generation-recombination (g-r) current in the depletion region
- band-to-band (B-B) tunneling
- trap-assisted (TAT) tunneling
- surface recombination (surf)

Figure 1.5 [2] illustrates schematically some of these mechanisms. Each of the components has its own individual relationship to voltage and temperature.

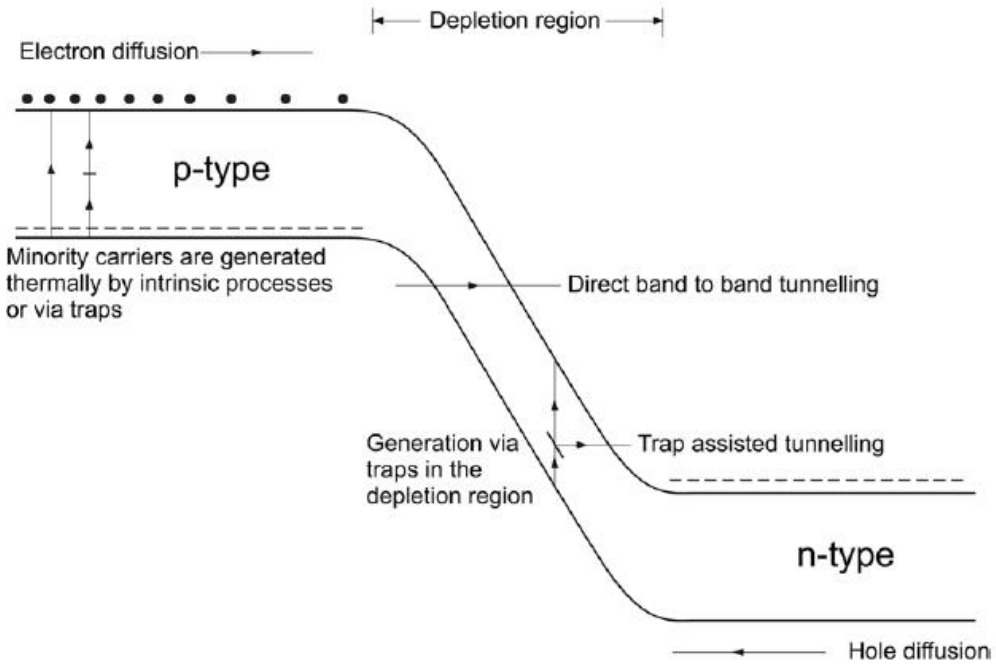

Figure 1.5: Schematic representation of some of the mechanisms by which dark current is generated in a reverse biased p-n junction.

Generation-recombination current in the depletion region corresponds to the thermal generation of electron and holes being in the depletion region and then drift of these carriers in opposite directions due to the strong electric field, therefore creating a current. When generated electrons and holes reach the n- and p- side of the junction respectively, they recombine and become majority carriers. Various generation mechanisms can be responsible for this, such as Auger and Shockley-Read-Hall generation via traps. More details on these mechanisms are given in the following chapter. In high performance infrared photodiodes such as HgCdTe infrared photodiodes, generation-recombination current usually dominates the dark current at low temperatures while diffusion current is dominant at high temperatures. The current corresponding to this can be given by:

$$I_{g-r} = AJ_{g-r} = q\int_{depl} GdV \tag{8}$$

which is the carrier generation profile ($cm^{-3}.s^{-1}$) integrated over the depletion region volume and multiplied by the electron charge q. Simple expressions can be obtained if we consider the carrier generation profile to be constant over the depletion region.

Another mechanism limiting the dark current in narrow-gap semiconductor infrared photodiodes is the band-to-band tunneling. This corresponds to electrons directly tunneling across the junction from the valence band to the conduction band. The usual direct tunneling calculations assume a particle of constant effective mass incident on a triangular or parabolic potential barrier. For the triangular potential barrier, the band-to-band tunneling current is given by the following expression [3]:

$$I_{b-b} = AJ_{b-b} = A\frac{q^3 EV_b}{4\pi^2\hbar^2}\sqrt{\frac{2m_e^*}{E_G}}\exp\left[-\frac{4\left(2m_e^*\right)E_G^{3/2}}{3q\hbar E}\right] \tag{9}$$

where E is the electric field profile (V/cm), V_b is the applied bias voltage, m_e^* is the electron effective mass (m_0) and E_G is the energy band-gap (eV). The band-to-band tunneling current is seen to have a strong dependence on energy gap and electric field. The electric field is dependent on the applied voltage and the doping concentration of the p-n junction. It is relatively insensitive to temperature and the shape of the junction barrier.

Tunneling is also possible by means of indirect transitions in which impurities or defects within the depletion region act as intermediate states. This process is referred to as trap-assisted tunneling. As illustrated in Figure 1.5, this is a two-step process in which one step is a thermal transition of a carrier between one of the bands and the trap, and the other is tunneling between the trap and the other band. Trap-assisted tunneling can occur at lower electric fields than direct band-to-band tunneling because the carriers have a shorter distance to tunnel. In the case of small electron effective mass such as in HgCdTe, the low density of states in the conduction band leads to the following approximate expression for the trap-assisted tunneling current [4]:

$$I_{tat} = AJ_{tat} = qAN_t\omega_c N_c W \tag{10}$$

$$\omega_c N_c = \frac{\pi^2 q m_e^* EM^2}{h^3\left(E_G - E_t\right)}\exp\left(-\frac{\left(m_e^*/2\right)E_G^{3/2}F(a)}{2qE\hbar}\right) \tag{11}$$

$$a = 2\left(\frac{E_t}{E_G}\right) - 1 \tag{12}$$

$$F(a) = \left(\frac{\pi}{2}\right) - a\left(1 - a^2\right)^{1/2} - \frac{1}{\sin(a)} \tag{13}$$

where N_t is the density of trap centers (cm^{-3}), $\omega_c N_c$ is the rate of the tunnel transition to the conduction band, W is the depletion region width (cm), E is the electric field profile (V/cm), E_t is the trap energy center in the band-gap from the valence band (eV) and M is the matrix element associated with the trap potential.

Finally, additional leakage currents due to the surface can occur. The termination of the crystal lattice at its surface creates unsaturated chemical bonds dangling into space outside the crystal. These bonds may react with anything available in the neighboring atmosphere. Therefore, the electronic and chemical properties at the surface are very different compared to those in the bulk. The surface can have a net charge which results in the creation of a depletion region at the surface. The surface also provides a discontinuity that can result in a large density of interface states. These traps generate minority carriers in the surface depletion region by the Shockley-Read-Hall mechanism in a similar way as what can happen in the junction depletion region. Therefore, the surface of actual infrared photodiodes must be passivated in order to control surface recombination, leakage and related noise. An ideal surface would be electrically neutral and would have a very low density of surface states. The generation current induced by surface recombination is calculated the same way as for the g-r current in the depletion region.

1.2.3 Spectral Response

The p-n junction photodiodes show a selective wavelength dependence of the spectral response per unit incident radiation power compared to the wavelength-independent response of thermal detectors (see Figure 1.6). Important figures of merit regarding the spectral response of infrared photodiodes are the responsivity (A/W or V/W) and the external quantum efficiency (or collection efficiency):

$$R = \frac{J_{ph}}{\phi} \tag{14}$$

$$\eta = \frac{J_{ph} hc}{\phi \lambda q} = R \frac{1.24}{\lambda} \tag{15}$$

where J_{ph} is the photocurrent density at the operation bias voltage (A/cm^2) corresponding to the incident radiation flux density ϕ (W/cm^2) at the particular wavelength λ (μm).

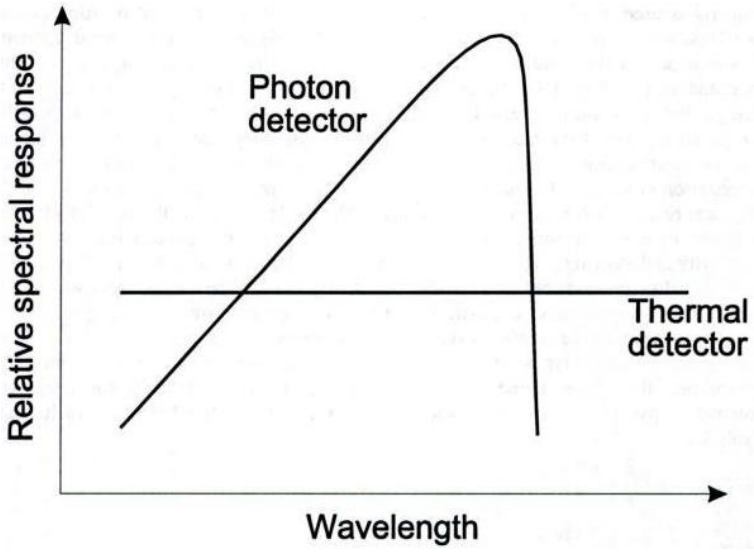

Figure 1.6: Relative spectral response for photon and thermal detector.

1.2.4 Noise and Background-Limited Performance

In a standard ideal infrared p-n photodiode operated at a small reverse bias, the noise current i_n ($A/Hz^{0.5}$) can be defined as:

$$i_n(V_b) = \sqrt{\left(\frac{4kT}{R_d A} + 2qJ_{dark} + 2qJ_{ph} \right) A} \tag{16}$$

$$i_n(0) = \sqrt{\left(\frac{4kT}{R_0 A} + 2qJ_{ph} \right) A} \tag{17}$$

where R_dA is the dynamic resistance-area product (ohm-cm^2) for a particular reverse bias voltage, J_{dark} is the magnitude of the dark current density (A/cm^2), J_{ph} is the magnitude of the photocurrent density in A/cm^2 due to the background scene typically modeled as black-body radiation at 300 K and A is the detector junction area (cm^2).

The first two terms correspond to the detector shot noise. Shot noise in p-n junction photodiodes consists of random fluctuations of the electric current which are caused by the fact that the current is carried by discrete charges such as electrons. The detector noise is related to the zero-bias resistance-area product R_0A under zero-bias operation (Equation (17)). It takes the form of a Johnson-Nyquist noise expression.

The detector noise current is also composed by the quadrature sum of several additional noise components which are shown here, such as the Johnson-Nyquist noise component due to the different resistances in the device (shunt, series, amplifier circuit), and the 1/f noise. The Johnson-Nyquist noise is the electronic noise generated by the thermal agitation of the charge carriers inside an electrical conductor at equilibrium.

The last term is the background photon shot noise due to the scene. For a photodiode exposed to a background flux, an additional generated photocurrent constitutes a statistically independent contribution to the noise current, called photon-induced shot noise, or background noise. For earth applications, the background scene is typically modeled as black-body radiation at 300 K. For space applications, the background scene may be modeled as a black-body radiation of less than 300 K, or its contribution may be ignored. The spectral photon flux exitance [photon/(s-cm^2-μm)] from a black-body is defined as:

$$M_{q,\lambda}(\lambda,T) = \frac{2\pi c}{\lambda^4} \cdot \frac{1}{\exp\left(\frac{hc}{T_s k\lambda}\right) - 1} \tag{18}$$

where T_s is the black-body temperature (K). The spectral photon flux exitance from a black-body at 300 K is shown in Figure 1.7.

The photocurrent (A/cm^2) induced by the background scene can be expressed as:

$$\begin{aligned} J_{ph} &= q\frac{1}{1+4f_{\#}^{\ 2}}\int_0^{\lambda_c}\left(M_{q,\lambda}(T_s,\lambda) - M_{q,\lambda}(T_d,\lambda)\right)\eta(\lambda)d\lambda \\ \Leftrightarrow J_{ph} &= q\frac{1}{1+4f_{\#}^{\ 2}}\int_0^{\lambda_c}\frac{2\pi c}{\lambda^4}\left(\frac{1}{\exp\left(\frac{hc}{T_s k\lambda}\right)} - \frac{1}{\exp\left(\frac{hc}{T_d k\lambda}\right)}\right)\eta(\lambda)d\lambda \end{aligned} \tag{19}$$

where $f_{\#}$ corresponds to the detector optics, λ_c is the photodiode cutoff wavelength (μm) defined as the wavelength corresponding to 50 % responsivity, T_s is the scene temperature (K), T_d is the detector temperature (K) and η is the detector quantum efficiency as defined earlier.

The focal ratio $f_{\#}$ of the detector optics is given by f/D where f is the lens focal length and D is the diameter of the entrance pupil. It is related to the field-of-view (FOV). A focal ratio $f_{\#}=0$ corresponds to 2π FOV. Typical $f_{\#}$ values in real infrared detector systems vary between 2 (FOV~30°) and 5 (FOV~10°) depending on the application.

The ultimate performance in infrared photodiodes is called *background-limited performance* (BLIP). BLIP is achieved when the total detector noise is smaller than the background noise.

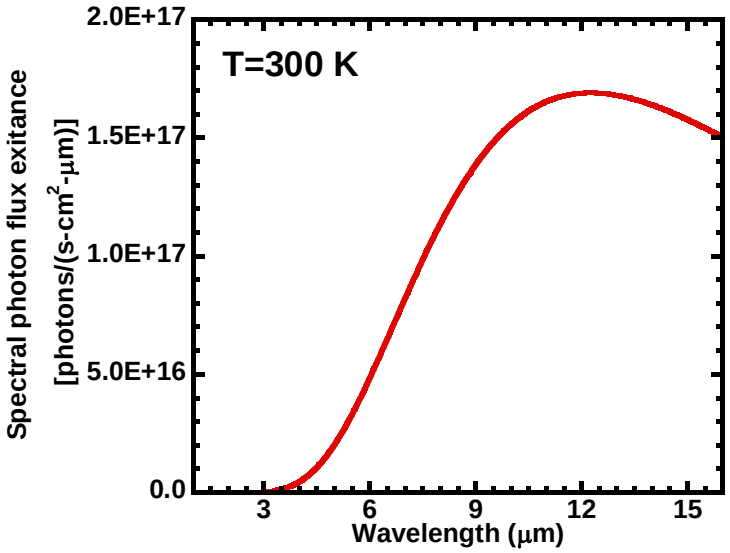

Figure 1.7: Spectral photon flux exitance versus wavelength from a black-body at 300 K.

*1.2.5 Detectivity D**

Detectivity D^* (cm.Hz$^{0.5}$/W) is the main parameter to characterize the performance of infrared photodiodes. It corresponds to a normalized signal-to-noise ratio combining all the parameters presented above. It can be defined as:

$$D^* = \frac{R_p \sqrt{A}}{i_n} \tag{20}$$

where R_p is the responsivity (A/W) at the peak wavelength λ_p, A is the photodiode junction area (cm^2) and i_n is the detector noise current ($A/Hz^{0.5}$).

As we can see in Figure 1.2, available commercial infrared detectors can achieve detectivities on the order 10^{10} $cm.Hz^{0.5}/W$ or higher in all the atmospheric windows of interest (SWIR, MWIR, LWIR and VLWIR). As mentioned earlier, a variety of semiconductor materials used in infrared PC and PV devices can achieve the near-theoretical limit for detectivity D^*. However, $Hg_{1-x}Cd_xTe$ is the only material that can achieve the near-theoretical limit for D^* in both MWIR and LWIR. $Hg_{1-x}Cd_xTe$ has the unique property that it can be tuned across the whole infrared spectrum by changing the Cd alloy fraction x. It is the ideal semiconductor material for infrared imaging as described in detail in the following chapter. It is currently the most widely used semiconductor for high performance cooled infrared imaging.

The theoretical limit curve shown in Figure 1.2 for ideal photovoltaic device is obtained by assuming that the detector achieves BLIP, i.e. only the background photon shot noise is considered in calculating the ideal D^* curve, and by assuming a fixed quantum efficiency. Only two factors therefore affect the ideal D^*: the peak responsivity and the background photon shot noise. As we can see in Figure 1.7, the background photon shot noise, which is the integral of the spectral photon flux exitance from a black-body at 300 K with constant quantum efficiency, increases as the cutoff wavelength goes from SWIR to LWIR. Thus, the ideal detectivity curve decreases going from SWIR to LWIR (Figure 1.2). Above 12 μm, the spectral photon flux exitance decreases (Figure 1.7). Therefore, the background photon shot noise does not increase significantly going from LWIR to VLWIR. On the other hand, the peak responsivity keeps increasing as the cutoff wavelength is increased for fixed quantum efficiency. This explains why the ideal D^* curve starts increasing again going from LWIR to VLWIR in Figure 1.2. However, it should be noted that commercial infrared detectors do not follow this theoretical trend. Experimental detectivity D^* values tend to decrease going from SWIR to VLWIR because the detector noise increases as the energy band-gap is decreased.

1.2.6 Fundamental Limitations and Proposed Solution

As mentioned earlier, commercial infrared detectors need to be cooled down to 77 K or lower in order to reduce the detector noise and achieve BLIP. As the temperature is increased, the detector noise becomes too high and decreases D^* by several orders of magnitude. It is interesting to understand the fundamental limitations in HgCdTe infrared detectors since HgCdTe is the dominant semiconductor material for infrared imaging. In HgCdTe infrared detectors, the dark current at high temperatures is limited by Auger generation and recombination (g-r). The Auger effect is an intrinsic g-r mechanism. Auger recombination can be considered to be the inverse process of impact ionization, i.e. Auger generation, where a three-particle Coulomb interaction occurs. More details on the Auger effect are given in the following chapter.

Auger processes become more important and degrade the performances of HgCdTe photodiodes as the energy band gap is decreased and/or the temperature is increased. This is illustrated in Figure 1.8. The zero-bias resistance-area product R_0A can vary by a few orders of magnitude depending on the CdTe alloy composition, i.e. the HgCdTe energy band-gap, and the temperature. To decrease the number of hot carriers and limit Auger effects, HgCdTe photodiodes require a cooling system to operate at 77 K. These cryogenic cooling systems limit the weight, size and power consumption of HgCdTe focal plane arrays (FPA). Therefore, there is great interest in increasing the operating temperature of HgCdTe photodiodes without sacrificing performance. Devices for this purpose are commonly referred as High Operating Temperature (HOT) HgCdTe infrared detectors. Although the ultimate goal is to achieve high sensitivity uncooled HgCdTe infrared sensors, the goal of this work is to analyze and develop this concept in order to pursue BLIP in thermoelectrically-cooled (TE-cooled) HgCdTe devices. We are therefore developing high sensitivity infrared imaging technology with operating temperature on the order of 180-200 K. $Hg_{1-x}Cd_xTe$ is the material of choice here because of its unique properties for infrared imaging as described in the following chapter. We believe it is the best suited material in order to achieve this goal. As far as we know, BLIP has not been reported in TE-cooled HgCdTe photodiodes in MWIR or LWIR bands

and efforts leading to this goal can potentially lead to major improvements in infrared imaging technology, including lighter and smaller systems with less power consumption.

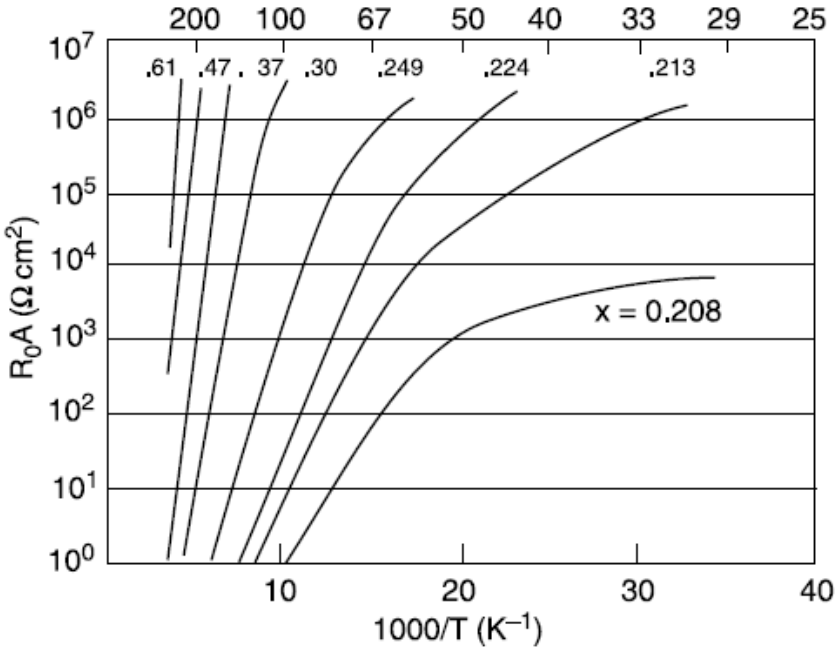

Figure 1.8: Performance of a variety $Hg_{1-x}Cd_xTe$ photodiodes made from a range of alloy compositions, as illustrated by the R_0A of the average array diode as a function of inverse temperature [5].

One promising approach to increase the operating temperature of HgCdTe devices was first proposed by Elliott and Ashley [6]. Since then, device designs have been proposed and discussed to suppress Auger processes in HgCdTe devices by reducing carrier densities below thermal equilibrium through the application of bias. These HOT detectors consist of a middle lightly doped 'ν' (n-type) or 'π' (p-type) active region which acts as an absorber contacted by heavily doped n+ and p+ larger band gap regions. Typical device structure and band diagram is shown in Figure 1.9 for the case of a middle lightly doped 'ν' (n-type) active region. If properly designed, an increasing reverse bias applied to this device results in a decrease of both minority hole and majority electron carrier concentrations in the middle layer below equilibrium values. This results in a decrease of Auger processes – and associated detector noise – in the active region of HOT devices. When operated under reverse bias conditions, HOT devices can therefore

potentially achieve BLIP at higher temperatures than standard HgCdTe infrared devices. More details on the operating principles of HOT devices will be given later.

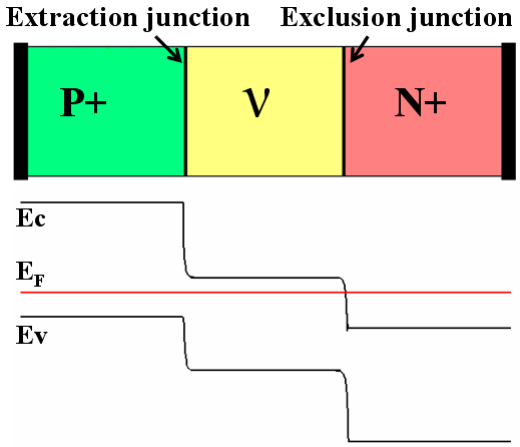

Figure 1.9: HgCdTe HOT infrared photodiode structure and its corresponding calculated energy band profile at zero bias.

Analytical [7] models were developed in order to study these devices. We believe that numerical models are more appropriate when analyzing these multi-layer structures, where realistic features such as compositional grading and implant/diffusion doping profiles are critical for accurate modeling. The general approach and effects of non-equilibrium operation of Auger-suppressed HgCdTe infrared photodiodes are well understood. However, the complex relationships of carrier generation and dependencies on non-uniform carrier profiles in the device prevent the development of simplistic analytical device models with acceptable accuracy. Finite element methods are used in this work to accurately model the devices and design optimized structures. This model includes self-consistent, steady-state solutions of Poisson's equation and the carrier continuity equations for carrier densities, Boltzmann transport theory and published models for generation-recombination processes in HgCdTe.

The experimental fabrication of Auger-suppressed HgCdTe photodiodes remained a challenge for a long time. Indeed, HgCdTe epitaxial growth and device processing technology could not achieve the material quality and device geometry required theoretically for such devices. State-of-the-art HgCdTe growth and processing techniques are used in this work in order to fabricate optimized Auger-suppressed HgCdTe infrared photodiodes. A full temperature-dependent device characterization is presented. We also

assess the potential of these novel devices to replace standard cryogenic cooled HgCdTe infrared devices.

In this chapter, we have given an introduction to IR imaging. We have also introduced important figures of merit for infrared photodiodes, and have pointed out the problem and limitations in HgCdTe devices addressed in this study. In Chapter 2, we give an overview of the main material parameters and recombination mechanisms in $Hg_{1-x}Cd_xTe$. This allows us to define the parameters models that are included in the HgCdTe numerical device model developed in this work. In Chapter 3, we focus on HgCdTe infrared devices. An overview of HgCdTe processing technology is given. We look at the operation, performance and limitations of standard HgCdTe IR photodiodes with a more practical and experimental point of view. The operating principles of our proposed HgCdTe HOT devices are also presented, along with a literature review on HOT devices. In Chapter 4, we present the details of the device model developed in this work in order to study HOT devices. In Chapter 5, our device model is used in order to predict and compare the performance of standard HgCdTe devices with HOT devices for response in both MWIR and LWIR. In Chapter 6, we take a close look at the predicted behavior of HOT devices using the device model. We choose one particular case of HOT device with cutoff wavelength of 5 μm (MWIR) and operating temperature of 200 K, and look at the influence of the main material and device parameters on the HOT detector noise and detectivity D^*. From what is learned in Chapter 5 and Chapter 6, we will see that our device model can be used to design optimized HgCdTe HOT devices for experimental device fabrication. In Chapter 7, we present the details of the material growth and device processing techniques employed in this study. We also talk more in details about the critical issue of p-type doping in HgCdTe and present the novel processing technique developed in order to achieve p-type doping in the fabricated HOT devices. Finally, in Chapter 8, we present the full temperature-dependent device characterization of HOT IR photodiodes fabricated in this work. The experimental device data is analyzed using our device model. From this, we are able to determine which processes limit the performance of the experimental HOT devices and which improvements are needed in order to achieve near-theoretical limit performance in future

HOT device designs. The main findings from this work and a discussion on future work for HgCdTe HOT technology are included in Chapter 9.

Two appendices are also included which are related to side studies done during this dissertation work, but which are not directly related to HgCdTe HOT devices. Appendix A describes the Monte Carlo simulation model that we used to study electron transport in HgCdTe. Some of the results from this Monte Carlo model are included in Chapter 2 when describing the carrier mobility in HgCdTe. Appendix B is an experimental study on using ohmic organic electrodes to contact HgCdTe instead of typical metal electrodes (such as Au or In) in order to reduce the stress in the material. A list of references used in this work is also included at the end.

Chapter 2
Properties of HgCdTe: Material

In this chapter, the important properties of the semiconductor $Hg_{1-x}Cd_xTe$ are introduced. First, we give an overview of growth techniques for HgCdTe. Then, the main material electronic and optical properties are presented. We explain why HgCdTe is so well-suited for infrared imaging applications. The main generation-recombination mechanisms in HgCdTe are also discussed. This allows introducing the HgCdTe material and recombination models and expressions included in the numerical model developed in order to study HgCdTe infrared photodiodes and which is further detailed in the following chapter. This also allows discussing some important limitations in HgCdTe, both intrinsic and extrinsic, i.e. related to material growth and device processing.

2.1 Crystal Growth

High-quality semiconductor material is essential to the production of high-performance and affordable infrared photodetectors. The main requirements of the material are low defect density, large size of wafers, uniformity and reproducibility of intrinsic and extrinsic properties. Steadily achieving these goals, preparation of $Hg_{1-x}Cd_xTe$ evolved from high-temperature melt grown bulk crystals to low-temperature liquid and vapor phase epitaxy.

2.1.1 Bulk Crystals

Good knowledge of phase diagrams is essential for proper design of the growth process. The phase diagrams and their implications for $Hg_{1-x}Cd_xTe$ crystal growth have been extensively discussed in the literature [1]. Although growth is not studied in this work, we present a brief overview of the main bulk and epitaxial growth techniques in order to discuss the evolution and state-of-the-art of HgCdTe technology.

Despite the rapid progress that has taken place in the last two decades in various epitaxial techniques for an HgCdTe ternary alloy system, bulk growth methods still play an important role in preparing device quality material and producing substrates for these epitaxial techniques. There are two main types of bulk growth techniques: growth from the melt and growth from the vapor. Much of HgCdTe bulk crystal growth development has been founded by industry. Details of these growth techniques therefore remain largely proprietary. Several historical reviews of the development of bulk HgCdTe have been published [8], [9]. Three prime techniques are used: solid state recrystallization (SSR), Bridgman and travelling heater method (THM).

SSR is crystal growth from the solid phase at temperatures close to the melting point. The SSR method has some drawbacks. As no segregation occurs, all impurities present in the charge are frozen in the crystal, and high-purity starting elements are required. The maximum diameter of the ingots is limited to about 1.5 cm, as the cooling rate of large-diameter charges is too slow for suppression of the segregation. Also, the crystal contains low grain boundaries.

In the Bridgman process, elemental Cd, Hg and Te are loaded into a clean silica ampoule, homogenized by melting/rocking. It is then frozen slowly from one end in a vertical system to produce single crystal or, more often, a large-grained ingot. Large crystal sizes coupled with a relatively large growth rate (1-2 mm/h) make this technique relatively cheap and versatile. However, only a limited part of the crystal can be used for specified cutoff wavelength detector fabrication. Also, high partial pressure of Hg can cause ampoule failure.

Growth by THM combines the advantages of low-temperature solution growth with steady-state conditions, as in zone melting. This technique has been used mainly for

Te-based ternary alloys. A homogenous alloy can be used as the starting ingot or segments of the binaries can be employed. Very slow growth rates (0.1 mm/h) are typical, but diameters up to 40 mm have been accomplished.

At present, bulk crystal growth from the liquid phase is most frequently used for fabrication of device-quality materials with ingot diameters of about 1.5 cm. They are used mostly for n-type single-element photoconductors, arrays, and Signal Processing In The Element (SPRITE) detectors for first-generation imaging and seeking systems. Other applications include high-reliability, space qualified custom detectors for various NASA instruments and various commercial systems such as infrared spectrometers. Good uniformity, excellent electrical purity (less than $1x10^{14}$ cm^{-3}), high mobilities and minority carrier lifetimes are standard features for commercially available materials. Cost of the device-quality material is still high, ranging from $500-$1000 for a wafer with a diameter of 1.5 cm. Bulk growth of HgCdTe has been largely unsuccessful for second- and third-generation photovoltaic applications because of material defects and regions of high dislocation density.

2.1.2 Epitaxial Layers

An increasing interest has been shown in the past two decades toward epitaxy of $Hg_{1-x}Cd_xTe$. The epitaxial techniques offer, in comparison with bulk growth techniques, the possibility to grow large area (<30 cm^2) epilayers. Epitaxial techniques also offer the possibility to grow sophisticated layered structures with good lateral homogeneity, abrupt and complex composition and doping profiles which can be designed to improve the performance of photodetectors. Typical applications include novel heterostructure devices for third-generation infrared systems based on HgCdTe such as two-color infrared photodiodes, avalanche photodiodes (APD) and our proposed Auger-suppressed HgCdTe infrared photodiode. CdZnTe is the most widely substrate for HgCdTe epitaxial growth. As illustrated in the following section, it is a lattice-matched substrate giving defect densities as low as 10^4 cm^{-2}. There is also a lot of research on alternative substrates in order to increase the size of the wafers and decrease the cost (typically $100-$500 per

square centimeter, polished) [1]. One potential candidate is CdTe-on-silicon but defect densities are still in the low 10^6 cm^{-2}.

The growth is performed at low temperatures which makes it possible to reduce the native defect density. Due to the low partial pressures of Hg, there is no need for thick-walled ampoules and the growth can be carried out in reusable production-type growth systems. The as-grown epilayers can be annealed in-situ at low temperatures. The epitaxial growth technology for HgCdTe has benefited greatly from the III-V epitaxial technology base. It is currently making rapid progress although its maturity lags approximately 5-10 years behind the III-V epitaxial technology.

Among the various epitaxial techniques, the Liquid Phase Epitaxy (LPE) is the most matured method. LPE is a single-crystal growth process in which growth from a cooling solution occurs onto a substrate. LPE is a demonstrated technology which can achieve high purity HgCdTe epilayers for high sensitivity cooled HgCdTe homojunction infrared photodiodes. However, LPE does not offer a good control of the junction dimensions which is critical in novel heterostructure HgCdTe devices.

The vapor phase epitaxy growth of HgCdTe is typically done by nonequilibrium methods: metal-organic chemical vapor deposition (MOCVD) and molecular beam epitaxy. The great potential benefit of MOCVD and MBE over other methods is the ability to modify the growth conditions dynamically during growth to tailor band gaps, add and remove dopants, prepare surfaces and interfaces, add passivations, perform anneals, and even grow on selected areas of the substrate. The growth control is exercised with great precision to obtain basic material properties comparable to those routinely obtained from equilibrium growth. The growth temperature is less than 200 °C for MBE but around 350 °C for MOCVD. Thus, it is more difficult to control the p-type doping in the MOCVD due to the formation of Hg vacancies (p-type dopants in HgCdTe) at higher growth temperatures. HgCdTe MBE technology offers low temperature growth under an ultrahigh vacuum environment, in-situ n-type and potentially in-situ p-type doping, and control of composition, doping and interfacial profiles. Table 2.1 summarizes the advantages and disadvantages of the major HgCdTe growth techniques.

Growth technique	Advantages	Disadvantages
Solid state recrystallization	• High purity • Low dislocation density (localized) • Production process	• Small ingots • Long growth-cycle times • Subgrain boundaries • Multiple layer impossible
Bridgman	• High purity • Low cost equipment • Production process	• High axial and radial nonuniformity • Low growth rate • Multiple layers impossible
Traveling heater method	• High purity • Single crystal growth possible • Large diameter ingots	• Long growth-cycle times • Axial nonuniformity • Multiple layers impossible
Liquid phase epitaxy	• High purity • Demonstrated technology • Production scale-up	• Melt retention (vertical dipping) • Poor interface sharpness (app. 2–3 μm) • Multiple layers difficult
Metalorganic chemical vapor deposition	• Good surface morphology • Sharp interfaces (< 1μm) • Production scale-up	• Purity of starting materials • Marginal electrical properties • Stringent substrate preparation
Molecular beam epitaxy	• Sharpest interfaces, superlattices • Low growth temperature • Good surface morphology • In-situ analysis	• Expensive equipment • Low growth rate • Stringent substrate preparation

Table 2.1: Comparison of bulk and thin-film HgCdTe growth techniques [1].

2.2 Fundamental HgCdTe Material Properties

2.2.1 Band Structure

$Hg_{1-x}Cd_xTe$ is a binary alloy direct band-gap semiconductor. Alloy of a semimetal (HgTe) and a semiconductor (CdTe). The electrical and optical properties of HgCdTe are determined by the energy gap structure in the vicinity of the Γ-point of the Brillouin zone. Figure 2.1 shows the calculated band structure of CdTe and HgTe [10].

The band-gap of HgCdTe is very dependent on the CdTe mole fraction x and the temperature as we can see in Figure 2.2 [5]. It has the unique property that it can be tuned across the whole infrared spectrum, including the two bands of interest MWIR and LWIR. In addition to that, it has high absorption coefficient, high electron mobility and large carrier lifetime. These are some of the reasons why HgCdTe infrared photodiodes offer nowadays the best performances for MWIR and LWIR response. The most widely used empirical expression to approximate the energy band-gap (eV) at the Γ-point is due to Hansen et al. [11].

This expression is used in this study and is given below:

$$E_G(x,T) = -0.30 + 1.93x - 0.81x^2 + 0.832x^3 + 5.35\times10^{-4}T(1-2x) \qquad (21)$$

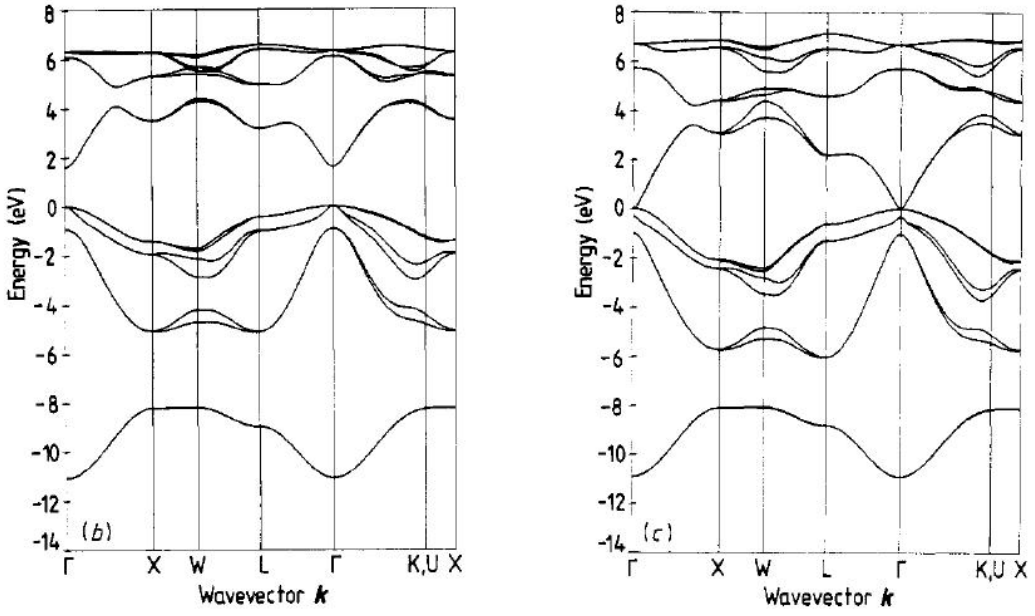

a) **b)**

Figure 2.1: Calculated band structures of a) CdTe and b) HgTe [10].

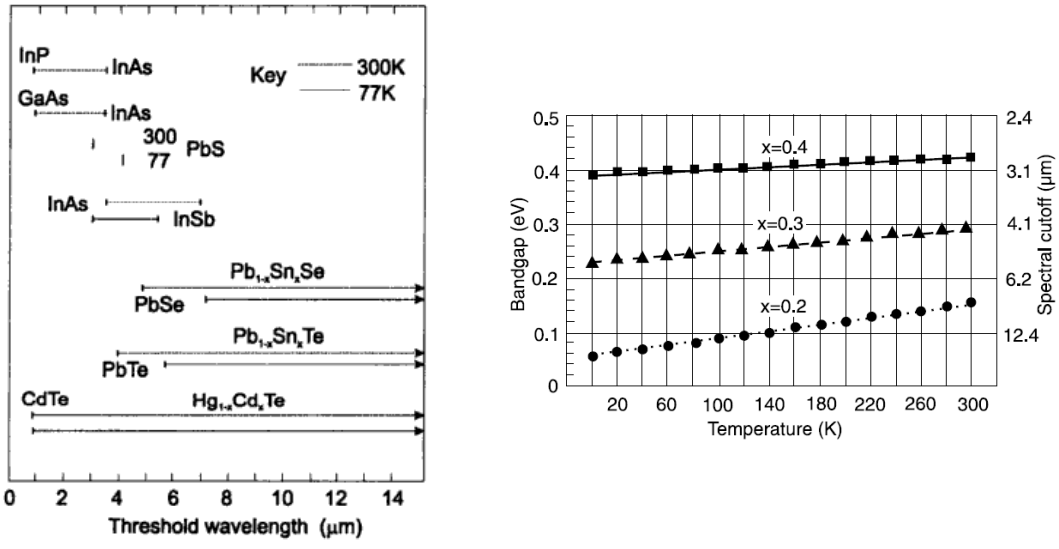

a) **b)**

Figure 2.2: a) Wavelength response covered by various infrared detectors fabricated from binary compounds and ternary alloys. The solid lines represent ranges covered 77 K, the dashed lines refer to 300 K. b) HgCdTe energy band-gap and cutoff wavelength as a function of temperature for different CdTe mole fractions x.

As we can see in Figure 2.3 [5], the band-gap can be tuned across a wide spectral range without any significant change from the lattice constant. This means that HgCdTe can be used to form nearly lattice-matched heterojunctions. It also has a lattice-matched substrate which is CdZnTe. Heterojunctions cannot be done with most III-V compounds such as InAs or InSb and lattice-matched substrates are limited. Therefore, HgCdTe is also the most appropriate material to take advantage of heterostructures such as in Double Layer Planar Heterojunction (DLPH) devices and third-generation infrared systems such as two-color (MWIR/LWIR) infrared sensors.

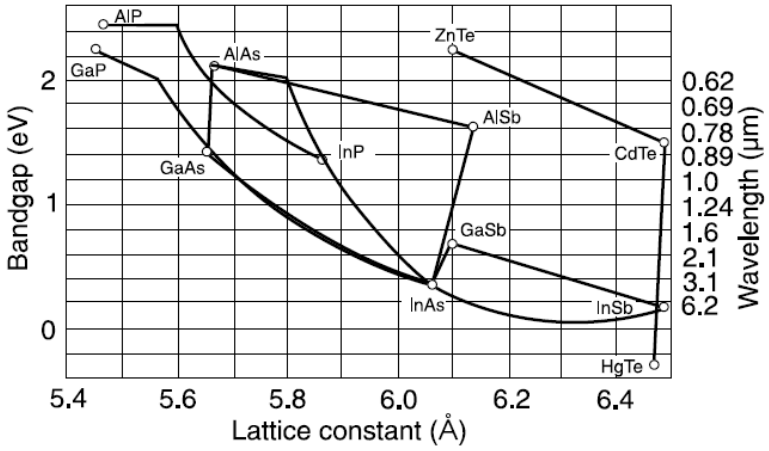

Figure 2.3: Comparison of the band-gap versus lattice constant variation with alloy composition for $Hg_{1-x}Cd_xTe$, with the lattice constant for a variety of III-V compounds [5].

The electron affinity χ (eV) can be approximated by the following expression [12] that we use in this study:

$$\chi(x,T) = 4.23 - 0.813\left[E_G(x,T) - 0.083\right] \tag{22}$$

2.2.2 Intrinsic Carrier Concentration and Carrier Effective Mass

The expression that we use in this work and that has become the most widely used is that of Hansen and Schmidt [13]:

$$n_i = \left(5.585 - 3.82x + 1.753\times10^{-3}T - 1.364\times10^{-3}xT\right)\times10^{14}E_g{}^{0.75}T^{1.5}\exp\left(-\frac{E_g}{2kT}\right) \tag{23}$$

Hansen and Schmidt calculated the intrinsic carrier concentration in HgCdTe using the Kane non-parabolic approximation for band structure, a value of 0.443 m0 for the heavy-hole effective mass and the approximate expression for E_G given above. These calculations have been fitted to obtain this approximate expression for n_i.

Figure 2.4 shows the intrinsic carrier concentration in HgCdTe for different values of Cd alloy compositions, x. We can see that the intrinsic carrier concentration can become quite large as the temperature is increased and/or the energy band-gap is decreased. The absorber doping concentration has to be usually as low as possible in HgCdTe infrared photodiodes in order to minimize recombination and maximize the minority carrier diffusion length. The lowest controllable doping level achievable in HgCdTe is on the order of $5x10^{14}$ cm^{-3} or $1x10^{15}$ cm^{-3}. Therefore, as discussed in the previous chapter, it is critical to cool down standard HgCdTe infrared devices in order to avoid the layers to become intrinsic due to thermal generation. Large equilibrium carrier concentration in the absorber layer of HgCdTe infrared photodiodes can result in significant Auger processes and reduced minority carrier diffusion length, i.e. the detector noise is increased and the detectivity D^* is decreased.

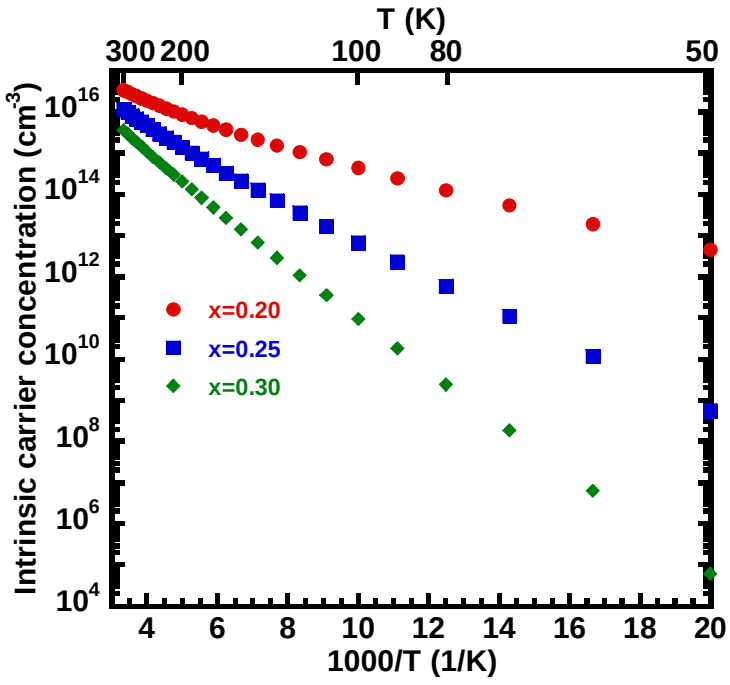

Figure 2.4: Intrinsic carrier concentration versus temperature for different Cd alloy compositions x in $Hg_{1-x}Cd_xTe$.

The electron effective mass m_e^* in the narrow-gap mercury compounds can be established according to the Kane band model. In this work, we use Weiler's expression [14] using Ep=19 eV, the spin-orbit splitting energy Δ=1 eV and F=-0.8:

$$m_e^* = \frac{1}{-0.6 + 6.333\left(\frac{2}{E_G} + \frac{1}{E_G + 1}\right)} \tag{24}$$

The heavy-hole effective mass m_h^* is taken in this work to be 0.55 m_0, which is a common value and is in the range of heavy-hole effective masses reported previously [15]. The light-hole effective mass is close to the electron effective mass [16], i.e. about two orders of magnitude lower than the heavy-hole effective mass. Due to the weak density of light holes and lack of information on their properties, we choose to neglect their contribution in the device operation in this work.

2.2.3 Carrier Mobility

Due to small effective mass, the electron mobility in HgCdTe is particularly high. Heavy-hole mobility is usually taken as two orders of magnitude lower than electron mobility. In HgCdTe device simulation, the electron mobility is usually taken from the empirical formula based on Scott's Hall data [17] ($cm^2/V/s$):

$$\mu_e = \frac{9\times10^8\left(\frac{0.2}{x}\right)^{7.5}}{Z^{2\left(\frac{0.2}{x}\right)^{0.6}}} \tag{25}$$

If T>50K, then Z=T, and if T≤50K, then:

$$Z = \frac{1.18\times10^5}{2600 - |T-35|^{2.07}} \tag{26}$$

Although experimental data on HgCdTe electron mobility can vary by a factor of two for a given case of temperature and Cd alloy composition [1], this empirical model gives a good fit of the low-field electron mobility in HgCdTe dependence on temperature and Cd alloy composition, x. However, the electron mobility in HgCdTe is also dependent on the electric field and the doping concentration. It is important to study these

dependences as part of the development of an HgCdTe device model. As far as we know, no analytical model for the electron mobility dependence on electric field and doping concentration in HgCdTe has been reported.

Monte Carlo simulations are performed in this work in order to calculate the electron mobility in HgCdTe. Monte Carlo has been used extensively to study transport in Si [18], [19], Ge [20] and III-V semiconductors such as GaAs [21]-[26], InGaAs [27] and AlGaAs [28]. Monte Carlo has also been used to study transport in HgCdTe [29], [30]. However, it is usually for one specific case of HgCdTe alloy composition and temperature or to study impact ionization in HgCdTe avalanche photodiodes (APD) [31], [32]. Hence, we developed our own model which can be easily used for our specific cases. In the Monte Carlo process, the electron is considered as a point particle whose scattering rates are given by the Fermi golden rules expression. The following scattering mechanisms are considered: ionized impurity scattering, alloy scattering, polar optical phonon scattering, acoustic phonon scattering and electron-hole scattering. The transport of one electron in a spherical non-parabolic Γ-valley conduction band is simulated. Details of the Monte Carlo model are given in Appendix A. We calculate the ratio of the drift velocity to the electric field v_d/E in order to calculate the low-field mobility at a given temperature. We choose the value of the electric field to be high enough to avoid the large statistical uncertainty originating from thermal motion, but low enough to verify the independence of this ratio from field strength.

First, our Monte Carlo calculations are compared with experimental data. Figure 2.5 shows the low-field electron mobility in HgCdTe versus Cd alloy composition obtained by Hall measurements at 77 K and 300 K [33] compared to our Monte Carlo calculations with a low donor concentration of $2x10^{15}$ cm^{-3}. Also shown is the calculation from the empirical model based on Scott's Hall data presented above. Our Monte Carlo calculations compares reasonably well with experimental data on electron mobility in a wide range of HgCdTe alloy compositions considering the spread in reported data for HgCdTe [1]. The range of alloy compositions considered here covers most of the range used for practical HgCdTe infrared photodiodes. Figure 2.6 shows the low-field electron mobility versus temperature obtained by Hall measurements for x=0.20 and x=0.36 [17] compared to our Monte Carlo calculations with a donor concentration of $2x10^{15}$ cm^{-3}. We

also show the calculation from the empirical model developed from this Hall data. Again, our Monte Carlo calculations compares well with experimental data in a wide range of temperatures between 77 K and 300 K. The dependence on x of the electron mobility results primarily from the dependence on x of the energy band-gap. The temperature dependence of the electron mobility comes primarily from the competition between various scattering mechanisms that are temperature-dependent.

Although our Monte Carlo calculations tend to be on the upper end of reported experimental data for electron mobility in HgCdTe, we believe this is expected from a theoretical model. From this, it is concluded that this model manages to reproduce well the low-field mobility dependence on both Cd alloy composition and temperature in our range of interest to study HgCdTe infrared devices. The advantage of this Monte Carlo model is that we can now study the electron mobility dependence on electric field and doping level which is not well documented.

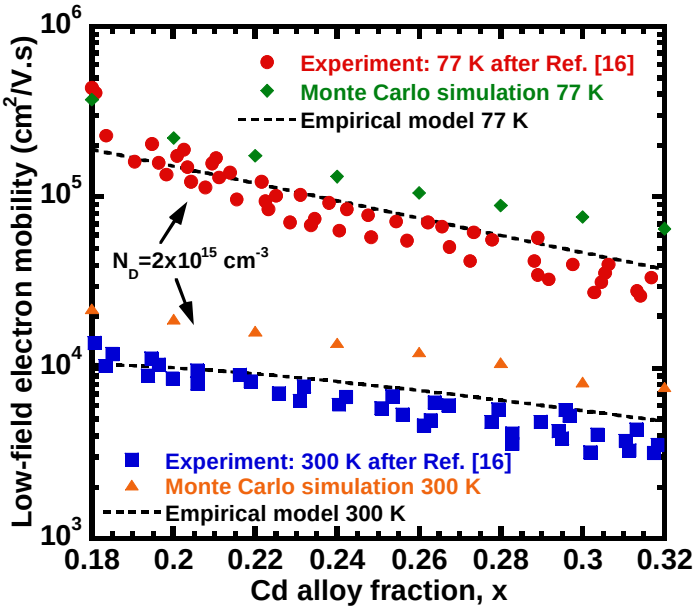

Figure 2.5: Low-field electron drift mobility in $Hg_{1-x}Cd_xTe$ versus Cd alloy composition. Experimental data at 77 K (circle) and 300 K (square) is taken from [33] and is compared with Monte Carlo calculations at 77 K (diamond) and 300 K (triangle). Also shown is the curve at 77 K and 300 K from the empirical model based on Scott's Hall data (dashed line).

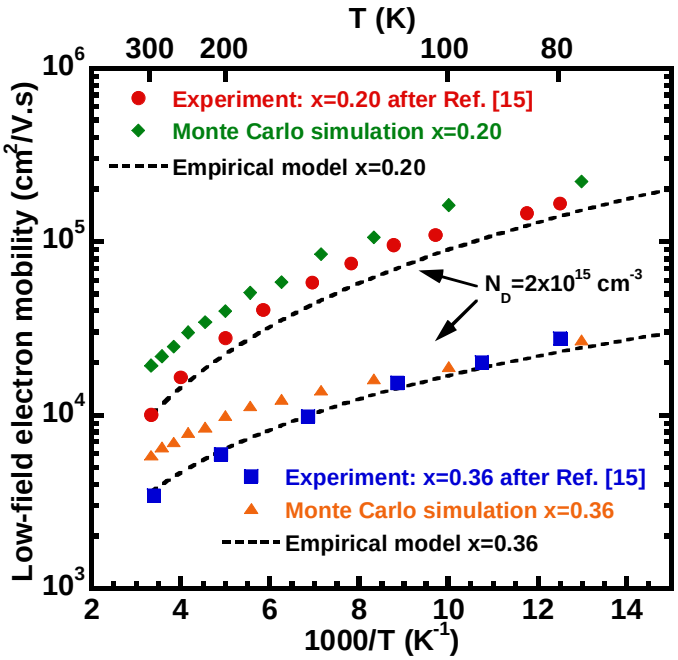

Figure 2.6: Low-field electron drift mobility in $Hg_{1-x}Cd_xTe$ versus temperature. Experimental data for x=0.20 (circle) and x=0.36 (square) is taken from [17] and is compared with Monte Carlo calculations for x=0.20 (diamond) and x=0.36 (triangle). Also shown is the curve for x=0.20 and x=0.36 from the empirical model based on Scott's Hall data (dashed line).

First, the low-field electron mobility dependence on donor doping level in HgCdTe is studied. We consider the case of a singly ionized donor such as indium, which is the common donor in HgCdTe, and realistic doping levels between 10^{14} cm^{-3} and 10^{17} cm^{-3}. Donors are fully ionized which is a reasonable assumption for our temperature range of interest 77-300 K as shown in a later section. Figure 2.7 shows the Monte Carlo calculations of the low-field electron mobility versus donor concentration at T=77 K for x=0.20 and x=0.30. As seen in Figure 2.7, these calculations can then be fitted to a simple formula which can be easily included in numerical simulation device models in order to take into account doping-dependent low-field mobility. In this case, we use a simplified Masetti's formula [34]:

$$\mu_e(N_D) = \mu_{\min} + \frac{\mu_{\max} - \mu_{\min}}{1 + \left(\frac{N_D}{C_r}\right)^{\alpha}} \tag{27}$$

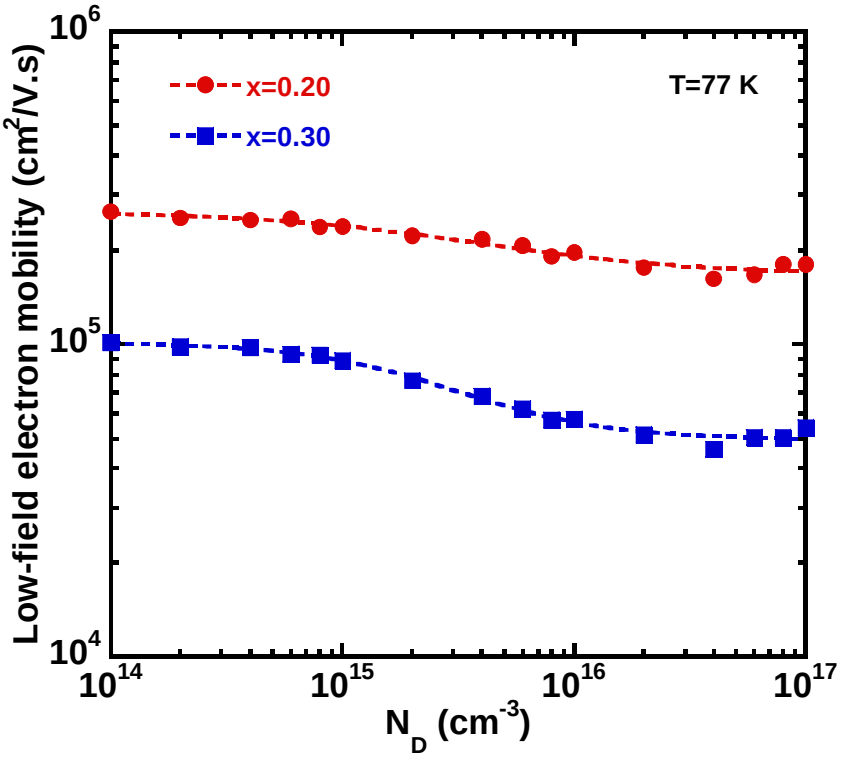

Figure 2.7: Monte Carlo calculations of the low-field drift mobility in HgCdTe versus donor concentration for x=0.20 (circle) and x=0.30 (square). Also shown is the fitting curve (dashed line) for each case. Fitting parameters for x=0.20 are: μ_{max}=2.6517x10^5, μ_{min}=1.6669x10^5, C_r=3.0720x10^{15} and α=0.90917. Pearson's R coefficient is 0.98149. Fitting parameters for x=0.30 are: μ_{max}=1.0122x10^5, μ_{min}=4.9538x10^4, C_r=2.3698x10^{15} and α=1.3095. Pearson's R coefficient is 0.99573.

The low-field electron mobility in p-type HgCdTe can also be calculated using this model. We consider that acceptors act as ionized impurity scattering centers and we also consider electron-hole scattering for these calculations. Singly ionized acceptors and full ionization are considered like in the case of arsenic p-type doping in HgCdTe. Arsenic is widely used as an acceptor in HgCdTe and full ionization in the range 77-300 K is a reasonable assumption as discussed in a later section. Results for x=0.20 and x=0.30 at T=77 K are shown in Figure 2.8 along with the curve fit obtained using Masetti's formula. According to our model, the doping dependence of the low-field drift mobility is similar in n-type and p-type HgCdTe, although the values of the mobility are different.

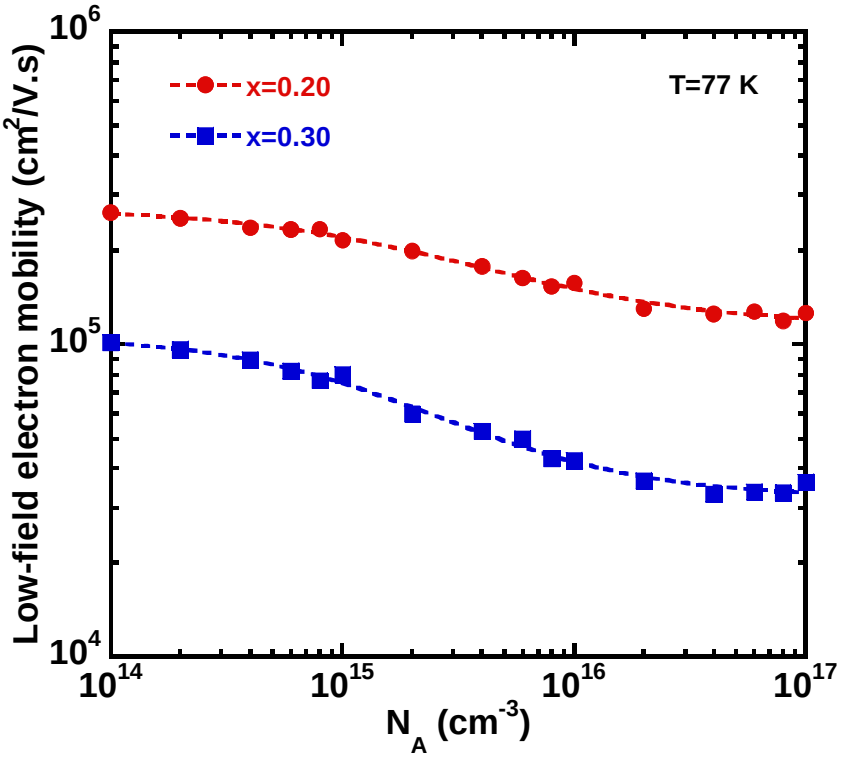

Figure 2.8: Monte Carlo calculations of the low-field drift mobility in HgCdTe versus acceptor concentration for x=0.20 (circle) and x=0.30 (square). Also shown is the fitting curve (dashed line) for each case. Fitting parameters for x=0.20 are: μ_{max}=2.7155x10^5, μ_{min}=1.1440x10^5, C_r=2.3346x10^{15} and α=0.83647. Pearson's R coefficient is 0.99632. Fitting parameters for x=0.30 are: μ_{max}=1.0637x10^5, μ_{min}=3.2324x10^4, C_r=1.3889x10^{15} and α=0.95536. Pearson's R coefficient is 0.99651.

From Figure 2.7 and Figure 2.8, it is found that the low-field electron mobility does not vary significantly for the levels of donor or acceptor doping considered here. Finally, our Monte Carlo model is used to study high-field transport in HgCdTe. It is conventional to cast the functional dependence of the electron high-field mobility $\mu_e(E)$ in terms of the electron drift velocity $v_d(E)$ dependence on the electric field through the relationship $v_d(E)= \mu_e(E)\cdot E$. Figure 2.9 shows the electron drift velocity in HgCdTe versus electric field for x=0.20 and x=0.30 obtained by Monte Carlo calculations. Again, these calculations can be fitted to a simple formula which can now be included in numerical simulation device models in order to account for high-field transport in HgCdTe. The fitting result is also shown in Figure 2.9. In this work, we use the Canali model [35]:

$$\mu_e(E) = \frac{\mu_{e,low}(x,T,N_A - N_D)}{\left(1 + \left(\frac{\mu_{e,low}(x,T,N_A - N_D)E}{v_{sat}}\right)^{\beta}\right)^{1/\beta}} \tag{28}$$

where $\mu_{e,low}$ is the low-field electron mobility ($cm^2/V.s$) which is determined as a function of Cd alloy composition, temperature and doping level as discussed previously, v_{sat} is the saturation velocity (cm/s) and is a fitting parameter along with β. Such analytical expressions for high-field transport can be easily included in HgCdTe device models to study avalanche photodiodes (APD) for example where electric field values can be high. However, the electric field values remain relatively low in the devices studied in this work.

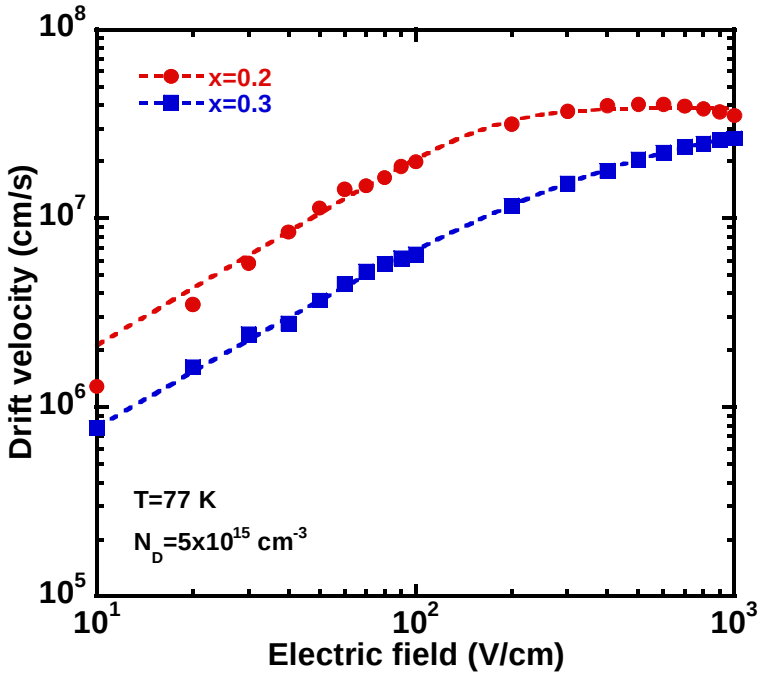

Figure 2.9: Monte Carlo calculations of the drift velocity in HgCdTe versus electric field for x=0.20 (circle) and x=0.30 (square). Also shown is the fitting curve (dashed line) for each case. Fitting parameters for x=0.20 are: v_{sat}=3.8604x10^7, α=3.3969. Pearson's R coefficient is 0.99538. Fitting parameters for x=0.30 are: v_{sat}=3.8053x10^7 and α=1.0784. Pearson's R coefficient is 0.99981.

All the main dependencies of the electron mobility in HgCdTe have been studied using this model. It is found that the temperature and Cd alloy fraction have the most

influence on the electron mobility and that it is not critical to consider high-field velocity saturation for the devices we study. Consequently, the empirical expression for the electron mobility (Equation (25)) gives a good approximation and is included in our HgCdTe device model. The heavy-hole mobility is considered to be a factor k of the electron mobility ($k \cdot \mu_e$). The factor k is taken as a fitting parameter varied around the value 0.01, which is the typical value used in HgCdTe device modeling.

2.2.4 Optical Properties

Optical properties of HgCdTe have been investigated mainly at energies near the band-gap. There still appears to be considerable disagreement among the reported results concerning absorption coefficients [1]. This is caused by different concentrations of native defects and impurities, non-uniform composition and doping, thickness inhomogeneities of samples, mechanical strains and different surface treatments. The absorption coefficient for optical carrier generation can be calculated within the Kane model, including the Moss-Burstein shift.

In high-quality HgCdTe samples, the measured absorption in the short-wavelength region is in good agreement with the Kane model calculation. The situation appears to be complicated in the long-wavelength edge by the appearance of an absorption tail extending at energies lower than the energy band-gap [1]. This tail has been attributed to the composition-induced disorder. We use Hougen's model in this work for the absorption coefficient in HgCdTe [36] which is widely used in HgCdTe device modeling. The absorption tail ($E \leq E_g$) obeys a modified Urbach's rule:

$$\alpha(E) = \alpha_0 \exp\left[s_w (E - e_o)\right] \tag{29}$$

For the high absorption region ($E > E_g$), the simplified Kane absorption is used:

$$\alpha(E) = \beta \sqrt{E - E_g} \tag{30}$$

Where:

$$\alpha_0 = \exp(53.61x - 18.88) \tag{31}$$

$$s_w = \frac{32670(1 + x)}{81.9 + T} \tag{32}$$

$$e_0 = 1.838x - 0.3424 + 0.148x^2 \tag{33}$$

$$\beta = \frac{\alpha_T}{\sqrt{E_T - E_g}} \tag{34}$$

$$\alpha_T = 100 + 5000x \tag{35}$$

$$E_T = \frac{1}{s_w}\ln\left(\frac{\alpha_T}{\alpha_0}\right) + e_0 \tag{36}$$

$$E_g = E_T - \frac{0.5}{s_w} \tag{37}$$

Direct band-gap semiconductors, such as HgCdTe, have a sharp onset of optical absorption as the photon energy, E, increases above the energy band-gap E_G. The measured optical absorption coefficient at T=77 K is illustrated in Figure 2.10 for a wide range of alloy compositions. Strong absorption coefficient in the infrared spectrum allows HgCdTe structures to absorb a very high percentage of the signal while being relatively thin.

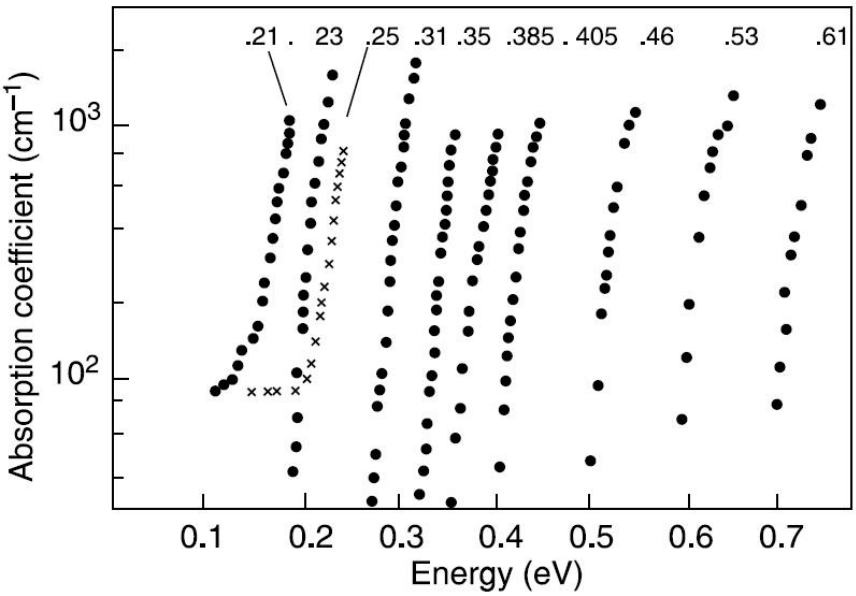

Figure 2.10: Optical absorption coefficient of $Hg_{1-x}Cd_xTe$ as a function of energy for different alloy compositions, x [5].

The high-frequency dielectric constant ε_∞ and the static dielectric constant ε_s are usually derived from reflectivity data in evaluating the real and imaginary parts of ε. The

dielectric constants are not a linear function of x and temperature dependences were not observed within the experimental resolution [1]. These dependencies can be described by the following relations which we use in this study:

$$\varepsilon_s(x) = 15.2 - 15.6x + 8.2x^2 \tag{38}$$

$$\varepsilon_s(x) = 20.5 - 15.5x + 5.7x^2 \tag{39}$$

2.2.5 Summary of Material Properties

To summarize, Table 2.2 and Table 2.3 lists the main material properties of $Hg_{1-x}Cd_xTe$ that we discussed in this section for x=0.2, x=0.3 and x=0.4 at T=77 K and T=300 K respectively.

	$Hg_{0.8}Cd_{0.2}Te$	**$Hg_{0.7}Cd_{0.3}Te$**	**$Hg_{0.6}Cd_{0.4}Te$**
Energy band-gap E_G (eV)	0.083	0.243	0.4019
Electron affinity χ (eV)	4.23	4.10	3.97
Intrinsic carrier concentration n_i (cm^{-3})	$9.98x10^{13}$	$1.20x10^{9}$	$1.02x10^{4}$
Electron effective mass m_e^* (m_0)	0.0063	0.0177	0.0282
Heavy-hole effective mass m_h^* (m_0)	0.55	0.55	0.55
Electron low-field mobility μ_e ($cm^2/V.s$)	$2x10^{5}$	$7x10^{4}$	$2x10^{4}$
Hole low-field mobility μ_h ($cm^2/V.s$)	$2x10^{3}$	$7x10^{2}$	$2x10^{2}$
Static dielectric constant ε_s	17.99	16.90	15.93
High-frequency dielectric constant ε_∞	12.31	11.03	9.87

Table 2.2: Material properties of $Hg_{1-x}Cd_xTe$ at T=77 K for x=0.2, x=0.2 and x=0.4.

	$Hg_{0.8}Cd_{0.2}Te$	$Hg_{0.7}Cd_{0.3}Te$	$Hg_{0.6}Cd_{0.4}Te$
Energy band-gap E_G (eV)	0.155	0.291	0.426
Electron affinity χ (eV)	4.17	4.06	3.95
Intrinsic carrier concentration n_i (cm^{-3})	$3.40x10^{16}$	$3.62x10^{15}$	$3.24x10^{14}$
Electron effective mass m_e^* (m_0)	0.0115	0.0209	0.0298
Heavy-hole effective mass m_h^* (m_0)	0.55	0.55	0.55
Electron low-field mobility μ_e ($cm^2/V.s$)	$2x10^4$	$8x10^3$	$3x10^3$
Hole low-field mobility μ_h ($cm^2/V.s$)	$2x10^2$	$8x10^1$	$3x10^1$
Static dielectric constant ε_s	17.99	16.90	15.93
High-frequency dielectric constant ε_∞	12.31	11.03	9.87

Table 2.3: Material properties of $Hg_{1-x}Cd_xTe$ at T=300 K for x=0.2, x=0.2 and x=0.4.

2.3 Generation-Recombination Mechanisms in HgCdTe

As we mentioned in the previous chapter, generation-recombination mechanisms directly affect the performance of infrared photodiodes. They are related with the minority carrier lifetime, i.e. with the minority carrier diffusion length. A short minority carrier diffusion length in the absorber region of the photodiode due to significant recombination induces a large diffusion dark current and reduced external quantum efficiency. Overall, this translates into a smaller detectivity D^* which was defined in the previous chapter.

For small deviations from equilibrium, the total net generation rate approximates the summation of the net generation rate for each g-r mechanism k:

$$G - R = \sum_k (G - R)_k = \sum_k -\frac{\Delta n}{\tau_k} \tag{40}$$

where τ_k is the carrier lifetime associated with the g-r mechanism k as defined in Equation (3). Under the condition of a small excess carrier concentration, the lifetimes

associated with these processes can be treated as independent. Therefore, the resultant total recombination lifetime can be calculated as:

$$\frac{1}{\tau} = \sum_{k} \frac{1}{\tau_k} = \frac{R - G}{\Delta n} \tag{41}$$

The lifetime of photo-generated electrons and holes are among the most parameters in HgCdTe infrared photodiodes. As such, it is critical to develop a clear understanding and proper interpretation of the minority carrier lifetime, along with that of the recombination mechanisms that govern it.

Electron-hole pairs can recombine in two ways. First, an electron can drop directly from the conduction band into an unoccupied state in the valence band. This is known as a direct band-to-band process. Second, an electron initially makes a transition to an energy level lying deep in the band-gap, subsequently recombining with a hole from the valence band. This is known as an indirect process. In the process of electron-hole pair recombination, an excess energy equal to the difference between the energy of the electron and the energy of the hole is released. This energy can be emitted as a photon. In this case, the recombination is said to be radiative. Alternatively, this energy can be dissipated in the lattice in the form of phonons. A third possibility is that this energy can be transferred to a third mobile carrier. This process is called the Auger process. In this work, we consider the most important g-r mechanisms in HgCdTe: Shockley-Read-Hall (SRH), radiative and Auger. We also discuss surface recombination which is a special case of SRH recombination and which can be important when studying HgCdTe infrared devices.

2.3.1 Auger Recombination

The Auger effect is an intrinsic g-r mechanism. Auger recombination can be considered to be the inverse process of impact ionization, i.e. Auger generation, where a three-particle Coulomb interaction occurs. Several band-to-band Auger processes involving different bands and transitions are possible. Beattie [37] has determined ten types of phonon-less Auger recombination mechanisms that are possible in a semiconductor with a single conduction band and a heavy-hole and light-hole band.

Figure 2.11 shows a schematic of Auger-1 and Auger-7. Because Auger-1 and Auger-7, of all the Auger mechanisms, have the smallest threshold ($E_T \sim E_G$, the energy band-gap) and have the largest combined density of states, they are the dominant mechanisms. Auger-1 is a two-band mechanism which involves two electrons colliding in the conduction band. One electron recombines with a heavy hole with the excess energy being transferred to another electron which is excited to a higher energy state in the conduction band. Auger-7 is a three-band mechanism which involves two heavy-holes colliding. One heavy-hole recombines with an electron in the conduction band while the other is filled by an electron in the light-hole band, therefore creating a more energetic hole in the light-hole band. In both mechanisms, energy conservation ($E_i+E_i'=E_f+E_f'$) and momentum conversation ($k_i+k_i'=k_f+k_f'$) are satisfied. Auger generation is simply the reverse process.

In this work, we consider Auger-1 using Blakemore [38] for the intrinsic Auger-1 lifetime $\tau_{A1}{}^{i}$ expression. We consider Auger-7 using Casselman and Petersen [39] for the intrinsic Auger-7 lifetime $\tau_{A7}{}^{i}$ expression. The following expression for the Auger recombination rate ($cm^{-3}.s^{-1}$) is based on Beattie and Landsberg [40]:

$$U_{Auger}^{net} = G_{A1}\left(pn^2 - nn_i^{\,2}\right) + G_{A7}\left(np^2 - pn_i^{\,2}\right) \tag{42}$$

$$G_{A1} = \frac{1}{2n_i^{\,2}\tau_{A1}{}^{i}} = \left[\frac{3.8\times10^{-18}\varepsilon_s^{\,2}\left(1+\frac{m_e^*}{m_h^*}\right)^{0.5}\left(1+2\frac{m_e^*}{m_h^*}\right)}{2n_i^{\,2}\, m_e^*\left|F_1F_2\right|^2\left(\frac{kT}{E_G}\right)^{1.5}} \times \exp\left(\frac{1+2\frac{m_e^*}{m_h^*}}{1+\frac{m_e^*}{m_h^*}}\frac{E_G}{kT}\right)\right]^{-1} \tag{43}$$

$$G_{A7} = \frac{1}{2n_i^{\,2}\tau_{A7}{}^{i}} = G_{A1}\left[\frac{\gamma'\left(1-\frac{5E_G}{4kT}\right)}{1-\frac{3E_G}{2kT}}\right]^{-1} \tag{44}$$

$$\frac{\tau_{A7}^{\ i}}{\tau_{A1}^{\ i}} = \frac{\gamma'\left(1-\frac{5E_G}{4kT}\right)}{1-\frac{3E_G}{2kT}} = \gamma \tag{45}$$

where n_i is the intrinsic carrier concentration (cm^{-3}), m_e^* and m_h^* are the electron and hole effective mass respectively (m_0) and E_G is the energy band-gap (eV). We use the overlap integral $|F_1F_2|$ and γ as fitting parameters in our HgCdTe device numerical model. The overlap integral $|F_1F_2|$ has been reported in the range 0.1-0.3 [1]. The γ-ratio has been reported in the range 3-60 [41].

Expressions used for the intrinsic carrier concentration and the electron and hole effective mass have been given in the previous section. The Auger-1 lifetime expression, shown below, is widely used in device modeling and can usually provide a reasonable fit to experimental data. The Auger-7 lifetime expression, also shown below, is also widely used, though Krishnamurthy and Casselman [42] have recently shown that this $1/p^2$ dependence is inaccurate at high doping levels $>10^{16}$ cm^{-3}. Expressions for the Auger-7 intrinsic lifetime and Auger-7 lifetime likely need to be reviewed using an accurate HgCdTe band structure:

$$\tau_{A1} = 2\tau_{A1}^{\ i}\frac{n_i^2}{n(n+p)} \tag{46}$$

$$\tau_{A7} = 2\tau_{A7}^{\ i}\frac{n_i^2}{p(n+p)} \tag{47}$$

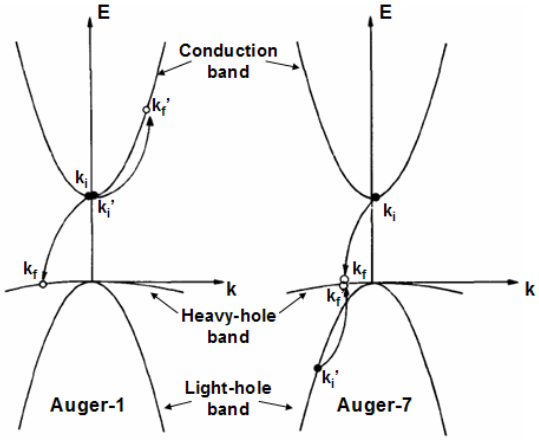

Figure 2.11: Schematic of Auger-1 recombination (left) and Auger-7 recombination (right); i and f denote initial and final states; • - occupied, ◦ - unoccupied.

For narrow-gap semiconductors such as HgCdTe, the thermal distribution of carriers induces a significant number of carriers having a kinetic energy larger than the threshold energy, i.e. the energy band-gap, for Auger-1 and Auger-7 generation mechanisms. In n-type HgCdTe, Auger-1 is the dominant Auger recombination mechanism [1]. Figure 2.12 and Figure 2.13 show the calculated Auger-1 lifetime in n-type HgCdTe versus temperature for x=0.2 and x=0.3 respectively and different values of donor concentration. As the Cd alloy fraction x decreases and as the donor concentration decreases, i.e. as the material becomes more intrinsic, the Auger-1 lifetime gets closer from the intrinsic Auger-1 lifetime. It is critical to decrease the donor concentration in the absorber layer of HgCdTe infrared photodiodes in order to have a high Auger-1 lifetime. From this, we also see that the Auger-1 lifetime drops significantly as the temperature is increased. The drop appears at a lower temperature as the Cd alloy fraction is decreased.

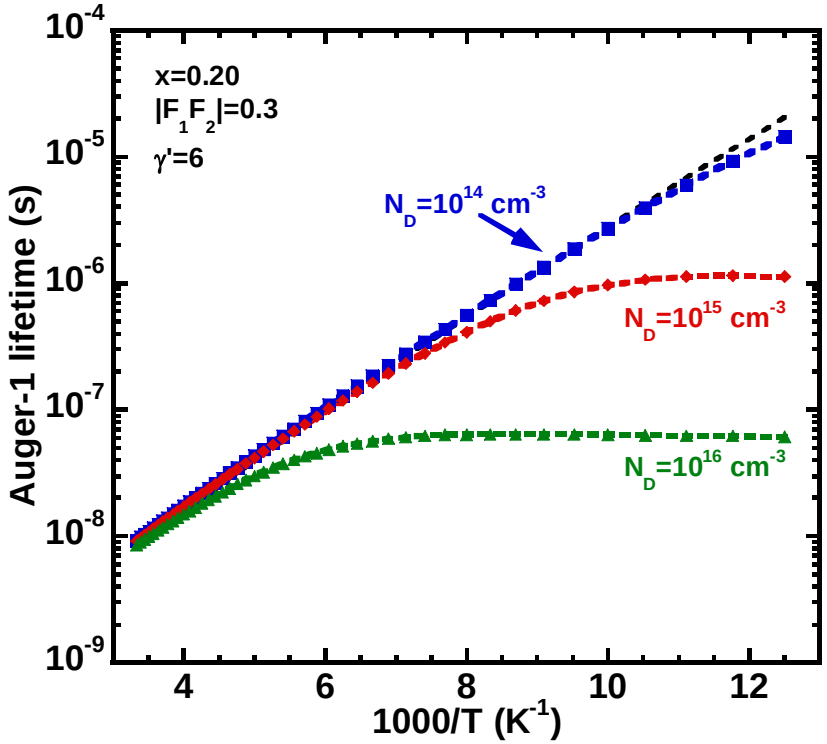

Figure 2.12: Calculated Auger-1 lifetime for $Hg_{0.8}Cd_{0.2}Te$ versus temperature for different values of donor concentration. Also shown is the intrinsic Auger-1 τ_{A1}^{i} lifetime (dashed line).

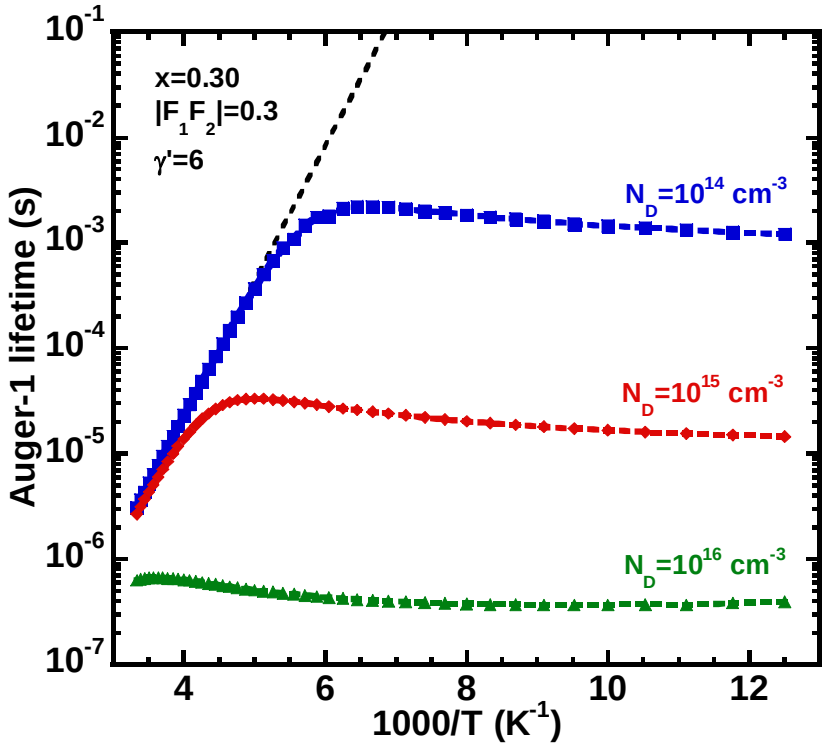

Figure 2.13: Calculated Auger-1 lifetime for $Hg_{0.7}Cd_{0.3}Te$ versus temperature for different values of donor concentration. Also shown is the intrinsic Auger-1 τ_{A1}^{i} lifetime (dashed line).

In p-type HgCdTe, Casselman and Petersen showed that there are ranges of temperature and CdTe mole fraction x such that Auger-7 is the dominant Auger mechanism [39]. This is shown in Figure 2.14 for x=0.2 and x=0.3 in p-type HgCdTe using the expressions that we presented above for Auger-1 and Auger-7 lifetimes. Auger-7 is more dominant as the acceptor concentration is increased. However, when the material becomes intrinsic, i.e. as the temperature is increased, Auger-1 becomes important as well. As we have seen above, the γ-ratio of the Auger-7 intrinsic carrier lifetime τ_{A7}^{i} and the Auger-1 intrinsic carrier lifetime τ_{A1}^{i} is reported in the range 3-60. Therefore, the Auger lifetime in p-type HgCdTe (where Auger-7 dominates) is usually longer than in n-type HgCdTe (where Auger-1 dominates).

In general, Auger processes are proportional to the carrier concentration present in the material. Therefore, they are important and play a major role in determining the maximum performance of HgCdTe infrared photodiodes. As the temperature is increased,

HgCdTe becomes more intrinsic and Auger processes limit the sensitivity of HgCdTe devices.

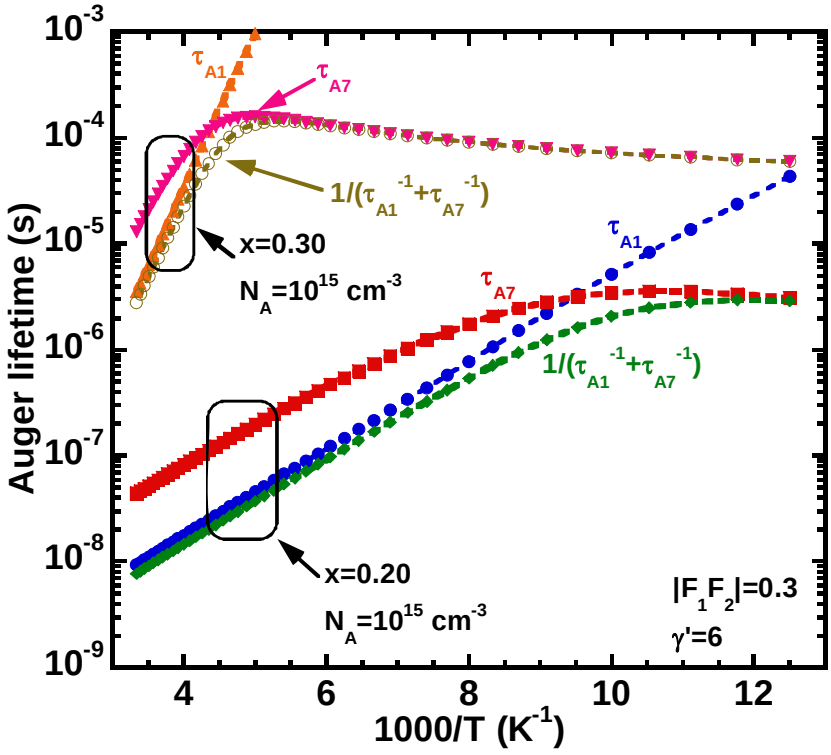

Figure 2.14: Calculated Auger-1 and Auger-7 lifetimes in p-type HgCdTe versus temperature for x=0.2 and x=0.3, and acceptor doping concentration of 10^{15} cm^{-3}.

2.3.2 Radiative Recombination

Radiative recombination is an intrinsic mechanism which involves the direct band to band recombination of an electron in the conduction band with a hole in the valence band. The excess energy is converted into a photon, as shown in Figure 2.15 below. This mechanism is of central importance in direct band-gap semiconductors such as HgCdTe and is the basis of light emitting diodes. In a non-degenerate semiconductor, the rate at which the electrons and holes are annihilated depends simultaneously on the concentration of electrons in the conduction band and the availability of holes in the valence band.

The theory of radiative recombination has been developed by van Roosbroeck and Shockley [43]. The expressions used in this work for the radiative recombination rate ($cm^{-3}.s^{-1}$) and the radiative lifetime in HgCdTe assuming parabolic bands and non-degenerate statistics are shown here:

$$U_{rad}^{net} = G_R\left(np - n_i^{\,2}\right) \tag{48}$$

$$G_R = 5.8\times10^{-13}\,\varepsilon_S^{\,2}\left(\frac{m_0}{m_e^{\,*}+m_h^{\,*}}\right)^{1.5}\left(1+\frac{m_0}{m_e^{\,*}}\right)\left(\frac{300}{T}\right)^{1.5}\left(E_G^{\,2}+3kTE_G+3.75k^2T^2\right) \tag{49}$$

$$\tau_{rad} = \frac{1}{G_R(n+p)} \tag{50}$$

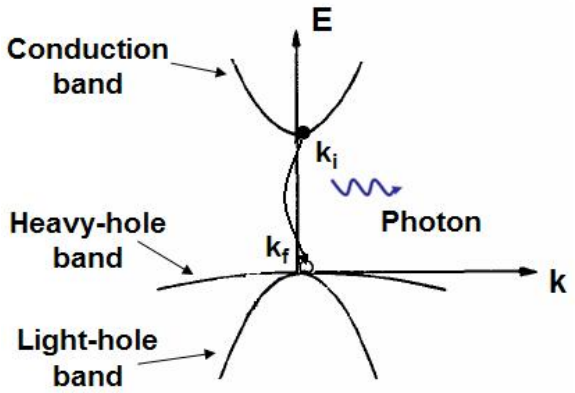

Figure 2.15: Schematic of radiative recombination.

As we can see from the equations above, the radiative lifetime is expected to be nearly similar in p-type HgCdTe and n-type HgCdTe as opposed to the Auger lifetime. Figure 2.16 and Figure 2.17 show the calculated radiative lifetime versus temperature in n-type HgCdTe for x=0.2 and x=0.3 respectively and different values of donor concentration. The radiative lifetime is nearly constant with temperature in the extrinsic region. As the material becomes intrinsic, i.e. as the temperature is increased, the radiative lifetime decreases. In the extrinsic region, the radiative lifetime has a weak dependence with Cd alloy composition, x. However, the radiative lifetime plays in general a larger role for HgCdTe material with larger values of x. This is simply because, in this case, the radiative mechanism is not dominated by other recombination mechanisms such as Auger which is less strong as the energy band-gap is increased.

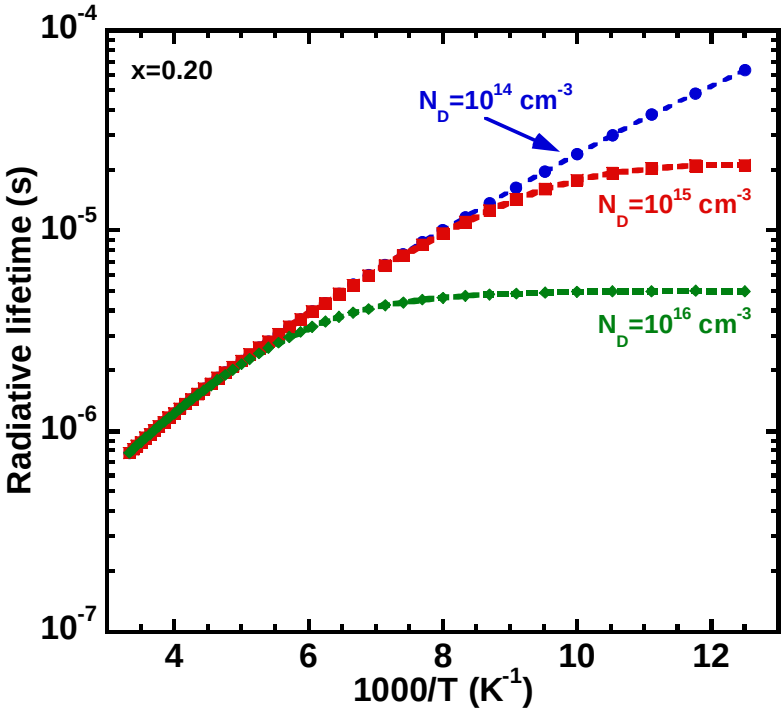

Figure 2.16: Calculated radiative lifetime in n-type HgCdTe versus temperature for x=0.2 and different values of donor concentration.

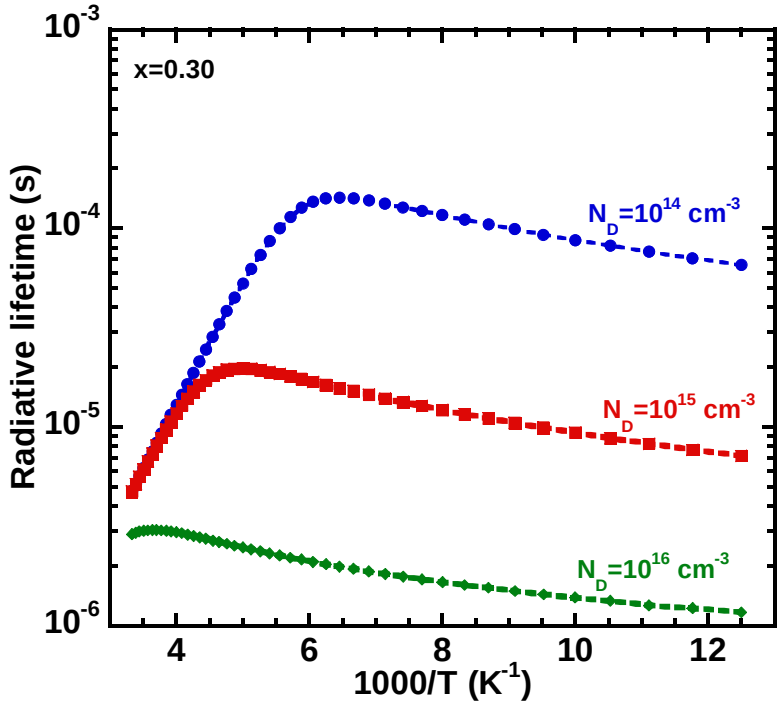

Figure 2.17: Calculated radiative lifetime in n-type HgCdTe versus temperature for x=0.3 and different values of donor concentration.

2.3.3 Shockley-Read-Hall Recombination

The Shockley-Read-Hall recombination mechanism involves the recombination of electron-hole pairs via defect levels within the energy band-gap of the material. Therefore, it is not an intrinsic process. The excess energy in this case is released via phonon emission. These defect levels in HgCdTe could be a result of vacancies, substitutional impurities, interstitial impurities, dislocations or grain boundaries. They can be introduced during HgCdTe growth, post-growth annealing treatments or during device processing. The effect of this mechanism on detector noise and external quantum efficiency can therefore be suppressed as HgCdTe processing improves. However, considering state-of-the-art HgCdTe material and device processing, it is currently an essential recombination mechanism to take into account.

The defect levels are commonly referred to as recombination centers. As recombination centers, they trap electron and holes. As generation centers, they successively emit them. The rates of generation and recombination depend on the individual nature of the center and its predominant occupation state of charge carriers, as well as on the local densities of those carriers in the conduction band and the valence band. The statistical theory for this recombination mechanism was first developed by Shockley and Read [44], and Hall [45]. The SRH model assumes non–degenerate statistics and considers that there is a single localized recombination center located at an energy level E_{trap} with the trap density N_{trap} (cm^{-3}) being much smaller that the majority carrier density.

The basic mechanisms are shown in Figure 2.18 [46]. There are four possible transitions via the localized recombination center by which electrons and holes can be captured and emitted. The localized state could either be empty or full. If it is empty, it can either capture an electron from the conduction band, as is shown in Figure 2.18(a) or it can emit a hole to the valence band, as is shown in Figure 2.18(d). Once it is filled, there again are two possibilities. It can emit the electron to the conduction band with an emission rate, as is shown in Figure 2.18(b), or capture a hole from the valence band, as is shown in Figure 2.18(c).

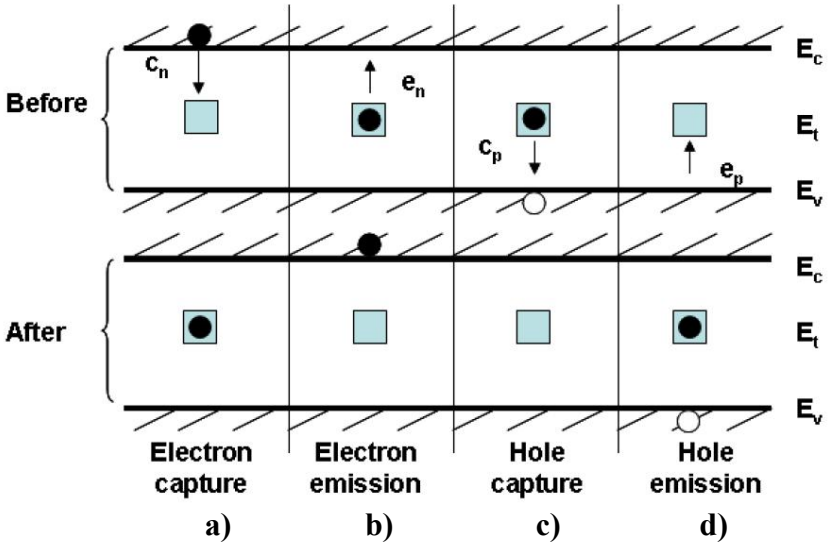

Figure 2.18: Schematic of Shockley-Read-Hall recombination [46].

The analysis of the various possibilities yields the expressions used in this work for the trap-determined net generation rate ($cm^{-3}.s^{-1}$) and carrier SRH lifetime τ_{SRH} (s):

$$U_{SRH}^{net} = \frac{np - n_i^{\,2}}{\tau_{p0}(n + n_1) + \tau_{n0}(p + p_1)} \tag{51}$$

$$n_1 = N_C e^{-\frac{E_{trap}}{kT}} \tag{52}$$

$$p_1 = N_V e^{-\frac{(E_G - E_{trap})}{kT}} \tag{53}$$

$$\tau_{n0} = (\sigma_n v_{th} N_{trap})^{-1} \tag{54}$$

$$\tau_{p0} = (\sigma_p v_{th} N_{trap})^{-1} \tag{55}$$

$$\tau_{SRH} = \frac{\tau_{n0}(p + p_1) + \tau_{p0}(n + n_1)}{n + p} \tag{56}$$

where E_{trap} is the defect level below the conduction band, n_1 and p_1 are the electron concentration (cm^{-3}) and the hole concentration (cm^{-3}) respectively when the Fermi level is coincident with the trap level, τ_{n0} (s) is the electron characteristic SRH lifetime in p-type HgCdTe, τ_{p0} (s) is the hole characteristic SRH lifetime in n-type HgCdTe, σ_n and σ_p are the capture cross-sections (cm^2) for electrons and holes respectively, N_{trap} is the trap density (cm^{-3}) and v_{th} is the carrier thermal velocity (cm/s). In this work, we use the electron and hole SRH lifetimes, τ_{n0} and τ_{p0}, as fitting parameters as their actual values

may vary significantly from one HgCdTe material to another, depending on growth and processing.

The SRH lifetime depends on alloy composition in $Hg_{1-x}Cd_xTe$, temperature, doping concentration, trap level E_{trap} and τ_{n0} and τ_{p0} which are related to the trap density N_{trap} and its capture cross-sections. Assuming a trap level at mid-gap and $\tau_{n0}=\tau_{p0}=1$ μs, Figure 2.19 shows the calculated SRH lifetime in n-type HgCdTe versus temperature for x=0.2 and x=0.3 and various donor concentrations. Relative to other recombination mechanisms, SRH can be dominant especially for layers with high dislocation densities (≥ high 10^5 cm^{-2}) commonly observed when HgCdTe layers are grown on substrates with large lattice mismatches such as CdTe/Si. It can also be dominant for low-doped samples, in which the Auger and radiative mechanisms are reduced. Data on SRH centers in n-type HgCdTe grown by MBE indicate neutral centers located at the intrinsic Fermi energy level [41]. The predominant SRH center in p-type MBE HgCdTe is associated with the post-growth annealing conditions that produce Hg vacancies [41]. A high concentration of dislocations in the material is also expected to form SRH centers [47]. In general, high-quality HgCdTe material is expected to have SRH lifetime >5 μs.

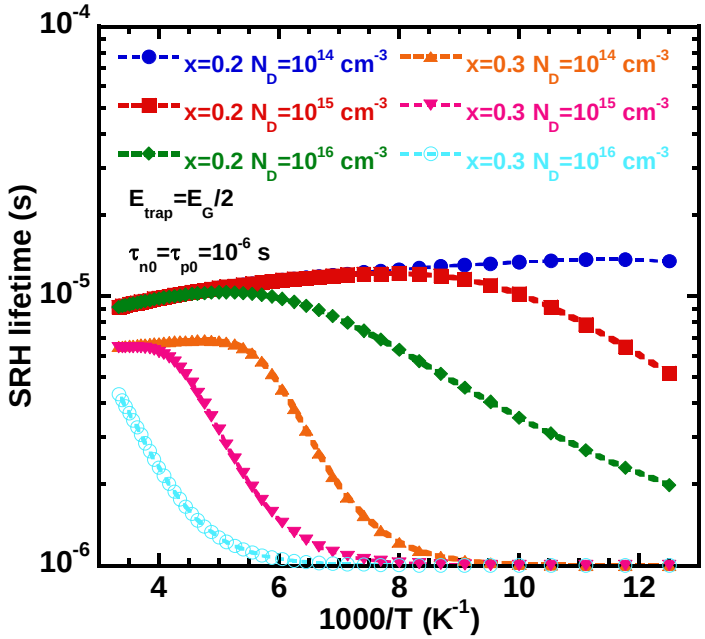

Figure 2.19: Calculated SRH lifetime in n-type HgCdTe versus temperature for x=0.2 and x=0.3 and various donor concentrations.

2.3.4 Surface Recombination

Surface recombination is a special case of the Shockley-Read Hall recombination mechanism [46], [47] in which the localized defect states are located at or near the surface. Therefore the kinetics can be described in a manner similar to that for the bulk SRH recombination mechanism. As that in bulk SRH recombination, the surface recombination rate is a function of the energy difference between the Fermi level and the surface trap energy level $E_{t,surf}$, which in turn depends on the amount of band bending at the surface. The equivalent expression for the surface SRH recombination rate ($cm^{-2}.s^{-1}$) which is used in this work is given below:

$$U_{SRH}^{surf,net} = \frac{np - n_i^2}{(n+n_1)/v_p + (p+p_1)/v_n} \tag{57}$$

$$n_1 = N_C e^{-\frac{E_{t,surf}}{kT}} \tag{58}$$

$$p_1 = N_V e^{-\frac{(E_G - E_{t,surf})}{kT}} \tag{59}$$

where v_n and v_p are the electron and hole surface recombination velocities (cm/s) which we use as fitting parameters in this work and $E_{t,surf}$ is the surface trap level below the conduction band.

Similarly as for the electron and hole characteristic SRH lifetime, the surface recombination velocity depends on the concentration of traps at the surface and their capture cross-sections. The total carrier recombination lifetime τ_{tot} is the combination of an effective "bulk" lifetime τ_{bulk}, which is the result of Auger, radiative and SRH recombination as discussed previously, and "surface" lifetime τ_{surf} which is the result of the surface recombination:

$$\frac{1}{\tau_{tot}} = \frac{1}{\tau_{bulk}} + \frac{1}{\tau_{surf}} \tag{60}$$

The surface recombination lifetime depends on the surface recombination velocity, but also the carrier diffusion coefficient and material thickness [46]. Surface recombination directly affects the detector noise and quantum efficiency of HgCdTe infrared photodiodes in a similar way than bulk recombination mechanisms. The goal of a

proper surface treatment and surface passivation is to minimize the density of surface states and their corresponding capture cross-sections by changing the surface potential. Proper passivation of the sidewalls can be a challenge especially for high-pixel-density HgCdTe infrared focal plane arrays with "mesa" structures.

2.3.5 Carrier Lifetime in $Hg_{1-x}Cd_xTe$

As mentioned earlier, under the condition of small excess carrier concentration, the total carrier lifetime can be computed from the independent lifetime of each recombination mechanism:

$$\frac{1}{\tau_{tot}} = \frac{1}{\tau_{bulk}} + \frac{1}{\tau_{surf}} = \frac{1}{\tau_{A1}} + \frac{1}{\tau_{A7}} + \frac{1}{\tau_{rad}} + \frac{1}{\tau_{SRH}} + \frac{1}{\tau_{surf}} \tag{61}$$

Auger processes play a major role in limiting the performance of HgCdTe infrared photodiodes, especially when the energy band-gap is decreased and the temperature is increased. This is illustrated in Figure 2.20. Considering Auger, radiative and SRH recombination, we see that the calculated total carrier lifetime is limited by Auger processes in the case of x=0.2 and $N_D=10^{15}$ cm^{-3} which can correspond to the absorber layer of an HgCdTe infrared photodiode with response in LWIR. In the case of x=0.3 and $N_D=10^{15}$ cm^{-3} (absorber layer of MWIR HgCdTe device), for the conditions of mid-gap trap level and characteristic SRH lifetime of 1 μs, Figure 2.21 illustrates that SRH can be the limiting mechanism of the carrier lifetime up to ~200 K. Above ~200 K, radiative and Auger processes become limiting mechanisms. If the doping concentration is higher, Auger processes will be more important.

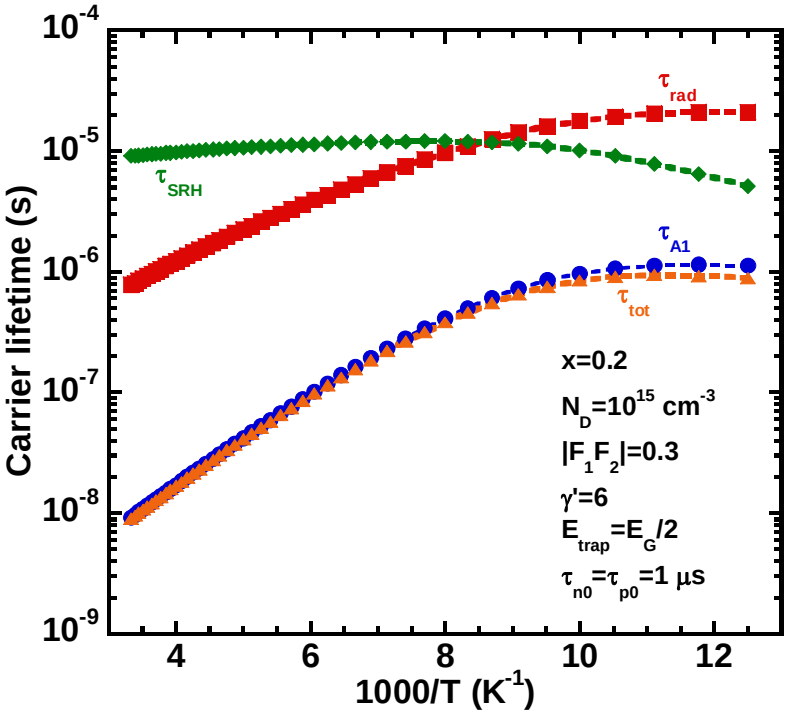

Figure 2.20: Calculated carrier lifetime in n-type HgCdTe versus temperature for x=0.2 and $N_D=10^{15}$ cm^{-3}.

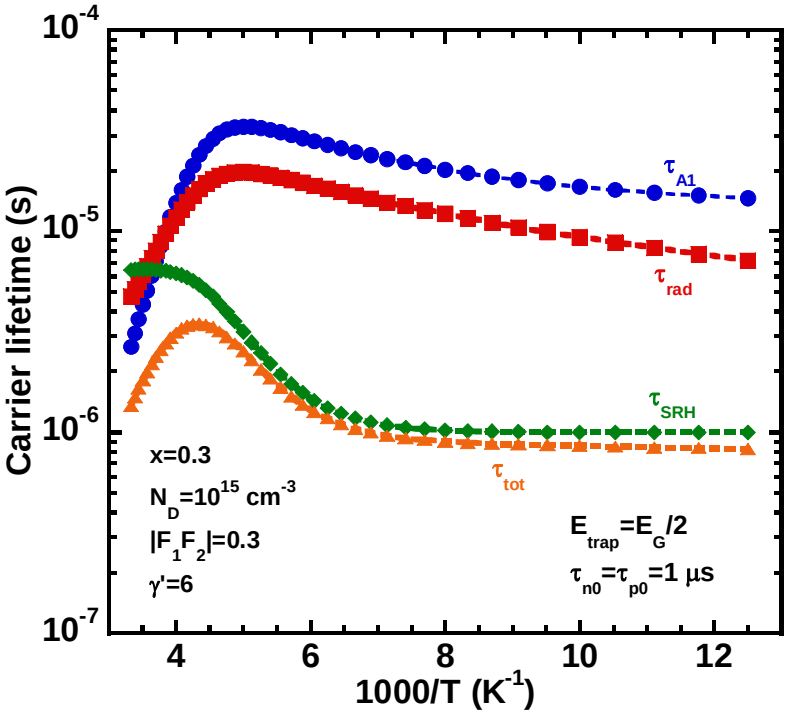

Figure 2.21: Calculated carrier lifetime in n-type HgCdTe versus temperature for x=0.3 and $N_D=10^{15}$ cm^{-3}.

Typically, the temperature dependence of the carrier lifetime in HgCdTe layers – measured for instance by photoconductive decay (PCD) – is fitted using the analytical expressions for the recombination lifetimes presented above. From this, one can determine which recombination mechanisms limit the carrier lifetime as we can see in the figure below [46].

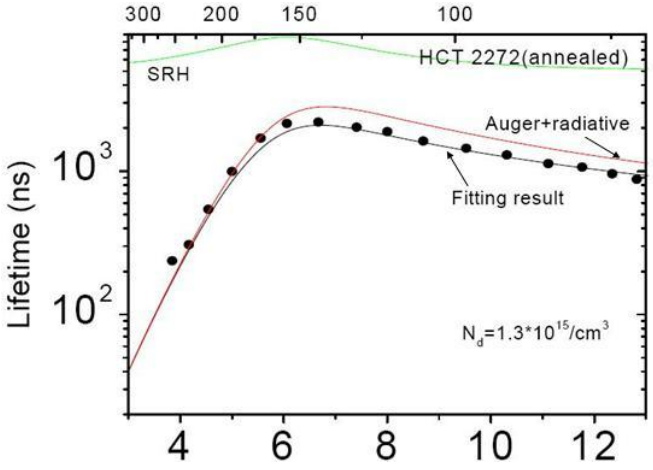

Figure 2.22: Measured minority carrier lifetime versus 1000/T for MCT 2272 with x=0.24, doping 1.3x10^{15} cm^{-3} and dislocation density = 3x10^5 cm^{-1}. Also shown is the fitting result (solid lines) [46].

Chapter 3
Properties of HgCdTe: Devices

Here we discuss state-of-the-art HgCdTe infrared technology. We discuss device processing, performance and limitations, relating to the figures of merit presented in the first chapter. We also present in further details the operation of the novel HgCdTe device structure that we propose in order to overcome these limitations.

3.1 HgCdTe Device Fabrication Technology

There are many different device architectures for HgCdTe infrared photodiodes [2], including mesa, planar and lateral n-on-p and p-on-n homojunction and heterojunction structures. The n-on-p stands for a thick p-type absorber with a thin n-type surface layer which can have the same energy band gap as the absorber (n-on-p) or a higher energy band gap (N-on-p). Since $m_e^* << m_h^*$ in HgCdTe, the kinetic energy of holes is much smaller than the one of electrons. Thus, Auger processes are reduced in p-type HgCdTe compared to n-type HgCdTe because the number of electrons and holes having a kinetic energy higher than the energy band gap is reduced. In addition, the electron mobility in HgCdTe is much larger than the hole mobility as in visible and near-IR PV devices. It is therefore preferred to have a p-type absorber in HgCdTe infrared photodiodes. On the other hand, the low doping required for the absorption layer is easier to achieve in n-type HgCdTe. In addition, the quality of the indium doped n-HgCdTe layers is well known to be better than arsenic doped p-HgCdTe layers, and the doping in these layers is well under control, with achievable minimum concentrations less than those in p-HgCdTe by more than one order of magnitude.

Figure 3.1 shows the device architecture for the P-on-n heterojunction mesa HgCdTe photodiode on CdZnTe. We give an overview of important processing steps in HgCdTe device fabrication through the example of this standard P-on-n HgCdTe photodiode. We emphasize on processing steps that are relevant to our study.

The most widely used substrate is CdZnTe, as we mentioned earlier, which has the important advantage to be nearly lattice-matched to HgCdTe (see Figure 2.3). The thickness of the absorber layer, typically a few microns, and Cd alloy fraction depend on the desired cutoff wavelength. The top p-type layer is typically less than a micron thick. It has a wider energy band-gap and is heavily doped in order to concentrate the depletion region in the absorber and to make the formation of an ohmic contact easier. This structure can be typically grown by MBE or MOCVD. These techniques offer precise control of the Cd alloy composition desired and the possibility of a nearly abrupt heterojunction. Compositional grading at the heterojunction with a thickness less than ~0.5 μm will usually appear due to Cd-Hg interdiffusion during subsequent annealing steps. Compositional grading is usually not detrimental to device performance. It may be beneficial in some cases in order to reduce potential band offsets.

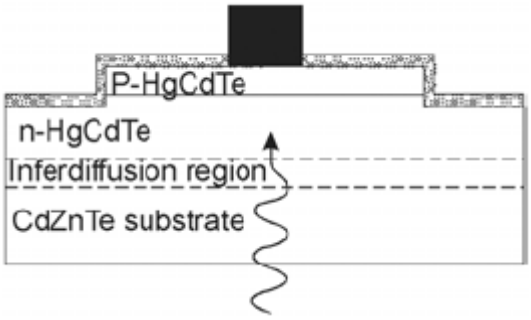

Figure 3.1: P-on-n mesa device architecture [2].

3.1.1 Doping of HgCdTe

Low doping $<10^{15}$ cm^{-3} is required in the n-type absorber region in order to maximize the diffusion length of photo-generated carriers. Low n-type doping can be

achieved in-situ during growth by LPE, MBE or MOCVD. Indium is the most widely used donor for HgCdTe. It is a shallow donor as we describe in the following chapter. Controllable n-type doping with indium can be achieved in-situ during MBE growth in the range $5x10^{14} – 10^{17}$ cm^{-3}.

The p-n junctions can be formed by numerous techniques, including Hg in- and out-diffusion, impurity diffusion, ion implantation, electron bombardment, doping during growth from vapor or liquid phase, and other methods. Starting from an as-grown vacancy-doped p-type HgCdTe layer (10^{16} cm^{-3} to 10^{17} cm^{-3}), in-diffusion of Hg at annealing temperatures of 200-250 °C neutralizes the vacancies. This effectively converts HgCdTe to n-type in the diffusion range of Hg and creates the p-n junction. The n-type conductivity is originated from a background donor impurity.

In our example, the as-grown HgCdTe layer will be n-type and it is necessary to convert the surface to p-type in order to create the p-n junction. Arsenic is the most widely used acceptor for HgCdTe. It is a shallow acceptor and has a low diffusion coefficient compared to other possible acceptors, such as gold or silver. Therefore, it makes it easier to control the location of the p-n junction. However, in-situ p-type doping with arsenic is currently a challenge with MBE-HgCdTe. Later in this work, we study low p-type doping in HgCdTe by arsenic ion implantation followed by thermal annealing. High p-type doping in HgCdTe can routinely be achieved by arsenic ion implantation followed by thermal annealing. The ion-implanted diffusion source is formed by a shallow implant with As to a dose of about $1x10^{14}$ cm^{-3} at energies of 50-350 keV. After implantation, the structures are annealed under Hg overpressure. The thermal annealing is usually a two-step annealing process:

1. 400-425 °C for 10-20 min: anneals out the radiation-induced damage, diffuses and electrically activates As by substituting As atoms on the Te sublattice
2. 250 °C for 24 hrs: annihilates Hg vacancies formed in the HgCdTe lattice during growth

The arsenic redistribution from the ion-implanted source (as well as from a grown source) typically exhibits a multicomponent behavior in which the tail component varies from sample to sample (Figure 3.2).

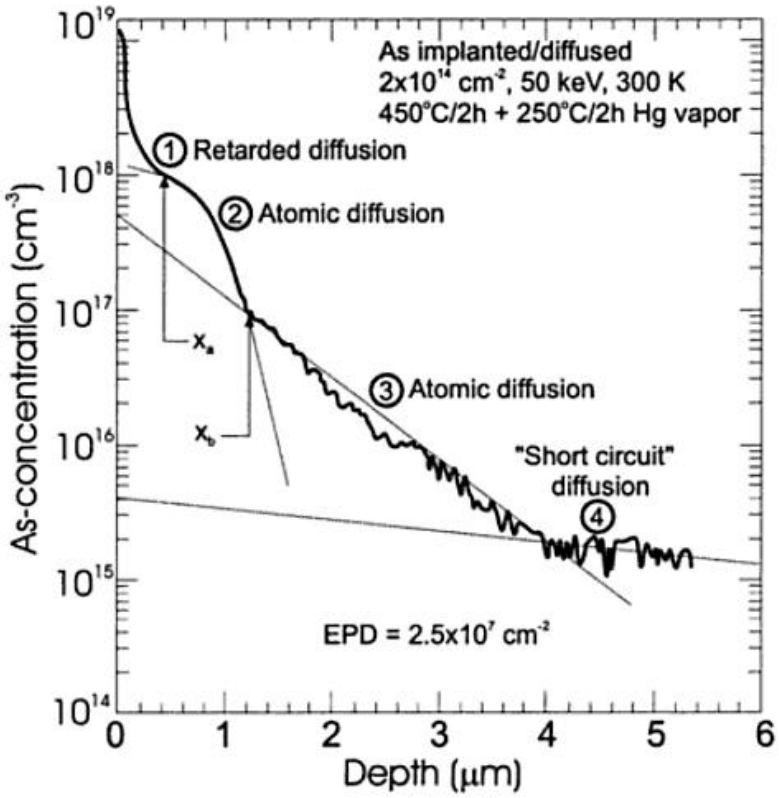

Figure 3.2: Typical example of As redistribution from the ion-implanted source (SIMS) and the proposed model for As diffusion from an ion-implanted source: (1) retarded diffusion; (2) atomic diffusion, As starts on Te sublattice; (3) atomic diffusion, As starts on metal sublattice; (4) short-circuit diffusion [1].

3.1.2 Mesa Delineation

Both wet etching and dry etching can be used to form the mesa [46]. Typical etchants for HgCdTe are bromine-methanol or bromine-lactic acid. Since the redox potential of bromine to bromide conversion is sufficiently high, the adsorbed bromine molecules will naturally react with tellurium anions Te^{-2} to oxidize them, yielding neutral tellurium Te^0:

$$Br_2 + Te^{-2} \rightarrow 2Br^- + Te^0 \tag{62}$$

The bromide anions react with Cd^{+2} and Hg^{+2} cations to etch away the materials. At room temperature, 1 % bromine-methanol by volume will etch almost the same thickness in 30 sec (~0.6 μm) than 2 % bromine-lactic acid by volume in 6 min.

3.1.3 Passivation of HgCdTe surface

Passivation of the HgCdTe surface, including the sidewalls in case of mesa structures, is a challenge in HgCdTe technology as we mentioned earlier when we described surface recombination. CdTe is considered the best passivant for HgCdTe [46] and can be deposited by thermal evaporation or MBE. ZnS is also widely used and it can be deposited by thermal or e-beam evaporation. Typical passivation layers are ~4000 Å thick. The parameters of interest for CdTe and ZnS are listed below in Table 3.1.

Parameter	**ZnS**	**CdTe**	**$Hg_{0.8}Cd_{0.2}Te$**
Refractive index	2.6	2.68	3.8
Band gap (eV)	3.8	1.65	0.08
Dielectric constant (ε_0)	7.45	10.7	17.7
Linear coefficient of thermal expansion $x10^{-6}$ (K^{-1})	0.75	1.9	2

Table 3.1: ZnS and CdTe parameters of interest.

3.1.4 Contact Metallization

The issues connected with contacts in photodiodes are contact resistance, contact surface recombination, contact 1/f noise, and long-term and thermal stability of devices. The common method of preparing ohmic contacts is by highly doping the surface region so that the space-charge layer width is substantially reduced and electrons tunnel through yielding low-resistance contacts. However, practical contacts for HgCdTe are often composed of several layers of different metals which are required to promote adhesion and reduce solid state reactions.

The most widely used metal for n-type HgCdTe is indium which creates an ohmic contact. In general, ohmic contact to p-type HgCdTe is more difficult to realize since a larger work function of the metal contact is required. Gold is widely used for p-type HgCdTe and exhibits ohmic characteristics [1].

3.2 HgCdTe Devices

3.2.1 Standard HgCdTe Infrared Photodiodes

The most widely used HgCdTe infrared photodiode is the Double-Layer Planar Heterojunction (DLPH) photodiode. DLPH HgCdTe photodiodes can be either n-on-p or p-on-n structures as we can see in Figure 3.3. As we have seen in the previous chapter, DLPH HgCdTe photodiodes operated at 77 K can achieve near-theoretical limit performance in both MWIR and LWIR infrared bands, i.e. detectivities D^* in the mid-10^{10} or 10^{11} cm.$Hz^{0.5}$/W range. BLIP is also achieved in this range for typical f-ratios $f_{\#}$ between 2 and 5, i.e. the detector internal noise is smaller than the background photon shot noise.

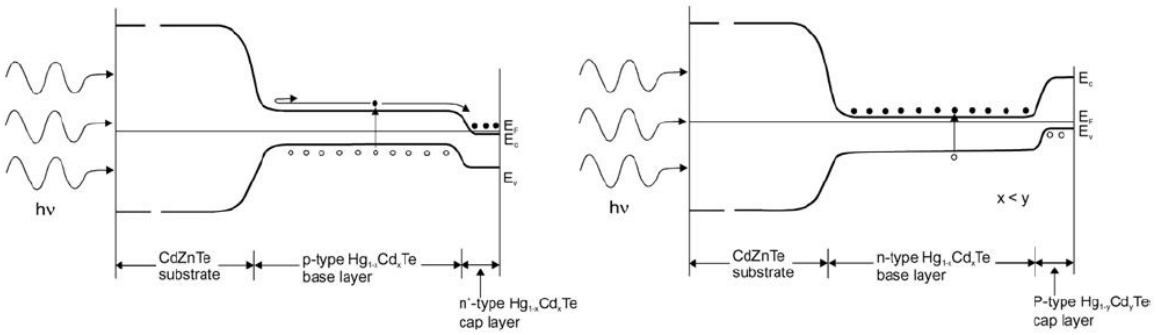

a) **b)**

Figure 3.3: Schematic band diagrams of n+-on-p homojunction a) and p-on-n heterojunction b) photodiodes [2].

Photoconductors were the first infrared devices based on HgCdTe which were developed starting in the sixties. Photodiodes are currently the most used HgCdTe devices for high sensitivity infrared imaging. Research for third-generation infrared systems started in the early nineties. Devices include two-color HgCdTe infrared detectors (MWIR/LWIR), avalanche photodiodes (APD) and novel heterojunction structures.

To better understand the leakage current mechanisms in these detectors, it is interesting to plot the resistance-area product R_0A versus temperature. As we mentioned previously, R_0A is an important figure of merit in HgCdTe photodiodes and it is directly related to the detectivity D^*. High impedance is necessary in order to reduce the detector

noise. We consider the case of an ideal abrupt HgCdTe one-sided p-n homojunction ($N_A=10^{19}$ cm^{-3} and $N_D=10^{15}$ cm^{-3}). We consider the two main current mechanisms in HgCdTe photodiodes: diffusion current and depletion region current from Shockley-Read-Hall recombination (g-r current). In this ideal case, the corresponding R_0A product (Ω-cm^2) for the diffusion current can be expressed as:

$$R_0 A_{diff} = \frac{kTN_D \tau_h}{q^2 L_h n_i^2} \tag{63}$$

where N_D is the n-type doping level in the absorber region (cm^{-3}), τ_h is the minority hole carrier lifetime (s), L_h is the hole diffusion length (cm), and n_i is the intrinsic carrier concentration (cm^{-3}).

The corresponding R_0A product (Ω-cm^2) for the g-r current can be expressed as:

$$R_0 A_{g-r} = \frac{V_{bi} \tau_{SRH}}{q n_i w} \tag{64}$$

where V_{bi} is the built-in voltage (V), τ_{SRH} is the characteristic SRH lifetime (s) and w is the depletion width (cm).

The total R_0A product (Ω-cm^2) is then given by:

$$\frac{1}{R_0 A_{tot}} = \frac{1}{R_0 A_{diff}} + \frac{1}{R_0 A_{g-r}} \tag{65}$$

Space-charge g-r R_0A varies with temperature as $1/n_i$; less rapidly than diffusion R_0A which varies as $1/n_i^2$. It is therefore possible to determine the limiting leakage current mechanism by plotting R_0A versus temperature. The minority hole carrier lifetime τ_h is calculated considering Auger, radiative and SRH processes as described in the previous chapter.

Figure 3.4 shows the calculated R_0A versus temperature for x=0.3 (MWIR). The SRH lifetime is set at 1 μs with a trap level at mid-gap. We see that above ~110 K, R_0A varies as $1/n_i^2$ which is characteristic of an ideal diffusion-limited photodiode. In this case, it is found that Auger-1 is the limiting mechanism in the diffusion current. Below ~110 K, R_0A varies as $1/n_i$ which is characteristic of g-r limited photodiode. Depletion region current is usually due to traps causing SRH generation. Traps can appear during growth due to lattice-mismatch with the substrate in the form of threading dislocations or during device processing due to impurities or passivation issues. In any case, they are

detrimental to the device performance and an ideal photodiode should be diffusion-limited. Diffusion-limited R_0A means that the photodiode is limited by intrinsic leakage mechanisms due to Auger or radiative processes, rather than by external mechanisms due to imperfections in growth and/or processing.

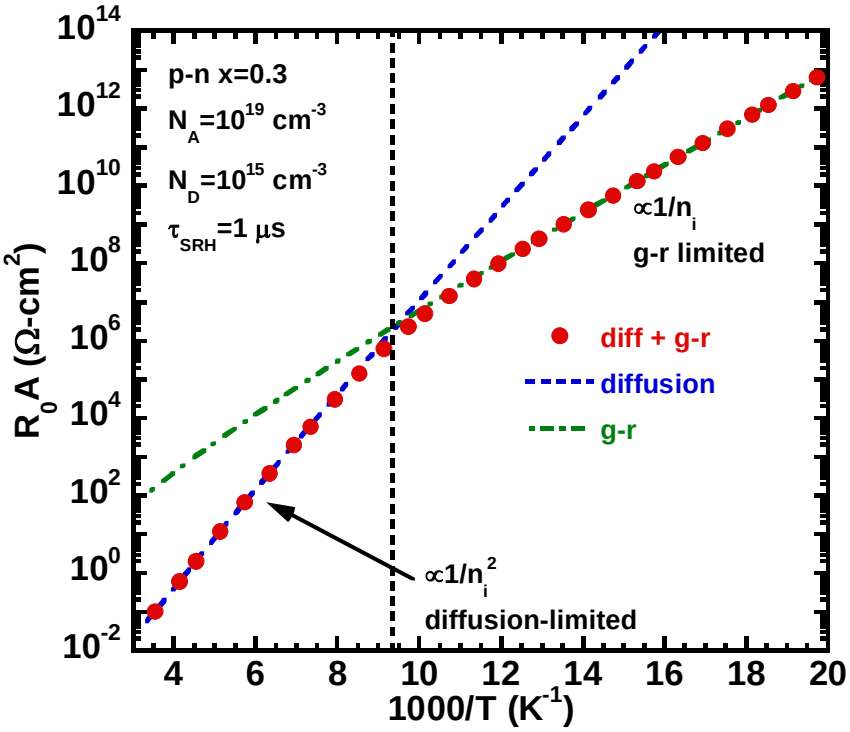

Figure 3.4: R_0A versus temperature in the case of one-sided abrupt HgCdTe p-n homojunction with x=0.3 and $N_D=10^{15}$ cm^{-3} considering diffusion current and depletion region g-r current.

Figure 3.5 shows the calculated R_0A versus temperature for x=0.2 (LWIR). The SRH lifetime is now set at 0.1 ns with a trap level at mid-gap. Even though the SRH lifetime is set at a much lower value than in the previous case, the photodiode is now diffusion-limited down to ~90 K due to stronger Auger-1 process hiding the g-r current. As we go to longer wavelengths, Auger-1 process causes R_0A to drop by several orders of magnitude.

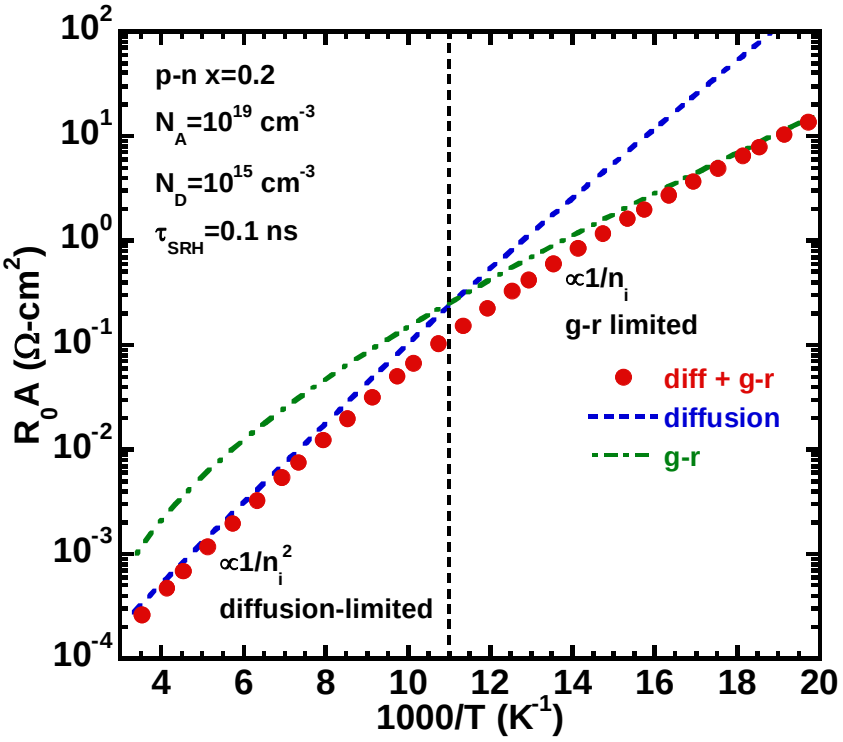

Figure 3.5: R_0A versus temperature in the case of one-sided abrupt HgCdTe p-n homojunction with x=0.2 and $N_D=10^{15}$ cm^{-3} considering diffusion current and depletion region g-r current.

Practical LWIR photodiodes usually have a higher dislocation density than MWIR photodiodes because the energy band gap is smaller and growth becomes more complicated. Figure 3.6 shows experimental data of R_0A versus temperature for LWIR photodiodes with dislocation densities of N=0 and $N=10^7$ cm^{-2}. The device becomes diffusion-limited at a higher temperature as the dislocation density increases.

Practical HgCdTe photodiodes also suffer from additional excess mechanisms such as band-to-band tunneling, trap-assisted tunneling through the depletion region due to dislocations for example, and surface effects such surface recombination or tunneling induced near the surface due to passivation issues. Tunneling mechanisms usually tend to appear at temperatures below 80 K, depending on the cutoff wavelength of the device and the quality of the material. Tunneling also has a strong bias dependence and can limit the reverse-bias I-V characteristic below 80 K, especially for LWIR HgCdTe photodiodes. Experimental data in Figure 3.6 deviate from both diffusion-limited and g-r limited behavior at low temperatures due to these additional excess mechanisms.

The modeling of tunneling and surface effects in HgCdTe devices is still a challenge. We are concerned in this work with high operating temperature HgCdTe photodiodes. Therefore, we will usually neglect these contributions.

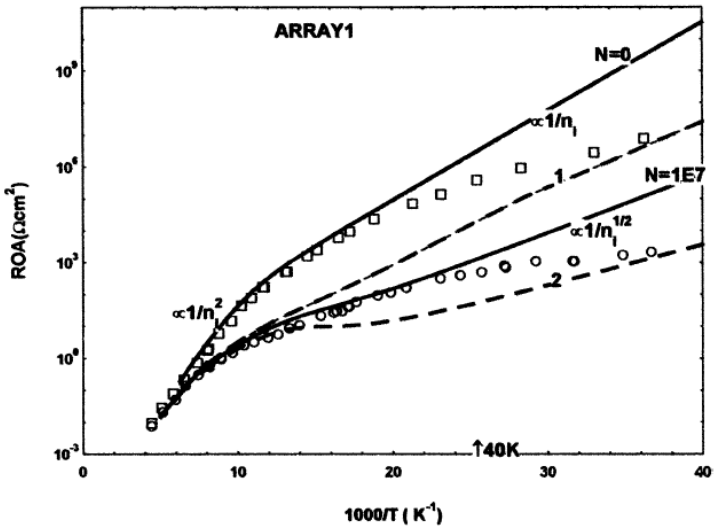

Figure 3.6: Temperature variation of R_0A of diodes with 9.5 μm cutoff wavelength. Points are the experimental data [48].

As we discussed several times previously, HgCdTe infrared photodiodes can achieve high sensitivity when operated at 77 K. At higher temperatures, the sensitivity is limited by the detector noise due to Auger processes, especially for longer wavelengths such as LWIR and VLWIR. This is a major limitation and achieving high sensitivity at higher temperatures would open the possibility of using TE-cooling systems, therefore reducing significantly the weight and power consumption of HgCdTe infrared systems. We propose in this work a novel HgCdTe device structure in order to overcome this and examine its operation and performance between 77 K and room temperature. We described this novel device structure in the previous chapter and give more details on its operation in the following section.

3.2.2 *Auger-Suppressed HgCdTe Infrared Photodiodes*

This device structure was first proposed by Elliott and Ashley [6]. The typical device structure and band diagram is shown in Figure 3.7. It is basically a p-i-n structure. However, because we are talking about narrow-gap semiconductors such as HgCdTe, the operation is not the same as for typical silicon p-i-n photodiodes. First, due to limitations in HgCdTe technology, the middle 'i' region is not actually undoped, but low-doped. We refer to it as lightly doped 'ν' (n-type) or 'π' (p-type). This is because the controlled doping of HgCdTe has to be at a higher level than the background doping due to native defects and impurities. The minimum controllable doping that can be achieved is on the order to mid-10^{14} cm^{-3}. Then, the intrinsic carrier concentration in HgCdTe is very high as the temperature is increased (see Figure 2.4). It can reach values as high as 10^{15} cm^{-3}, or even 10^{16} cm^{-3}, i.e. values higher than the actual extrinsic doping level. Therefore, since Auger processes are directly proportional to the number of electrons and holes available, they result in large detector noise in HgCdTe IR devices operated at high temperatures where the absorber layer is intrinsic at equiblibrium.

The P+/π or N+/ν heterojunction is referred to as the exclusion junction. The N+/π or P+/ν heterojunction is referred to as the extraction junction. For example, we consider a P+/ν/N+ structure operated at high temperature so that the 'ν' absorber region is intrinsic in thermal equilibrium. In this case, the intrinsic carrier concentration is in the mid-10^{15} cm^{-3} for T=280 K. When HgCdTe is highly n-type doped like in the N+ region, the Fermi level lies in the conduction band. The energy required to generate e-h pairs by Auger generation is therefore increased to a value higher than the energy band gap, hence hole generation is decreased in the N+ region. Now, when applying an increasing reverse bias, the P+/ν extraction junction extracts the minority holes from the 'ν' absorber region faster than they can be injected from the N+ region. Therefore, the hole concentration drops significantly, below its thermal equilibrium value, in the absorber ν region. The electron concentration is then also reduced below the equilibrium value in order to maintain charge neutrality.

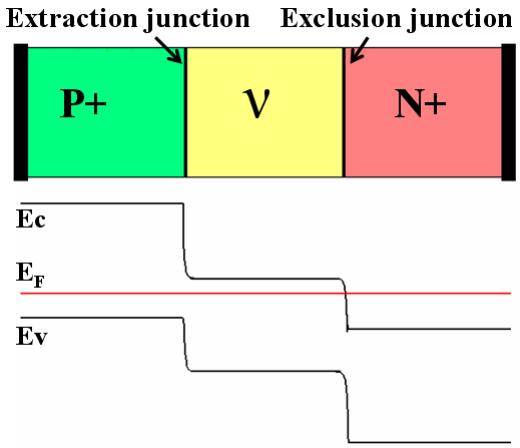

Figure 3.7: HgCdTe HOT infrared photodiode structure and its corresponding calculated energy band profile at zero bias.

As the reverse bias is increased, the electron concentration in the absorber region will eventually go from the intrinsic level (mid-10^{15} cm^{-3}) down to the extrinsic doping level (mid-10^{14} cm^{-3}) as we can see in Figure 3.8a. This decrease of electron and hole concentration in the absorber region by several orders of magnitude as the reverse bias is increased results in significant reduction of Auger processes. Figure 3.8b shows how the net calculated Auger recombination rate is reduced in the absorber layer of a MWIR HgCdTe HOT structure as the reverse bias is increased. When reverse biased, HOT devices can suppress Auger processes in the absorber layer and reduce the associated dark current. The detector noise at high temperatures is reduced compared to standard HgCdTe DLPH devices. Thus, high sensitivity at high temperatures can potentially be achieved.

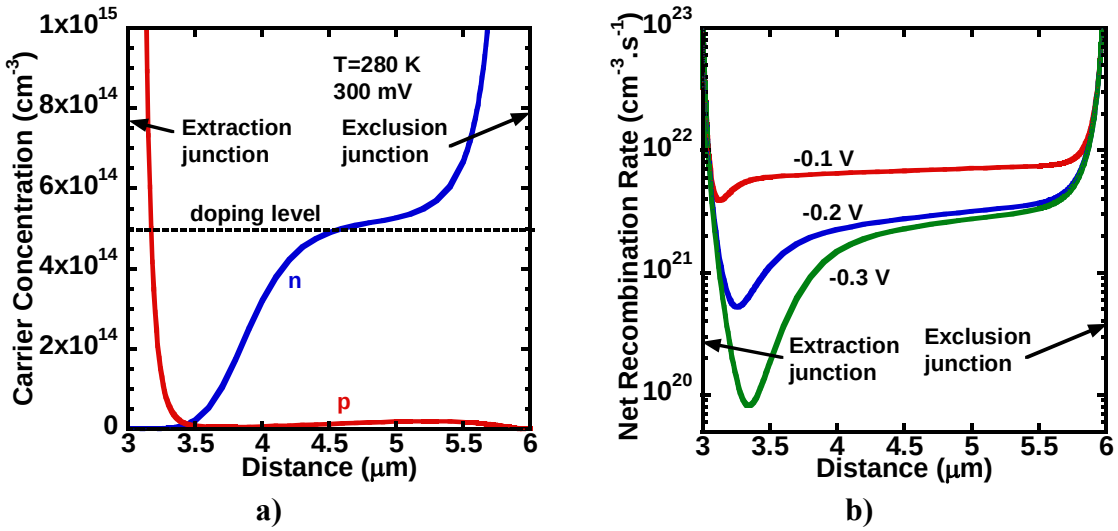

Figure 3.8: a) Calculated electron and hole concentration in the absorber layer of a MWIR HOT structure at 280 K and 300 mV reverse bias. Also indicated is the doping level in the absorber layer. b) Net Auger recombination rate at different applied reverse biases.

Auger suppression in HOT HgCdTe devices translates into a unique negative differential resistance (NDR) in the reverse bias current-voltage (I-V) characteristics, which has been experimentally observed in devices grown by MOVPE [49] and MBE using silver as an acceptor dopant [50] as we can see in Figure 3.9. More recently, we reported Auger suppression in LWIR MBE-grown devices using arsenic as an acceptor dopant [51].

Current device performance suffers from large excess 1/f noise [52] which makes them useless for imaging applications where the frequency is relatively small. However, they can be used in high-frequency applications such as CO_2 laser heterodyne detectors. 1/f noise is a signal with a frequency spectrum such that the power spectral density is proportional to the reciprocal of the frequency. It is generally believed to be related to the level of dark current in HgCdTe devices [52], [53], and also to imperfections in the device fabrication process such as poor surface passivation [53] leading to surface trap-assisted tunneling (TAT) [54]. However, there is no clear agreement on the origin of 1/f noise in HgCdTe devices. HOT devices also suffer from non-uniformities and poor process control in HgCdTe technology. This makes it a challenge to fabricate the multilayer structures with enough precision and with the doping and low impurity concentration required to achieve full Auger suppression.

Because of this non-equilibrium operation and this unusual I-V characteristic, it is not possible to use traditional analytical models for standard HgCdTe photodiodes – such as the ones used in the previous section to plot R_0A versus temperature – to study HgCdTe HOT photodiodes. Indeed, the whole concept of Auger suppression is based on the *non-equilibrium* carrier concentration in the device as the reverse bias is increased. It is therefore critical to solve the *semiconductor equations* in order to really understand the operation of these devices. Hence, numerical models [55], [56] have been developed in order to study these devices. In the following chapter, we present the numerical model that we developed [56] in order to model and design optimized Auger-suppressed HgCdTe infrared photodiodes.

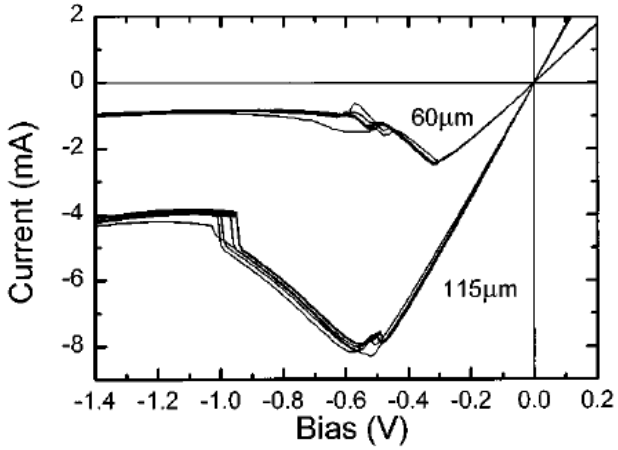

Figure 3.9: I-V characteristics for Auger-suppressed HgCdTe infrared detectors for two different device junction diameters [50].

Chapter 4
HgCdTe Device Simulation Model

Including analytical and empirical expressions for HgCdTe material parameters (energy band gap, electron affinity, intrinsic carrier concentration, carrier effective mass, carrier mobility, dielectric constant and absorption coefficient) as described in the previous chapter, we develop a numerical model in order to study and design optimized HgCdTe HOT infrared photodiodes. We believe numerical models are more appropriate than analytical models when analyzing these multi-layer hetero-structures. We can account for realistic implant/diffusion doping profiles and compositional grading in this model. First, we present details on the simulation methodology. We detail aspects of our simulation model that were developed specifically for HgCdTe in order to make it more accurate and realistic. Finally, we compare calculations from our simulation model with experimental published data on standard HgCdTe infrared photodiodes in order to validate our model.

4.1 Simulation Methodology

4.1.1 Introduction to Semiconductor Modeling

Semiconductor modeling can be divided into three different branches which are inter-related: process, device and circuit simulation. *Process modeling* usually comes first. It corresponds to the simulation of the different fabrication steps such as implantation or diffusion. The output can be the doping profile in the material for example. Using this doping profile, one can go to the next level which is *device*

modeling. In this case, you usually solve a set of fundamental physics equations in order to derive the electrical, optical or thermal properties of the device. Using these device simulations, one can create compact models for the devices and go the next and final level which is *circuit simulation*. We are interested in this work in device modeling applied to HgCdTe.

The traditional view of semiconductor device modeling is based around a carrier transport model described by a set of semiconductor equations and characterized in terms of either classical, semi-classical or quantum physical models. The majority of current semiconductor device models are based on the *classical* semiconductor equations which are derived from the first two moments of the Boltzmann Transport Equation (BTE). The classical semiconductor equations are Poisson's equation, and electron and hole continuity equations, and are shown in the next section. This classical approach is widely for micron-scale devices based on Si, GaAs, III-V and II-VI materials. The drift-diffusion model transport model has some limitations, especially for devices with regions of very high electric fields. High electric fields can cause substantial electron heating as seen in sub-micron devices or avalanche photodiodes (APD). In this case, the *semi-classical* models are more appropriate. One possible model can be a classical drift-diffusion model combined with data obtained from Monte-Carlo simulations. These data are typically the carrier velocity or impact ionization coefficient – in the case of an APD – versus electric field. Another possible model can be the hydrodynamic model. The hydrodynamic model is a more complete model for carrier transport than the drift-diffusion model and is also derived from BTE. These semi-classical models are not as common as classical ones mostly because they can be much more computationally-intensive. Finally, for another class of devices, it is more appropriate to use *quantum physical* models. These devices are nanoscale devices or devices for which the output is mostly dependent on tunneling processes. The main quantum physical model is the Schrödinger-Poisson model.

A classical approach is used in this work. We use the classical carrier transport model applied to II-VI semiconductor $Hg_{1-x}Cd_xTe$. Models for HgCdTe material parameters used in this model have been presented previously. Details on the recombination mechanisms taken into account in this model and expressions of their rates have also been presented previously. The drift-diffusion model is also modified in order

to account for degeneracy and conduction-band non-parabolicity in HgCdTe as described in the following sections.

4.1.2 Drift-Diffusion Model

Steady-state numerical simulations are performed using *Sentaurus Device* [57], a commercial package by Synopsys. Geometrical device structures are generated using a meshing engine of one, two or three dimension quadtree-based simulation grids. We use the drift-diffusion model which is widely used for the simulation of carrier transport in semiconductors. Sentaurus Device self-consistently determines a full coupled solution of the Poisson's equation and the continuity equations for electrons and holes using an approximate Newton method [58] with Gaussian elimination. The partial differential equations are discretized in the simulation grid using a finite-difference discretization based on the box method [59] and the Scharfetter-Gummel method and solved at each node:

$$\varepsilon \Delta \psi = -q\left(p - n + N_D - N_A\right) \tag{66}$$

$$\nabla \cdot \overrightarrow{J_n} = q\left(U_{tot} + \frac{\partial n}{\partial t}\right) \tag{67}$$

$$-\nabla \cdot \overrightarrow{J_p} = q\left(U_{tot} + \frac{\partial p}{\partial t}\right) \tag{68}$$

where ε is the permittivity (F/m), ψ is the electrostatic potential (V), n and p are the electron and hole concentrations respectively (cm^{-3}), N_D and N_A are the donor and acceptor concentrations respectively (cm^{-3}), J_n and J_p are the electron and hole current densities respectively (A/cm^2), and U_{tot} is the net carrier recombination rate ($cm^{-3}.s^{-1}$).

The current densities for electrons and holes are given by:

$$\overrightarrow{J_n} = -qn\mu_n \vec{\nabla}\Phi_n \tag{69}$$

$$\overrightarrow{J_p} = -qp\mu_p \vec{\nabla}\Phi_p \tag{70}$$

where μ_n and μ_p are the electron and hole mobilities respectively ($cm^2/V.s$), and Φ_n and Φ_p are the electron and hole quasi-Fermi potentials respectively (V).

For current-voltage calculations, this method is typically estimated to give a maximum error of ±5 %. In the case of ohmic contacts, simple Dirichlet boundary conditions are applied, where the surface potential ψ_s and electron and hole concentrations, n_s and p_s, are fixed. The electron and hole quasi-Fermi potentials are equal and are set to the applied bias of that electrode, i.e. $\Phi_n=\Phi_p=V_{applied}$. The surface potential ψ_s is fixed at a value consistent with the charge neutrality condition:

$$n_S - p_S = N_D - N_A \tag{71}$$

For HgCdTe, the net carrier recombination rate U_{tot} is the sum of the net Auger, radiative and Shockley-Read-Hall (SRH) recombination rate which are included at any location within the device. Expressions for these rates are given in the previous chapter. We can also consider surface recombination using the expression defined previously. In this case, the following boundary conditions are used at the surface:

$$\overrightarrow{J_n} \cdot \vec{n} = qv_n\left(n - n_0\right) \tag{72}$$

$$\overrightarrow{J_p} \cdot \vec{n} = -qv_p\left(p - p_0\right) \tag{73}$$

where v_n and v_p are the electron and hole surface recombination velocities respectively (cm/s), and n_0 and p_0 are the equilibrium electron and hole concentrations respectively (cm^{-3}).

The optical generation rate G_{opt} also has to take into account different absorption coefficient in an HgCdTe heterostructure device. For a given location in the device, it will depend on the Cd alloy fraction x and the wavelength as we have seen previously when defining the expression used for the absorption coefficient in HgCdTe, but also on the path of the incident radiation. If we consider an HgCdTe heterostructure with three regions along the y-axis $[0,y_1]$ (alloy fraction x_1), $[y_1,y_2]$ (alloy fraction x_2) and $[y_2,y_3]$ (alloy fraction x_3), and illumination starting at y=0, the optical generation rate ($cm^{-3}.s^{-1}$) for a uniform absorption coefficient $\alpha(x,\lambda)$ can be written as:

$$\begin{cases} G_{opt} = \dfrac{\phi}{E_{ph}(\lambda)} \times \alpha(x_1,\lambda) e^{-\alpha(x_1,\lambda)y} & 0 \le y \le y_1 \\ G_{opt} = \dfrac{\phi}{E_{ph}(\lambda)} \times \alpha(x_2,\lambda) e^{-\alpha(x_1,\lambda)y} e^{-\alpha(x_2,\lambda)(y-y_1)} & y_1 \le y \le y_2 \\ G_{opt} = \dfrac{\phi}{E_{ph}(\lambda)} \times \alpha(x_3,\lambda) e^{-\alpha(x_1,\lambda)y} e^{-\alpha(x_2,\lambda)(y_2-y_1)} e^{-\alpha(x_3,\lambda)(y-y_{31})} & y_2 \le y \le y_3 \end{cases} \quad (74)$$

$$E_{ph} = \frac{hc}{\lambda} \quad (75)$$

where ϕ is the incident radiation flux (W/cm^2), E_{ph} is the photon energy (Joule) and α is the absorption coefficient of HgCdTe (cm^{-1}).

We include all the HgCdTe material parameters using the analytical and empirical expressions defined in the previous chapter. We use Anderson's model [60] for the band alignment at heterojunctions. We can also model $Hg_{1-x}Cd_xTe$ regions with a linearly-graded Cd mole fraction, x. The mole fraction dependencies of the band gap, the electron affinity and the dielectric constant is taken into account using a cubic spline interpolation, and the electron and hole mobility and the electron effective mass using a linear interpolation based on the analytical models defined previously.

Next, we discuss the issues of carrier degeneracy and conduction band non-parabolicity in HgCdTe, and dopant ionization, which are critical points for HgCdTe device modeling.

4.1.3 Carrier Degeneracy and Conduction Band Non-Parabolicity

HgCdTe is a narrow-gap semiconductor that exhibits a non-parabolic conduction band and high carrier degeneracy. Effects of those two factors need to be taken into account to avoid significant errors in HgCdTe device modeling [61], [62], [63], especially when considering n-type layers with doping values >10^{16} cm^{-3}. As we can see in Figure 4.1, Jo et al. [62] shows that significant errors in calculating the Fermi energy level relative to n-type doping level can occur when using the Maxwell-Boltzmann distribution function (non-degenerate, parabolic) or Fermi-Dirac statistics (degenerate, parabolic).

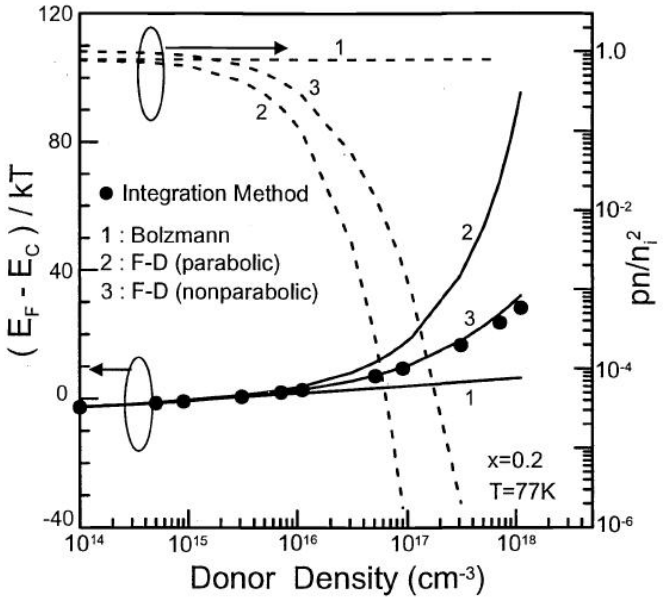

Figure 4.1: The reduced Fermi energy of $(E_F-E_C)/kT$ and pn/n_i^2 as a function of the donor density [62].

For n-type HgCdTe regions, the electron carrier density is given by the following expression which takes into account the carrier degeneracy and the conduction band non-parabolicity:

$$n = \frac{2N_C}{\sqrt{\pi}} \int_0^{\infty} \frac{\varepsilon^{1/2}(1+\alpha\varepsilon)^{1/2}(1+2\alpha\varepsilon)}{1+\exp(\varepsilon-\phi_F)} d\varepsilon \tag{76}$$

$$\alpha = \frac{kT}{E_g}\left(1-\frac{m_e^*}{m_0}\right)^2 \tag{77}$$

where N_C is the density of states in the conduction band (cm^{-3}), ϕ_F is the reduced Fermi energy level $(E_F-E_C)/kT$ and α is the non-parabolicity factor. The energy zero is taken to be at the bottom of the conduction band.

Using the above theoretical expression is not advised for efficient HgCdTe device modeling. Several groups have proposed simple approximations to this expression [61], [62], [63]. Quan et al. [63] have discussed that Ariel's model [61] is only valid for weak degeneracy and does not take into account the electron effective mass dependence on Cd alloy fraction and temperature. Quan's approximation [63] is in the form of Boltzmann's approximation:

$$\phi_F = \ln\left(\frac{n}{B_0 N_C}\right) + B_1\left(\frac{n}{N_C}\right)^{\alpha_1} + B_2\left(\frac{n}{N_C}\right)^{\alpha_2} \tag{78}$$

$$B_0 = 1 + 3.75\alpha + 3.281\alpha^2 - 2.461\alpha^3 \tag{79}$$

$$B_1 = 0.994 - 3.333\alpha \tag{80}$$

$$\alpha_1 = 0.526 + 0.236\exp\left(-\frac{\alpha + 0.00211}{0.0279}\right) \tag{81}$$

$$\alpha_2 = 0.624 - 12.8\alpha + 128\alpha^2 - 541\alpha^3 \tag{82}$$

$$B_2 = -\left(0.577 - 7.93\alpha + 78.6\alpha^2 - 349\alpha^3\right) \tag{83}$$

Jo et al. [62] gives the following approximation which can be easily solved iteratively using an accurate approximation of the Fermi-Dirac integrals [64]:

$$n = N_C\left[F_{1/2}(\phi_F) + 3.75\alpha F_{3/2}(\phi_F)\right] \tag{84}$$

Both approximations have been found to fit closely the theoretical expression for the electron distribution function in a wide range of doping levels and Cd alloy fraction. However, these approximations have only been validated for T=77 K which is the typical operating temperature of HgCdTe infrared photodiodes. The HgCdTe device studied in this work operates at increased temperatures. Therefore, we compare these two approximations with the theoretical expression between 77 K and room temperature. Equation (75) is numerically evaluated using recursive adaptive Lobatto quadrature.

Figure 4.2 shows the results for x=0.2. We plot the reduced Fermi energy $\phi_F=(E_F-E_C)/kT$ versus temperature for different n-type doping levels between 10^{14} cm^{-3} and 10^{18} cm^{-3} calculated by Quan's approximation [63], Jo's approximation [62] and by numerically evaluating the theoretical expression. Both approximations fit the theoretical expression quite well in a wide range of doping levels and temperatures for x=0.2. Some deviations appear for $N_D=10^{18}$ cm^{-3} for T<120 K. This corresponds to high level of degeneracy and we will not encounter this case in realistic simulations of HgCdTe devices where the maximum n-type doping level will be around 10^{17} cm^{-3}. Figure 4.3 shows the same calculations but for x=0.3. Again, both approximations fit closely the theoretical expression. Some deviations appear for $N_D=10^{18}$ cm^{-3} for T<100 K which is a not so realistic situation.

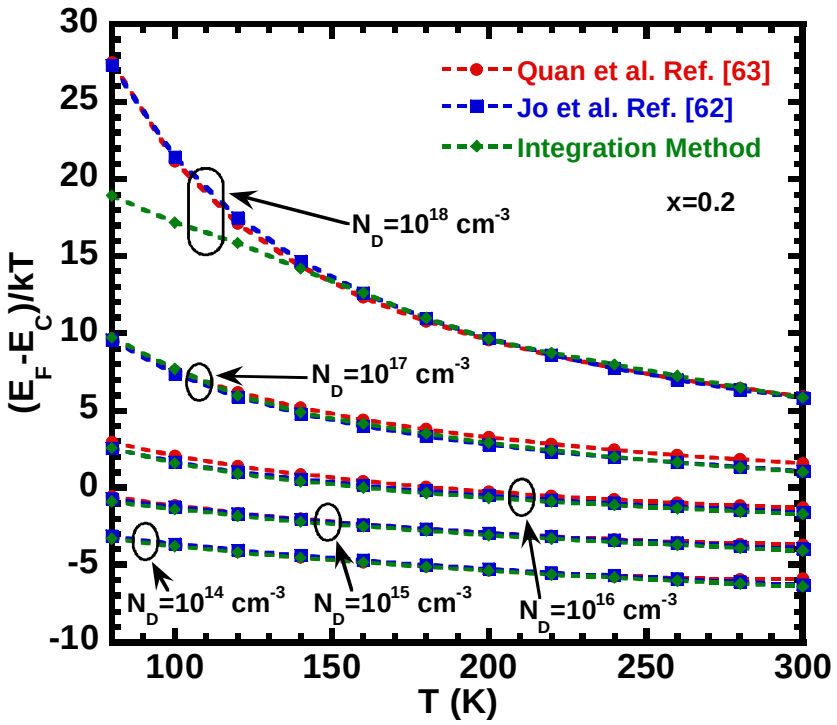

Figure 4.2: Reduced Fermi energy $(E_F-E_C)/kT$ versus temperature for n-type $Hg_{0.8}Cd_{0.2}Te$ calculated by different methods for varying donor doping densities.

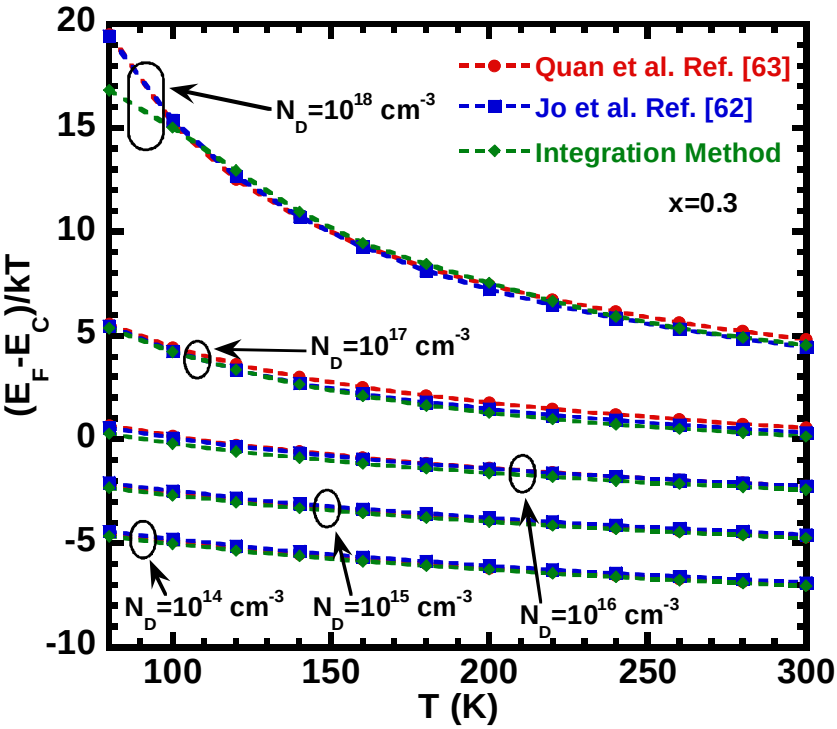

Figure 4.3: Reduced Fermi energy $(E_F-E_C)/kT$ versus temperature for n-type $Hg_{0.7}Cd_{0.3}Te$ calculated by different methods for varying donor doping densities.

In our HgCdTe numerical model, Sentaurus Device uses Fermi-Dirac statistics for parabolic bands:

$$n = N_C F_{1/2}\left(\frac{E_{Fn} - E_C}{kT}\right) \tag{85}$$

$$p = N_V F_{1/2}\left(\frac{E_V - E_{Fp}}{kT}\right) \tag{86}$$

Consequently, in order to account for carrier degeneracy and conduction band non-parabolicity, we distinguish n-type and p-type HgCdTe layers. Since the heavy-hole band can be considered strictly parabolic, we use Equation (85) for p-type HgCdTe layers. For n-type HgCdTe layers, we use Jo's approximation. By using a simple iteration scheme, we adjust the density of states in the conduction band N_C in Equation (84) so that Equation (84) becomes equivalent than Jo's approximation. This means that, for a given n-type doping level, Equation (84) which uses this adjusted N_C and Jo's approximation will give the same Fermi energy relative to the bottom of the conduction band (E_F-E_C).

4.1.4 Ionization of Dopants

Here we discuss the ionization of dopants in HgCdTe. As mentioned previously, arsenic is widely used as p-type dopant in HgCdTe. Arsenic doping can be done either in-situ during MBE growth for example, although this is still a challenge due to its amphoteric behavior, or ex-situ by ion implantation followed by an activation thermal annealing. Due to low heavy-hole effective mass compared to electron effective mass in HgCdTe, it is a challenge to measure the hole concentration in arsenic-doped HgCdTe by Hall. However, it is possible to measure the arsenic concentration by secondary ion mass spectroscopy (SIMS). 100 % activation of arsenic is currently possible in HgCdTe by thermal annealing. Arsenic is a shallow acceptor. Its acceptor level is dependent on the Cd alloy fraction and doping level. This dependence (meV) has been given by the following expression [65]:

$$E_a = 42x + 1.36 - 1.4 \times 10^{-5} N_A^{1/3} \tag{87}$$

Here, arsenic is considered to be a singly ionized acceptor. We determine the Fermi energy that satisfies the charge neutrality condition by using an iterative scheme and Jo's approximation for the electron distribution function defined in the previous section:

$$n + n_D + p + p_A = N_D - N_A \tag{88}$$

$$n_D = \frac{N_D}{1 + \frac{1}{2}\exp\left(\frac{E_d - E_F}{kT}\right)} \tag{89}$$

$$p_A = \frac{N_A}{1 + \frac{1}{4}\exp\left(\frac{E_F - E_a}{kT}\right)} \tag{90}$$

where n_D and n_A are the density of electrons bound to the donors and the density of holes bound to acceptors respectively (cm^{-3}). This scheme is used in order to calculate the hole concentration in arsenic-doped HgCdTe versus temperature in our range of interest for the temperature, doping level and Cd alloy fraction.

Figure 4.4 and Figure 4.5 show the calculated hole concentration versus temperature for x=0.2 and x=0.3 in the case of arsenic doping with $N_A=10^{15}$ cm^{-3} and $N_A=10^{17}$ cm^{-3} respectively. In this work, we typically consider HgCdTe devices operating between 80 K and 300 K. For $N_A=10^{15}$ cm^{-3} and x=0.2, we see the saturation range with nearly 100 % activation for T<100 K. For T>100 K, the material becomes intrinsic. For $N_A=10^{15}$ cm^{-3} and x=0.3, we also see the saturation range with nearly 100 % ionization for T<230 K. The intrinsic range appears for T>230 K. For $N_A=10^{17}$ cm^{-3} and both x=0.2 and x=0.3, the saturation range is about 100<T<300 K. T<100 K is the freeze-out range. However, for T=80 K, ionization for x=0.2 and x=0.3 is about 70 % and 60 % respectively. We believe that this small freeze-out occurring at high doping levels will not have a significant impact in HgCdTe device modeling. Thus, we consider 100 % ionization in the case of p-type doping in our numerical model.

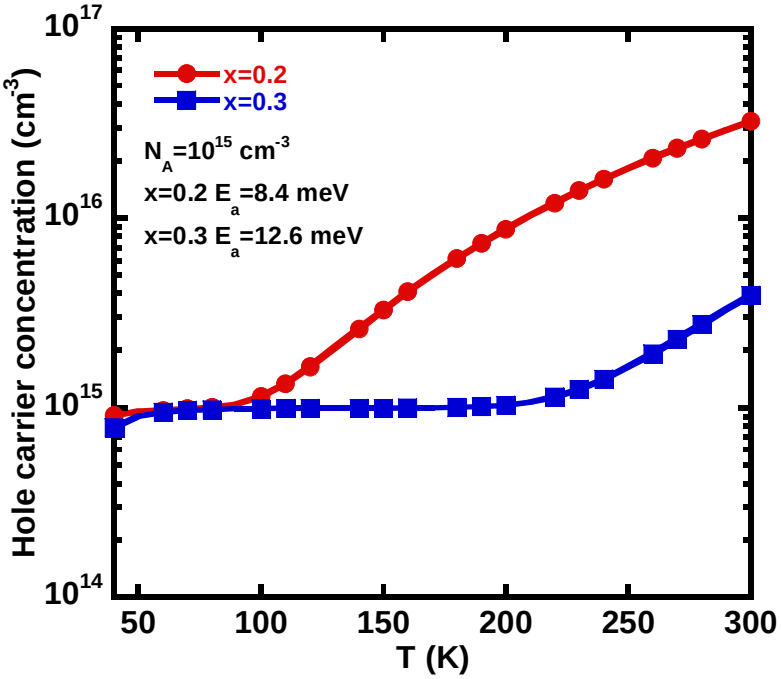

Figure 4.4: Hole carrier concentration versus temperature in the case of arsenic doping with $N_A=10^{15}$ cm^{-3} for x=0.2 (circle) and x=0.3 (square).

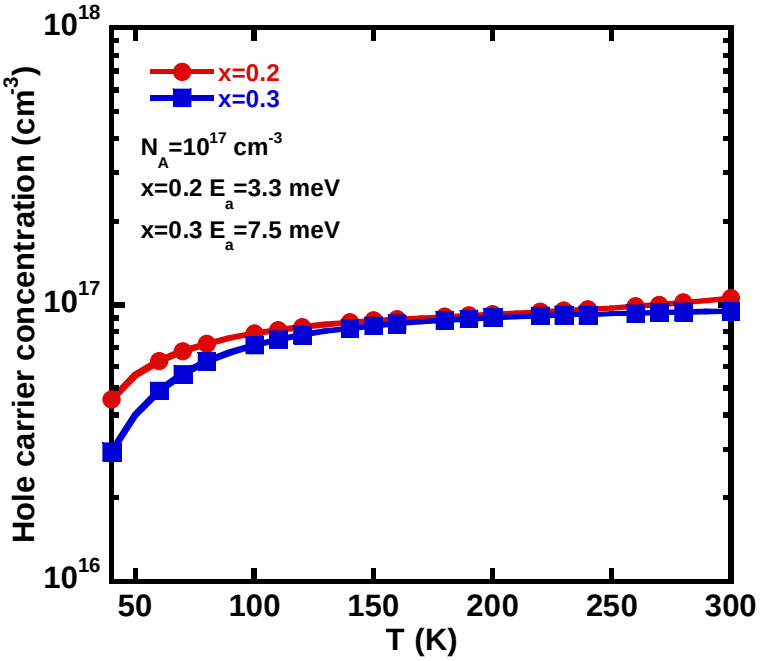

Figure 4.5: Hole carrier concentration versus temperature in the case of arsenic doping with $N_A=10^{17}$ cm^{-3} for x=0.2 (circle) and x=0.3 (square).

In the case of n-type HgCdTe, indium is the most widely used donor. Most of the indium is assumed to be present in In_2Te_3 dissolved in HgCdTe and only a small fraction of indium on Hg lattice sites acting as donors [66]. Due to the complexity of the indium interaction with HgCdTe, it is not possible to use our simple iterative scheme in order to determine the ionization of indium in n-type HgCdTe. However, indium is considered a shallow donor in HgCdTe [67]. Reports indicate that its donor level is merged with the conduction band and that no carrier freeze-out is observed [68]. Therefore, 100 % ionization is also considered in our numerical model for indium-doped HgCdTe in our range of interest for the temperature, doping level and Cd alloy fraction.

4.2 Model Validation

One of most important and most challenging problems facing the development of a simulation model is that of determining whether this model is an accurate representation of the actual system under study. We are concerned with HgCdTe infrared photodiodes in this case. It should be emphasized that this "validation" procedure is concerned with measuring the accuracy of the simulation model as a real-world analog and not with the "verification" of the correctness of the computer program.

The developed simulation model was presented in details in the previous section. We determine the representativeness of the simulation output data in this section. The most definitive test of the validity of a simulation model is to establish that the model output data closely approximates the output data that would be expected from the actual system. Most of the published experimental data for HgCdTe photodiodes correspond to standard DLPH HgCdTe devices. Therefore, we validate our model by 1D simulation of DLPH HgCdTe devices (simulation of a cross-section of the vertical devices). We are interested in this work in HgCdTe photodiodes with response in the MWIR and LWIR infrared windows and operated between 77 K and room temperature. Below is a list of the main parameters in our numerical model for a given HgCdTe layer:

- t: thickness of the layer (μm)
- $N_{D,A}$: donor/acceptor concentration (cm^{-3})
- x: Cd alloy fraction

- k: ratio of hole mobility and electron mobility (electron mobility is fixed using the model described previously) taken around the usual value for HgCdTe which is 0.01
- $|F_1F_2|$: overlap integral in Auger-1 recombination which we assume in the range of reported values 0.1-0.3
- γ: ratio of Auger-7 intrinsic lifetime and Auger-1 intrinsic lifetime assumed in the range of reported values 3-60
- E_{trap}: trap level for SRH recombination (eV)
- τ_{n0} (τ_{p0}): SRH characteristic lifetime (μs) assuming the value is the same for electrons and holes
- v_{sur}: surface recombination velocity (cm/s) at the interface between HgCdTe and the passivation layer

As mentioned previously, one typical figure of merit for HgCdTe photodiodes is the resistance-area product R_0A plotted versus the inverse temperature. Therefore, we compare published experimental data and our simulation output for R_0A versus cutoff wavelength going from MWIR to LWIR of an HgCdTe photodiode operated at 77 K. Our numerical model is used to calculate R_0A versus cutoff wavelength for a DLPH HgCdTe p-on-n device operated at 77 K. The simulation results are visually compared with data taken from different sources [76], [77]. Different substrates and different growth techniques have been used for the experimental data as indicated in Figure 4.6. We assume step doping profiles with the electrical junction at the metallurgical junction. We do not consider surface recombination due to passivation layer in this case. We use typical values for the parameters used in the simulation of the HgCdTe p-on-n DLPH as described below.

Top p-type layer:

t=1 μm, x=0.3, $N_A=5\text{x}10^{17}$ cm^{-3}, k=0.01, $|F_1F_2|=0.3$, $\gamma=6$, $E_{trap}=E_{Fi}$ (intrinsic Fermi level), $\tau_{n0}=\tau_{p0}=5$ μs.

Absorber n-type layer:

t=5 μm, $N_D=2\text{x}10^{15}$ cm^{-3}, k=0.01, $|F_1F_2|=0.3$, $\gamma=6$, $E_{trap}=E_{Fi}$ (intrinsic Fermi level), $\tau_{n0}=\tau_{p0}=5$ μs.

The simulation result is also shown in Figure 4.6, along with the ideal analytical diffusion-limited R_0A (considering Auger and radiative processes only). Our simulation results compare well with published experimental data taken from different sources and obtained with different processing techniques. Experimental and simulation data follow the diffusion-limited trend for LWIR HgCdTe. For MWIR HgCdTe, experimental and simulation data deviate from this trend due to g-r current in the depletion region (SRH processes). In this case, our simulation calculations for R_0A are on the upper end of published experimental data, which is expected from a theoretical model.

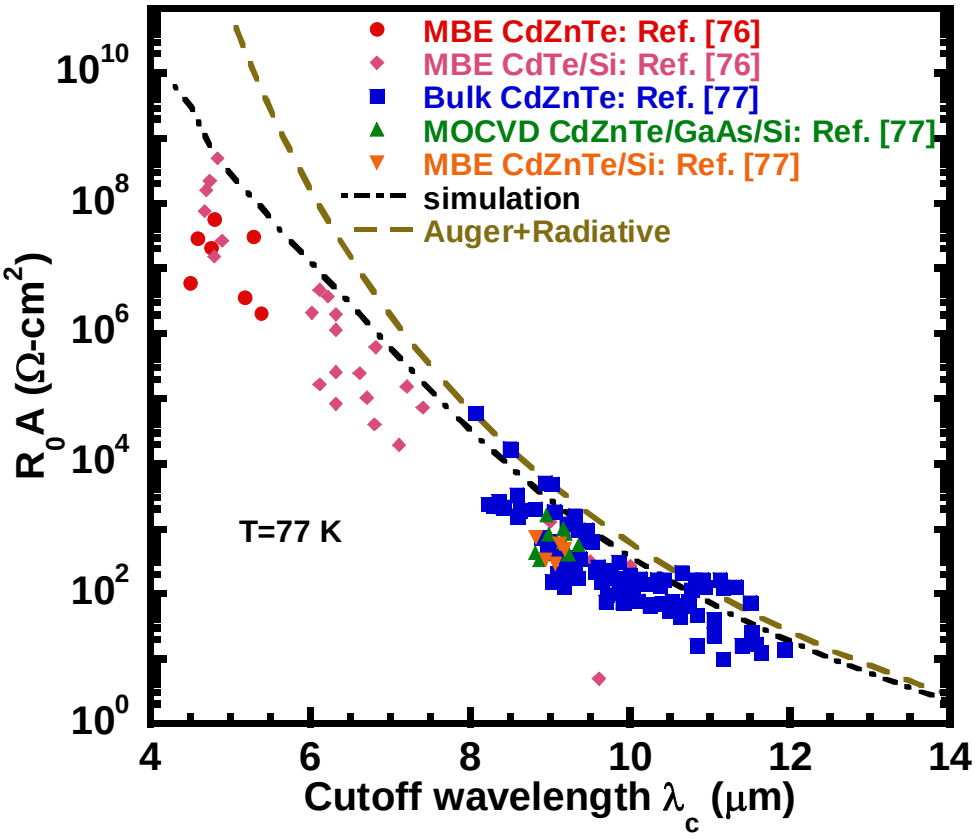

Figure 4.6: Experimental R_0A versus cutoff wavelength HgCdTe p-n DLPH using different substrates taken from different published reports. The curves obtained from our simulation model (dash-dot line) and from the ideal diffusion-limited R0A (considering Auger and radiative processes, dashed line) are also shown.

The ultimate figure of merit for infrared detectors is the detectivity D^*. Using the device parameters shown above, the detectivity D^* is calculated using our numerical

model for a DLPH device at 80 K with different cutoff wavelengths (from MWIR λ_c=5 μm to LWIR λ_c=12 μm). The Cd alloy fractions are adjusted in order to adjust the cutoff wavelength. The calculated D^* values are compared with the theoretical and experimental data shown in Figure 1.2. We assume a 300 K background scene and 2π FOV. The results are shown in Figure 4.7. The simulated line for a DLPH at 80 K is comparable to the ideal photovoltaic line. It is only slightly lower because the detector noise is taken into account in our simulation. This confirms that HgCdTe DLPH devices can achieve BLIP when operated at 80 K for both MWIR and LWIR. The simulated spectral response of D^* for DLPH with λ_c=5 μm and λ_c=12 μm is also comparable to what is expected from commercial HgCdTe detectors.

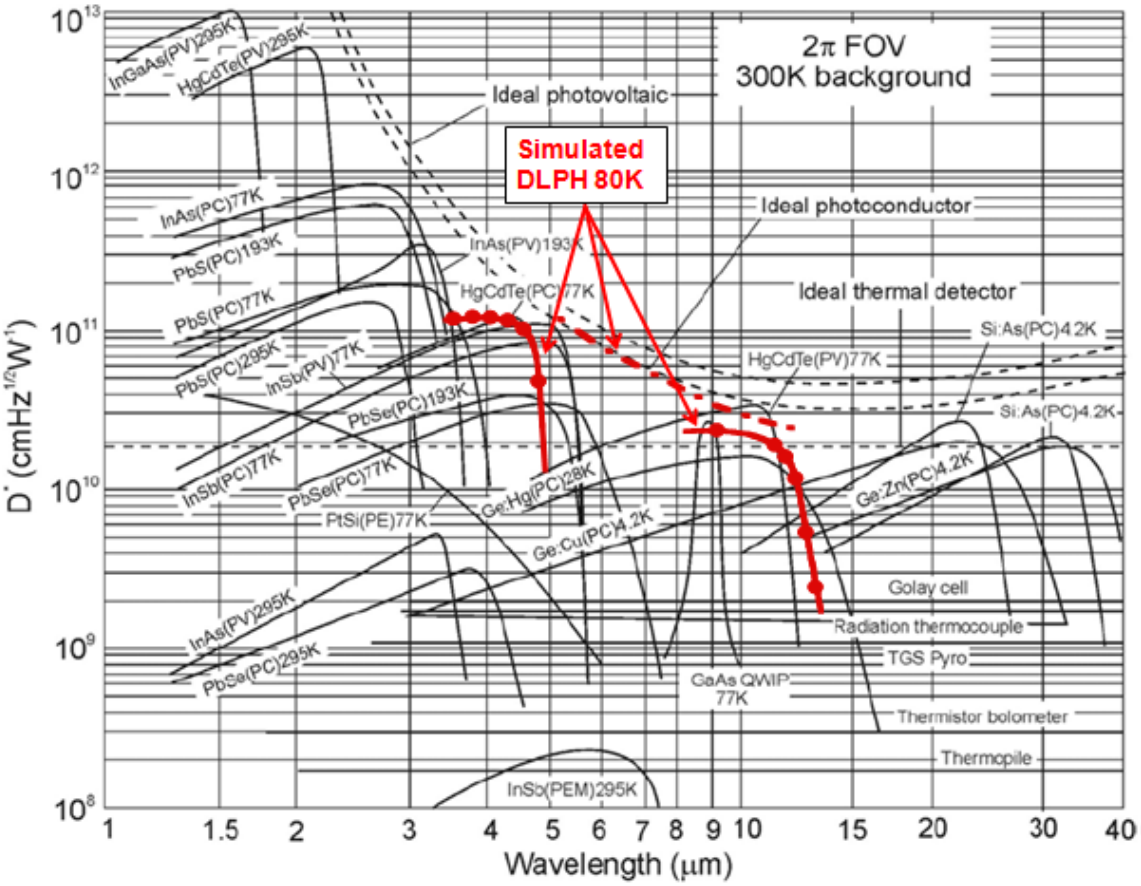

Figure 4.7: D^* from commercial detectors operated at the indicated temperatures. Also shown is the simulated line for a DLPH at 80 K with cutoff varying from 5 μm to 12μm, and the simulated spectral responses of D^* for DLPH at 80 K with λ_c=5 μm (MWIR) and λ_c=12 μm (LWIR).

Our simulation calculations of the device electrical characteristics, such as R_0A, give similar results than experimental data for standard HgCdTe DLPH devices at 77 K with different cutoff wavelengths (from MWIR to LWIR) taken from different sources [76], [77]. In addition, our simulation calculations of D^* is also comparable to what is expected from commercial HgCdTe infrared detectors with different cutoff wavelengths.

In the next chapter, our simulation model is used in order to study and compare the performance of standard HgCdTe DLPH devices and that of our proposed Auger-suppressed HgCdTe photodiodes.

Chapter 5

Comparison Study Between Current and Proposed Device Architecture

We presented in the previous chapter the numerical model developed in order to study HgCdTe photodiodes. Here this numerical model is used in order to compare the performance of our proposed Auger-suppressed HgCdTe infrared photodiodes (P+/ν/N+ structure) with the equivalent current state-of-the-art HgCdTe infrared DLPH devices (P+/ν structure). Both architectures are comparedwith response in both MWIR and LWIR windows.

The potential improvements of using our proposed Auger-suppressed HgCdTe infrared photodiodes are determined in terms of standard figures of merit, such as dark current or detectivity D^*, and in terms of temperature of operation which is the main driving force behind this work. We assume step doping profiles with the electrical junction at the metallurgical junction. We do not consider surface recombination due to passivation layer in this case. We use typical values for the parameters used in the simulation of the two structures. Figure 5.1 shows the base structure for the HgCdTe DLPH device (left) and HOT device (right). Top illumination is used for the spectral response calculations.

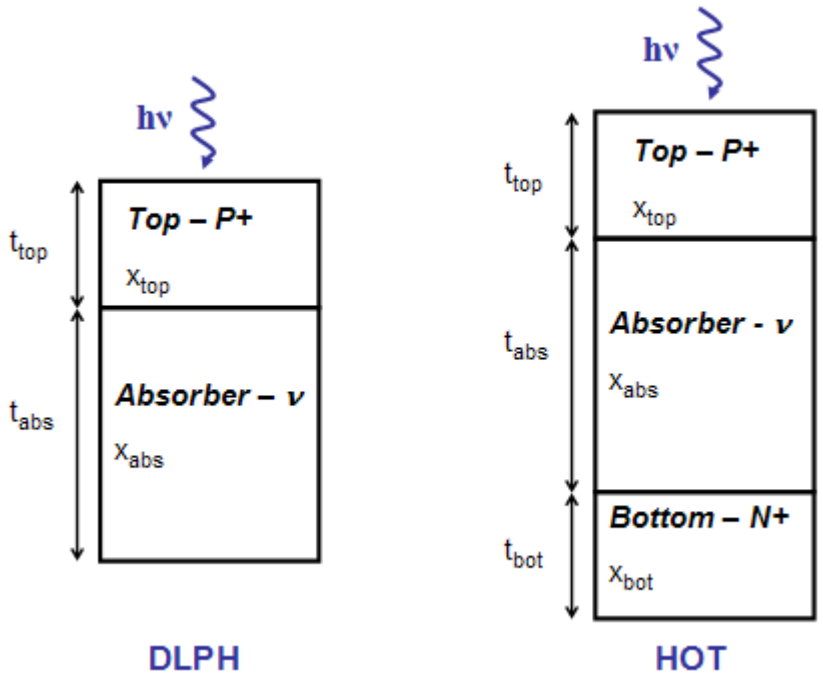

Figure 5.1: Base structure for the DLPH (left) and HOT (right) HgCdTe devices.

5.1 Performance Comparison

5.1.1 MWIR Devices

Top p-type P+ layer (common for DLPH and HOT):

t_{top}=1 μm, x_{top}=0.4, N_A=5x10^{17} cm^{-3}, k=0.01, $|F_1F_2|$=0.3, γ=6, E_{trap}=E_{Fi} (intrinsic Fermi level), τ_{n0}=τ_{p0}=1 μs.

Absorber n-type ν layer (common for DLPH and HOT):

t_{abs}=3 μm, x_{abs}=0.3, N_D=1x10^{15} cm^{-3}, k=0.01, $|F_1F_2|$=0.3, γ=6, E_{trap}=E_{Fi} (intrinsic Fermi level), τ_{n0}=τ_{p0}=1 μs.

Bottom n-type N+ layer (HOT):

t_{bot}=1 μm, x_{bot}=0.4, N_D=1x10^{17} cm^{-3}, k=0.01, $|F_1F_2|$=0.3, γ=6, E_{trap}=E_{Fi} (intrinsic Fermi level), τ_{n0}=τ_{p0}=1 μs.

Figure 5.2 shows the calculated energy band diagram at zero bias for the DLPH and HOT devices. The band profile changes as the temperature is increased and the absorber layer is becoming more and more intrinsic.

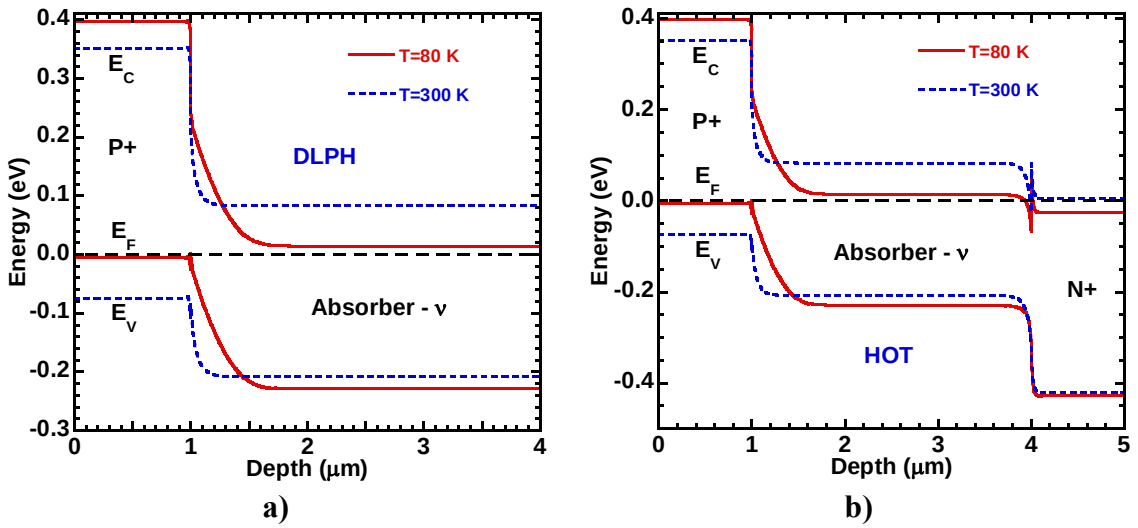

Figure 5.2: Energy band profile at zero bias for a) DLPH and b) HOT at 80 K and room temperature.

Figure 5.3 shows the calculated current-voltage characteristics for both structures between 80 K and room temperature. The dark current in the HOT structure is about one or two orders of magnitude lower than the one in the DLPH structure at high temperatures (>200 K). This is due to Auger suppression in the absorber. However, we do not observe clear negative differential resistance (NDR) in the I-V due to Auger suppression because it is hidden by other leakage currents such as g-r current due to SRH processes.

Figure 5.4 and Figure 5.5 show the calculated responsivity and external quantum efficiency, respectively, for the DLPH and HOT devices at different temperatures. Response in the MWIR window is observed for all cases. We also observe a shift towards lower cutoff and peak wavelengths, λ_c and λ_p, as the temperature is increased. This corresponds to the increase in energy band gap of the HgCdTe absorber layer as the temperature is increased for a fixed x_{abs}. Below ~3 μm, the responsivity and quantum efficiency spectral response are affected by absorption at the top P+ layer.

The calculated responsivity and quantum efficiency are limited by the minority carrier diffusion length and the absorber thickness for a given wavelength. For the DLPH device, the responsivity and quantum efficiency are significantly lower than for the HOT device at all temperatures. This is because the minority carrier diffusion length is in the range of the absorber layer thickness for the DLPH device (~2.8 μm at 80 K). For the

HOT device, the minority carrier diffusion length is much larger than the absorber thickness due to Auger suppression in the absorber (>10 μm at 80 K). Therefore, the quantum efficiency is nearly 100 % in a wide range of temperature (<200 K), only limited by the absorption volume.

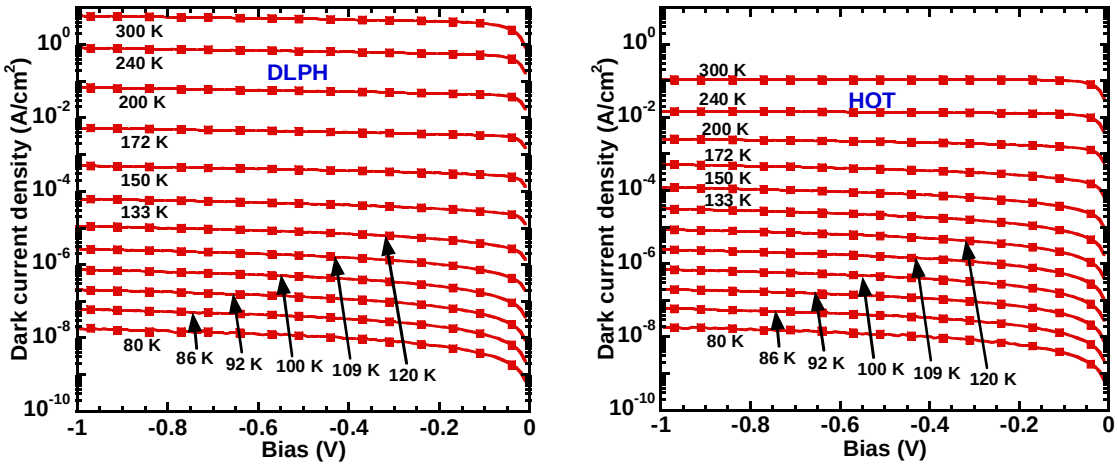

Figure 5.3: Calculated current-voltage characteristic for a) DLPH and b) HOT at different temperatures.

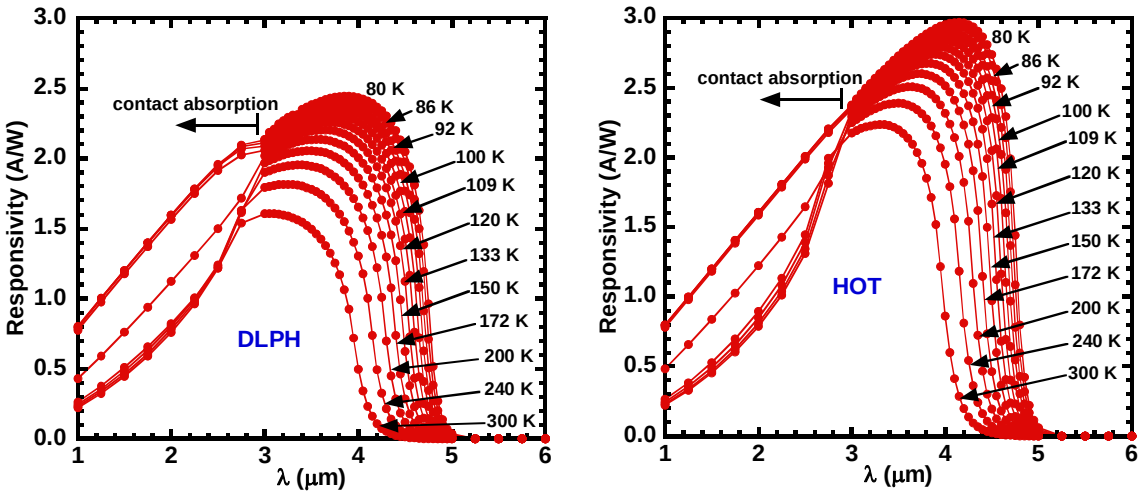

Figure 5.4: Calculated responsivity versus wavelength for a) DLPH and b) HOT at different temperatures.

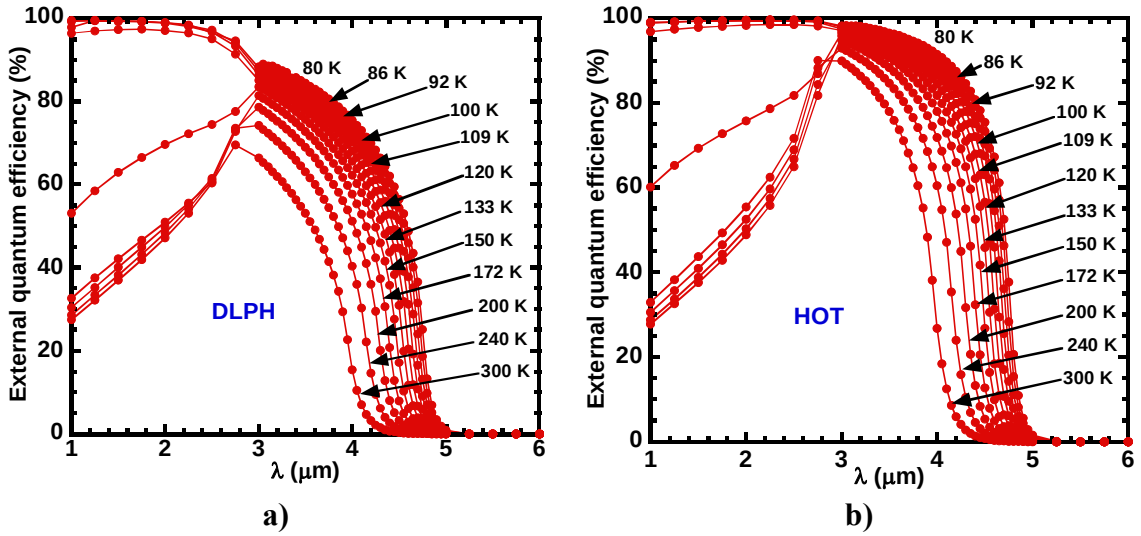

Figure 5.5: Calculated external quantum efficiency versus wavelength for a) DLPH and b) HOT at different temperatures.

Figure 5.6 shows the calculated dark current density at 100 mV reverse bias and detectivity D^* versus temperature for the DLPH and HOT devices. The background scene is assumed to be a black-body at 300 K and $f_{\#}$=3. Below ~120 K, both devices are in BLIP and have nearly the same dark current and detectivity D^*. Above 120 K, the detector noise starts increasing above the background noise due to Auger processes in the absorber, and the devices are becoming diffusion-limited. The maximum temperature for BLIP is ~130 K and ~160 K for the DLPH and HOT devices respectively. The increase in BLIP for the HOT device is ~30 K. Indeed, the increase in dark current with temperature is significantly lower for the HOT device compared to the DLPH device. This is due to Auger suppression in the absorber for the HOT device. Consequently, the detectivity D^* for the HOT device becomes larger than the one for the DLPH device as the temperature is increased, reaching one order of magnitude larger at room temperature.

For T=180 K (λ_c~4.4 μm) where TE-cooling is potentially applicable, J_{dark}~6×10^{-4} A/cm^2 and D^*~2×10^{11} cm.Hz$^{0.5}$/W for the HOT device, which is a high value for the detectivity of an HgCdTe infrared detector at such high temperature. BLIP at 180 K can be achieved for the HOT device by increasing the FOV to ~50°. In this case, the detectivity D^* goes down to ~8×10^{10} cm.Hz$^{0.5}$/W.

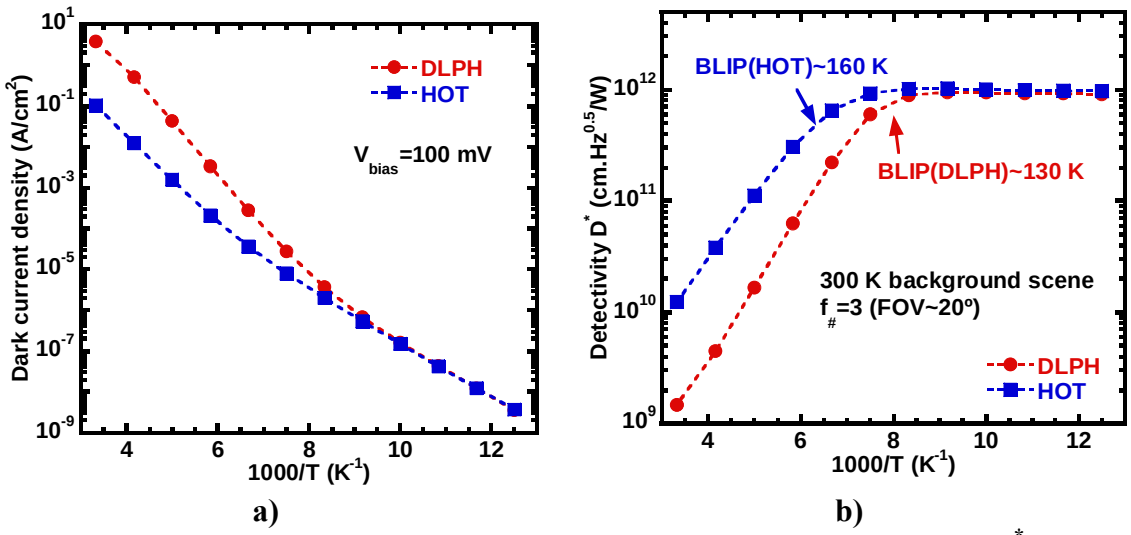

Figure 5.6: a) Calculated dark current density and b) detectivity D^* versus temperature for the DLPH and HOT devices. Background scene at 300 K and $f_{\#}$=3 is assumed.

5.1.2 LWIR Devices

Top p-type P+ layer (common for DLPH and HOT):

t_{top}=1 μm, x_{top}=0.3, N_A=5x10^{17} cm^{-3}, k=0.01, $|F_1F_2|$=0.3, γ=6, E_{trap}=E_{Fi} (intrinsic Fermi level), τ_{n0}=τ_{p0}=1 μs.

Absorber n-type ν layer (common for DLPH and HOT):

t_{abs}=3 μm, x_{abs}=0.2, N_D=2x10^{15} cm^{-3}, k=0.01, $|F_1F_2|$=0.3, γ=6, E_{trap}=E_{Fi} (intrinsic Fermi level), τ_{n0}=τ_{p0}=1 μs.

Bottom n-type N+ layer (HOT):

t_{bot}=1 μm, x_{bot}=0.3, N_D=2x10^{15} cm^{-3}, k=0.01, $|F_1F_2|$=0.3, γ=6, E_{trap}=E_{Fi} (intrinsic Fermi level), τ_{n0}=τ_{p0}=1 μs.

Figure 5.7 shows the calculated energy band diagram at zero bias for the DLPH and HOT devices. Again, the band profile changes as the temperature is increased and the absorber layer is becoming more and more intrinsic.

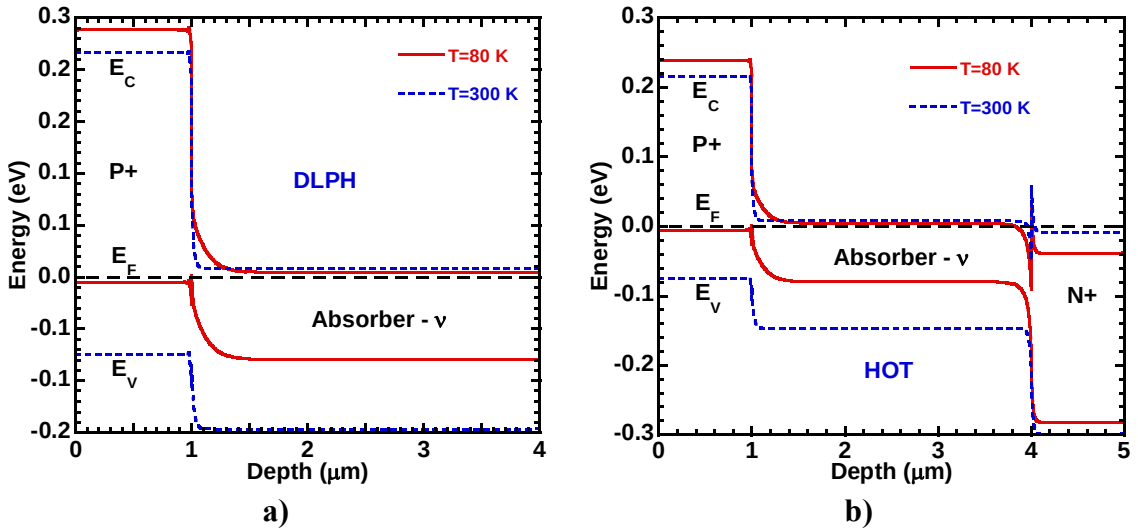

Figure 5.7: Energy band profile at zero bias for a) DLPH and b) HOT at 80 K and room temperature.

Figure 5.8 shows the calculated current-voltage characteristics for both structures between 80 K and room temperature. Again, the dark current of the HOT device is much smaller than the one of the DLPH device in the whole temperature range due to Auger suppression in the absorber. In addition, above ~109 K, clear NDR is observed in the I-V, which becomes higher and higher as the temperature is increased. This is because Auger processes are dominant in LWIR HgCdTe – contrary to MWIR HgCdTe – and become stronger as the temperature is increased.

Figure 5.9 and Figure 5.10 show the calculated responsivity and external quantum efficiency, respectively, for the DLPH and HOT devices at different temperatures. Response in the LWIR window is observed up to ~200 K. We also observe a shift towards lower cutoff and peak wavelengths, λ_c and λ_p, as the temperature is increased. Again, this corresponds to the increase in energy band gap of the HgCdTe absorber layer as the temperature is increased for a fixed x_{abs}. Below ~4 μm, the responsivity and quantum efficiency spectral response are affected by absorption at the top P+ layer.

Like in the MWIR case, the calculated responsivity and quantum efficiency are limited by the minority carrier diffusion length and the absorber thickness for a given wavelength. For the DLPH device, the responsivity and quantum efficiency are more significantly lower than for the HOT device at all temperatures than in the MWIR case. This is because the minority carrier diffusion length is in the range of the absorber layer

thickness for the DLPH device (~2.3 μm at 80 K). For the HOT device, the minority carrier diffusion length is much larger than the absorber thickness due to Auger suppression in the absorber (>10 μm at 80 K). Therefore, the quantum efficiency is nearly 100 % in a wide range of temperature (<200 K), only limited by the absorption volume.

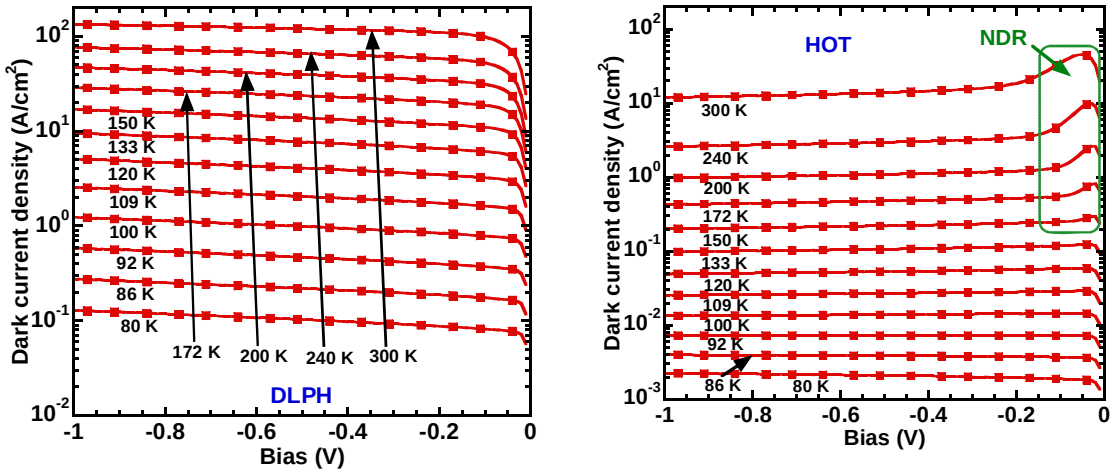

Figure 5.8: Calculated current-voltage characteristic for a) DLPH and b) HOT at different temperatures.

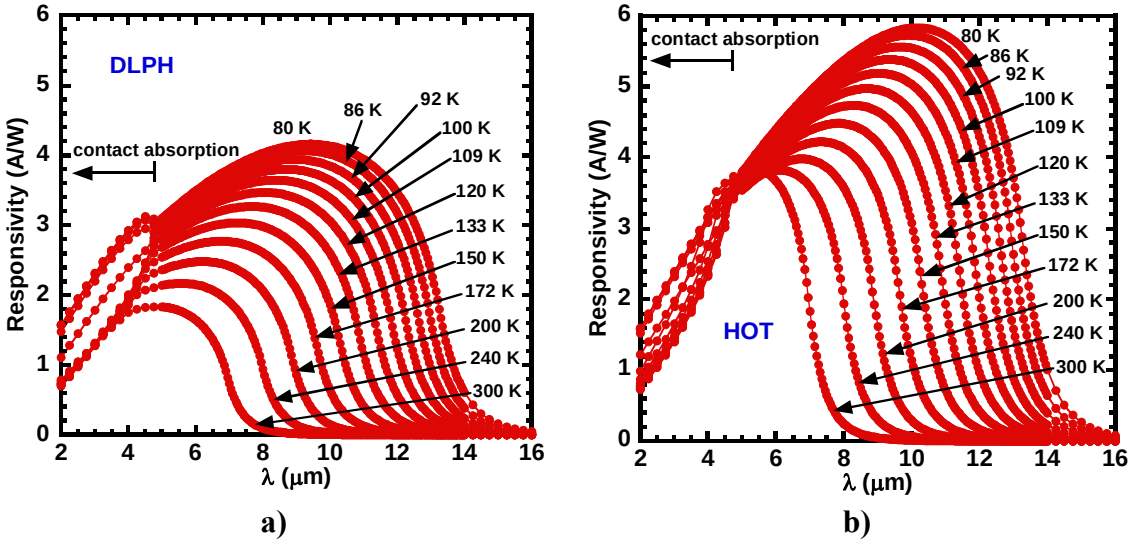

Figure 5.9: Calculated responsivity versus wavelength for a) DLPH and b) HOT at different temperatures.

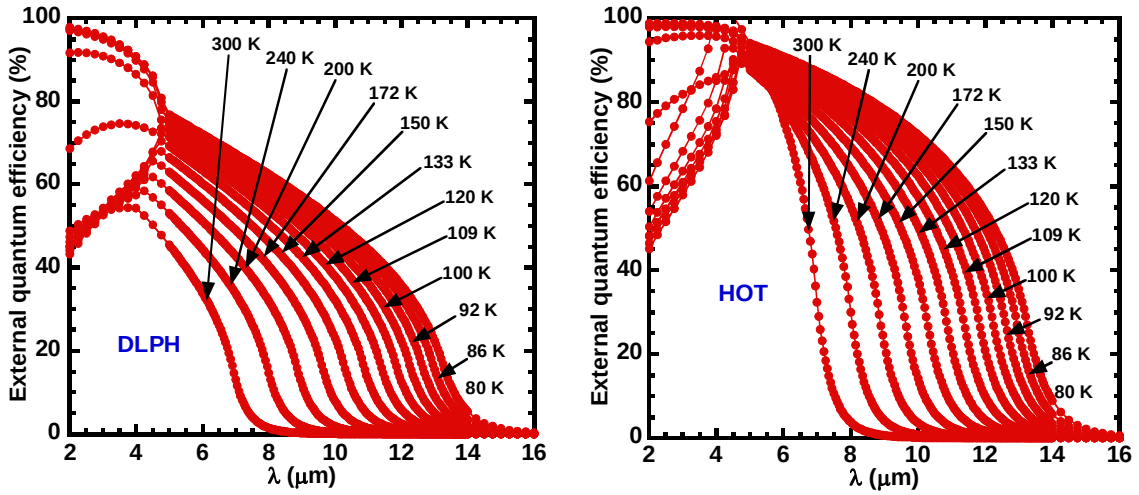

Figure 5.10: Calculated external quantum efficiency versus wavelength for a) DLPH and b) HOT at different temperatures.

Figure 5.11 shows the calculated dark current density at 100 mV reverse bias and detectivity D^* versus temperature for the DLPH and HOT devices. The background scene is assumed to be a black-body at 300 K and $f_{\#}$=3. Contrary to the MWIR case, Auger processes for LWIR HgCdTe are significant even at 80 K. Therefore, the DLPH detector noise at 80 K is already higher than the background noise (not BLIP) for this optics system. This is also true for the HOT device where the detector noise at 80 K is in the same range as the background noise.

However, the HOT device has a significantly lower dark current (about two orders of magnitude) and higher detectivity D^* (about one order of magnitude) than the DLPH device at 80 K due to Auger suppression in the absorber. This improvement of the HOT device remains steady as the temperature is increased and starts decreasing above ~200 K because the increase in Auger processes is higher than Auger suppression. This trend is opposite to the one in the MWIR case, due to the relative importance of Auger processes in MWIR (Auger processes become dominant over SRH processes above ~150 K) and LWIR (Auger processes are dominant from 80 K to room temperature).

For T=180 K (λ_c~9.5 μm) where TE-cooling is potentially applicable, J_{dark}~$7x10^{-1}$ A/cm^2 and D^*~$8x10^9$ cm.Hz$^{0.5}$/W. Although BLIP at 180 K does not seem achievable at this point for LWIR HOT, the potential high detectivity value is unmatched for HgCdTe LWIR detectors at this temperature.

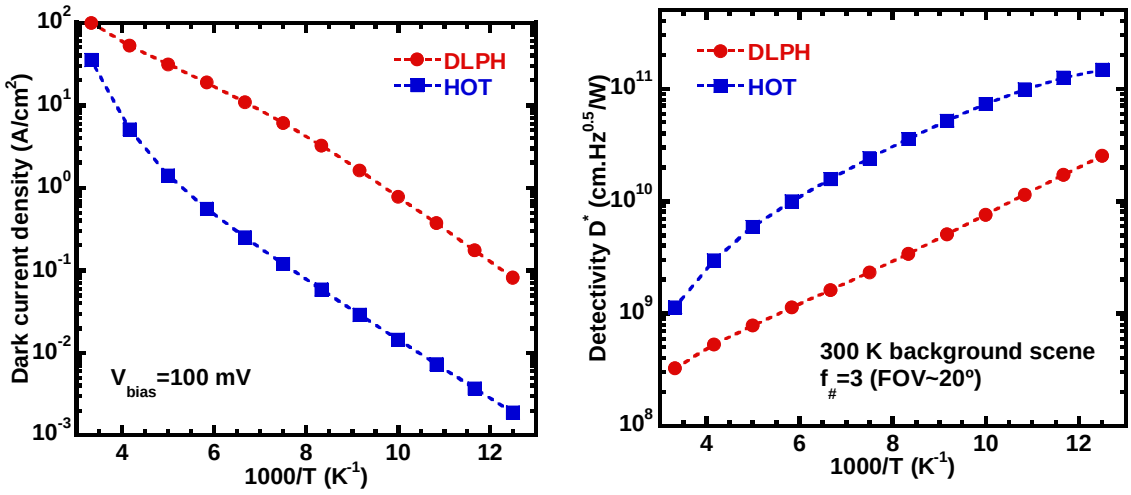

Figure 5.11: a) Calculated dark current density and b) detectivity D^* versus temperature for the DLPH and HOT devices. Background scene at 300 K and $f_{\#}$=3 is assumed.

To summarize, the performance improvements of HOT devices compared to standard DLPH devices is more visible in the LWIR range due to stronger Auger processes. The calculated dark current in the HOT device is about two orders of magnitude lower than the one in the DLPH device in a wide range of temperatures due to Auger suppression in the absorber layer. The calculated detectivity is also about one order of magnitude higher in the HOT device. However, BLIP may potentially be achievable at TE-cooling temperatures for HOT in the MWIR range according to our simulation model. The improvements of the HOT device in the MWIR range become significant for temperatures of operation above ~180 K.

Improving the operating temperature of HgCdTe infrared detectors is the central issue of this study. The improvements of the HOT device in terms of optimum operating temperature are calculated using our numerical model and presented in the following section.

5.2 Operating Temperature Improvements

Here we determine the potential of using HgCdTe HOT technology in terms of increased T_{BLIP} compared to standard HgCdTe DLPH technology for response in both

MWIR and LWIR windows. BLIP has been defined in the first chapter. T_{BLIP} corresponds to the temperature at which the detector noise is equal to the background photon shot noise. It is therefore the maximum temperature of operation in order to achieve BLIP. It shows how much a given infrared detector needs to be cooled down to achieve its best performance.

The detector noise for the HOT and DLPH devices is calculated at 200 mV reverse bias. The background photon shot noise is calculated assuming a background scene at 300 K and 2π FOV. FOV of 2π is chosen because we are mostly interested in the difference of T_{BLIP} between the HOT and DLPH devices. The quantum efficiency is assumed to be 100 % for both devices.

In this analysis, the Cd alloy composition in the absorber layer, x_{abs}, is adjusted as the temperature of operation is changed in order to maintain a *constant cutoff wavelength* λ_c. Figure 5.1 shows the base structure for the DLPH device (left) and HOT device (right). The thicknesses of the different layers are fixed. The Cd composition of the "top" and "bottom" layers is always fixed to (x_{abs}+0.1) for consistency. The p-type doping in the "top" layer is fixed at $5x10^{17}$ cm^{-3}. The n-type doping of the "absorber" layer is fixed at $1x10^{15}$ cm^{-3}. The n-type doping of the "bottom" layer in the HOT device is fixed at at $5x10^{17}$ cm^{-3}. The overlap integral $|F_1F_2|$ for Auger-1 recombination is fixed at 0.3 and the ratio of Auger-7 over Auger-1 lifetimes γ is fixed at 6.

Figure 5.12 shows the calculated T_{BLIP} versus cutoff wavelength λ_c for DLPH and HOT assuming $\tau_{n0}=\tau_{p0}=5$ μs. We see that the HOT device can achieve BLIP at significantly higher temperatures than the DLPH device. The improvement in T_{BLIP} ranges from ~40 K (λ_c=12 μm, LWIR) to ~50 K (λ_c=5 μm, MWIR). As observed in the previous section, we see that MWIR HOT can potentially BLIP at operating temperatures >180 K, which opens the possibility to achieve high sensitivity infrared imaging using TE-cooling.

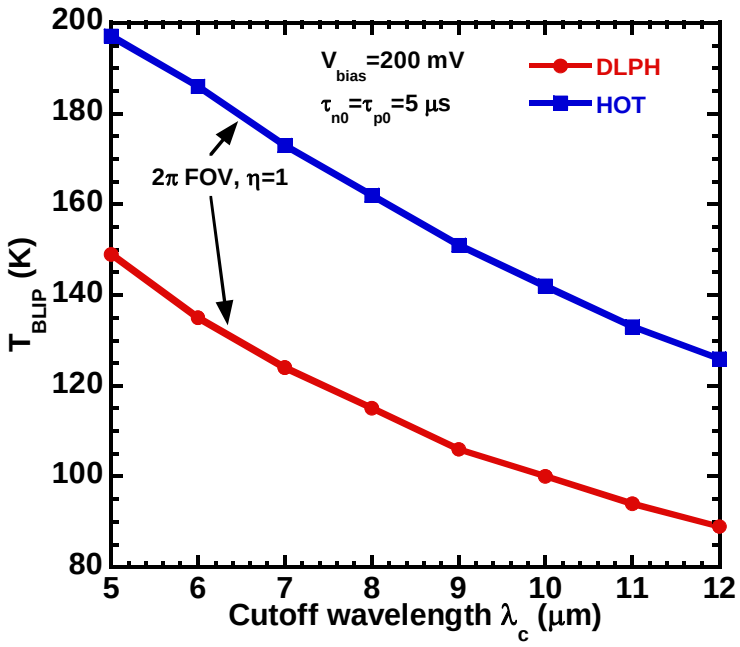

Figure 5.12: Calculation of the temperature required to achieve BLIP versus cutoff wavelength for the DLPH and HOT devices ($\tau_{n0}=\tau_{p0}=5$ μs). Background at 300 K, 2π FOV and η=1 is assumed.

Figure 5.13 shows the calculated TBLIP versus τ_{n0} (τ_{p0}) for MWIR and LWIR. The SRH characteristic lifetime for electrons τ_{n0} (and holes τ_{p0}) is related to the trap concentration in the HgCdTe layers causing SRH recombination. It is therefore a measure of the quality of the crystal and should be as long as possible.

We see that T_{BLIP} for the HOT device is more sensitive to τ_{n0} (τ_{p0}) than the one for the DLPH device. This is because the DLPH device rapidly becomes diffusion-limited, i.e. limited by Auger processes, as the temperature of operation is increased. Auger processes are significantly reduced in HOT devices and therefore these devices are much more sensitive to the crystal quality. The same reason explains why both devices are more sensitive to τ_{n0} (τ_{p0}) in the MWIR range than in the LWIR range. Indeed, Auger processes are more important in LWIR HgCdTe and the crystal quality has less influence.

The HOT improvement in terms of T_{BLIP} is therefore maximized for τ_{n0} (τ_{p0}) as long as possible. T_{BLIP} does not change much for the DLPH device in the MWIR range and LWIR range for $\tau_{n0}=\tau_{p0}>1$ μs and $\tau_{n0}=\tau_{p0}>0.1$ μs respecitvely.

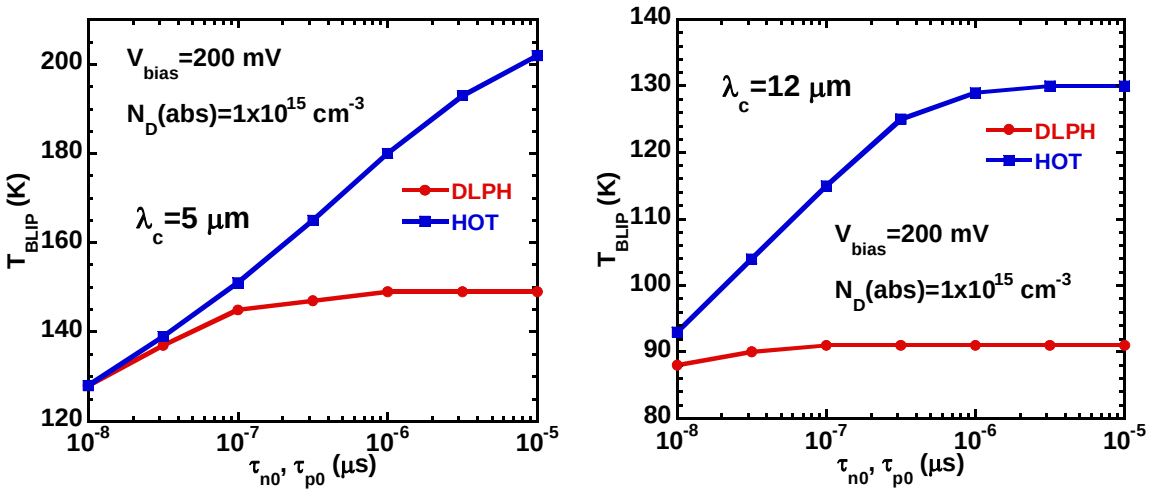

a) b)

Figure 5.13: T_{BLIP} versus τ_{n0} (τ_{p0}) for a) λ_c=5 μm (MWIR) and b) λ_c=12 μm (LWIR).

This study highlights that the improvements of HgCdTe HOT technology are highly dependent on the complex relationship of a number of competing parameters. The main ones are the cutoff wavelength of the DLPH device it is compared with, and also the crystal quality. We point out several general trends which characterize the expected improvements of HgCdTe HOT technology compared to standard HgCdTe technology:

- Improvements in detectivity D^* are more significant for LWIR for T<150 K
- Improvements in detectivity D^* are more significant for MWIR for T>150 K
- Improvements in T_{BLIP} are slightly better for MWIR (~50 K) than for LWIR (~40 K)
- Improvements in T_{BLIP} are maximized as τ_{SRH} is increased
- T_{BLIP} in HOT devices is more sensitive to τ_{n0} (τ_{p0}) than T_{BLIP} in DLPH devices

This initial study can also be used to develop a unique "lookup" table. This table would give the expected ideal improvement in terms of T_{BLIP} of the HgCdTe HOT device compared to the corresponding HgCdTe DLPH device for a particular case of cutoff wavelength, and τ_{n0} (τ_{p0}). Although the potential of these HOT photodiodes is great and could induce an important breakthrough in high sensitivity infrared imaging, our numerical model indicates that this technology is even more sensitive than standard HgCdTe infrared technology in terms of material quality.

To further illustrate the results from Figure 5.12, the simulated detectivities D^* for DLPH device at 80 K, HOT device at 120 K and HOT device at 180 K with cutoff wavelength going from MWIR to LWIR are shown in Figure 5.14. BLIP can be achieved for HgCdTe DLPH devices cooled down to 80 K in both MWIR and LWIR as mentioned before. HOT devices operated at 180 K can achieve BLIP in MWIR, but not in LWIR. TE-cooling is compatible with MWIR HOT devices for high sensitivity infrared imaging. HOT devices operated at 120 K can achieve BLIP in both MWIR and LWIR. This represents an improvement of 40 K for LWIR infrared imaging.

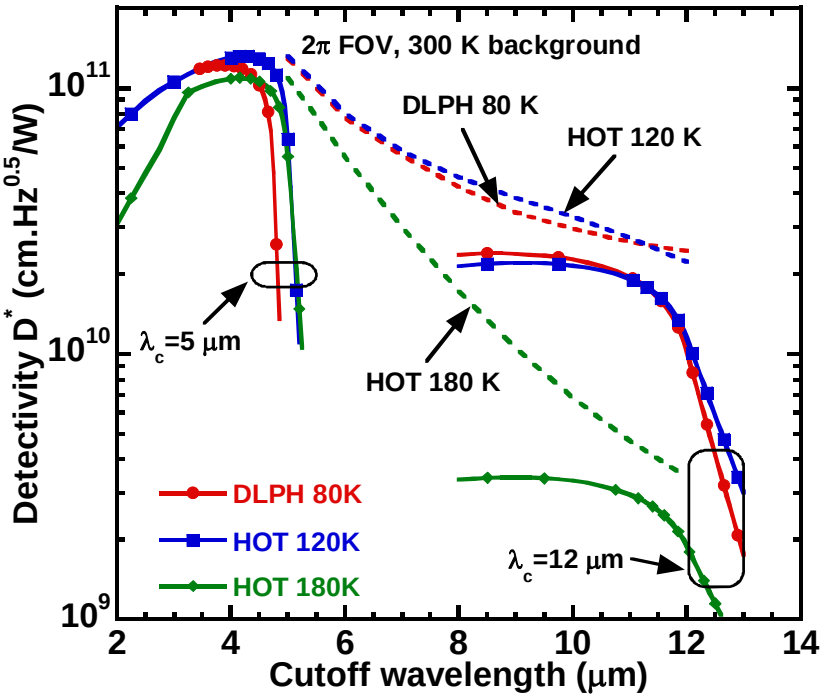

Figure 5.14: Calculated detectivity D^* versus cutoff wavelength for DLPH device at 80 K, HOT device at 120 K and HOT device at 180 K. Also shown are the spectral responses of D^* for these three cases with λ_c=5 μm (MWIR) and λ_c=12 μm (LWIR).

In the next chapter, we design and optimize a particular HgCdTe HOT photodiode using our numerical device model. Response in MWIR and operating temperature of 200 K is chosen in pursue the idea of using TE-cooling with HOT devices. By choosing a specific case, we can also look more carefully at the effect of the different parameters on the device performance.

Chapter 6

Modeling and Design Considerations of Auger-Suppressed HgCdTe Photodiodes

In the previous chapter, we compared the performance of standard cooled HgCdTe infrared photodiodes and of our novel HOT HgCdTe photodiode using our numerical model. We evaluated the potential improvements of using the novel structure in our infrared windows of interest (MWIR and LWIR). It is found that improvements of HOT detectors are more visible in the LWIR range. However, BLIP at TE-cooled temperatures (180-200 K) may be easier to achieve, both theoretically and experimentally, in the MWIR range.

Here we choose a particular case of infrared response and temperature of operation in order to study the behavior and operation of Auger-suppressed detectors. Our numerical model is used to simulate an HOT detector with response in the MWIR range (cutoff wavelength λ_c=5.5 μm) and temperature of operation of 200 K [56]. We provide quantitative calculations on the dependence of detector performance on material parameters and device geometry. 1D simulation is used in order to optimize the material structure and doping levels. The detector structure and corresponding calculated band diagrams are shown in Figure 6.1.

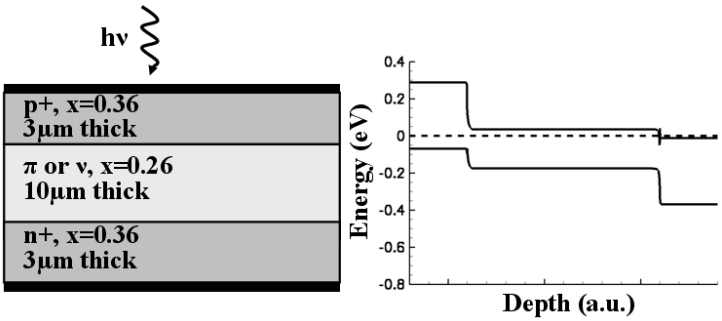

Figure 6.1: MWIR HOT detector structure and its corresponding energy band profile at zero bias.

Finally, 2D simulation is used to model an HOT structure with realistic features such as doping and compositional grading at interfaces, a graded HgCdTe composition in the absorber layer, and diffused doping profile for the top P^+ extraction layer. This realistic structure is compared to the equivalent unrealistic structure with constant doping profiles and abrupt junctions.

6.1 Design Considerations of HOT HgCdTe Photodiodes

6.1.1 Influence of the Absorber Width

The absorber layer width in the HOT structure (Figure 6.1) is important in determining the degree of Auger suppression and optical absorption. When reverse biased, the carrier concentrations significantly drop near the N+/ν exclusion junction, then increase as we move away from the junction due to carrier generation. It is therefore important to have the P+/ν extraction junction close enough to the N+/ν junction in order to keep the carrier concentrations below equilibrium values in the absorber layer. Auger suppression may be achieved in the HOT structure for a sufficiently thin absorber layer. However, if the absorber layer becomes too thin, the spectral response drops due to reduced absorption volume.

The dependence of calculated dark current density at 300 mV reverse bias on absorber width is shown in Figure 6.2, where dark current decreases with decreasing absorber layer width corresponding to decreasing carrier generation rate. A doping concentration $N_D=1x10^{15}$ cm^{-3} is assumed in the absorber layer and electron and hole

SRH lifetime τ_{n0} and τ_{p0} of 1 μs for both. The calculated detectivity (background scene of 300 K and 2π FOV) follows the dark current dependence on absorber width, with the exception of thin layers where optical absorption is decreased (Figure 6.2). Here we observe a maximum detectivity of 2.9×10^{10} cm.Hz$^{0.5}$/W for a width of 2-3 μm, representing the optimal absorber thickness to provide Auger suppression without sacrificing optical absorption efficiency. For an absorber layer width smaller than 2.2 μm, the absorber layer is fully depleted. The optimal Auger-suppressed photodiode has therefore a nearly fully or fully depleted absorber layer [78]. For the next sections, an absorber layer width of 3 μm is chosen.

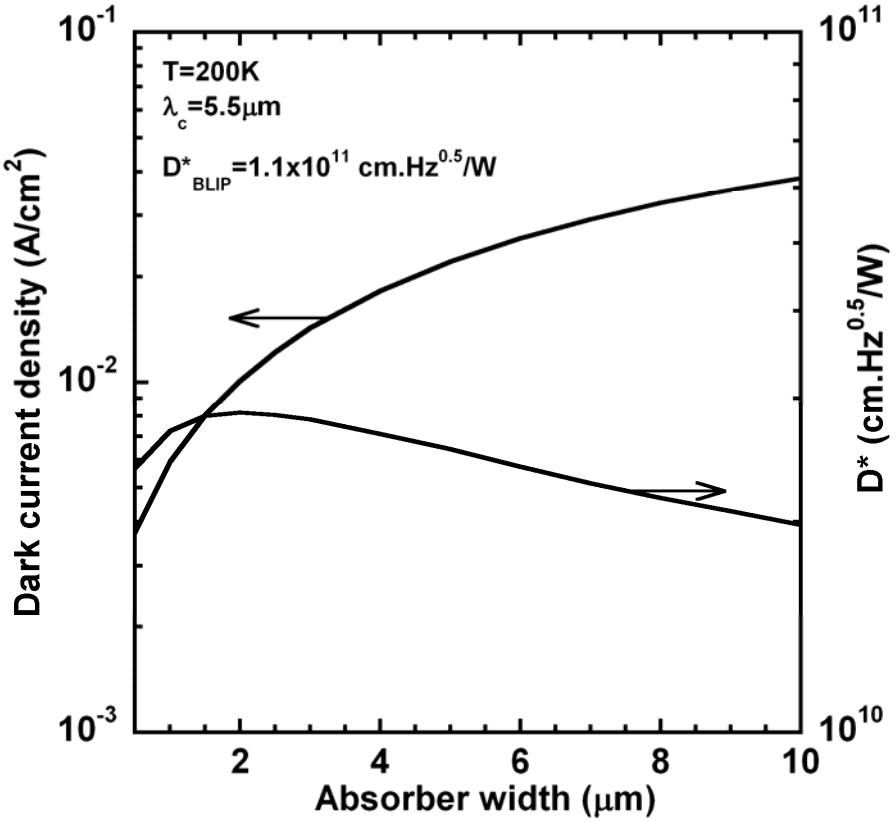

Figure 6.2: Calculated detectivity and dark current density at 300 mV reverse bias versus absorber layer width at 200 K with $N_D=10^{15}$cm^{-3} in the absorber layer and $\tau_{n0}=\tau_{p0}=1$ μs. Background scene is represented as a black-body at 300 K with FOV of 180°.

6.1.2 *Influence of the doping and composition of the N+ and P+ layers*

We next studied the effects of the two heavily doped layer thicknesses in the range 0.2-4 μm and found that their influence on detector performance is limited. The N+ region should be thick enough that any carriers injected by the negative bias contact can neither diffuse nor drift to the exclusion junction. Optimal performance is observed for exclusion/extraction layer thickness higher than 0.4 μm.

Increasing the doping and composition of the P+ extraction layer increases the ability of the layer to extract the generated carriers as it concentrates the depletion region mostly in the absorber layer. For the N+ exclusion layer, the energy barrier to generate e-h pairs should be high enough to minimize Auger generation and the corresponding minority hole concentration in this layer. The roles of the exclusion and extraction layers can be achieved by combining the effects of a heterojunction and the heavy doping of these layers.

The doping of the exclusion and extraction layers were studied in the range $5x10^{15}<N_{doping}<1x10^{18}$ cm^{-3}. The CdTe alloy composition of these layers was also studied in the range $0.26<x<0.40$. We computed the dark current density as a function of the P+ and N+ alloy composition for a given doping (Figure 6.3a), as well as the dark current density as a function of the P+ and N+ doping for a given alloy composition (Figure 6.3b). For $N_A=1x10^{17}$ cm^{-3} in the P+ extraction layer, the dark current decreases with increasing alloy composition and saturates for $x>0.35$. For $N_D=1x10^{17}$ cm^{-3} in the N+ exclusion layer, the dark current saturates for $x>0.29$. For $x=0.36$ in the P+ extraction layer, the dark current saturates for $N_A>1x10^{17}$ cm^{-3}. For $x=0.36$ in the N+ layer, the energy barrier to generate e-h pairs is high enough that the doping does not have any effect on the dark current. From these results, it appears that the P+ extraction layer is more sensitive to alloy composition and doping than the N+ exclusion layer.

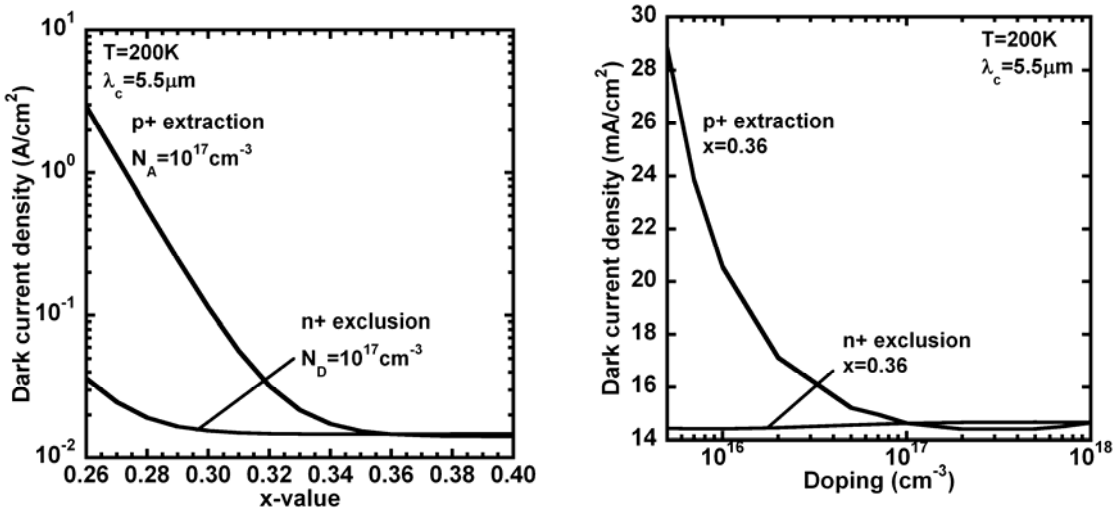

a) **b)**

Figure 6.3: a) Dark current density at 300 mV reverse bias versus composition of the P+ and N+ layers at a given doping with $N_D=10^{15}cm^{-3}$ in the absorber layer and $\tau_{n0}=\tau_{p0}=1$ μs; b) Dark current density at 300 mV reverse bias versus doping of the P+ and N+ layers at a given composition with $N_D=10^{15}cm^{-3}$ in the absorber layer and $\tau_{n0}=\tau_{p0}=1$ μs.

6.1.3 Influence of the doping and SRH lifetime in the absorber layer

Doping and SRH lifetime are expected to play major roles in detector performance, where there is a complex relationship between these parameters and the ultimate carrier lifetime in the absorber. Furthermore, the carrier lifetime will be non-uniform due to variations in carrier density. In HgCdTe, the SRH lifetime has been reported to vary between 0.2 μs and 10 μs [79] depending on the temperature for n-type doped HgCdTe layer grown by MOCVD with x=0.224 and $N_D=6.6x10^{14}$ cm^{-3}. Data on Shockley-Read centers in n-type MBE HgCdTe indicate neutral centers located at the intrinsic Fermi energy level [41]. The predominant SRH center in p-type MBE HgCdTe is associated with the annealing conditions that produce Hg vacancies [41]. A high concentration of dislocations in the material is also expected to form SRH centers [47].

Here, doping density and SRH lifetime were studied for the range $1x10^{14}<N_{doping}<5x10^{16}$ cm^{-3} and 0.1-100 μs respectively. For lifetimes of 0.1-1 μs, SRH processes dominate Auger processes in the absorber layer (Figure 6.4). A decrease in dark current is then observed when the doping increases from 10^{14} cm^{-3}. This is related to

a decrease of the hole density in the absorber layer as the doping is increased which induces a decrease of the SRH recombination rate. However for a larger SRH lifetime, Auger processes become dominant for doping larger than 10^{16} cm^{-3} and the dark current increases as doping is increased, as expected for Auger-limited operation. For SRH lifetimes larger than 5 μs, Auger processes are always dominant and the dark current increases with increasing doping.

Our modeling suggests that absorber doping concentrations less than 10^{16} cm^{-3} and SRH lifetime of 5 μs or larger are desired for the optimal performance of P+/ν/N+ detectors with an absorber layer cutoff of 5.5 μm operated at 200 K and 300 mV reverse bias.

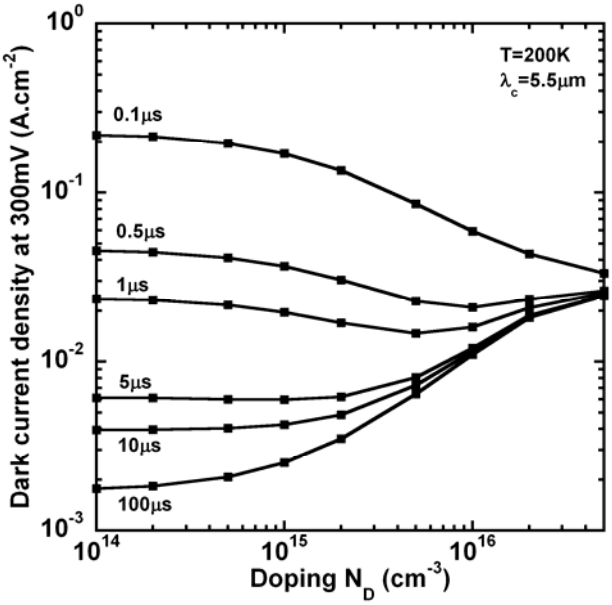

Figure 6.4: Dark current density at 300 mV reverse bias versus absorber layer doping for several SRH lifetime values.

6.2 2D Detector Structure

In this section, we study a HOT device structure in two dimensions using the previous one dimensional simulation results. The detector device has a planar structure (Figure 6.5), which may be achieved using materials growth by molecular beam epitaxy

(MBE), and a P+ region for junction formation (extraction layer) that may be achieved by ion implantation and diffusion. The carrier SRH lifetime is chosen to be 5 μs.

A device with constant doping and HgCdTe composition in each layer is compared to a more realistic device that includes doping and compositional grading at interfaces, a graded HgCdTe composition in the absorber layer, and diffused doping profile for the p+ extraction layer. The $Hg_{1-x}Cd_xTe$ composition grading in the absorber layer ranges from x=0.25 to 0.27, and provides a built-in electric field to aid extraction of photo-generated carriers. The P+ doping profile is defined as a Gaussian profile with a peak concentration of 10^{18} cm^{-3} at the surface with a junction depth of 1 μm and lateral factor of 0.8.

The current-voltage characteristics are very similar for the detector with uniform doping and composition, and the detector with graded profiles (Figure 6.6a), with a lower dark current for the graded structure. R_0A product values are $1.8x10^3$ ohm-cm^2 for the step structure and $2.0x10^3$ ohm-cm^2 for the graded structure. The minority carrier diffusion length is about 15 μm, larger than the absorber layer width. The calculated spectral response is also very similar for the two back-side illuminated structures (Figure 18b), with a slight increase in peak responsivity and wider detector cutoff for the graded structure. The resulting detectivities calculated for the two structures differ by only 10 percent and are about half D^*_{BLIP} for an ideal photodiode which is $1.1x10^{11}$ cm.$Hz^{0.5}$/W. It is apparent that step doping and compositional profiles may be used as a first order approximation to the detector performance, though graded profiles in actual detector structures should be included for improved accuracy.

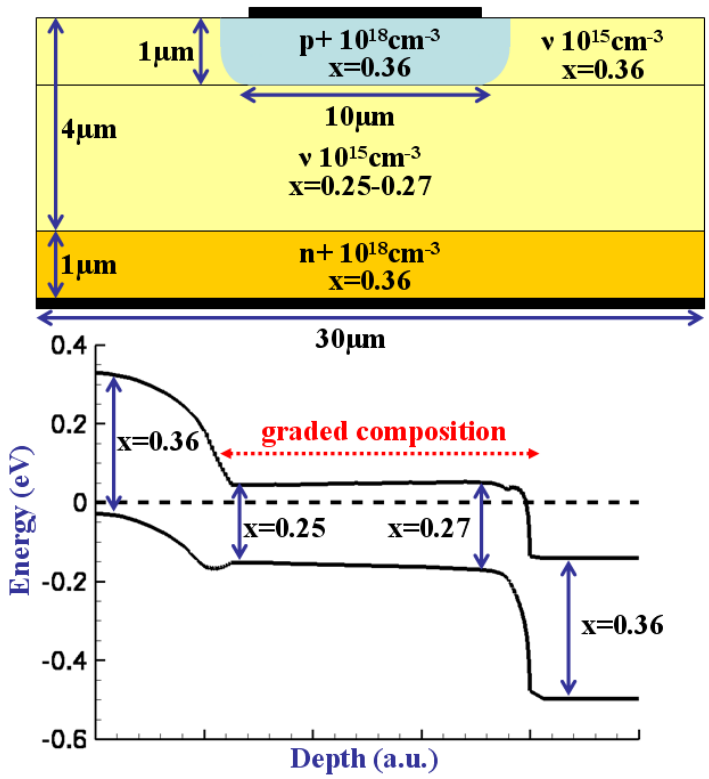

Figure 6.5: MWIR HOT 2D detector structure and its corresponding energy band profile.

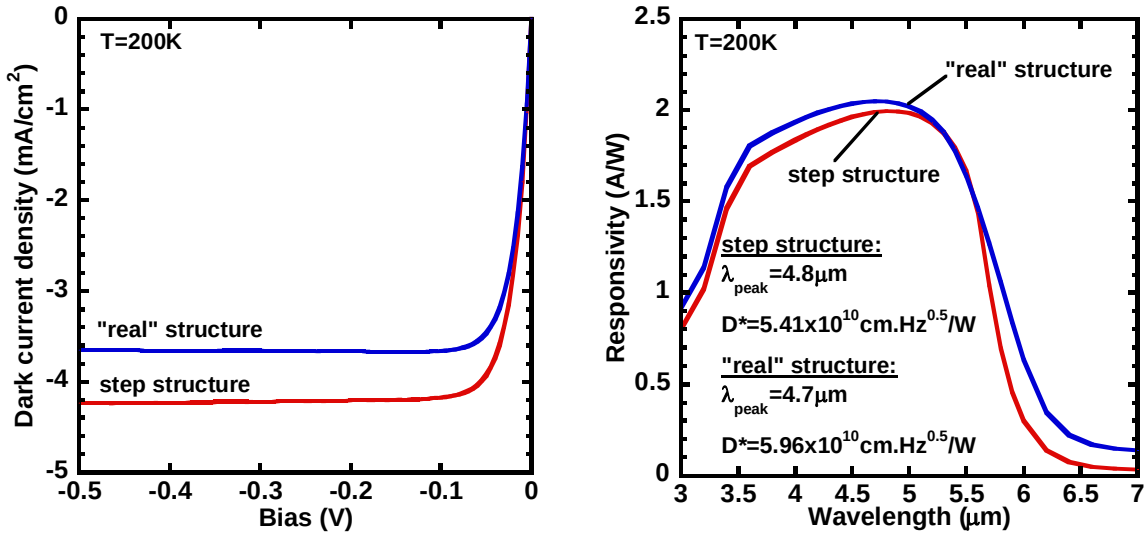

a) **b)**

Figure 6.6: a) Calculated I-V characteristic at 200 K for 2D structure with and without implant/diffusion profiles and graded composition layers; b) Calculated responsivity versus wavelength of the two back-side illuminated structures. $N_D=10^{15}cm^{-3}$ in the absorber layer and $\tau_n=\tau_p=5$ µs. Background scene is a black-body at 300 K with FOV of 180°.

6.3 Summary

In this section, non-equilibrium operation conditions were analyzed in HOT HgCdTe detectors using finite element modeling. The effects of HgCdTe composition, doping concentrations, and SRH lifetimes on detector performance were examined for a MWIR detector operating at T=200 K in order to understand the influence of each parameter. The most influential parameters on detector performance were found to be those of the absorber layer, including thickness, doping, and SRH lifetime.

The dark current in the device, limited by Auger generation, is minimized when the absorber layer doping is smaller than 10^{16} cm^{-3}. It is also preferable to have SRH lifetimes larger than 5 μs so that SRH is intrinsically dominated by Auger processes. An absorber layer thickness of approximately 3μm is recommended based on the tradeoff between absorption efficiency and Auger suppression. The exclusion and extraction layers were found to provide optimal performance for HgCdTe composition and doping levels above critical values. For the device examined, optimal performance is obtained for an extraction layer with $x>0.35$, $N_A>1x10^{17}$ cm^{-3}, and an exclusion layer with sufficient band offset achievable with $x=0.36$ and a range of doping.

The presented detector modeling identifies tradeoffs associated with HOT detector design, provides quantitative calculations regarding the dependence of detector structure parameters on performance, and serves to guide the design of future HOT detectors. It also confirms the potential of achieving BLIP performance at TE-cooling temperatures for HgCdTe HOT MWIR photodiodes. Next, we focus on the experimental fabrication and characterization of Auger-suppressed HgCdTe infrared photodiodes.

Chapter 7

HgCdTe Auger-Suppressed Structure Growth and Device Fabrication

The numerical models presented in the previous chapters provided great insight about the operation and performance of HgCdTe Auger-suppressed infrared photodiodes using the numerical model that we developed. We developed tools and a methodology in order to design optimized HOT detectors. We also have a better idea of how different device parameters and operation conditions will affect the performance of these detectors. As more complex and expensive growth and fabrication tools (such as molecular beam epitaxy) are more used in HgCdTe technology, there is a greater demand for models capable of increasing our understanding of how these devices operate and capable of predicting accurate quantitative results. This numerical model answers the need to minimize development costs and lead-time associated with introducing new designs of the highly competitive HgCdTe semiconductor industry.

Based on this knowledge, we now explore the growth and fabrication of optimized HOT detectors. In this chapter, the specific growth technique and processing steps employed in our study are presented. We discuss some of the experimental issues. We also present results on the novel processing techniques that we developed and that are potentially applicable to HOT technology (see section 7.2) and HgCdTe technology in general (see Appendix B). This work was performed in collaboration with EPIR Technologies, Inc., the Microphysics Laboratory (MPL) at the University of Illinois at Chicago (UIC), and the US Army Research Laboratory (ARL). The HOT structures are designed and optimized at the University of Michigan using the device model presented in the previous chapters. The HgCdTe layers are then grown by EPIR Technologies, Inc.

Device processing and testing work is shared between the author and ARL. Several batches are performed as part of this study. Some of them were processed and tested by the author using the facilities of MPL at UIC, while the others were processed and tested by ARL.

7.1 HgCdTe Growth and Device Processing

7.1.1 HgCdTe HOT Device Structure

As mentioned previously, there are two possible configurations for HgCdTe Auger-suppressed detectors: P+/ν/N+ structure ('ν' meaning low n-type doping absorber region) and P+/π/N+ structure ('π' meaning low p-type absorber region). The *concentration of Shockley-Read centers should be at a minimum* in order to obtain the full benefits of Auger suppression (τ_{SRH}>5 μs). *Low doping* is also required in the absorber layer (less than ~10^{16} cm^{-3}) in order to minimize dark current. Consequently, the P+/π/N+ structure seems preferable for the room temperature operation of HOT detectors due to the longer Auger lifetime in the p-type HgCdTe absorber layer compared to the n-type absorber layer. On the other hand, the low doping required for the absorption layer is easier to achieve in n-type HgCdTe grown by MBE. In addition, the quality of the indium doped n-HgCdTe layers is known to be better than arsenic doped p-HgCdTe layers. The doping in these layers is also well under control, with achievable minimum concentrations less than those in p-HgCdTe by more than one order of magnitude.

Low p-type doping of HgCdTe is hard to achieve in HgCdTe. Controlling the p-type doping by incorporating arsenic during MBE growth is still a topic of intense research. Based on the aforementioned reasons, we choose the P+/ν/N+ structure for the HgCdTe HOT growth and device fabrication in this study. However, we will present in the next section a novel processing technique developed in order to achieve low p-type doping in HgCdTe.

The base structure for the HgCdTe HOT device proposed in this study is shown in Figure 7.1. It is designed at the University of Michigan. The structure is described below and is aimed for response in the MWIR band or the LWIR band. The first HgCdTe layer,

Region I, is a wide band gap layer with high n-type doping ~10^{17} cm^{-3} in order to achieve the N+ layer of the HOT structure. High n-type doping is achieved in-situ during MBE growth. The active HgCdTe layer, *Region II*, is about 3-6 μm thick depending on the desired cutoff wavelength. This layer is low n-type doped with indium during MBE growth to achieve a concentration of ~1-2x10^{15} cm^{-3}. The top HgCdTe window layer, *Region III*, is of wider gap compared to the active HgCdTe layer and is initially low n-type doped. This layer is about <1 μm thick and is initially low n-type doped.

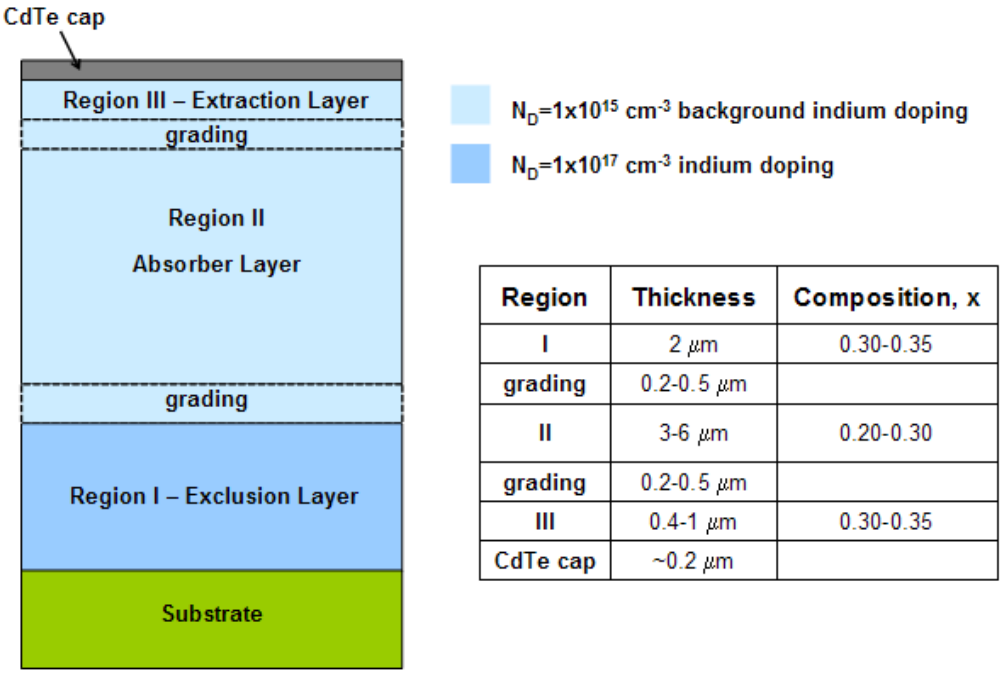

Region	Thickness	Composition, x
I	2 μm	0.30-0.35
grading	0.2-0.5 μm	
II	3-6 μm	0.20-0.30
grading	0.2-0.5 μm	
III	0.4-1 μm	0.30-0.35
CdTe cap	~0.2 μm	

Figure 7.1: Schematic diagram of the HOT device architecture grown by MBE.

7.1.2 Growth by Molecular Beam Epitaxy

HgCdTe molecular beam epitaxy (MBE) technology offers low temperature growth under an ultrahigh vacuum environment, in-situ n-type doping with indium, and control of composition, doping and interfacial profiles. The successful development of the MBE growth technique for multi-layer HgCdTe makes it possible to grow complex device structures such as our Auger-Suppressed HgCdTe infrared photodiode.

HgCdTe HOT layers are grown by MBE at EPIR Technologies, Inc. MBE growth is carried out in a Riber 32P Compact system. The MBE growth chamber is equipped with a valved Hg cell that enables instantaneous adjustment of the Hg flux during growth, an in-situ reflection high-energy electron diffraction (RHEED) gun, and an ellipsometer to achieve real-time monitoring of the crystalline structure and the composition. Substrates used in this study are (211)-orientated CdZnTe and CdTe/Si. Te-terminated (211) substrates, i.e. (211)B, are usually employed. Defect densities in the low 10^4 cm^{-2} can be achieved by MBE growth of HgCdTe on lattice-matched CdZnTe. The CdZnTe substrates are acquired from Nikko Material, Inc. The use of CdTe/Si substrates, which is a high-quality and cost-effective substrate that is available in large areas, creates the possibility for large format focal plane arrays (FPA). The CdTe/Si substrates are grown by MBE at EPIR Technologies. CdTe(211)/Si substrates, with x-ray rocking curve full width at half-maximum (FWHM) lower than 100 arcsec and etch pit densities below 10^6 cm^{-2}, are used for the HgCdTe growth [80]. High-purity (nominal 99.99999%) solid polycrystalline CdTe, elemental Te and Hg are used as source materials for growth. The flux of the CdTe and Te cells are controlled by means of their temperatures in order to obtain the HgCdTe target composition and growth rate. The Hg flux is automatically controlled by adjusting the corresponding needle valve and the cell temperature [81].

The defect formation mechanisms for HgCdTe (211)B grown by MBE has been studied by many groups [81], [82]. Small changes in growth temperature and HgCdTe/substrate mismatch produce variable surface topography. Nano-ripple formation and cross-hatch patterning are the predominant structural features observed. Crosshatched patterns that consist of crossed lines with 44 deg to 45 deg angles are usually found on the surfaces of MBE-grown HgCdTe epilayers of relatively high quality and without large densities of micro- or macro-defects (typically low 10^4 cm^{-2} or less), on both (211)B CdZnTe bulk substrates and CdTe/Si substrates. A typical crosshatched pattern of HgCdTe grown by MBE on a (211)B CdTe/Si substrate is shown in Figure 7.2. The patterns on the surfaces of HgCdTe grown on bulk CdZnTe substrates are normally lower in height than those grown on CdTe/Si substrates. These features are associated with slippage along these planes and consequently with misfit dislocation formation.

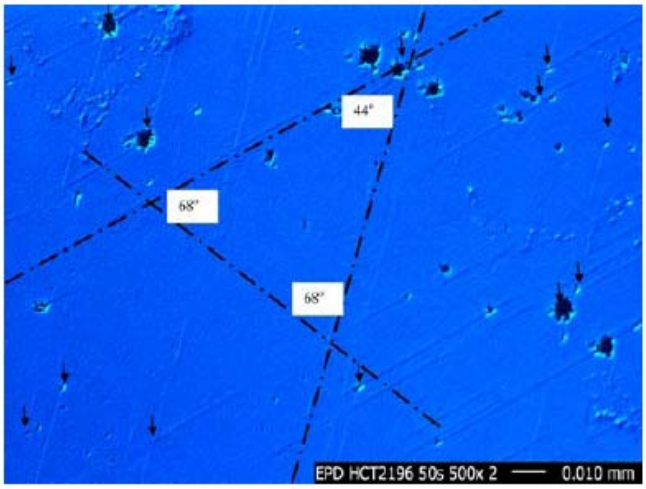

Figure 7.2: Nomarski optical microscope image of HgCdTe grown on CdZnTe (211)B substrate after 50 s of dislocation decorative etch (designated EPD) using Schaake's etchant. The directions of the crosshatched lines as well as the characteristic angles are labeled. The arrows show that the crosshatch lines are sometimes terminated by etch pits, namely dislocations in the crystal. The EPD for this sample is in the range of mid-10^5 cm^{-2} [81].

Three types of surface defects are usually observed in as-grown MBE HgCdTe [81], [82]: needle defects, hillocks and voids. Needle defects are predominant at low-temperature growth. They are stoichiometric and always show one ridge that is higher than the other (Figure 7.3a). At a median growth temperature (189 °C), hillock defects dominate. Hillocks appear on flat growth surfaces due to different growth rates. Void defects dominate at high temperature growth. Large void defects with sizes from several micrometers to tens of micrometers are the most common defects in MBE-grown HgCdTe. They arise due to Hg-deficient growth conditions [81]. A number of other reasons can also cause the formation of voids of various sizes, such as:

- dust particles left on the surface during the substrate cleaning process due to contaminated deionized (DI) water
- flakes dropping from the chamber walls during growth
- substrate mounting or transferring between chambers

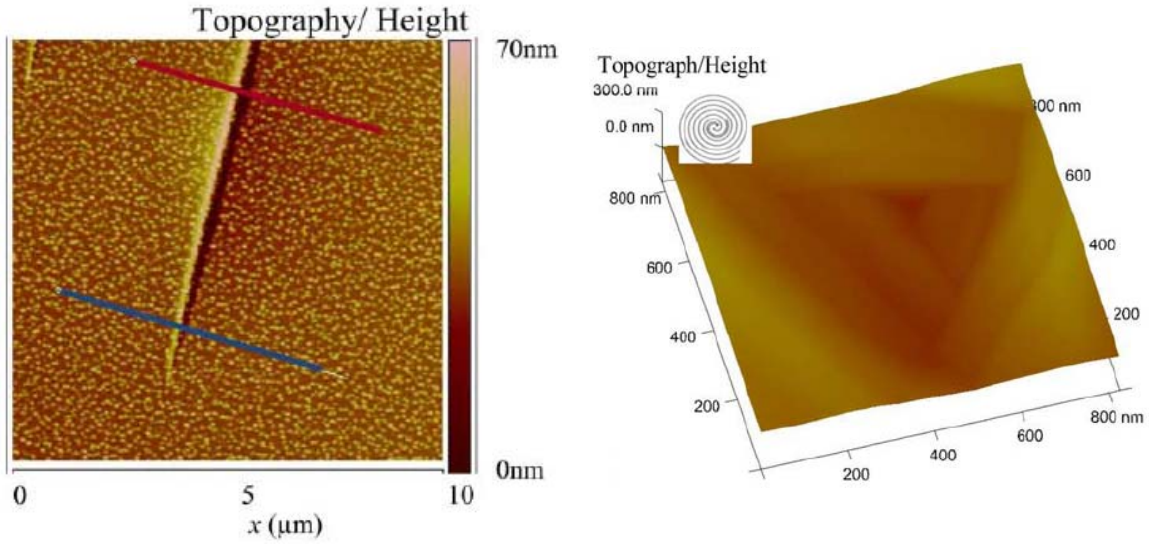

a) **b)**

Figure 7.3: Atomic force microscopy (AFM) image of a) a long needle defect and b) a void defect on a MBE HgCdTe sample [81].

The technology for the substrate cleaning, in-situ oxide removal, nucleation and growth already exists at EPIR Technologies and is implemented for this project. The HgCdTe layers are characterized using Fourier transform infrared transmission measurements (FTIR), X-ray diffraction (XRD), and temperature dependent Hall measurements. The exact HgCdTe mole fraction, which determines the cutoff wavelength of the detectors, layer thickness, distribution of defects, carrier concentrations and mobilities, which are critical to achieving high detector performance, are accurately determined by using these characterization techniques.

A HgTe/CdTe superlattice (SL) interfacial layer has been developed to block substrate roughness as well as to prevent threading dislocations propagating from the CdZnTe substrate into the HgCdTe active layer by introducing artificial slip planes perpendicular to the growth direction [81]. During SL interfacial layer growth, the Te and CdTe cell shutters are opened alternately under fixed Hg flux, resulting in HgTe well layers and barrier layers that are close to pure CdTe in composition, having a Cd mole fraction of 0.90-0.95. The average growth rate of the HgTe layers of the SL is about 0.3-0.4 nm/s, whereas it is 0.10-0.15 nm/s for CdTe layers. A HgTe/CdTe (5 nm/5 nm) SL was found to be a reasonable choice, allowing the surface roughness to be effectively smoothened while simultaneously reducing the generation of misfit dislocations in HgTe

layers that occurred when these layers were too thick. The average growth rate of HgCdTe alloys is 0.6-0.7 nm/s.

RHEED is used to determine if two-dimensional growth of the HgCdTe layers occurs. Figure 7.4 shows the RHEED patterns of one HOT layer grown on CdZnTe substrate at various stages of growth. The streaky patterns for both samples show that two-dimensional single crystal growth took place throughout the growth. The RHEED patterns become dimmer due to rougher surfaces after long durations of growth. This effect can usually be more clearly seen on HgCdTe layers grown on CdTe/Si substrates.

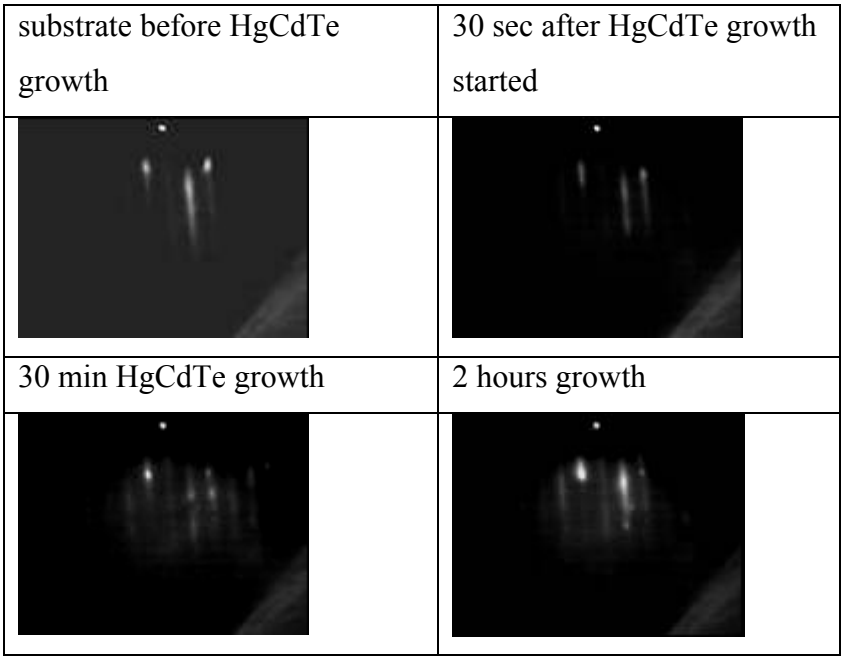

Figure 7.4: RHEED patterns of HgCdTe HOT layers during growth.

In-situ spectroscopic ellipsometry (SE) is used during growth for monitoring the composition variations and surface quality. Optical models are set up to fit the experimental data in order to determine parameters of interest such as the surface roughness and optical constants (related to layer composition). Information regarding the HgCdTe layer characteristics during growth is obtained by employing parametric dispersion models and simultaneously fitting the spectroscopic ellipsometry spectra [83]. The spectroscopic ellipsometry fitting results for LWIR HgCdTe HOT layers grown on CdZnTe is shown in Figure 7.5. We can see that the surface roughness remained at a low level during the HgCdTe growth. This correlates with the streaky RHEED patterns shown

in Figure 7.4. SE data of the different interfacial layers between the HgCdTe layers and the substrate are not shown due to the proprietary nature of the content.

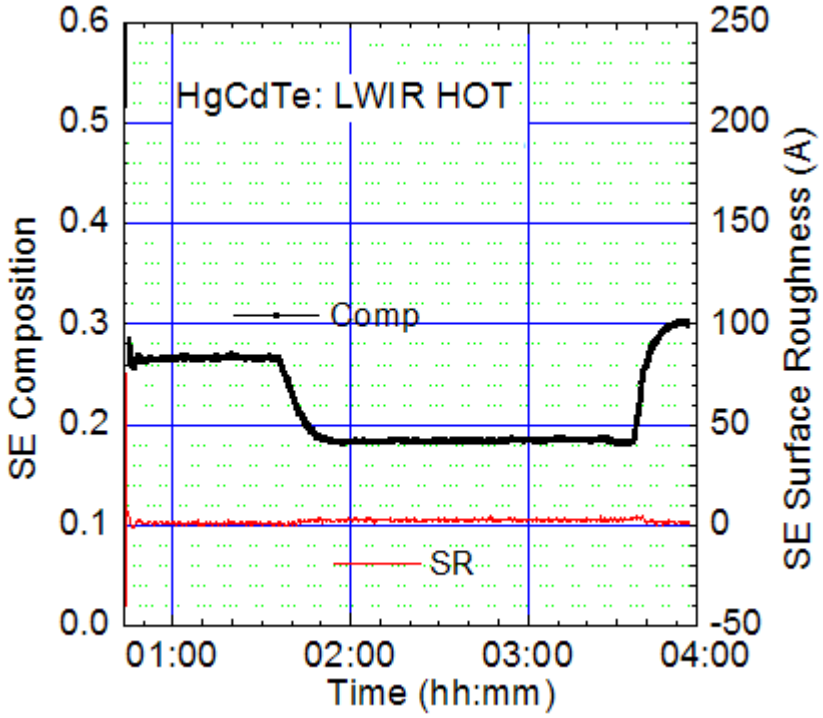

Figure 7.5: Ellipsometry data for HgCdTe HOT layers grown by MBE.

FTIR spectra of the samples are used to determine the HgCdTe composition and layer thickness. Our thickness fitting program is designed for single compositional HgCdTe layers. For the multi-layer HOT structures, certain fitting errors are expected from this fitting. Figure 7.6 shows the FTIR data for HgCdTe HOT layers grown on CdZnTe.

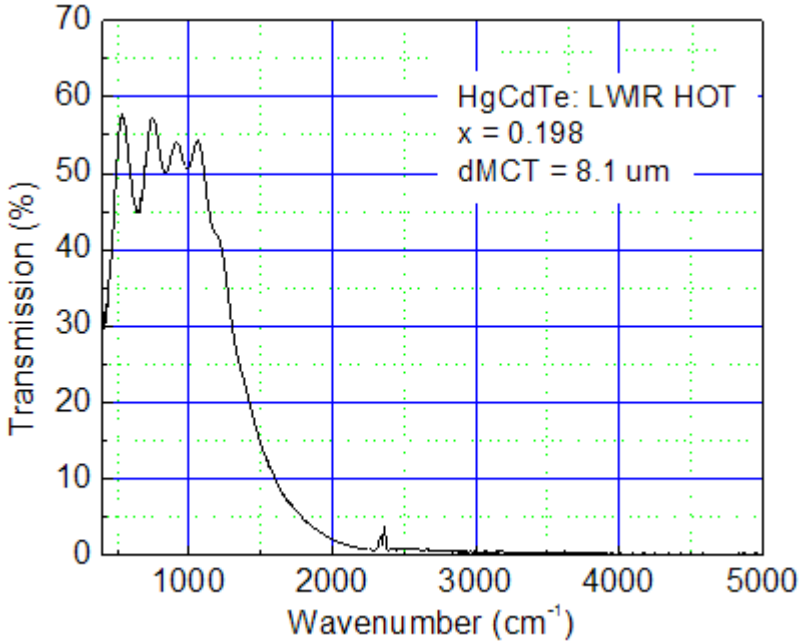

Figure 7.6: FTIR data for LWIR HgCdTe HOT layers grown by MBE.

In-situ n-type doping with indium of HgCdTe layers grown by MBE is fairly well under control at EPIR Technologies. Process conditions to obtain doping with concentrations in the range $5x10^{14}$ cm^{-3} to $>1x10^{17}$ cm^{-3} are calibrated and reproducible. Carrier concentration and mobility can be measured using temperature-dependent Hall measurements. Figure 7.7 shows typical temperature-dependent Hall measurement data for low n-type doped MWIR HgCdTe layers [80]. Doping concentrations below 10^{15} cm^{-3} can be observed in what could be 'ν' absorber layers in HgCdTe HOT devices. Layers become intrinsic above ~200 K as expected for low n-type MWIR HgCdTe layers. Mobilities on the order of 10^4 $cm^2/V.s$ are also observed as expected.

For HgCdTe HOT samples, the multi-layer structure makes it more difficult to use temperature-dependent Hall measurements in order to verify the doping concentration in the layers. If we look at the HOT structure shown in Figure 7.1, Region III is typically etched away using a bromine-based etchant in order to perform Hall measurements on the absorber region ('ν' layer, Region II). However, due to the presence of the buried highly conductive N+ region (Region I), Hall data indicate a mix of transport contributions from Regions I and II. Typical Hall data in the case of MWIR HOT HgCdTe are shown in Figure 7.8. However, since growth calibration of individual layers is performed by EPIR

Technologies before the growth of our HgCdTe HOT structures, we can estimate the expected n-type doping levels.

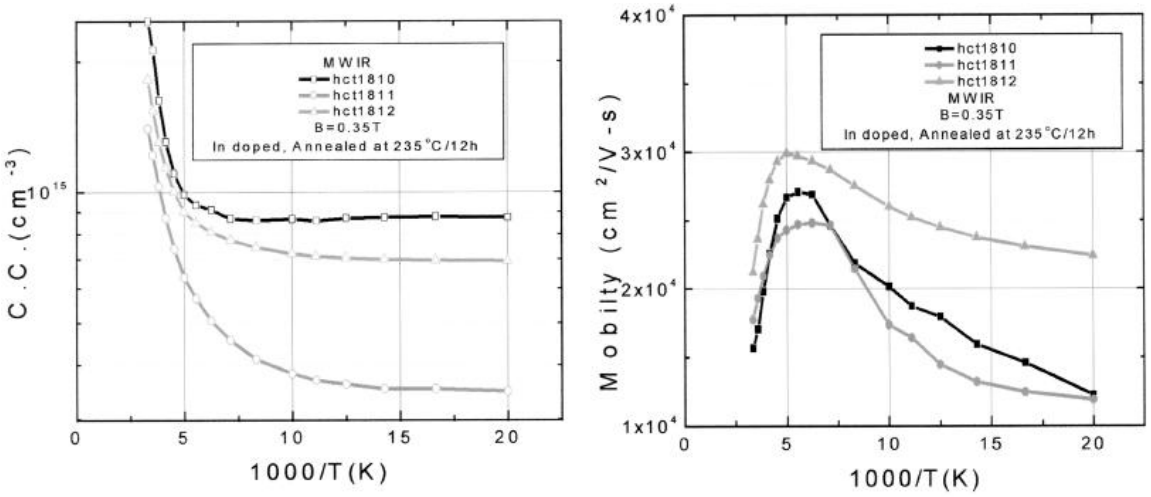

Figure 7.7: Temperature dependence of the a) carrier concentration and b) mobility for an MWIR HgCdTe sample [80].

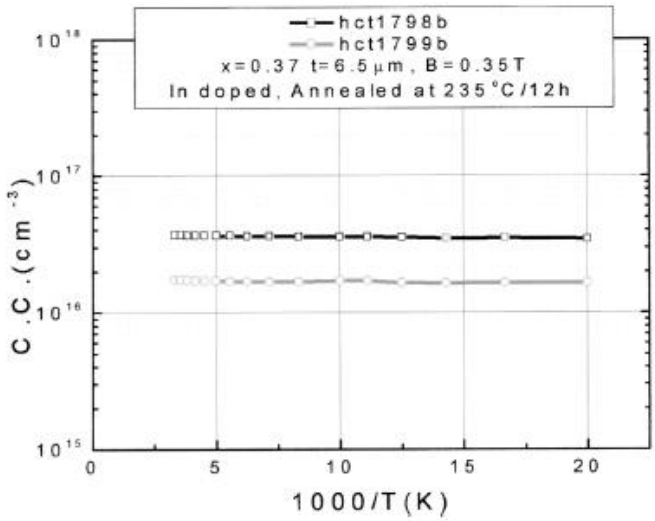

Figure 7.8: Temperature dependence of the carrier concentration for an MWIR HOT HgCdTe sample (N+/ν layers, Regions I and II) [80]

7.1.3 Device Fabrication

AutoCAD software is used to prepare the layout of the masks needed for the fabrication of these devices. A 4"×4" iron oxide mask is exposed (flashed with ultraviolet

light) using a MANN 3600 pattern generator. After the pattern is flashed onto the mask using the pattern generator, the resist on the mask is developed to remove the resist from the exposed areas. Development of the resist is done using a Shipley Microposit 351 Developer, which is diluted in DI water at a concentration of 1:3. Next, the iron oxide on the areas without the resist is removed with an iron oxide etchant. Finally, all of the resist is removed from the mask by submerging the mask in acetone for about 3 minutes.

Single circular devices with junction diameters ranging from 40 μm to 240 μm are fabricated on a single 10x10 mm^2 die. Both *planar* and *mesa* HOT structures are fabricated on a single die. This way, we have the possibility to make a comparison of the device performance of both structures, nearly independently of the fluctuations in the process and the non-uniformity between different wafers. Figure 7.9 shows a cross-section of the HOT planar device. Figure 7.10 shows a cross-section of the equivalent HOT mesa device after the complete fabrication processing sequence described below. Both are fabricated on the same die using a single mask set. The mesa structures is etched down to the bottom N+ layer in order to place the N-contact electrode directly on the N+ layer.

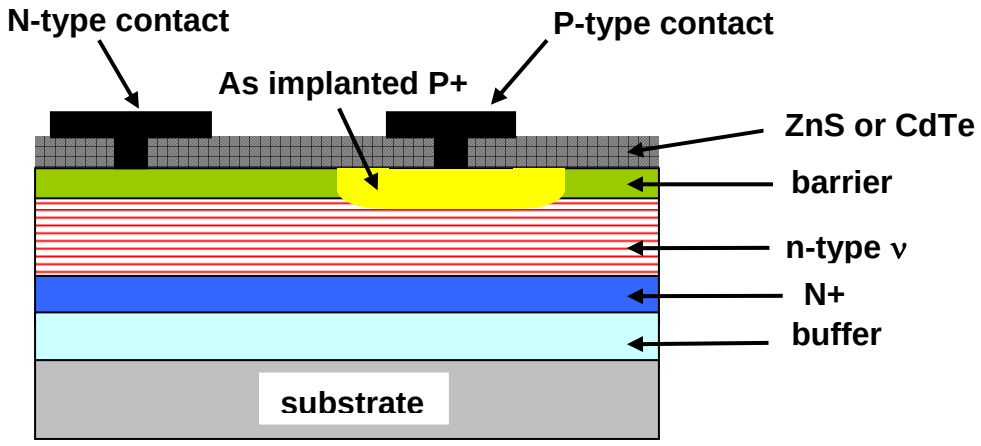

Figure 7.9: Schematic diagram of a fabricated planar P+/ν/N+ device.

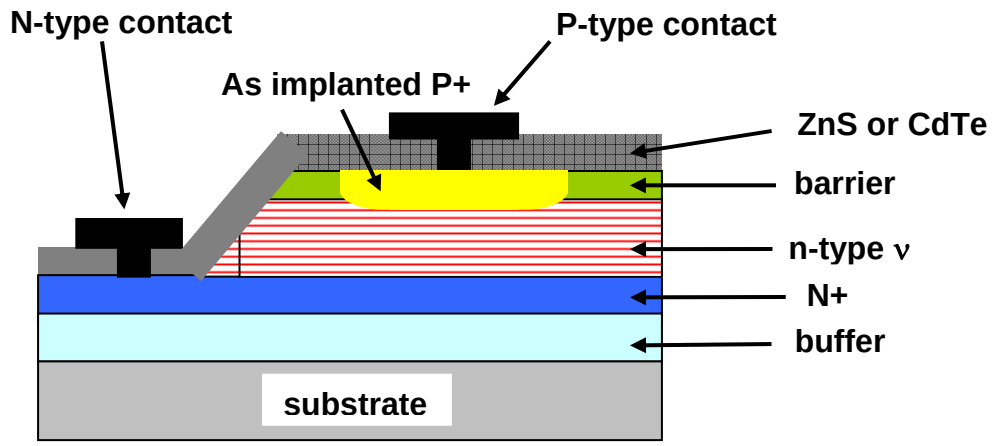

Figure 7.10: Schematic diagram of a fabricated mesa P+/ν/N+ device.

Figure 7.11 shows the top-view layout of a single device and an expanded view of the active area.

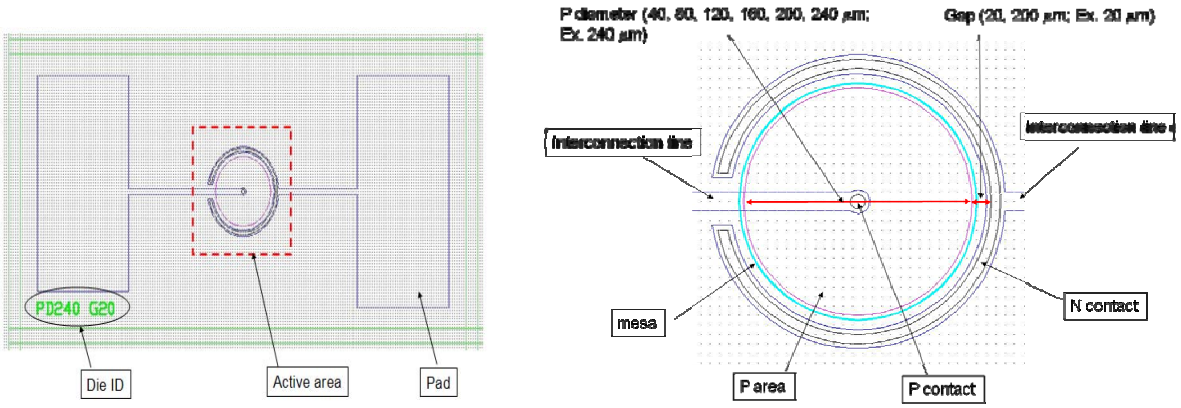

a) **b)**

Figure 7.11: a) HOT device layout and b) active area layout.

Different test patterns are also included on the mask design. P- Transfer-Length Method (TLM) and N-TLM areas are designed to determine the ohmic contact parameters as well as the contact resistances. P- Metal Insulator Semiconductor (MIS) and N-MIS areas are designed to test the quality of the ZnS passivation layer.

The process flow for both planar and mesa HOT structures is summarized in Figure 7.12 and described in more details here. In the first device processing step, the HgCdTe/CdTe (or HgCdTe/CdZnTe) structures are chemically etched with a cutting line grid of 200 µm width. The grid is defined to permit etching prior to cutting the

underlying substrate with a dicing saw. This is done to avoid damage associated with the cutting process. The mask also defines the alignment marks on the sample to facilitate the processing that follows.

The next step in the processing sequence – (1) in Figure 7.12 – is to create the p-type layer. A thick double photoresist technique with an undercut structure is used as the mask layer for ion implantation in order to easily remove the photoresist without residue of implant-hardened photoresist. Windows are selectively opened by photolithography using a MJB-3 contact mask aligner to define the implant areas. Arsenic is implanted with a dose of $1x10^{14}$ cm^{-3} and energy of 350 keV. A two-step post implant annealing sequence at 425 °C and 250 °C is then done using a closed tube annealing system. Post-implant annealing is necessary to electrically activate the arsenic and remove Hg vacancies. We employ a closed tube annealing method with the samples separated from the Hg source. The annealing is carried out in a two-zone furnace with a 5-degree temperature difference between the sample and the Hg source. The internal diameter of the tube sets a limit on one of the dimensions of the sample. More details on the annealing system will be given later on. Arsenic diffuses slightly during the annealing process and the p-type concentration in the top P+ layer is $\sim 10^{17}$ cm^{-3}.

The next mask – (2) in Figure 7.12 – is designed to mesa etch the HgCdTe top P+ and absorber 'ν' and layers to allow accesss to the underlying N+ layer and fabricate the HOT mesa structures (Figure 7.10). A diluted solution of bromine in latic acid is used as the wet etchant with an etching rate of aproximately 0.2 μm/minute.

The sample is then loaded into an e-beam chamber for ZnS passivation film deposition – (3) in Figure 7.12 – immediately after the preparation process. This preparation process includes a slight etching of the HgCdTe top surface in order to remove any native oxide layer and to improve the adhesion of the passivation layer. A 4000 Å ZnS film is deposited using a deposition system with a rotating holder to assure conformal step coverage and a good electrical isolation.

The next step in the process is opening the windows for the N-type metal contact using lithography and depositing indium. Indium provides a good ohmic contact to N-HgCdTe. A few hundred angstroms of indium are deposited in a Varian electron beam evaporation system. The next step in the sequence is opening windows for the top P-type

metal contacts of the devices. The ZnS passivation layer is first chemically removed. Then a thin 200 Å gold layer is selectively grown in an e-beam evaporation system. Finally, the bonding/test metal pads are defined by depositing thick Ti/Au bi-metal layers (t~5000 Å) on top of the P- and N-contacts of the diode. All metal deposition steps are followed by a lift-off in acetone for 10-15 min. The final structures are obtained after step (4) in Figure 7.12.

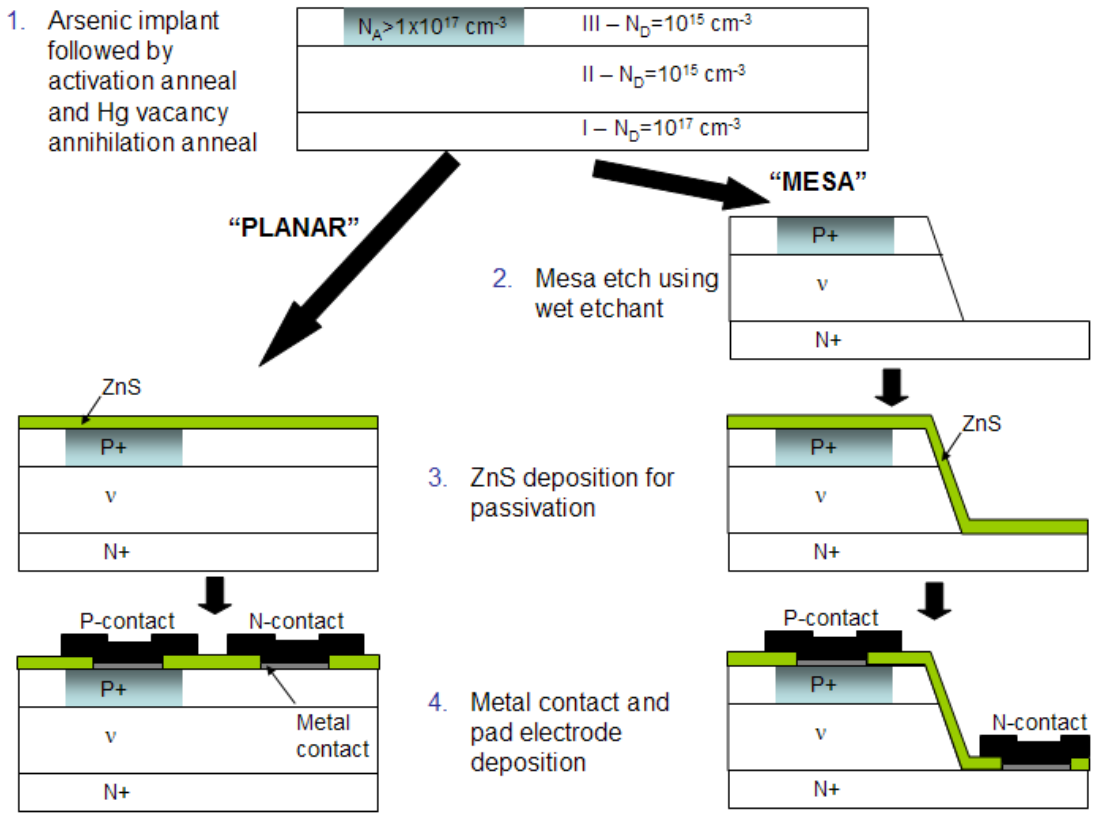

Figure 7.12: Schematic depicting the process flow.

7.2 Arsenic Diffusion in HgCdTe for Low P-type Doping

In parallel of device fabrication of HgCdTe HOT photodiodes with P+/ν/N+ structure, 'ν' meaning low n-type absorber, we also investigate a novel processing technique in order to achieve HOT devices with P+/π/N+ structure, 'π' meaning low p-type absorber. HgCdTe HOT infrared photodiodes with P+/π/N+ structure were

fabricated by the US Army Research Laboratory using this processing technique. Initial device results will be presented in the next chapter.

First, we review published work on arsenic diffusion in HgCdTe. Then, we describe the experimental setup used in this study and present the results obtained.

7.2.1 Background

Given its amphoteric behavior [84], it is a challenge to achieve controllable in-situ p-type doping of MBE-grown HgCdTe using *arsenic*. However, its low diffusion coefficient compared to other dopants and shallow activation energy [85] makes it the best choice for p-type doping in HgCdTe. Therefore, it becomes interesting to develop understanding and control of other ways to achieve p-type doping in HgCdTe with arsenic, such as *ion implantation* and *annealing*.

High p-type doping in the order of 10^{17} cm^{-3} for P^{+}-n DLPH by arsenic ion implantation and annealing can be reproducibly achieved using a typical implantation dose of $5x10^{13}$ cm^{-2} and energy of 200 keV. This is usually followed by an arsenic activation anneal at 425 °C for 10 min and a Hg vacancy annihilation anneal at 250 °C for 24 hr. Low p-type doping for HgCdTe absorber layer by arsenic ion implantation and annealing has only been looked recently [51] and is based on the concept of fast arsenic diffusion under controlled low mercury vapor pressure P(Hg) anneal.

Arsenic has been found to redistribute during thermal annealing by a multi-component mechanism composed by a Gaussian component and a fast diffusing component [86]. The fast diffusing component controls the location of the p-n electrical junction of the photodiode. In HgCdTe heterostructures, the Cd-Hg interdiffusion at high temperatures 400-450 °C or long annealing times 1-2 hr competes with the arsenic diffusion to determine the location of the electrical junction. Cd-Hg interdiffusion coefficient across the pseudobinary at 400 °C is $2x10^{-12}$ $cm^2.s^{-1}$ to $5x10^{-15}$ $cm^2.s^{-1}$ and arsenic diffusion coefficient $D(As)_{400°C}$ is about $3x10^{-14}$ $cm^2.s^{-1}$.

To avoid potential barriers in the valence band, Bubulac et al. [86] developed a two-step annealing technique to decouple arsenic diffusion and Cd-Hg interdiffusion during thermal anneal using an open-tube annealing system, namely in an MOCVD

reactor. First, the sample is annealed at 300 °C for 30 min under very low P(Hg)~0, i.e. in Te-saturated conditions (on the Te phase boundary), where arsenic exhibits a fast diffusing tail $D(As)_{300°C} = 0.5x10^{-13}$ $cm^2.s^{-1}$ and the Cd-Hg interdiffusion rate is very low. Then, arsenic is activated to p-type under an Hg-saturated anneal for ~15 min without further arsenic diffusion and with some interdiffusion in the heterointerface. Figure 7.13 shows the doping and compositional profiles as-implanted and after each anneals in the HgCdTe structure grown my MOCVD on GaAs.

Similar results were obtained by doing a first anneal in conditions chosen from inside the existence domain if the $Hg_{1-x}Cd_xTe$ phase equilibria under P(Hg)~0.01 atm and a sample temperature of 350 °C where $D(As)\sim 2x10^{-13}$ $cm^2.s^{-1}$. The results are shown in Figure 7.14. In both cases, no change in structural properties of the material was observed by EPD on an angle-lapped layer. As Hg overpressure is not being provided during the anneal, the material loses Hg from the surface and is converted continuously to a higher x composition and eventually to the x=1 (CdTe). This acts as a self-limiting process to Hg out-diffusion.

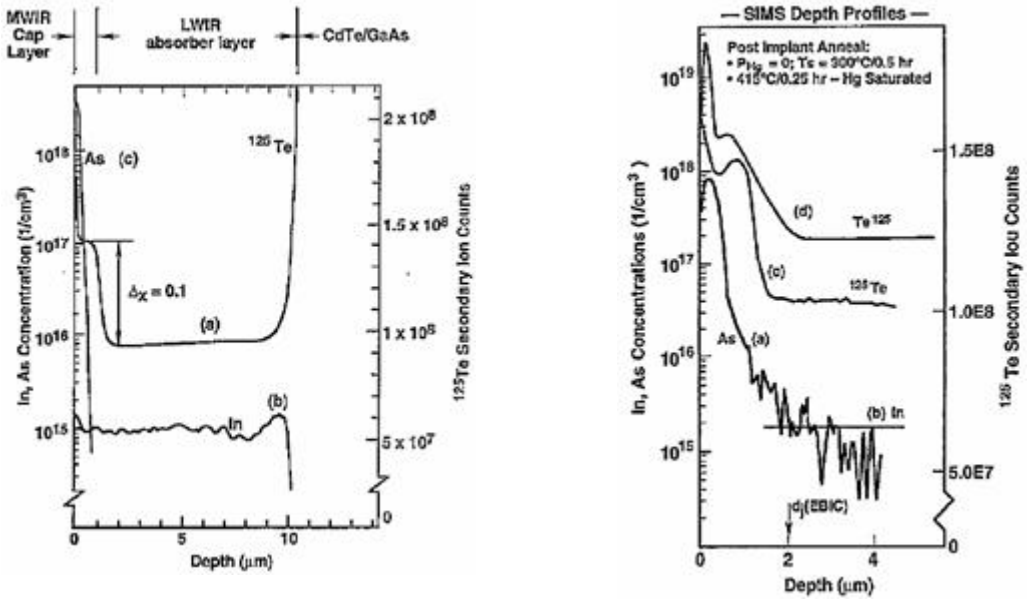

a) **b)**

Figure 7.13: a) The as-grown structure and material characteristics as determined by SIMS analysis: (a) compositional profile (^{125}Te), (b) In concentration, (c) As as-implanted profile. b) Annealed As and compositional SIMS (^{125}Te) profile: (a) As diffused, (b) In level, (c) compositional profile (diffusion anneal), (d) compositional profile (activation anneal). P(Hg)=0. [86].

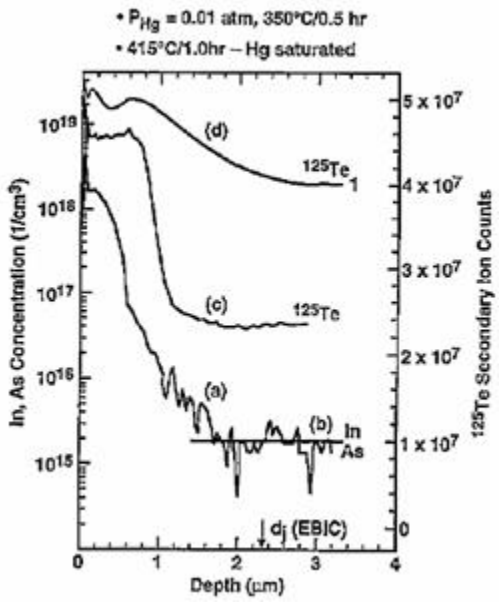

Figure 7.14: Annealed As and compositional SIMS (^{125}Te) profiles: (a) As diffused, (b) In level, (c) compositional profile (diffusion anneal), (d) compositional profile (activation anneal). P(Hg)=0.01 atm. [86].

Extended work by Bubulac et al. [87] was performed at different annealing temperatures using the same annealing system. It was mentioned that P(Hg) was estimated from P-T tables using the furnace temperature. It was found a transition in the enhanced diffusion of arsenic from an exponential to a Gaussian redistribution. This transition is controlled by temperature at a given P(Hg) as we can see in Figure 7.15 and Figure 7.16.

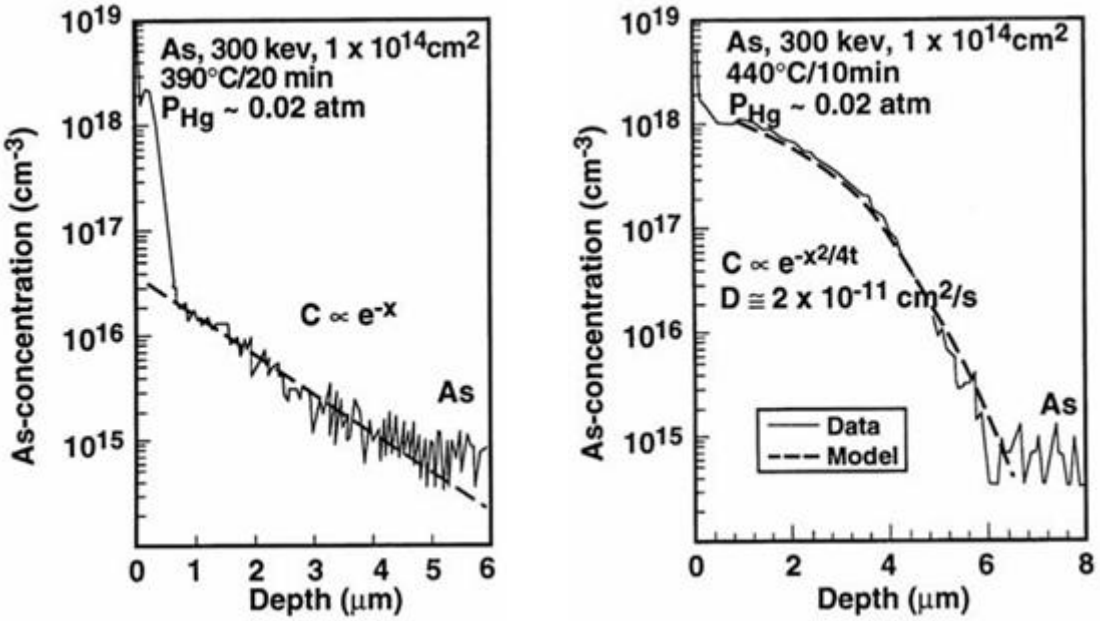

a) b)

Figure 7.15: As-redistribution (SIMS) in post-implant anneal in open-tube (MOCVD reactor) at P(Hg)~0.02 atm (within the existence domain but close to Te-phase boundary) for MOCVD double-layer HgCdTe: a) at 390 °C for 20 min, and b) at 440 °C for 10 min [87].

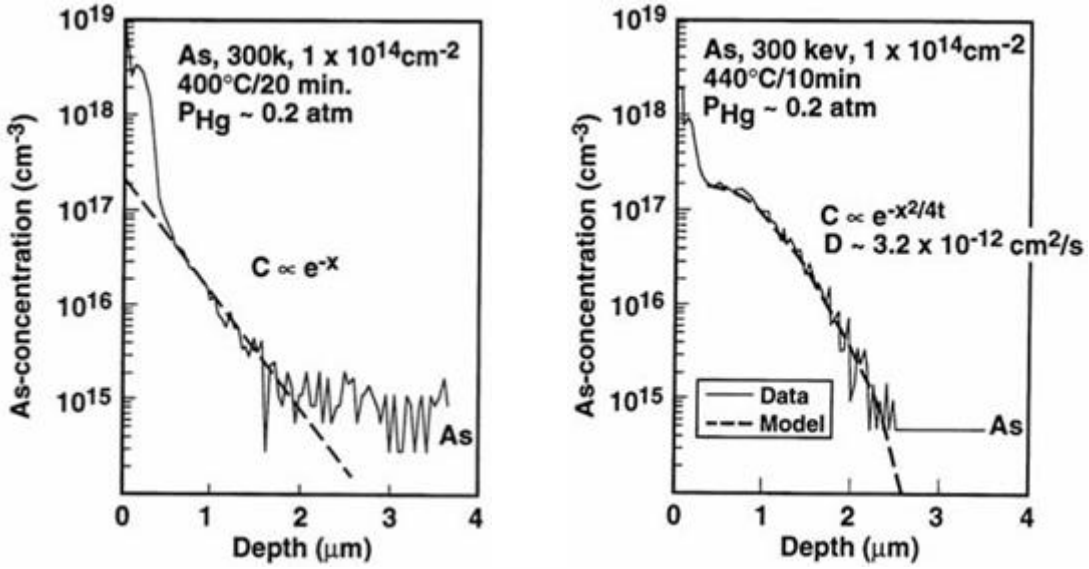

a) b)

Figure 7.16: As-redistribution (SIMS) in post-implant anneal in open-tube (MOCVD reactor) at P(Hg)~0.2 atm (within the existence domain) for MOCVD double-layer HgCdTe: a) at 400 °C for 20 min, and b) at 440 °C for 10 min [87].

Shin et al. [88] reported similar results on arsenic implantation and diffusion in MBE-grown HgCdTe samples. The open tube annealing furnace used in these

experiments was a LPE vertical furnace modified for high temperature annealing. Figure 7.17 shows the arsenic profiles under Hg-saturated conditions and for P(Hg)<0.5 atm. The Hg partial pressure inside the anneal tube was estimated from Hg-pressure versus temperature data. At 436 °C, the diffusion coefficient increased from a slow component, $D(As)=2.1x10^{-13}$ $cm^2.s^{-1}$, to two diffusion coefficients, $D(As)=1.7x10^{-12}$ $cm^2.s^{-1}$ and a fast component $D(As)=1.35x10^{-11}$ $cm^2.s^{-1}$ when the Hg pressure decreased to <0.5 atm. It is mentioned that, since the Hg vacancy concentration is inversely proportional to the Hg partial pressure, the defects involved in the diffusion process could be Hg vacancies for the slow component, and other defects induced by high temperature annealing under low Hg-partial pressure for the fast component.

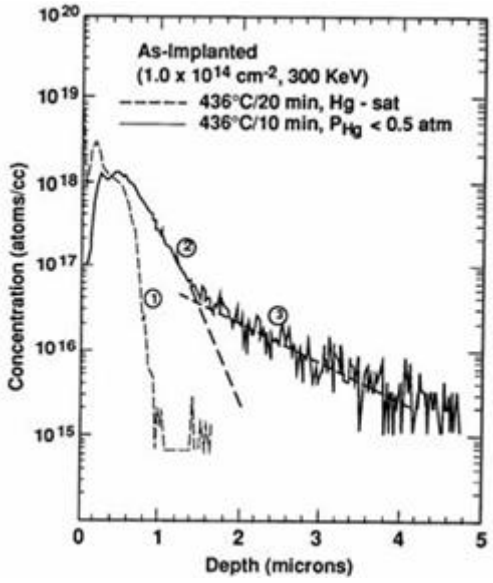

Figure 7.17: Secondary ion mass spectroscopy profiles for arsenic concentration of an ion implanted as-doped HgCdTe for (1) arsenic after saturated Hg partial pressure anneal, and (2) and (3) arsenic after low Hg pressure anneal [88].

Enhancement of arsenic diffusion coefficient under low P(Hg) was also reported by Chandra et al. [89] on in-situ arsenic doped HgCdTe layers grown by LPE on CdZnTe annealed in a sealed and closed ampoule placed in a multi-zone annealing furnace. Figure 7.18 shows the arsenic profiles determined by SIMS for annealing at 350 °C and P(Hg)=0.16 atm and different annealing times. Similar experiments were also performed at different P(Hg). Figure 7.19 shows the dependence of arsenic diffusion coefficient D(As) at 350 °C on P(Hg). Additional results by Chandra et al. [90] on the arsenic

diffusion coefficient dependence on P(Hg) obtained at 375 °C, 400 °C and 425 °C are shown in Figure 7.20.

Shaw [91] gives the following Arrhenius relation for the arsenic diffusion coefficient ($cm^2.s^{-1}$) at Hg saturation obtained by doing a least squares fit of various experimental data:

$$D(As) = 1.52 \times 10^{-4} \exp\left(\frac{-1.28eV}{kT}\right) \quad (91$$

A least squares fit of the results on arsenic diffusion coefficient ($cm^2.s^{-1}$) obtained by Chandra et al. [89] at 350 °C under various Hg pressures gives the following relation according to Shaw [91]:

$$D(As) = (9 \pm 5) \times \frac{1}{P(Hg)^{3.6 \pm 1.4}} \quad (92$$

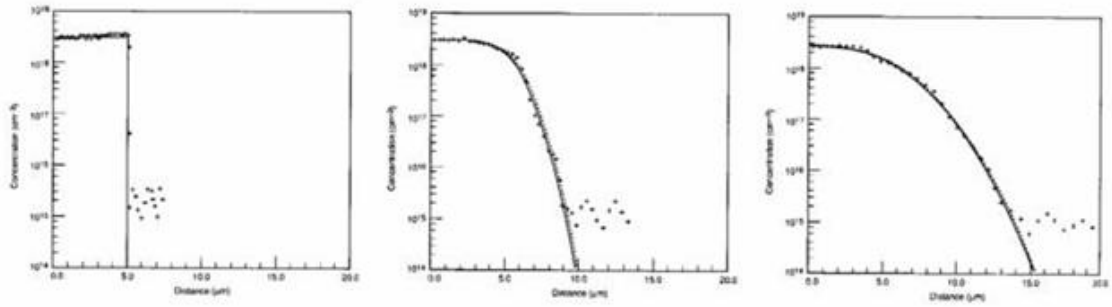

a) **b)** **c)**

Figure 7.18: a) As-grown profile. b) Distribution of arsenic after 1 hr at 350 °C, P(Hg)=0.16 atm, the solid line shows the best fit obtained assuming composition independent Fickian diffusion. (Right) Distribution of arsenic after 1 hr at 350 °C, P(Hg)=0.16 atm, the solid line shows the best fit obtained assuming composition independent Fickian diffusion [89].

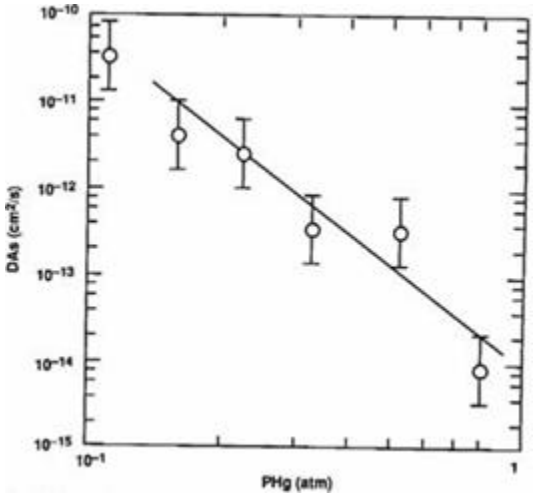

Figure 7.19: Dependence of the diffusion coefficient of arsenic at 350 °C in mercury cadmium telluride on the Hg overpressure [89].

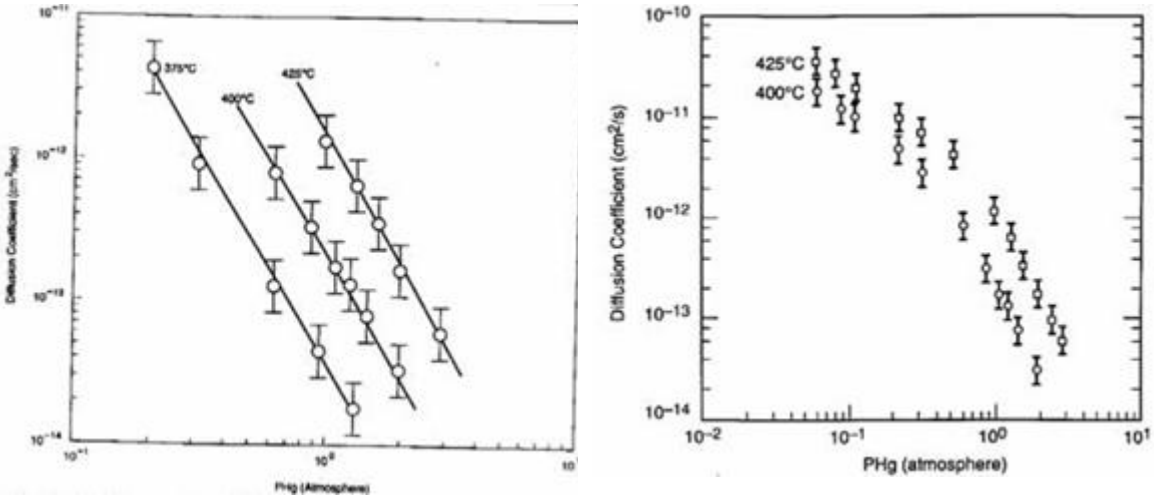

Figure 7.20: Dependence of the diffusion coefficient of arsenic at 375 °C, 400 °C and 425 °C in mercury cadmium telluride on the Hg overpressure [90].

7.2.2 Annealing Setup

The MBE growth occurs in Te rich conditions. Subsequently, the as-grown samples invariably contain Hg vacancies. The Hg vacancies act as acceptors in HgCdTe. They can also introduce defect states in the band gap that act as recombination centers that limit the lifetime of carriers in the HgCdTe material. *Thermal annealing* is an effective technique to fill the Hg vacancies. The annealing parameters are carefully chosen to fill the Hg vacancies as well as to activate the dopants. Usually, a two- or three-step annealing procedure is adopted as mentioned previously.

A specially designed quartz ampoule is used as shown in Figure 7.21. The annealing setup is located in the Microphysics Laboratory (MPL) at the University of Illinois at Chicago. The tube is divided into two compartments with constriction in between. The Hg source remains in the bottom compartment while the sample remains in the top compartment. The tube is evacuated, back-filled with argon and sealed. The annealing is then carried out in a two-zone furnace. The temperatures of the HgCdTe sample zone and the Hg zone can be controlled independently. Due to heat transfer between the two zones and the temperature variability inside the furnace, the temperatures near the locations of the HgCdTe sample and the mercury (points A and B in Figure 7.21) have been measured and calibrated in the furnace using thermocouples.

The n-type annealing usually involves 235 °C for 24 hrs, while to activate the p-type dopants (say in the case of arsenic implanted on n-type base layers) at least a two step anneal involving 425 °C for 10 min followed by 235 °C for 24 hrs is employed. The first step ensures proper site transfer for arsenic while the second step ensures Hg-vacancy filling.

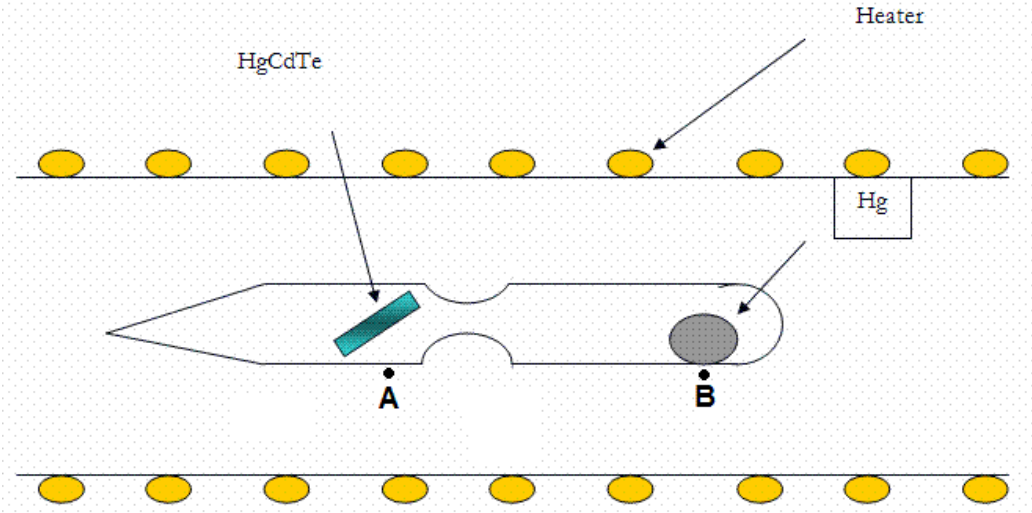

Figure 7.21: The annealing arrangement for closed tube in a two-zone furnace.

7.2.3 *Low P-type Doping Results in HgCdTe HOT structures*

Previously, we reported on a novel technique in order to achieve low p-type doping in HgCdTe by arsenic ion implantation and annealing [51]. As reported and described in details in the previous section, low P(Hg) anneal induces more Hg vacancies in HgCdTe which enhances the arsenic diffusion coefficient compared to Hg-saturated anneal [90]. The concept of our novel technique is illustrated in Figure 7.22 below. First, the arsenic SIMS profile in the HOT structure (with LWIR absorber layer) after ion implantation is shown. The different HOT device layers are also shown. Most of the arsenic is initially concentrated in the top P+ extraction layer. After annealing at T=300 °C for 16 Hrs under low P(Hg), *deep diffusion* of arsenic is obtained. Arsenic diffused all the way through the HOT absorber layer. After a standard arsenic activation anneal, the absorber layer becomes effectively p-type. P-type doping levels in the buried absorber layer now range from 10^{15} cm^{-3} to 10^{16} cm^{-3}. These initial annealing experiments were performed at the US Army Research Laboratory (ARL). Here, we develop this concept and optimize it for our annealing setup.

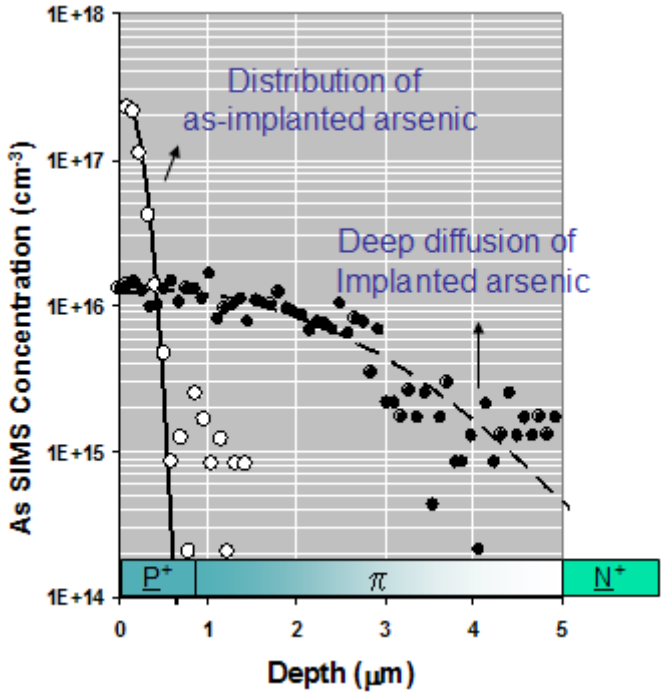

Figure 7.22: As-implanted and post-anneal arsenic SIMS profile in the HOT layer with LWIR absorber [51].

In this work, we use previously MBE-grown HOT structures with LWIR absorber layer (Figure 7.1) in order to effectively compare results with those previously obtained. Similar conditions than those used by ARL [51] are used.

Both the sample and Hg temperature during annealing are held at 300 °C in this first experiment. This corresponds to P(Hg)~0.32 atm. The annealing time is ~20.5 Hrs. The Hg annealing temperature was controlled by placing a thermocouple directly next to the Hg location in the ampoule. Previous experiments in our setup have shown that the temperature inside the ampoule is less than 10 °C higher than the temperature just outside at the same spot. Figure 7.23 shows the Cd alloy fraction in the HOT structure obtained by secondary ion mass spectroscopy (SIMS) after this first annealing experiment. The different layers in the structure are also indicated. This profile is similar to the one obtained in-situ during MBE growth by spectral ellipsometry (SE) and shown in Figure 7.5. Therefore, this annealing process does not affect the Cd-Hg interdiffusion, i.e. the Cd-Hg interdiffusion rate in this process is very low. Consequently, by proper control of this process, we can effectively control the placement of the electrical junction. This is more difficult to achieve at higher temperatures where the As diffusion competes with Cd-Hg interdiffusion.

We also note that, as Hg overpressure is not being provided during the anneal, the material loses Hg from the surface (top P+ layer) and is converted continuously to a higher x composition. This has been observed previously [86]. As explained earlier, this acts as a self-limiting process to Hg out-diffusion.

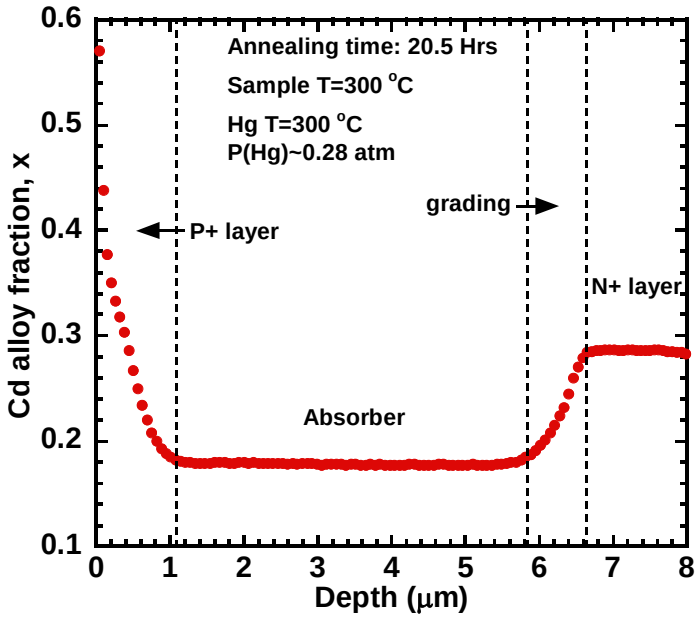

Figure 7.23: Cd alloy composition after annealing obtained by SIMS in LWIR HgCdTe HOT structure.

Next, the arsenic profile obtained by SIMS from this first experiment is shown. It is also compared to the arsenic profile obtained from a second experiment (Figure 7.24). In the second experiment, the sample is held at a temperature of 300 °C while the Hg is held at a temperature ~240 °C. This corresponds to a lower P(Hg) than in the first experiment, i.e. P(Hg)~0.07 atm. The annealing time in this second experiment is 16 Hrs.

We also fit these experimental data on arsenic implantation and diffusion profiles obtained using our novel technique in order to extract and compare the arsenic diffusion coefficient in the two experiments. The implantation specifications are energy of 200 keV and ion dose of $5\text{x}10^{13}$ cm^{-2}. The following Gaussian profile models the redistribution of the as-implanted profile (cm^{-3}) due to diffusion [92]:

$$C_{As}(x,t) = \frac{Q}{\sqrt{2\pi}\sqrt{2D_{As}t+\sigma^2}} \exp\left[-\frac{(x-R)^2}{2\sigma^2+4D_{As}t}\right] \qquad (93$$

where Q is the arsenic ion dose (cm^{-2}), D_{As} is the arsenic diffusion coefficient ($\text{cm}^2.\text{s}^{-1}$) for a particular annealing condition and R (nm) and σ (nm) are the range and standard deviation of the arsenic implant respectively.

The data is fitted using the Levenberg-Marquardt algorithm. Pearson's R coefficient for all fitting is always >0.9. R and σ have been determined from previous

as-implanted profile (t=0). We obtained R=37 nm, σ=18 nm. The SIMS arsenic profile for the first experiment (higher P(Hg)) is shown in Figure 7.24a where we see that arsenic diffuses slightly to create a p-n junction located at a depth ~0.6 µm, the level of indium n-type doping being at $1x10^{15}$ cm^{-3}. The SIMS arsenic profile for the second experiment (lower P(Hg)) is shown in Figure 7.24b. As expected, deeper diffusion of arsenic is obtained and the p-n junction location is now at a depth ~2.5 µm. The different layers in the HOT structure are also shown on both figures. The absorber layer being located in the depth range 1-5 µm, low p-type doping in the absorber is obtained in the second experiment ranging from 10^{15} cm^{-3} to less than 10^{16} cm^{-3} which is similar to the results obtained previously [51].

The arsenic diffusion coefficient in both experiments has also been extracted using a Gaussian fit. In the first experiment with high P(Hg), D(As) is ~$2x10^{-15}$ $cm^2.s^{-1}$. In the second experiment with low P(Hg), D(As) is ~$6x10^{-14}$ $cm^2.s^{-1}$. This represents a factor 30 increase compared to the first experiment.

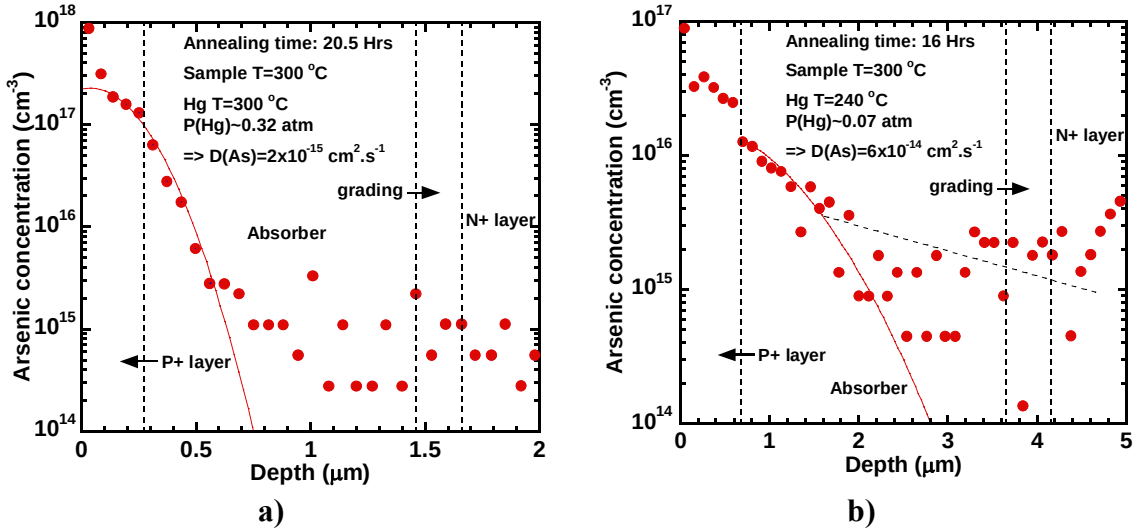

Figure 7.24: Post-anneal arsenic profiles obtained by SIMS under different Hg partial pressures as indicated on the figures a) and b). Data is fitted using a Gaussian fit (solid lines). The tail due to channeling is also shown (dotted lines).

These results demand for additional work. This novel process needs to be applied to additional HgCdTe HOT structures and annealing conditions need to be varied. However, these results are very promising as they successfully reproduce and confirm the

initial results that were obtained using the furnace at ARL [51]. We also added more insight than in the previous study by reviewing in details past results on arsenic diffusion in HgCdTe, measuring the Cd alloy composition by SIMS and fitting the arsenic profile SIMS data in order to extract the arsenic diffusion coefficient.

In the next chapter, we present HgCdTe HOT device results using this novel process and reported previously [51]. We use our numerical model in order to simulate these experimental HOT devices. We analyze the limiting current mechanisms by fitting the current-voltage characteristic.

Chapter 8
HgCdTe HOT Device Experimental Results

Here we present experimental electrical and optical characteristics of LWIR HgCdTe Auger-suppressed photodiodes with cutoff wavelength λ_c=10.4 μm at 100 K obtained in collaboration between the US Army Research Laboratory (ARL) and EPIR Technologies, Inc [51], [93]. This data is the best obtained out of the different HOT device fabrication cycles performed (on two different HOT LWIR wafers and one HOT MWIR wafer) and correspond to a batch processed by ARL. In this work, our main focus is to present clear evidence of *Auger suppression* in our devices at different temperatures and to perform a detailed analysis of the experimental data.

The device structure is then simulated and the experimental data is fitted using our numerical model [94]. Based on this fitting, the current mechanisms limiting the dark current in these photodiodes are extracted. We also discuss design and fabrication considerations in order to optimize future HgCdTe Auger-suppressed photodiodes.

8.1 Device Structure

The three-layer P+/π/N+ planar structure was grown by MBE by EPIR Technologies on lattice-matched CdZnTe substrate. The bottom $Hg_{1-x}Cd_xTe$ layer, region I, is ~2 μm thick with cadmium fraction x=0.30. The absorber layer, region II, is ~5 μm thick with x=0.22. The measured cutoff wavelength λ_c is ~10.4 μm at 100 K and ~7.4 μm at 250 K. The top layer, region III, is ~1 μm thick with x=0.30. LWIR HgCdTe was chosen for the absorber layer because the effect of Auger suppression is more visible than for MWIR HgCdTe as we have seen previously. The device is designed with wider band-

gap (x=0.30) at the top and bottom layer compared to the absorber layer (x=0.22) in order to achieve the exclusion and extraction layers respectively.

Region I is in-situ heavily doped n-type with indium concentration of 10^{17} cm^{-3}. The background concentration in regions II and III is n-type with indium at ~10^{15} cm^{-3}. The ex-situ p-type doping of the absorber and the top layers was achieved using arsenic implantation, followed by a deep diffusion anneal at 350 °C for 16 hours under low Hg partial pressure as described in the previous chapter. Following the diffusion anneal, an activation anneal was performed at 400 °C for 10 min, followed by a mercury vacancy annihilation anneal at 235 °C for 24 hrs. Typical secondary ion mass spectroscopy (SIMS) profiles show an arsenic concentration in the low 10^{16} cm^{-3} for the top layer and an arsenic concentration in the range 10^{15}-10^{16} cm^{-3} for the absorber layer (Figure 7.22). A critical aspect of our novel diffusion process is the ability to maintain a good HgCdTe surface even after successful deep diffusion of As using a low Hg partial pressure. Figure 8.1 and Figure 8.2 show the surface under optimized arsenic deep diffusion conditions before and after annealing. The HgCdTe surface will become rough if the arsenic diffusion annealing conditions are not optimized.

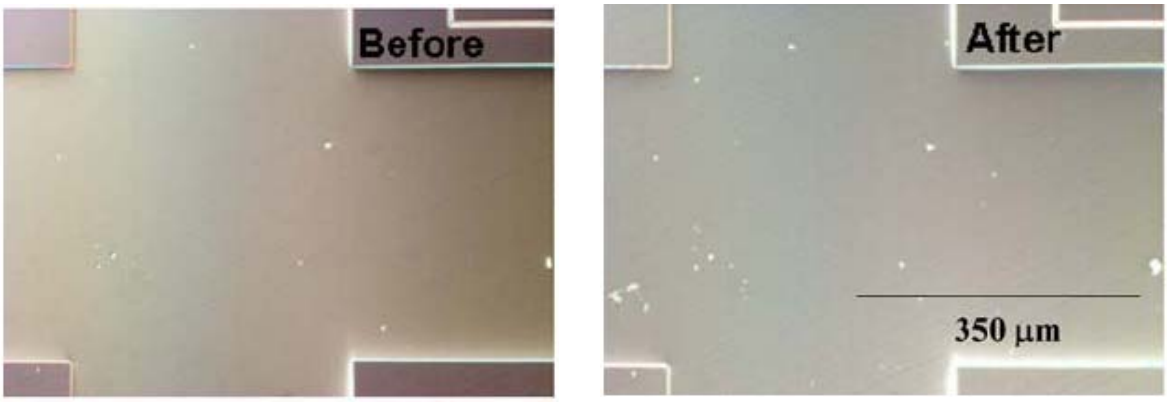

a) **b)**

Figure 8.1: Surface morphology under Nomarski microscope a) before and b) after diffusion anneals [93].

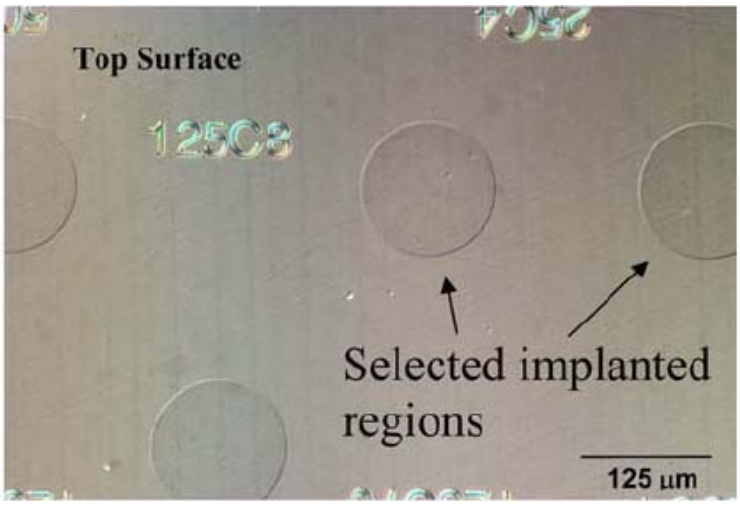

Figure 8.2: Implanted regions under Normarski microscope after complete anneals [93].

The surface is then passivated by deposition of ZnS, and the p-type and n-type metal contacts are formed by gold evaporation. A schematic of the process flow is shown in Figure 8.3 and the final planar device structure is shown in Figure 8.4. More details on the MBE growth and the device processing were given in the previous chapter.

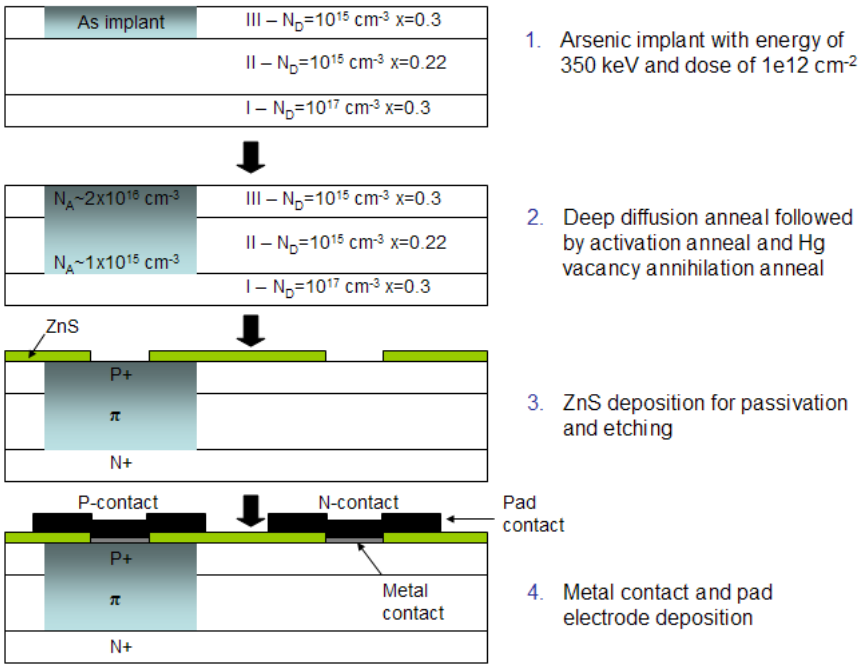

Figure 8.3: Schematic depicting the process flow.

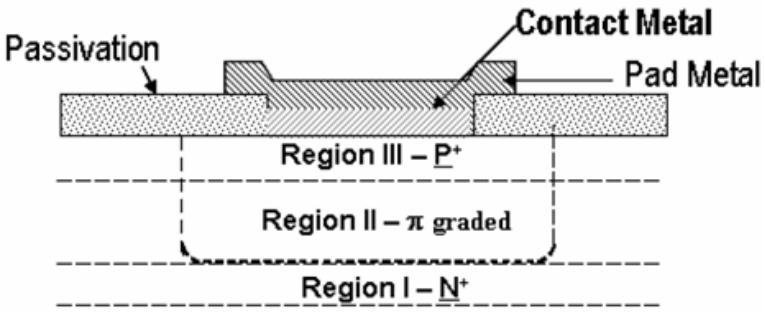

Figure 8.4: Planar device structure.

8.2 Experimental Device Results

8.2.1 Electrical Characteristics

Planar circular devices with varying diameters were fabricated. Figure 8.5 shows the current-voltage characteristics at 300 K for selected HgCdTe P+/π/N+ devices. The photodiode reverse-bias leakage current seems to be limited by a *series resistance* in the device up to ~400 mV. It also shows a *strong negative differential resistance* (NDR) at ~400-500 mV which we attribute to *strong Auger suppression* in the device [51]. We observe ~50 % decrease in the dark current at room temperature which is consistent with previous results obtained on HgCdTe P+/ν/N+ mesa devices grown by MOCVD [49] and MBE [50]. In addition, this is the first report of Auger suppression in HgCdTe P+/π/N+ planar devices.

Traces from similar devices coincide very well, indicating a good uniformity of the layer. The residual differences are attributable to non-uniformities in the processing. The onset voltage of Auger suppression appears to occur at different voltages for the two different device diameters. We believe this is due to the different voltage drop across the series resistances for the two sets of diodes as we will explain later.

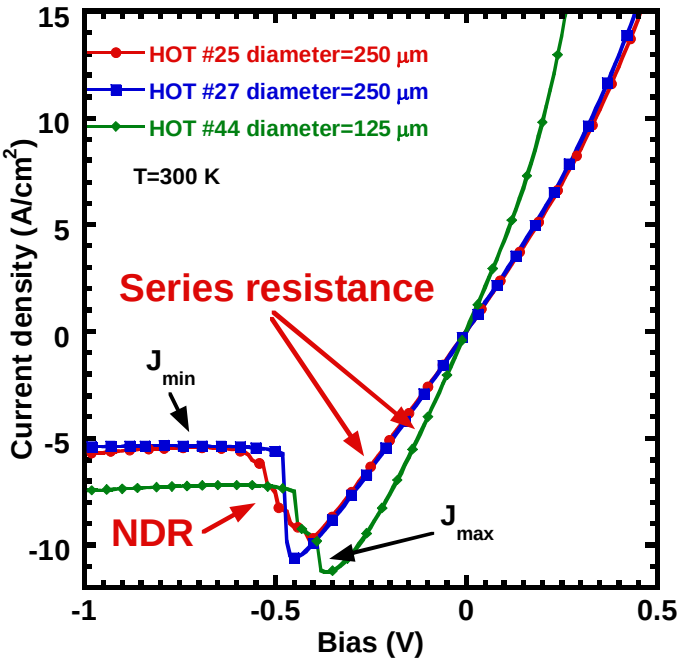

Figure 8.5: Current-voltage characteristics at 300 K for selected devices.

Figure 8.6 shows the temperature-dependent current-voltage characteristics for one selected HOT device. NDR is observed between 120 K and 300 K, becoming higher as the temperature is increased which is consistent with clear Auger suppression in the device. The onset voltage of Auger suppression decreases as the temperature is decreased. This onset voltage at a particular temperature is the result of the series resistance in the device, which increases as the temperature is decreased, and the photodiode leakage current magnitude, which decreases as the temperature is decreased.

After Auger suppression, the dark current saturates up to a certain bias voltage. Above this bias voltage, the dark current increases probably due to tunneling processes in this LWIR HgCdTe photodiode. This is confirmed by the fact that this onset voltage for tunneling processes decreases as the temperature is decreased.

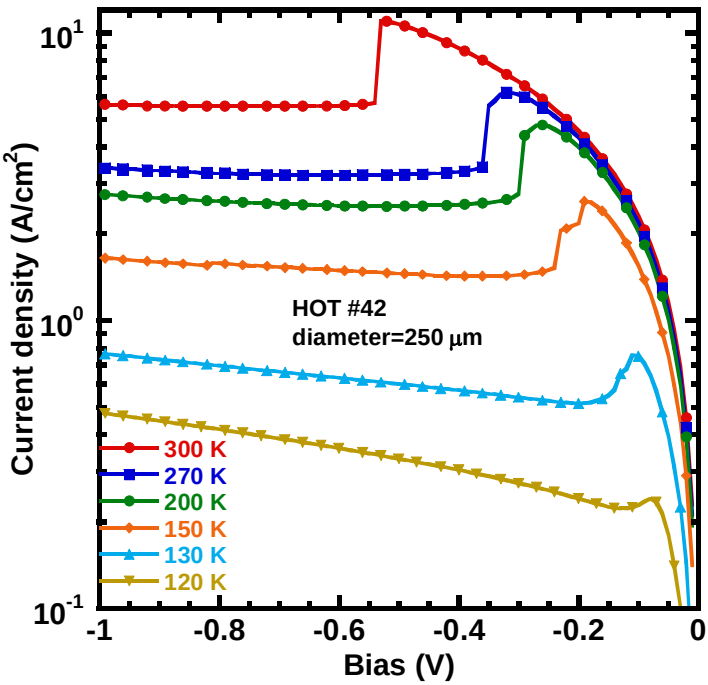

Figure 8.6: Reverse-bias current-voltage characteristics for HOT #42 at different temperatures.

8.2.2 Optical Characteristics

Spectral response versus wavelength was measured under backside-illuminated conditions on HOT #22 (diameter of 250 μm). Figure 8.7 shows the response versus wavelength on device #22 at 100 K [93]. The measured cutoff wavelength λ_c is approximately 10 μm at 100 K (LWIR). The calculated response per photon versus wavelength is also displayed in Figure 8.7 and can be seen to be near-classical behavior. The slight drop in response at shorter wavelengths (<4 μm) is attributed to absorption in the N+ layer.

The detectors are non-antireflection coated at the back of the CdZnTe substrate and hence approximately 22% absorption is lost to reflection losses. The measured quantum efficiency at -0.1 V for a wavelength of 7 μm is 54 % at 100 K, which indicates the good quality of the HgCdTe.

The spectral response at 250 K was also measured and is shown in Figure 8.8. A near-classical response was also observed. The measured cutoff wavelength is

approximately 7.4 μm at 250 K. Next, we use our numerical model in order to simulate these HgCdTe P+/πN+ devices and analyze the experimental device data.

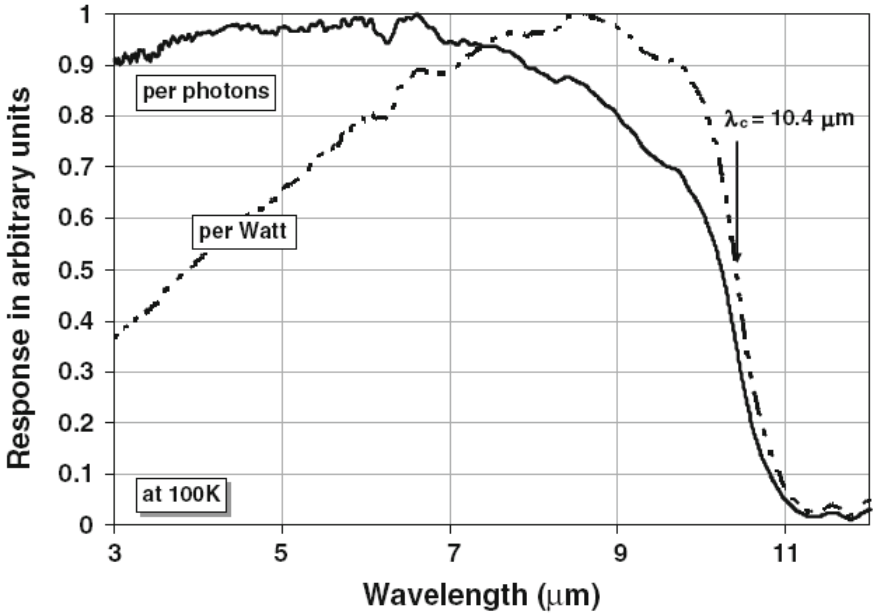

Figure 8.7: Measured spectral response versus wavelength at 100 K for a 250 μm-diameter device (HOT #22). Both spectral responses, per photon and per Watt, show near-classical behavior. The cutoff wavelength is defined as the 50% spectral response point from the peak wavelength [93].

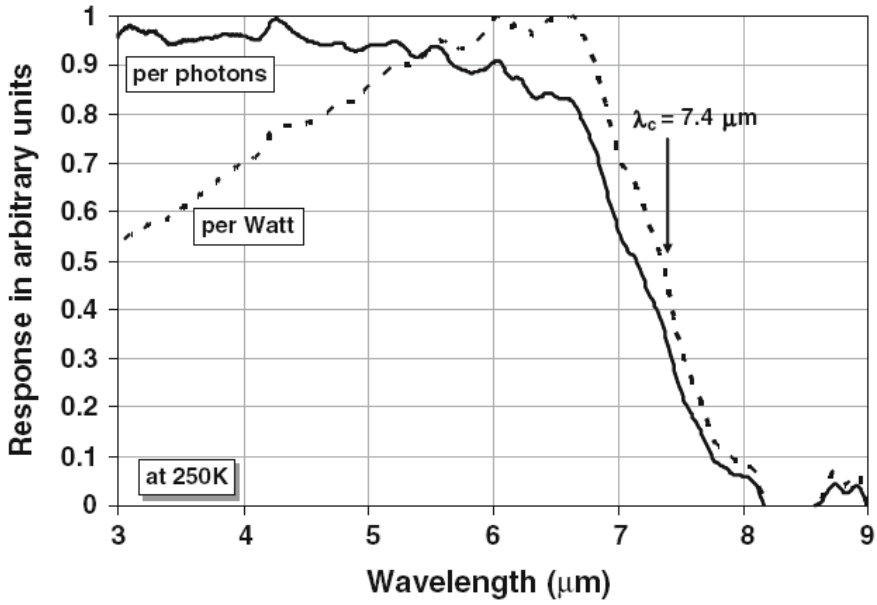

Figure 8.8: Measured spectral response versus wavelength at 250 K for a 250 μm-diameter device (HOT #22). The obtained cutoff wavelength is 7.4 μm at 250 K [93].

8.2.3 *Detectivity Measurements*

The detectivity D^* on HOT #42 is measured at different temperatures ranging from 120 K to room temperature. It is a circular planar device with an active area diameter of 250 μm. It is measured using the setup in the Microphysics Laboratory (MPL) at the University of Illinois at Chicago (UIC) which is described below. The setup is composed of a black-body simulator set at 500 K. Therefore, we measure the detectivity D^*_{500K} for a 500 K black-body infrared source, which is a standard temperature along with 2800 K. The frequency chopper is set to 1000 Hz. The HOT sample is mounted inside an HDL-5 dewar from IRLabs, Inc. The sample is cooled with liquid nitrogen and the temperature can be controlled from 77 K to room temperature. The HOT device is wired to a low-noise current-to-voltage pre-amplifier. The model is MCT-1000 capacitive transimpedance amplifier from Infrared Systems Development. Typical noise values are <1.5 nV/√Hz referred to the input. The HOT device is connected to the input BNC connector with an SMA – BNC cable. Positive and Negative 15 Volt DC power supplies are used. The detector bias is internally provided, and the reverse bias voltage is adjustable from typically 0 V to -2.5 V. The electrical bandwidth is internally set to 1.5Hz to 200Khz. Adjustable gain provides variable signal amplitude typically from 50 to 1000 times. The signal from the preamplifier then goes to a 7265 DSP lock-in amplifier from Signal Recovery. The signal from the frequency chopper is used as the reference signal. From this, both signal voltage and RMS noise voltage can be extracted to calculate D^*. The Field-of-View (FOV) is about 90°.

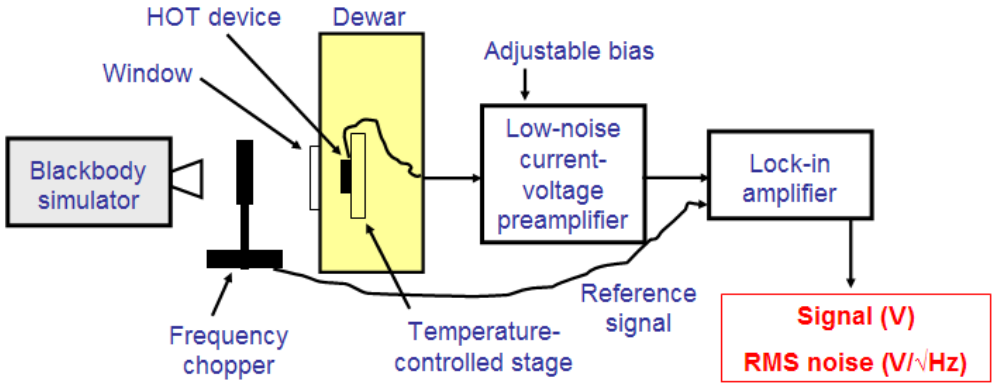

Figure 8.9: Schematic of the detectivity measurement setup.

The expression to calculate the detectivity D^* is slightly different than the one given in Equation (20) and used in our device model, as voltages are measured for the signal and the RMS noise:

$$D^* = \frac{R_{500K}\sqrt{A_j}}{v_n} \tag{94}$$

$$R_{500K} = \frac{V}{P_{BB}} \tag{95}$$

$$P_{BB} = \frac{\sigma\left(T_s^{\,4} - T_b^{\,4}\right) \times tran \times L_{ad}^{\,2} \times A_j}{4d^2} \tag{96}$$

where R_{500K} is the responsivity for a 500 K black-body IR source (V/W), A_j is the detector active area (cm^2), v_n and V are the RMS noise voltage (V/√Hz) and signal voltage (V) respectively measured from the lock-in amplifier, P_{BB} is the total radiation power arriving on the detector (W), σ is the Stefan-Boltzmann constant, T_s and T_b are the black-body source and background temperatures respectively (K), tran is the transmission of the window material of the dewar, L_{ad} is the limiting aperture diameter of the black-body source (cm), and d is the distance between the black-body and the detector (cm). Below we give the list of parameters used in our D^* setup:

Detectivity measurement setup parameters:

A_j=250x250 μm^2; T_s=500 K; T_b=300 K; tran=0.75 (ZnSe); L_{ad}=1 inch; d=7 inch.

Figure 8.10 shows the measured detectivity D^* for a 500 K black-body IR source versus temperature. The estimated BLIP detectivity D^* for a 500 K black-body is ~$2x10^{10}$ cm.$Hz^{0.5}$/W. The measured D^* at 120 K is in the low 10^9 cm.$Hz^{0.5}$/W. As far as we know, this is the highest reported value of D^* for an HgCdTe IR detector with LWIR response operated at 120 K. However, it is about one order of magnitude than the ideal D^*_{BLIP}. This shows that there is still room for improvement, as discussed in more details in the following section.

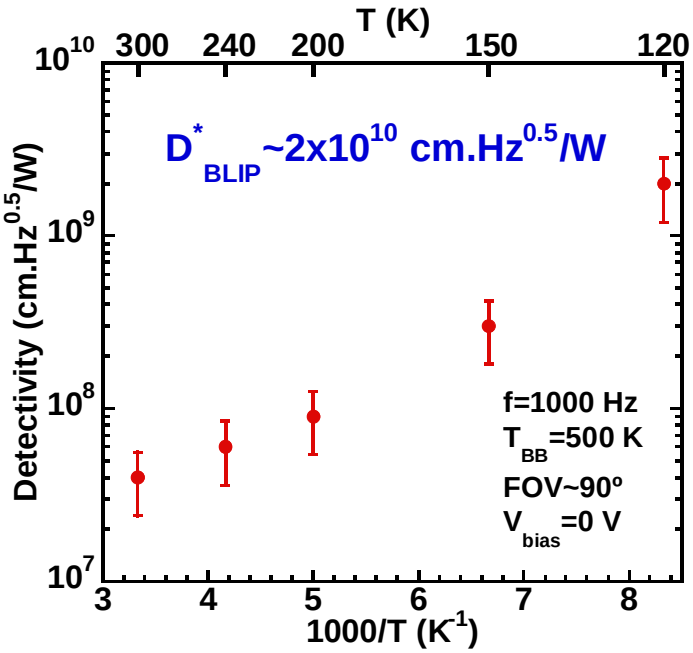

Figure 8.10: Detectivity D^* for 500 K black-body versus temperature with FOV=90°, frequency of 1000 Hz and zero bias.

As the temperature is increased, the measured detectivity D^* drops significantly, down to the mid-10^7 cm.Hz$^{0.5}$/W at 300 K. We believe that this is due partly to the increase in the HOT dark current, but mostly to an increase of 1/f noise. In order to support this, we measure the detectivity versus bias at different temperatures (Figure 8.11a). From the experimental I-V data, we expect to see a decrease of the detector noise, hence an increase of the detectivity D^*, as the reverse bias is increased, due to the Auger reduction and dark current decrease in the HOT device. This is slightly observed for T<150 K and bias less than ~100 mV. However, due to large error bars and presence of 1/f noise, it is not possible to clearly observe this effect. The 1/f noise is expected to increase as the reverse bias is increased and, therefore, hides the Auger reduction effect. As the temperature is increased, D^* decreases more as the reverse bias is increased due to an increase in 1/f noise.

We also measure the RMS noise voltage versus temperature at different frequencies and reverse bias of 100 mV (Figure 8.11b). It was not possible to measure the signal voltage, hence D^*, because the frequency chopper only operates at 1000 Hz. Also, our setup only allows us to measure discrete data points for the RMS noise voltage at

different frequencies, and not the complete frequency spectrum. The increase in RMS noise voltage at lower frequencies due to 1/f noise is more significant at higher temperatures. This supports that the 1/f noise increases as the temperature is increased. This is confirmed by previous reports on HOT experimental device data [52]. However, we believe that the excess of 1/f noise in our experimental HOT devices is lower than in previous HOT devices, as our measured D^* at 300 K is in the mid-10^7 cm.$Hz^{0.5}$/W, compared to mid-10^5 cm.$Hz^{0.5}$/W at 300 K [52] for HOT devices with LWIR response. Additional noise and detectivity studies on our HOT devices are needed to support this.

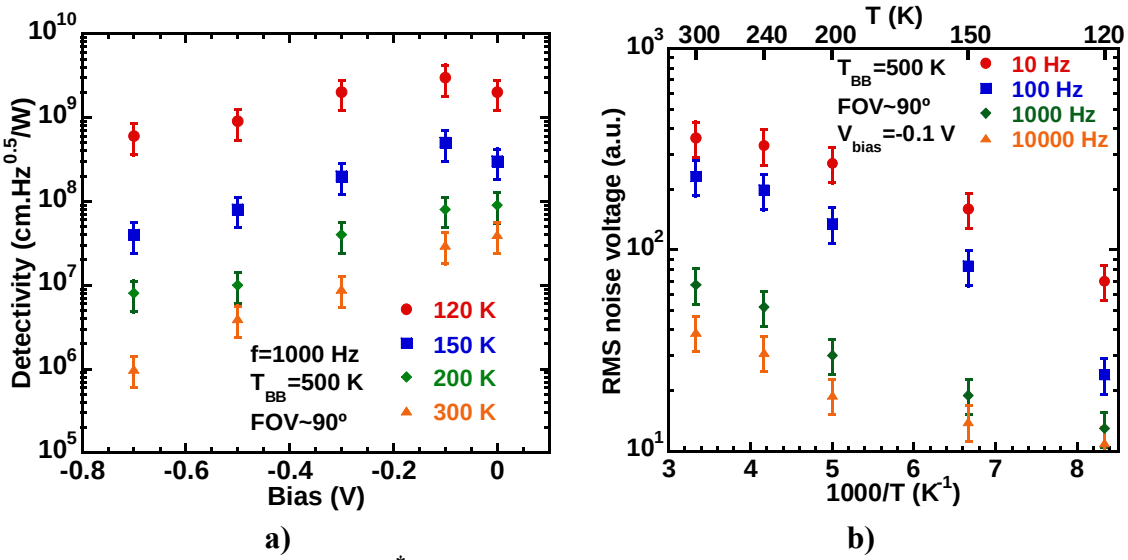

Figure 8.11: a) Detectivity D^* versus bias at different temperatures and b) RMS noise voltage versus temperature at different frequencies for reverse bias of 100 mV.

8.3 Device Simulation

8.3.1 Simulation Setup

Our numerical model is used in order to simulate these HgCdTe P+/π/N+ photodiodes [94]. The initial Cd alloy fraction and doping profile used in our model is shown in Figure 8.12, along with the corresponding calculated equilibrium energy band diagram at T=300 K in Figure 8.13. A Gaussian curve is used in the simulation model to represent the arsenic implant/diffusion profile, following experimentally measured SIMS data. The n-type doping profile in device model is taken from designed values for in-situ

indium doping of HgCdTe during MBE growth. The Cd alloy profile, including compositional grading at the two junctions, is taken from experimentally measured spectroscopic ellipsometry (SE) data and included in the simulation using a linear interpolation of the HgCdTe material parameters.

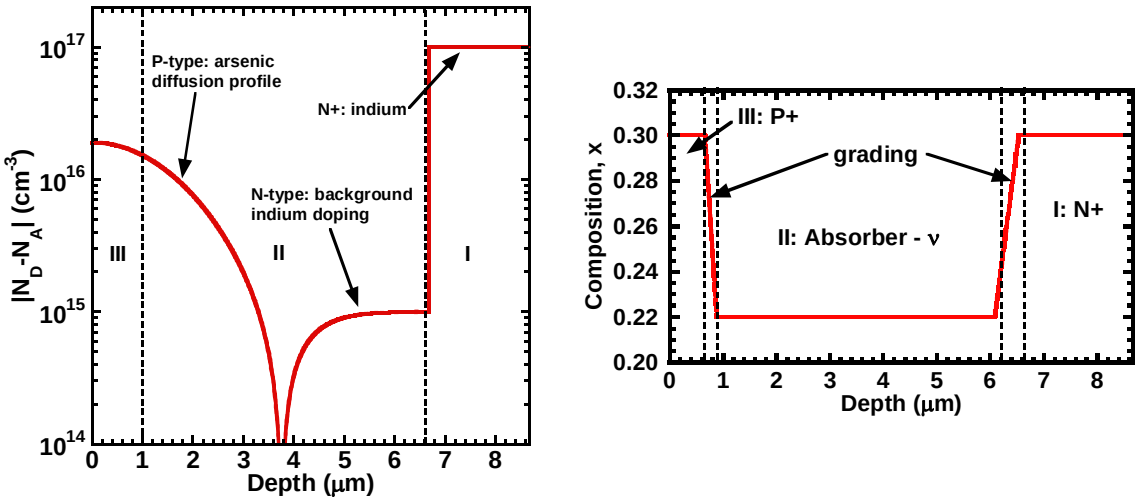

a) b)

Figure 8.12: a) Doping profile and b) cadmium fraction profile in the simulated structure.

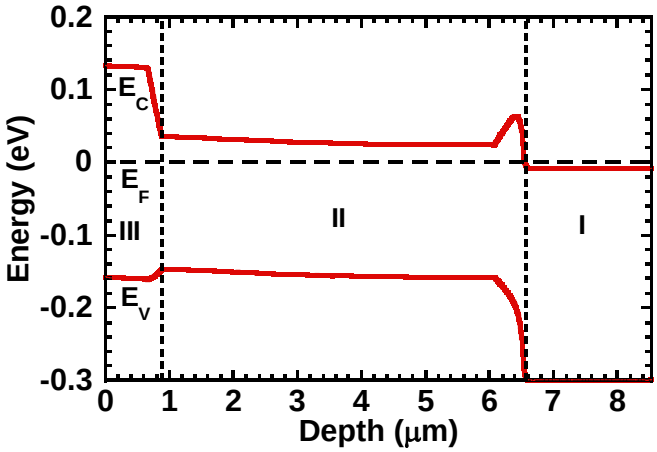

Figure 8.13: Calculated energy band diagram of the HOT structure at zero bias and T=300 K.

The calculated energy band diagram for this device at 1 V reverse bias and T=300 K is shown in Figure 8.14a. *Partial depletion of the absorber layer* is achieved by increasing the reverse bias (depletion width is ~2-2.5 μm). From this observation, we can

remember a point critical to understand the behavior of these HgCdTe HOT photodiodes: classical p-i-n photodiodes with fully-depleted absorber are very hard to achieve in HgCdTe technology. This is because of the value of the lowest controllable doping achievable in HgCdTe and because thick absorber regions (at least a few microns) are needed in order to detect the infrared radiation. In a way, our fabricated HgCdTe P+/π/N+ devices are therefore "partially" acting as classical p-i-n photodiodes when operated under high enough reverse bias.

The calculated equilibrium and non-equilibrium (1 V reverse bias) carrier concentration is shown in Figure 8.14b. Under equilibrium, the LWIR absorber layer is essentially intrinsic. As the reverse bias is increased, the electron and hole concentration decreases by several orders of magnitude due to the effect of the exclusion/extraction layers. The hole concentration decreases down to the extrinsic p-type doping level for a depth <4 μm (non-depleted region). This initial simulation seems to confirm that the NDR observed experimentally is due to strong Auger suppression in the device, but further analysis is required. More can be learned by fitting the experimental device data using our device model.

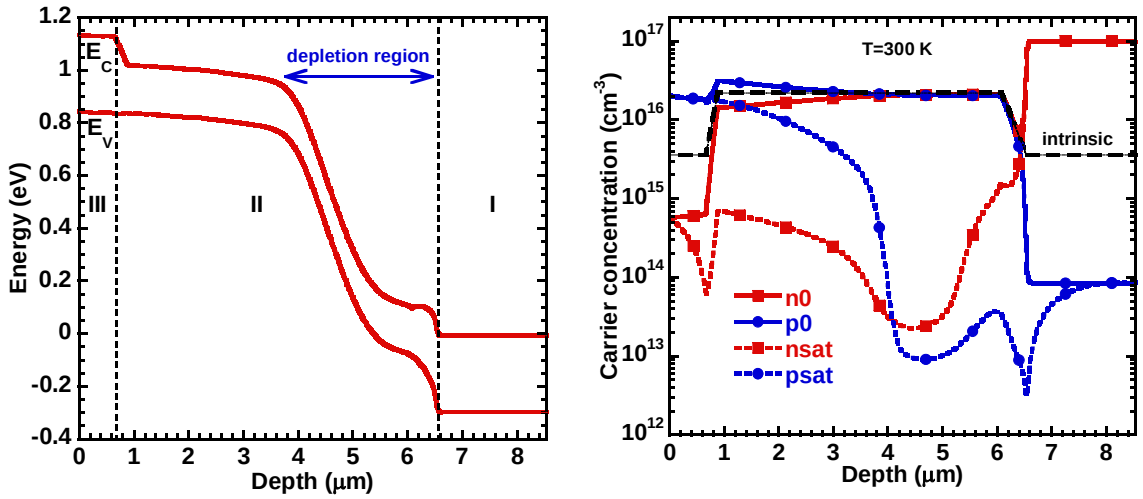

Figure 8.14: a) Energy band diagram at 300 K for 1 V reverse bias and b) electron and hole carrier concentration in the structure at zero bias and 1 V reverse bias. Also shown is the intrinsic carrier level (dashed line).

8.3.2 Fitting Methodology

Our device model is used to fit the temperature-dependent current-voltage data of HOT #42 shown in Figure 8.6. We do a 1D simulation of a cross-section of the device. Therefore, we *initially ignore the effect of the series resistance* which will be analyzed in a separate section. We do not consider surface recombination due to passivation layer. We also ignore the effect of tunneling mechanisms.

In order to fit the I-V data for each temperature (120 K, 130 K, 150 K, 200 K, 270 K, 300 K), we fit the maximum leakage current experimental value before Auger suppression (J_{max}) and the minimum leakage current experimental value after Auger suppression (J_{min}) as illustrated in Figure 8.5. In our model, J_{min} is taken as the calculated current density at 500 mV reverse bias which is found to be high enough for dark current saturation (neglecting the series resistance). J_{max} is taken as the maximum calculated current density between zero bias and 500 mV reverse bias. The temperature-dependent experimental values for J_{min} and J_{max} that we are fitting are shown in Figure 8.15, along with the corresponding experimental reverse bias value.

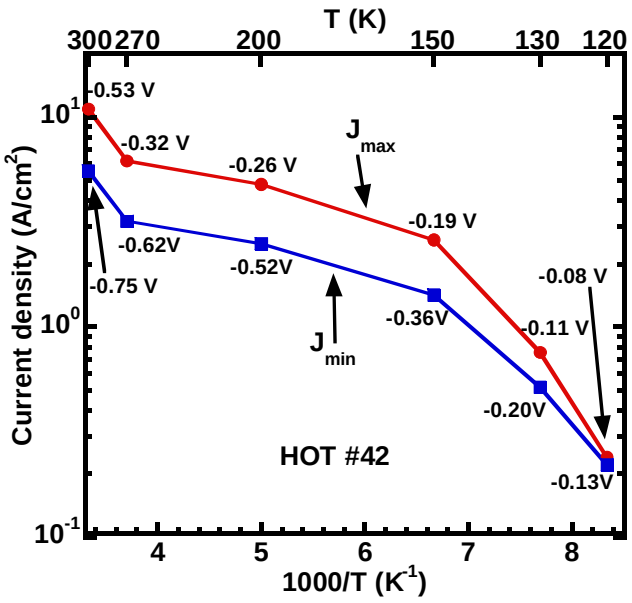

Figure 8.15: Experimental absolute value of the current densities J_{min} and J_{max} versus temperature from HOT #42.

First, we notice that, if we use in our model the Cd alloy composition x(III) obtained from SE data (Figure 8.12b), our simulation calculations at T=300 K result in calculated J_{min} and J_{max} much higher than the experimental data (Case I in Figure 8.16). This is because the dark current in this case is limited by the electron diffusion current in the top P+ layer at T=300 K, $J_{n,diff}(P+)$, which is large at room temperature because the intrinsic carrier concentration is high for x(III)=0.30 in the P+ layer (Case I) and the electron mobility is very high. Therefore, it seems that the SE data for Cd alloy profile do not agree with the experimental data.

Indeed, SE data is taken during growth and the Cd alloy composition may be very different before and after device processing, especially due to the annealing steps. One possible explanation arises from the experimental SIMS data shown in Figure 7.23 in the previous chapter. This data shows the Cd alloy composition obtained after the deep diffusion annealing step (under low P(Hg)) to obtain p-type doping in the absorber layer. We observed that the top P+ layer is converted continuously to a higher x composition because not enough Hg is being provided to compensate for Hg out-diffusion. This has also been observed previously [86]. Based on this data, we set the Cd alloy composition profile in the top P+ layer, x(III), as a *fitting parameter* in the form of a linear grading $x_{top} \rightarrow 0.3$ (with $x_{top} > 0.3$).

Case II (x(III)=0.35→0.30) corresponds to x=0.35 at the top surface and x=0.30 at the bottom of the P+ layer with a *linear grading* between the two. The calculated I-V for Case II is also shown in Figure 8.16. We see that Case II results in a much lower electron diffusion current in the top P+ layer (but still higher than the experimental data). Therefore, we conclude that our assumption of a linear grading for x(III) may be justified.

As seen in Figure 8.15, the experimental points for J_{min} and J_{max} at T=300 K do not follow the trend observed for T<270 K. This is due to the electron diffusion current in the top P+ layer $J_{n,diff}(P+)$. Also, J_{min} and J_{max} are expected to be nearly constant between 270 K and 300 K if they were following the trend observed for T<270 K. Therefore, the approximation below is used in order to calculate the linear grading profile of x(III) in our fitting:

$$J_{\min,300K} - J_{\min,270K} = J_{n,diff}(P+)_{300K} - J_{n,diff}(P+)_{270K} \quad (97)$$

where $J_{min,300K}$ and $J_{min,270K}$ are the experimental values, and $J_{n,diff}(P+)_{300K}$ and $J_{n,diff}(P+)_{270K}$ are the values extracted from our simulations.

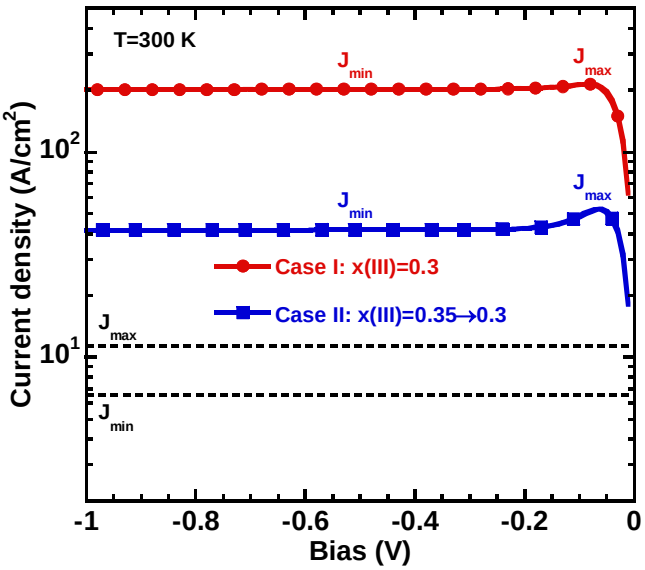

Figure 8.16: Calculated current-voltage characteristics at 300 K for Cases I and II. Also shown are the values for experimental J_{min} and J_{max}.

The two other fitting parameters are the ones that are found to have the most influence on the calculated device characteristics: $|F_1F_2|$ in the absorber layer which is related to the magnitude of Auger-1 processes, and the SRH characteristic lifetime τ_{n0} ($=\tau_{p0}$, assuming the same for electrons and holes) in the absorber layer which is related to the concentration of traps, impurities, dislocations, or other elements causing SRH recombination as well as their capture cross-sections (see Equations (54) and (55)). As we mentioned already, there is no clear agreement on the value of $\gamma=\tau_{A7}^{i}/\tau_{A1}^{i}$ in HgCdTe which is related to the magnitude of Auger-7 processes. Consequently, we set $\gamma=6$ in this study which is the most common value used.

Figure 8.17 shows the effect of each of these two parameter (for a given x(III)) on the calculated I-V at 300 K. We observe that $|F_1F_2|$ mostly has an influence on the value of $(J_{max}-J_{min})$ and therefore the strength of the NDR. The SRH lifetime τ_{n0} (τ_{p0}) has an influence on the values of both J_{min} and J_{max}, but mostly on J_{min}.

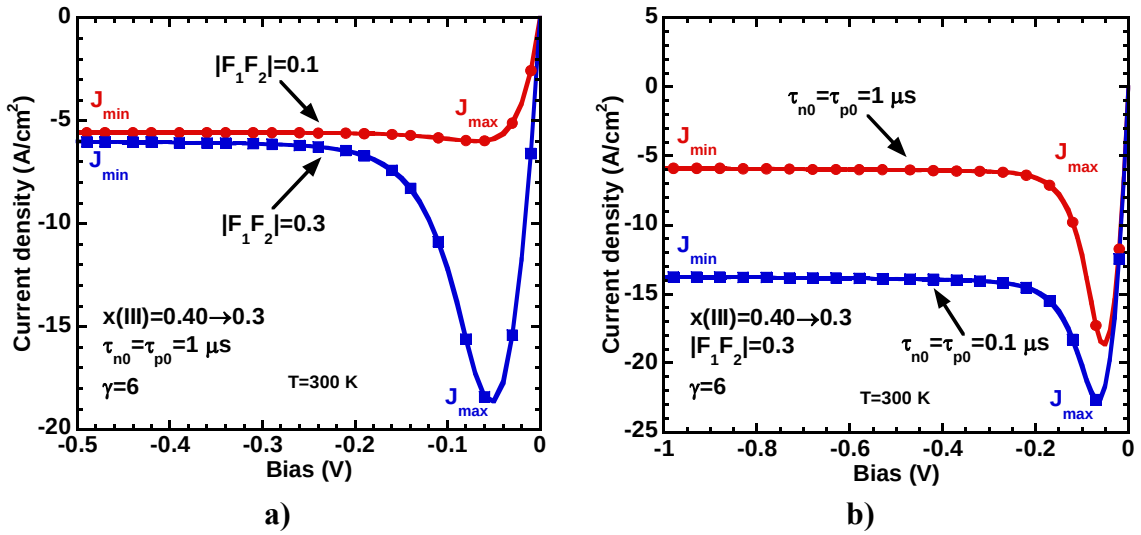

Figure 8.17: Calculated I-V at 300 K for two different values of a) $|F_1F_2|$ and b) τ_{SRH}.

Below we summarize the parameters used in our device model to fit the experimental I-V characteristics. In this case, the temperature dependence of $|F_1F_2|$ and τ_{SRH} is taken into account. The Cd alloy profile in the top P+ layer x(III) is constant with temperature. The doping profile (Figure 8.12a) and device geometry are taken from experimental data and designed values. Compositional grading between each region interface is taken into account. Figure 8.18 summarizes the fitting algorithm resulting from the initial analysis. The fitting for each temperature is usually obtained after 2-3 iterations maximum.

Top p-type P+ layer (Region III):

Fixed: t=0.66 μm, k=0.01, $|F_1F_2|$=0.3, γ=6, $E_{trap}=E_{Fi}$ (intrinsic Fermi level), $\tau_{n0}=\tau_{p0}$=1 μs.

Fitting parameter: x(III)=x_{top}→0.3 (linear grading, x_{top} is the Cd fraction at the surface resulting from the arsenic diffusion anneal).

Absorber p-type π layer (Region II):

Fixed: t=5.2 μm, x(II)=0.22, γ=6, $E_{trap}=E_{Fi}$, k=0.01.

Fitting parameters: $|F_1F_2|$=0.1-0.3, $\tau_{n0}=\tau_{p0}$=0.01-10 μs.

Bottom n-type N+ layer (Region I):

Fixed: t=2 μm, k=0.01, $|F_1F_2|$=0.3, γ=6, $E_{trap}=E_{Fi}$ (intrinsic Fermi level), $\tau_{n0}=\tau_{p0}$=1 μs.

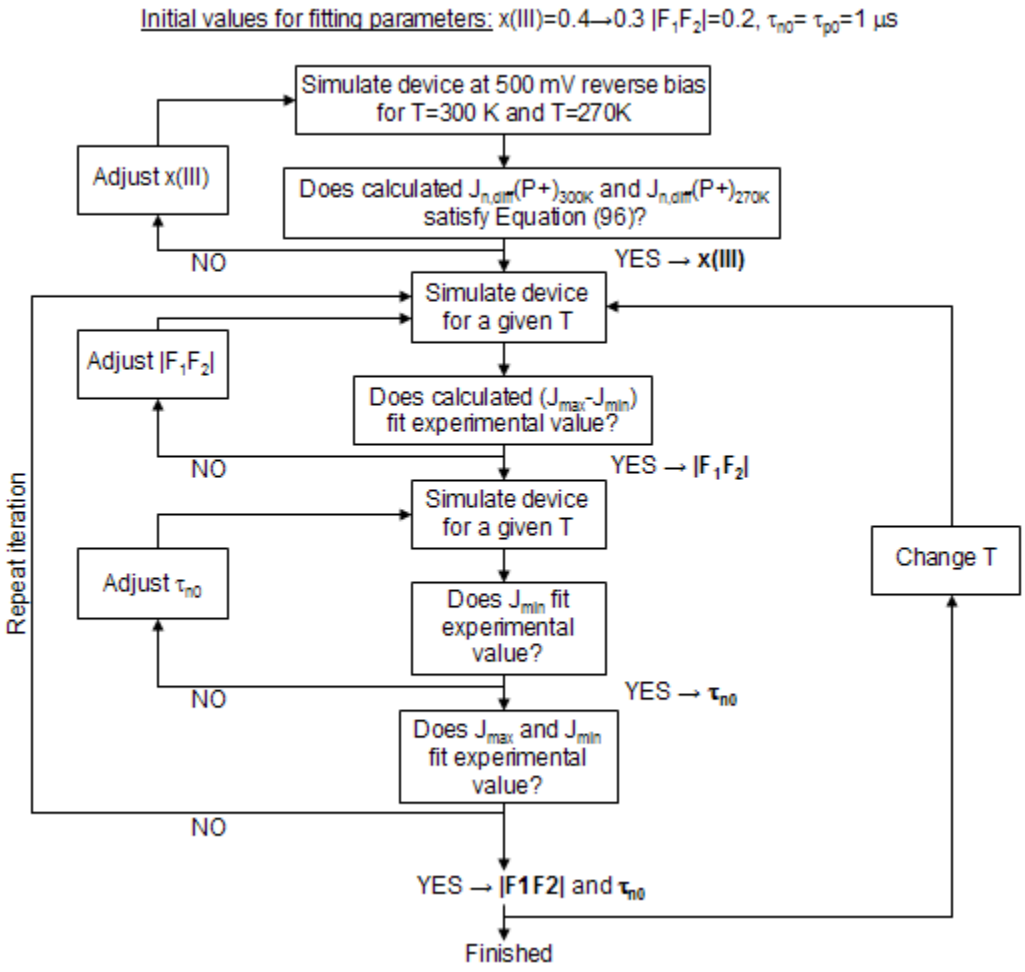

Figure 8.18: Fitting algorithm.

Detailed analysis of dark I-V characteristics of standard HgCdTe p-n photodiodes is possible using fitting software which includes all of the possible current components in the device, including band-to-band tunneling, trap-assisted tunneling and ohmic shunt current [95]. Such software programs use a limited number of fitting parameters and provide valuable information on the dominant current components in the device at different reverse biases and temperatures. However, most of these existing programs could not be applied to the devices considered here because of the peculiar form of their I-V characteristics corresponding to suppression of Auger processes as the reverse bias is

increased. Here we use our numerical model in order to provide a unique analysis of HgCdTe Auger-suppressed device experimental data.

Ultimately, the goal of this fitting is to understand what mechanisms are limiting the leakage current just before (J_{max}) and after (J_{min}) Auger suppression. The total leakage current J_{tot} can be expressed as the sum of the electron diffusion current in the top P+ layer, $J_{n,diff}(P+)$, the hole diffusion current in the bottom N+ layer, $J_{p,diff}(N+)$, and the absorber layer current J_{abs}:

$$J_{tot} = J_{n,diff}(P+) + J_{abs} + J_{p,diff}(N+) \tag{98}$$

As seen in Figure 8.14, the absorber layer current is a combination of diffusion and g-r current, depending on the reverse bias. However, it is much more interesting to define it as the sum of an Auger-1 current in the absorber, J_{A1}, an Auger-7 current in the absorber, J_{A7}, and an SRH current in the absorber, J_{SRH}:

$$J_{abs} = J_{A1} + J_{A7} + J_{SRH} \tag{99}$$

This way, we can determine the recombination mechanisms limiting the leakage current in the HgCdTe HOT photodiodes. J_{min} and J_{max} are fitted at each temperature using the set of three fitting parameters described earlier, and we extract from our simulation calculations the corresponding value for each current component mentioned in these last two equations. The values for the Auger and SRH currents in the absorber are determined by switching "on" and "off" each recombination mechanism separately in our device model. The fitting result is presented in the following section.

8.3.3 Fitting Result

The fitting result gives a Cd alloy profile in the top P+ layer x(III)=0.300-0.414. Figure 8.19 shows the resulting Cd alloy profile in the device and the corresponding equilibrium band diagram at room temperature. Table 8.1 summarizes the fitting parameters for each temperature.

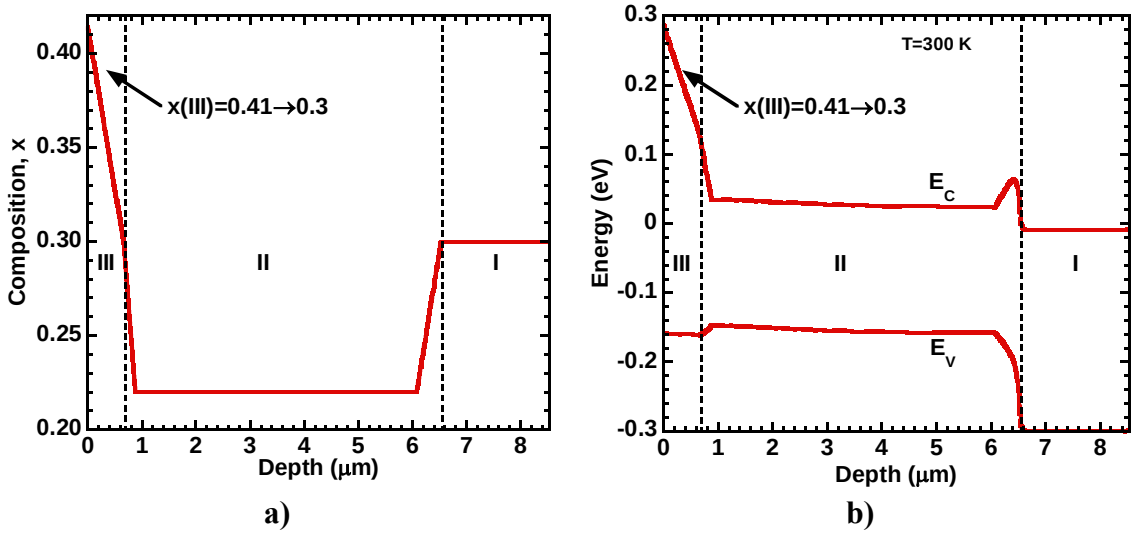

a) b)

Figure 8.19: a) Fitted Cd alloy profile and b) corresponding zero bias energy band diagram at T=300 K.

T (K)	x(III)	$\|F_1F_2\|$	$\tau_{n0}=\tau_{p0}$ (s)	J_{max} (A/cm^2)		J_{min} (A/cm^2)	
				Exp.	*Sim.*	*Exp.*	*Sim.*
120	Linear grading: 0.41→0.3	0.29	2.8×10^{-7}	0.24	0.24	0.22	0.21
130		0.28	3.3×10^{-7}	0.76	0.75	0.52	0.51
150		0.26	3.7×10^{-7}	2.60	2.51	1.42	1.49
200		0.25	3.8×10^{-7}	4.78	4.85	2.49	2.41
270		0.21	3.5×10^{-7}	6.19	6.12	3.19	3.21
300		0.20	3.4×10^{-7}	10.96	10.83	5.54	5.52

Table 8.1: Fitting parameters. R^2>0.99 for the fittings of both J_{max} and J_{min}.

Both the assumption made about x(III) and its fitting value are consistent with experimental SIMS data shown in Figure 7.23. The parameter x(III) is mainly a factor for T>270 K. So the main two fitting parameters are $|F_1F_2|$ and τ_{SRH}. Given the assumptions made in this fitting, also because we only have two main fitting parameters, and because we consider their temperature-dependence, we are confident that we obtained a unique solution. R^2 values for the fitting of J_{max} and the one of J_{min} support this as they are both higher than 0.99.

In addition, the different values found for $|F_1F_2|$ in the device absorber are within the range of reported values for Auger in HgCdTe (0.1-0.3). It is also expected to vary

with temperature as it is related to the band structure of HgCdTe. However, there is not a clear agreement on its temperature-dependence. Therefore, we cannot really comment on the fact that it goes down from ~0.3 at 120 K to ~0.2 at 300 K according to our fitting result.

The fitting parameter τ_{n0} (τ_{p0}) is equal to the inverse product of trap concentration, capture cross-section and thermal velocity v_{th} (see Equations (54) and (55)). The trap concentration and capture cross-section can be considered constant with temperature. Therefore, τ_{n0} (τ_{p0}) is expected vary as "$1/v_{th}$" with temperature. Figure 8.20 shows that the fitting parameter τ_{n0} (τ_{p0}) indeed varies as "$1/v_{th}$", i.e. as $T^{-0.5}$, for T>150 K. For T<150 K, it deviates slightly from the "$1/v_{th}$" line. This could indicate tunneling processes in the devices such as trap-assisted tunneling (TAT). Tunneling processes are expected to appear at low temperatures in LWIR HgCdTe devices. Hurkx models TAT by multiplying the capture cross-section with a tunneling factor, which can explain the deviation of the fitted τ_{n0} (τ_{p0}) for T<150 K.

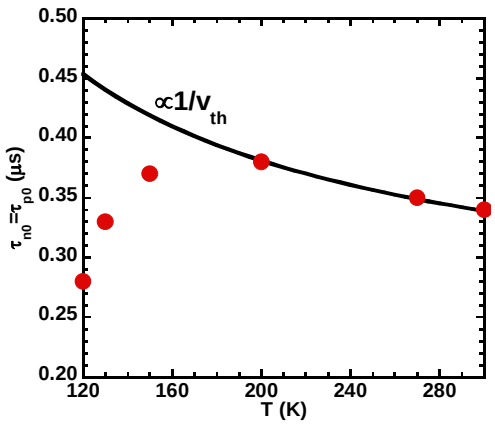

Figure 8.20: Fitting parameter τ_{n0} (τ_{p0}) versus temperature.

Figure 8.21 shows the calculated reverse bias I-V characteristics after fitting for each temperature. As mentioned earlier, we do not consider any series resistance here. The calculated dark current saturates after Auger suppression for T>200 K which is also observed in the experimental data. However, the calculated dark current also saturates after Auger suppression as the reverse bias is increased for T<200 K, whereas it increases in the experimental data. This is because we do not

consider tunneling processes in our device model. However, since the experimental values for J_{min} are taken at low reverse bias values for T<150 K (Figure 8.15), tunneling processes are not the main factor in limiting J_{min}.

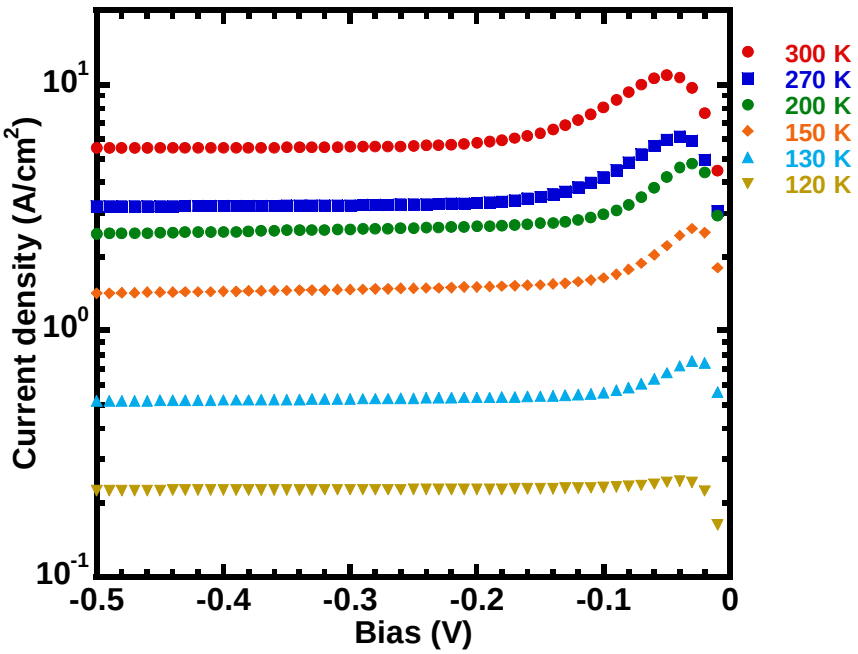

Figure 8.21: Calculated I-V characteristics after fitting for each temperature.

8.3.4 Analysis of J_{max} and J_{min}

Figure 8.22 shows the calculated magnitude of J_{max} after fitting, along with the different magnitudes of the leakage current components. According to our fitting result, the maximum current *before Auger suppression*, J_{max}, is limited by a SRH current in the absorber at T=120 K. This SRH current obtained in our model may be associated in the experimental device with a background trap concentration introduced during growth and/or processing. This SRH current has a weak dependence with temperature. It can also be related with threading dislocations in the device as we have described previously causing SRH recombination and/or trap-assisted tunneling, especially at lower temperatures as confirmed by a decreasing fitted τ_{n0} (τ_{p0}) as the temperature is decreased. Determining the real causes and origins of this SRH current would require more

information about the devices than we currently have. Therefore, we will leave this analysis for future work. We simply point out that, according to our model, the level of SRH is relatively high in these devices in the whole temperature range and that SRH recombination is the limiting mechanism for J_{max} up to ~130-140 K.

At T=120 K, both Auger-1 and Auger-7 currents in the absorber are very low compared to J_{SRH} because the intrinsic carrier concentration in the absorber is still relatively low. However, both currents rapidly increase as the temperature is increased. The Auger-1 current in the absorber limits J_{max} above ~130-140 K.

Finally, the hole diffusion current in the bottom N+ layer stays relatively weak at all temperatures. The electron diffusion current in the top P+ layer has some influence on J_{max} above 270 K.

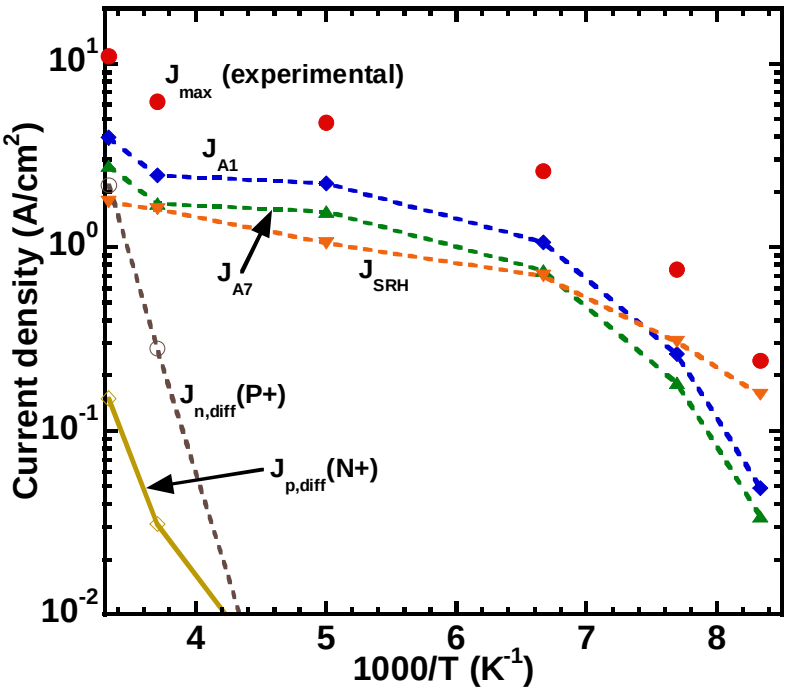

Figure 8.22: Experimental values for J_{max} versus temperature. Also shown are the the calculated Auger-1 current in the absorber J_{A1} (filled diamond), Auger-7 current in the absorber J_{A7} (filled upper triangle), SRH current in the absorber J_{SRH} (filled lower triangle), electron diffusion current in the top P+ layer $J_{n,diff}$(P+) (empty circle), and hole diffusion current in the bottom N+ layer $J_{p,diff}$(N+) (empty triangle).

Figure 8.23 shows the calculated magnitude of J_{min} after fitting, along with the different magnitudes of the leakage current components. According to our fitting result, the maximum current *after Auger suppression* (and before tunneling processes), J_{min}, is limited by a SRH current in the absorber between 120 K and room temperature. This confirms what we observed in the analysis of J_{max}, which is that there is a high concentration of traps/dislocations. This is expected in LWIR HgCdTe and can be reduced as the HgCdTe growth and processing technology develops.

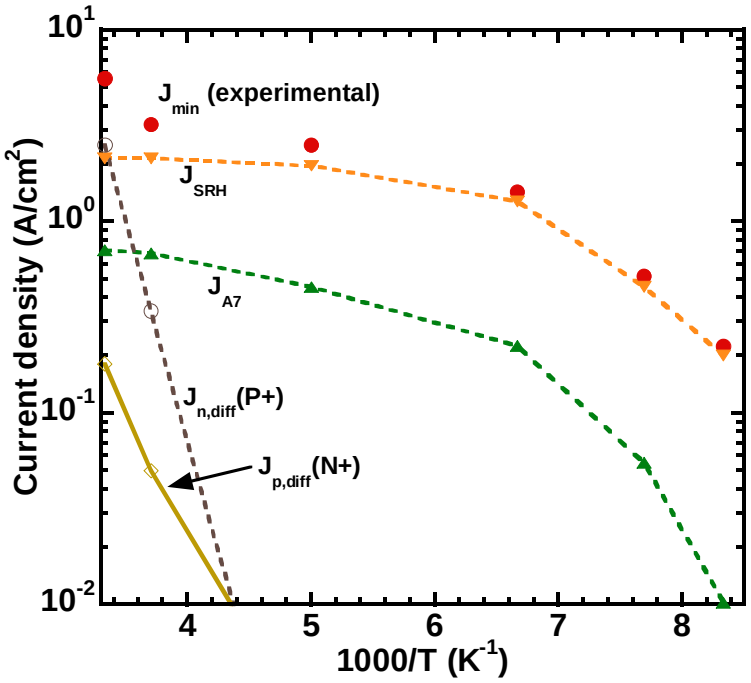

Figure 8.23: Experimental values for J_{min} versus temperature. Also shown are the Auger-7 current in the absorber J_{A7} (filled upper triangle), SRH current in the absorber J_{SRH} (filled lower triangle), electron diffusion current in the top P+ layer $J_{n,diff}$(P+) (empty circle), and hole diffusion current in the bottom N+ layer $J_{p,diff}$(N+) (empty triangle).

The Auger-1 current J_{A1}, which was found to limit J_{max} (Figure 8.22), *is fully suppressed* as the reverse bias is increased and is therefore not shown in Figure 8.23. The Auger-7 current in the absorber J_{A7} increases as the temperature is increased. Although it is not found to limit J_{min}, it shows that the Auger-7 current is only partially suppressed in the device. The "residual" Auger-7 current arises from the extrinsic p-type doping level in the absorber which ranges from 10^{15} cm^{-3} to 10^{16} cm^{-3} (Figure 8.12). The amount of

Auger-7 suppression is ~70 % according to our results. The hole diffusion current in the bottom N+ layer stays relatively weak at all temperatures, as observed when analyzing J_{max}. The electron diffusion current in the top P+ layer has some influence on J_{min} above 270 K.

This analysis gives us significant insight on the limiting leakage current mechanisms in experimental LWIR HOT devices, both *before* and *after* Auger suppression. To complete this analysis, we study the series resistance effect observed in these devices in the next section.

8.3.5 Effect of the Series Resistance

So far, the effect of the series resistance observed in the HOT experimental device data (Figure 8.5 and Figure 8.6) was not considered. The onset voltage for Auger supression is very important since it determines the optimal bias of operation of these detectors. Ideally, this onset voltage should be *as close to zero bias as possible* in order to reduce possible noise sources such as 1/f noise which has been shown to limit the performances of these Auger-suppressed detectors [52]. The position of the onset voltage in our devices is essentially limited by the *series resistance*. Figure 8.24 shows a schematic of the HOT device along with the series resistance. For a given temperature and a given bias applied, the actual voltage across the photodiode depends on the value of the series resistance and the ideal V=f(I) function calculated using our device model. Part of the bias applied results in a potential drop across the series resistance.

The circuit shown in Figure 8.24 is implemented using a MATLAB program and the calculated ideal current-voltage characteristics for the P+/π/N+ device at each temperature. Figure 8.25 shows the calculated I-V characteristics at T=300 K for several values of the series resistance ranging from the ideal zero series resistance to 100 Ohms. The series resistance *only affects the onset voltage and not the values of* J_{min} *and* J_{max}. The onset voltage ranges from ~0.05 V reverse bias for the ideal case to ~0.6 V reverse bias for a series resistance of 100 Ohms.

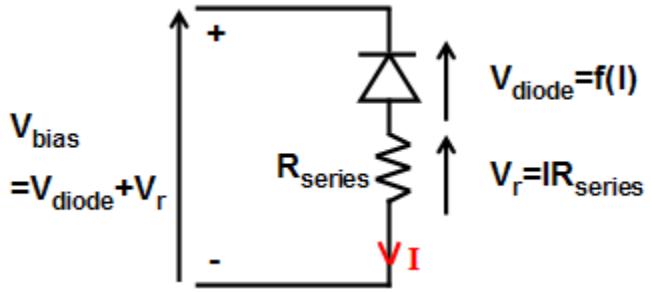

Figure 8.24: Schematic of the HOT photodiode and the series resistance.

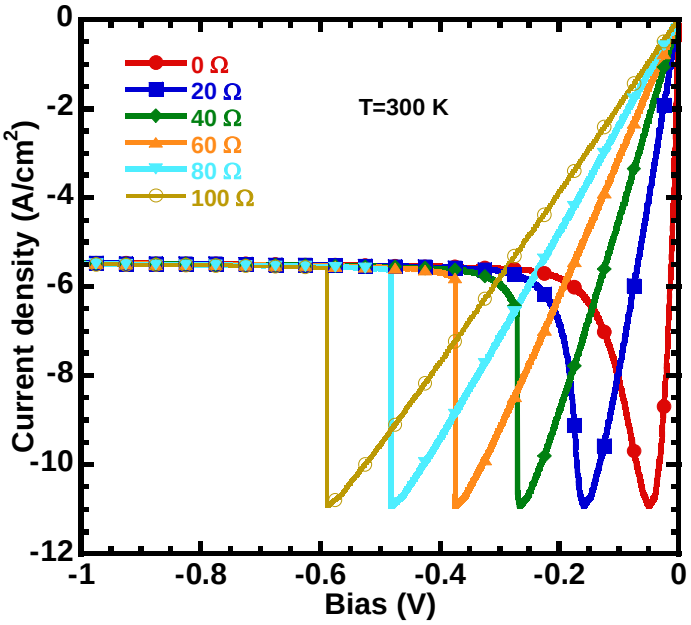

Figure 8.25: Calculated reverse bias dark I-V characteristics at T=300 K for several values of the series resistances in the device.

A series resistance of 89 Ohms is found to fit the I-V data for HOT #42 at room temperature (Figure 8.26a). The calculated voltage across the photodiode V_{diode} and the series resistance V_r is shown in Figure 8.26b as a function of the applied bias V_{bias}. For V_{bias}<500 mV, most of the potential drop occurs across the series resistance.

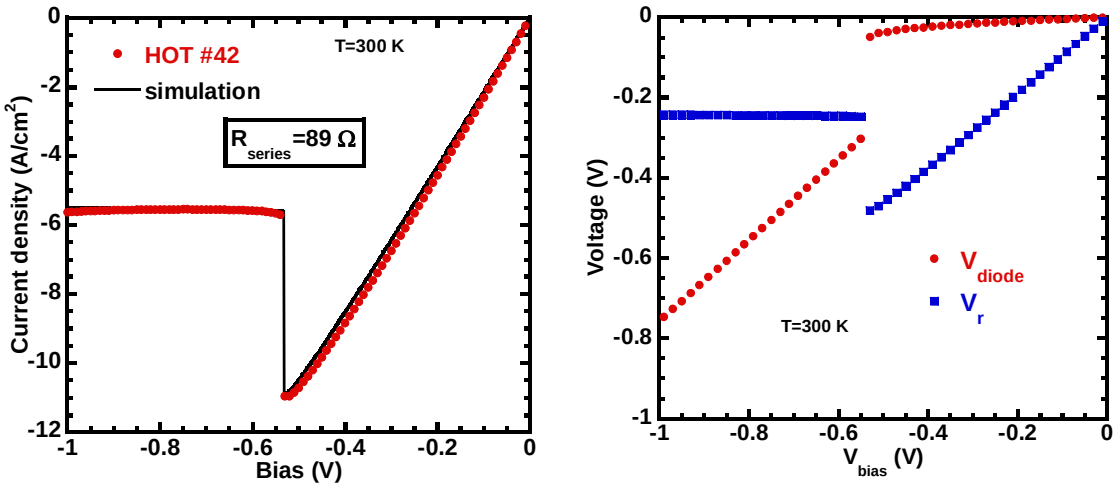

a) b)

Figure 8.26: a) Reverse-bias dark I-V measured for HOT device #42 at room temperature along with the simulated fitting curve (including the series resistance). b) Calculated voltage across the diode and the series resistance at room temperature as a function of the applied bias.

Figure 8.27 shows the fitting result at different temperatures. Table 8.2 shows the extracted values of the series resistance in the device at the different temperatures. The series resistance increases as the temperature is decreased.

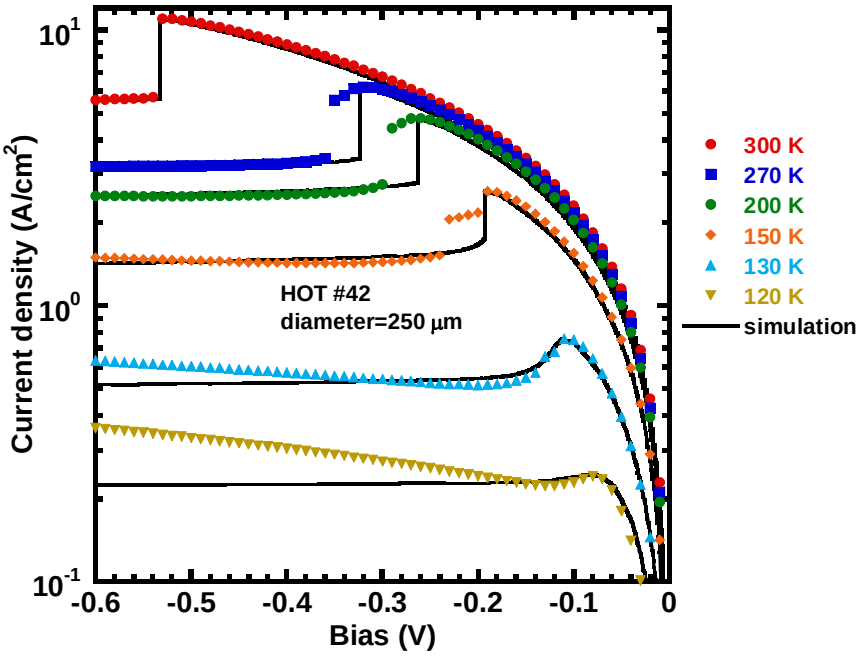

Figure 8.27: Reverse bias dark I-V measured between 120 K and 300 K for HOT device #42 along with the simulated fitting curve (solid line).

T (K)	R_{series} (Ω)
120	334
130	216
150	125
200	98
270	92
300	89

Table 8.2: Calculated values of the series resistance in the device at different temperatures.

One possible contribution to the series resistance in the device comes from the device geometry. As we can see in Figure 8.28, the P- and N- contacts are separated by a distance L in our HOT *planar* structure. Therefore, a series resistance is induced by the electron transport in the absorber ν layer and the bottom N+ layer. This can be seen as two series resistances in parallel. Most of the electron transport will likely occur in the bottom N+ layer which has a lower resistivity than the low n-type doped absorber layer.

The resistivity in these two layers is shown in Table 8.3 at different temperatures between 120 K and 300 K. We see that, indeed, the resistivity in the bottom N+ layer is lower than the one of the absorber layer. The resistivity of the bottom N+ layer increases as the temperature is increased because of a decreasing electron mobility, therefore acting as a metal. The resistivity of the absorber layer decreases as the temperature is increased due to the increasing intrinsic carrier concentration, and becomes comparable to the one of the bottom N+ layer at room temperature.

The calculated horizontal resistance for these two layers as well as the resulting total series resistance is shown in Table 8.3. In Case I, we use our current device geometry (diameter of 250 μm and the actual thickness of the layers) and a distance L between the P- and N-contact giving a total series resistance matching the one extracted from the experimental data at room temperature: 89 Ohms (L~768 μm). The total series resistance is expected to decrease as the temperature is decreased, which is the opposite than observed experimentally (Table 8.2). Therefore, although this series resistance certainly has an influence on the experimentally measured series resistance, it is not the only series resistance in the device.

The vertical HgCdTe layers and junction series resistances have been found to be much smaller than the horizontal one we just considered, hence it is not important in this case. Consequently, the P- and/or N- contact resistances may be the main causes. In this case, the Gold/P-HgCdTe contact resistance is expected to be higher than the Indium/N-HgCdTe one. This is especially true since the p-type doping level in the top P+ layer is not so high (~$2x10^{16}$ cm^{-3}) and that the Cd alloy fraction at the surface may be higher than designed according to our fitting result (~0.414 compared to 0.3). This could produce a gold contact resistance that decreases as the temperature is increased, following the experimental observation. Additional work is required to verify this claim. However, this could support the P-type contact issues reported to explain the relatively low quantum efficiency measured at -0.1 V and 7 μm at 100 K (~54 %) [93].

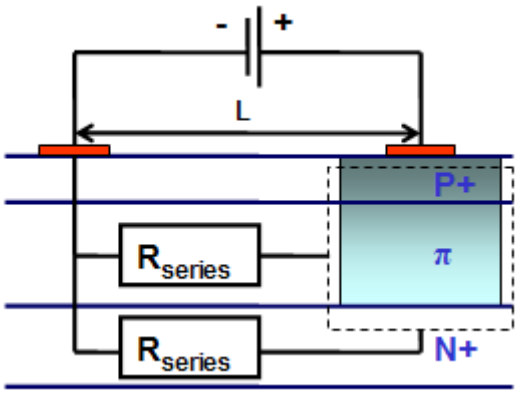

Figure 8.28: Schematic of the device geometry and the series resistance.

In the design of future focal plane arrays (FPA) based on these HgCdTe Auger-suppressed photodiodes, the series resistance observed will have to be taken into account. The P-contact resistance that we may have observed in our devices can be decreased to nearly zero by increasing the p-type doping in the P+ layer. As we mentioned earlier, gold is usually an ohmic contact to P-HgCdTe and we believe that this can be corrected easily in future HOT designs.

However, the horizontal series resistance also needs to be considered. Indeed, standard FPAs usually have common N-contacts located at the periphery of the array. This leads to different horizontal series resistance values depending on the pixel position in the array. This is usually not a problem in standard cooled HgCdTe FPAs because the

low dark and photocurrent levels suppress the effect of this horizontal series resistance. However, it has to be considered for HOT devices. In Case II, we use a typical HgCdTe 320x256 FPA device geometry (40 μm pixel and layer thickness of our actual devices) with a P- to N-contact distance L of 300 μm which is about the maximum distance for a pixel located at the center of the array. Table 8.3 shows what total series resistance values can be expected at different temperatures in this realistic case.

T (K)	ρ(ν) Ω-cm	ρ(N+) Ω-cm	Case I (Ω)			Case II (Ω)		
			R(ν)	*R(N+)*	R_{tot}	*R(ν)*	*R(N+)*	R_{tot}
120	$1.1x10^{-1}$	$2.6x10^{-3}$	662	40.7	38.3	1616	99.3	93.6
130	$1.2x10^{-1}$	$3.0x10^{-3}$	710	46.2	43.3	1732	113	106
150	$1.1x10^{-1}$	$3.8x10^{-3}$	676	57.8	53.3	1652	141	130
200	$6.9x10^{-2}$	$5.9x10^{-3}$	407	90.6	74.1	993	221	181
270	$3.8x10^{-2}$	$9.4x10^{-3}$	223	145	87.9	545	354	215
300	$3.1x10^{-2}$	$1.1x10^{-2}$	185	171	89.0	453	418	217

Table 8.3: Resistivity and resistance values for the absorber layer (Region II, ν) and the bottom N+ layer (Region I) at different temperatures and for different cases.

In order to reduce the effect of this horizontal series resistance in HOT FPAs, the doping in the bottom N+ layer or its thickness can be increased. In addition, as HgCdTe HOT technology improves, lower leakage current levels will be achieved which will reduce the effect of the series resistance. As determined previously, HOT LWIR devices have the potential to achieve BLIP at T=120 K (40 K higher than standard technology). At this temperature, such a value for the total resistance R_{tot} in the FPA case (Case II in Table 8.3) would have no effect on the onset voltage of the experimental HOT LWIR devices fabricated in this work.

8.3.6 Performance Improvement

Finally, the saturation current in our *experimental* device (J_{min}) is compared to the one in a standard HgCdTe DLPH photodiode simulated using our device model. We also

compare J_{min} to the dark current in a simulated *ideal* HOT photodiode with the same fixed cutoff wavelength than the experimental device (~10.4 μm at 100 K). We plot the dark current at 200 mV reverse bias versus T using our numerical model for ideal HOT and DLPH photodiodes (x(abs)=0.22), characterized by a low n-type doping in the absorber, N_D(absorber)=1x10^{15} cm^{-3}, and a much longer τ_{n0}=τ_{n0}=5 μs that what we observed experimentally.

As seen in Figure 8.29, the fabricated HOT device gives a lower saturation current J_{min} than for the ideal DLPH at all temperatures. Above ~200 K, both ideal and experimental HOT devices have comparable dark current. Below 200 K, the experimental HOT device has a much larger saturation current than the ideal HOT device which shows the room for improvement that can be achieved by optimizing the growth and fabrication process. Improvements are especially needed in terms of *lower doping levels in the absorber layer* and *less traps/dislocations causing SRH recombination*.

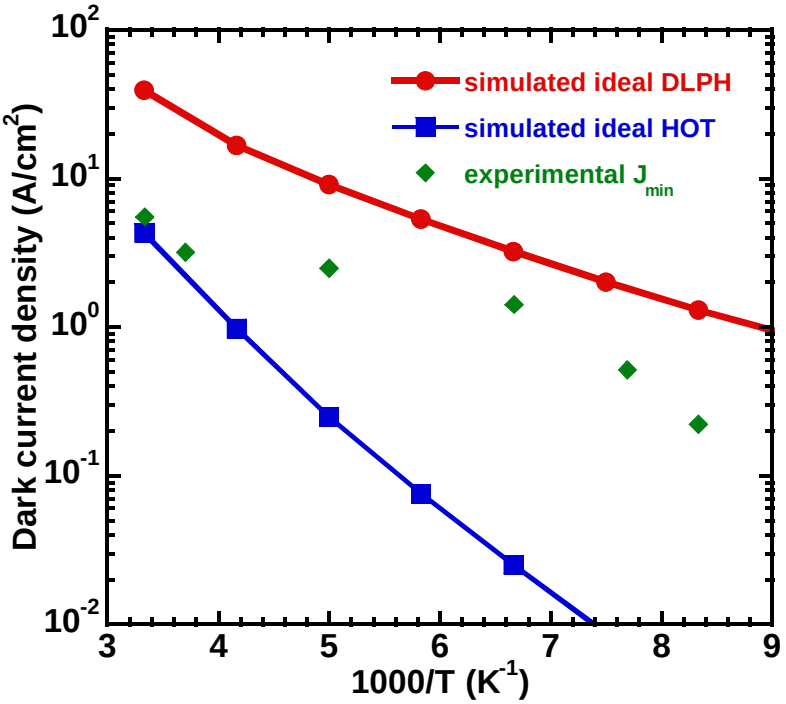

Figure 8.29: Calculated dark current density at 200 mV reverse bias for an ideal DLPH and HOT devices (with x(abs)=0.22) and experimental J_{min} versus temperature.

8.4 Future Design Considerations

As a summary, we have presented in this chapter a temperature-dependent electrical and optical characterization of fabricated HgCdTe Auger-suppressed photodiodes with response in LWIR (λ_c~10.4 μm at 100 K). A clear NDR is observed with a decrease of the maximum photodiode leakage current of ~8 % at 120 K up to ~50 % at room temperature. This NDR is attributed to strong Auger suppression in the device occurring as the reverse bias is increased. A detectivity D^* in the low-10^9 cm.$Hz^{0.5}$/W for a 500 K black-body and FOV=90° is measured at 1000 Hz and T=120 K for a selected HOT device under zero bias. D^* is measured in the mid-10^7 cm.$Hz^{0.5}$/W at 300 K. Excess 1/f noise – but lower than previously reported – is observed, which increases as the temperature and the reverse bias are increased, hence hiding the Auger reduction observed in the experimental I-V.

The experimental HOT devices are simulated using our numerical model. Current-voltage experimental data for HOT #42 is fitted between 120 K and 300 K. It is found that the Cd alloy profile in the top P+ layer may be higher than designed (linear grading from ~0.414 at the surface down to 0.3 at the bottom of this layer) as a result from the low P(Hg) deep diffusion anneal. The I-V analysis performed led to the following findings summarized in Table 8.4.

	J_{max} (before Auger suppression)	**J_{min} (after Auger suppression)**
J_{A1}	Limiting above ~130-140 K.	Completely suppressed, confirms that NDR is associated with *full* Auger-1 suppression.
J_{A7}	Follows J_{A1} contribution.	Contribution because of *partial* Auger-7 suppression (~70 %) due to the p-type doping profile.
J_{SRH}	Limiting up to ~130-140 K.	Limiting between 120 K and 300 K.
$J_{n,diff}$ (P+)	Important above 270 K due to high electron mobility and intrinsic carrier level.	
$J_{p,diff}$(N+)	Negligible due to small hole mobility.	
Series resistance	Determines onset voltage for a given temperature and photodiode leakage current level. Value decreases as the temperature increases. May be due to the P-contact resistance. Horizontal series resistance in the device contributes to total series resistance and needs to be taken into account.	

Table 8.4: Current-voltage analysis results.

From these findings, we can highlight some key points in order to reach the full potential of these HgCdTe HOT devices:

- the concentration of traps/dislocations which contribute to SRH recombination need to be reduced, especially for LWIR HgCdTe, in order to reduce the dark current level after Auger suppression, and possibly the 1/f noise observed in these devices; it is especially critical at lower temperatures where Auger processes are less dominant; this can be done by optimizing the MBE growth of HgCdTe and the substrate/HgCdTe interface, as well as the device processing steps.
- lower absorber layer doping levels, either in-situ n-type or p-type using the method we presented, need to be achieved in order to achieve full Auger-1 and Auger-7 suppression and to increase the depletion layer width forming in the absorber as the reverse bias is increased, i.e. to act more like a classical p-i-n photodiode.
- the doping in the top P+ layer need to be increased in order to eliminate the contribution from the electron diffusion current at high temperatures and reduce possible contact issues
- the onset voltage for Auger suppression needs to be as close to zero bias as possible in order to reduce 1/f noise; this can be done by eliminating the effect of the series resistance; the contact resistance can be reduced to nearly zero by a high enough p-type doping in the top P+ layer and gold electrodes; the horizontal series resistance from the P- to N-contact distance can be reduced by increasing the doping in the bottom N+ layer and its thickness; the series resistance effect is eliminated if the photodiode dark current is low enough.

In order to optimize the p-type doping profile in these HOT devices (i.e. achieve higher doping levels in the top P+ layer and lower doping levels in the absorber), we are proposing a novel double implantation process [93]. This process is based on the deep diffusion anneal step that we presented in the previous chapter combined with a second arsenic implant to achieve higher doping levels in the top P+ layer. Figure 8.30 shows initial and promising SIMS results obtained to illustrate the concept.

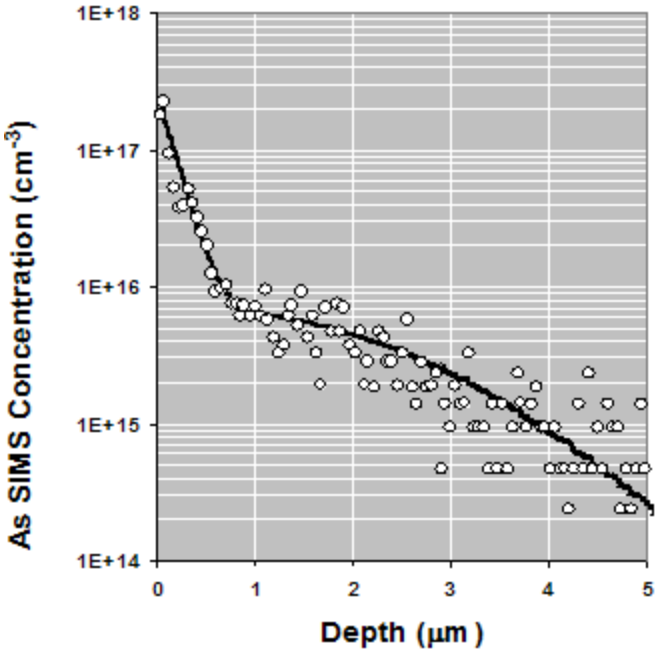

Figure 8.30: Arsenic SIMS profile after double implantation process.

Chapter 9
Summary

Non-equilibrium operation was studied in three-layer (P+/ν/N+ or P+/π/N+) HgCdTe infrared photodiodes, also referred as Auger-suppressed or HOT photodiodes. When properly designed, an increasing reverse bias results in a significant decrease of both minority and majority carrier concentration in the middle absorber layer. This means that Auger processes and the associated leakage current are greatly reduced in these HgCdTe devices.

Because the key feature of these devices is closely linked with the non-equilibrium operation, the carrier concentration profiles and the resulting recombination rates in the device which are found to be highly non-uniform and space-dependent, it is critical to solve the semiconductor equations in order to develop a better understanding of the operation of these devices. Therefore, previous analytical models developed to study these devices offer only a limited insight. In addition, standard analytical models used to study HgCdTe infrared photodiodes are not suited for these devices. Thus, we have developed a numerical device model that self-consistently solves the Poisson equation and the electron and hole continuity equations. This model is based on the TCAD tool Sentaurus by Synopsys. HgCdTe material and recombination parameters are included in the model and have been reviewed in this work. In the development of this device model, features specific to semiconductor HgCdTe were studied, such as the acceptor and donor ionization in HgCdTe. Nearly 100 % ionization can be assumed for arsenic (p-type) and indium (n-type) doping in HgCdTe our temperature range of interest (77 K to room temperature), for typical doping levels ranging from ~10^{15} cm^{-3} to ~10^{17} cm^{-3} and HgCdTe cutoff wavelength in the

MWIR and LWIR infrared windows. Carrier degeneracy and conduction band non-parabolicity is also taken into account in our HgCdTe device model. Simulation output calculations of electrical and optical characteristics of HgCdTe DLPH devices are comparable with published experimental data from different sources for both MWIR and LWIR.

Temperature-dependent performance of HOT and standard DLPH devices with response in MWIR and LWIR were compared using numerical simulations. We compared the calculated current-voltage characteristics, spectral response of the responsivity and detectivity D^*. The improvement in terms of increased operating temperature T_{BLIP} is also determined. It is found that the MWIR HOT device starts over-performing the corresponding MWIR DLPH device as the temperature is increase, i.e. as Auger processes become more and more important. The detectivity D^* for the HOT device at 300 K is about one order of magnitude higher than the one for the DLPH device. It is also found that BLIP at 180 K can be achieved for ideal MWIR HOT devices. This opens up the possibility of achieving TE-cooled MWIR HOT infrared devices with high sensitivity. For LWIR HOT devices, the improvement is maximized for T<150 K. This is because Auger processes are already high in LWIR HgCdTe at these temperatures, and become too high at higher temperatures. BLIP does not seem achievable at 180 K for LWIR HOT devices. However, ideal LWIR HOT devices can achieve BLIP at 120 K, i.e. at 40 K higher than standard LWIR DLPH devices. This represents also a significant advance in LWIR HgCdTe technology.

Then, we optimized an HgCdTe MWIR HOT photodiode operated at 200 K. The most critical parameters are mainly those of the absorber layer. Controlled lower absorber doping levels ($<1x10^{14}$ cm^{-3}) than what is currently achieved in HgCdTe is required to achieve the full potential of the MWIR HOT devices. Better crystal quality and better device processing control are also required to increase the SRH lifetime (>5-10 μs), even in LWIR HgCdTe. However, maximizing the improvements of HOT devices compared to standard DLPH devices by improved HgCdTe growth and device processing is only visible, and therefore only makes sense to pursue, for MWIR HOT devices operated at temperatures >150 K and LWIR HOT devices operated at temperatures ~80-150 K.

Finally, we presented a full temperature-dependent device characterization of fabricated HgCdTe Auger-suppressed photodiodes designed using our device model. High-quality optimized HgCdTe heterostructures were successfully grown by MBE. The device fabrication steps were presented in details. A novel processing technique to achieve low p-type doping in HgCdTe by fast arsenic diffusion was also presented and used in the fabrication of these HOT photodiodes. A clear NDR was observed with a decrease of the maximum photodiode leakage current of ~8 % at 120 K up to ~50 % at room temperature. This NDR is attributed to strong Auger suppression in the device occurring as the reverse bias is increased. This is the first report of Auger suppression in HOT devices with p-type absorber layer (P+/π/N+). The detectivity D^* for a 500 K black-body and FOV=90° was measured at different temperatures. The highest detectivity D^* value was measured at 120 K (low-10^9 cm.$Hz^{0.5}$/W) and is about one order of magnitude lower than the ideal BLIP D^*. This is the highest reported value of D^* for a HgCdTe IR device with LWIR response operated at 120 K. The measured D^* decreases as the temperature and the reverse bias are increased, due to an increase in detector dark current, but mostly due to the presence of 1/f noise.

The experimental HOT devices were also simulated using our numerical model. By fitting the temperature-dependent current-voltage experimental data for one selected device where clear NDR is observed, we confirmed that the NDR is due to Auger suppression. More specifically, NDR is attributed to full suppression of Auger-1 processes and partial suppression of Auger-7 processes. The percentage of Auger-7 suppression is ~70 %. After Auger suppression, the remaining leakage current is mostly limited by a high SRH recombination component in these devices. This component can be due to a high concentration of traps and dislocations in these HgCdTe HOT layers, especially the LWIR absorber which is more sensitive to the growth and processing. Part of the leakage current is also due to a "residual" Auger-7 current in the absorber due to the extrinsic p-type doping level which ranges from 10^{15} cm^{-3} to 10^{16} cm^{-3}. We also explained the series resistance observed in the experimental data. Its value solely affects the onset voltage for Auger suppression, and not the total dark current magnitude. The series resistance needs to be as small as possible, or its effect as reduced as possible, in order to have the onset voltage as close to zero bias as possible. This can be important in

reducing the 1/f noise observed in these devices. It is also important in designing future infrared FPAs with high uniformity based on HOT devices. Its value is not just due to the series resistance in the HgCdTe layers, but could also be due to the P-contact resistance, with a value that decreases with temperature, as observed in the extracted series resistance experimental values in the devices.

Future HOT device designs need to address simultaneously the different aspects pointed out in this work. In-situ indium doping by MBE is one way to pursue the goal of achieving lower controlled absorber doping levels. Another way is to develop and optimize the arsenic deep diffusion annealing process to achieve lower p-type doping levels. The proposed double implantation process may be a first step in this direction. Achieving longer SRH lifetimes will require a better control of the HgCdTe growth by MBE for example, as well as a better control of the device processing, especially the surface passivation. These two key points are both extrinsic and mainly dependent on the improvement of HgCdTe technology. The series resistance effect can also be suppressed when lower HOT dark currents are achieved, or by optimizing the HgCdTe metal contacts. It can also be done by decreasing the series resistance of the HgCdTe contact layers, such as the bottom N+ layer in our devices, with increased doping levels.

Appendix A
Monte Carlo Model

Here we describe the Monte Carlo model used to study electron transport in HgCdTe. In the Monte Carlo process, the electron is considered as a point particle whose scattering rates are given by the Fermi golden rules expression. We simulate the transport of one electron in a spherical non-parabolic Γ-valley conduction band. The Fortran source code was originally written to study electron transport in GaAs. The program was kindly made available for use by Dr. Jasprit Singh of the University of Michigan [98]. It was modified afterwards for HgCdTe.

We consider the following scattering mechanisms: ionized impurity scattering, alloy scattering, polar optical phonon scattering, acoustic phonon scattering and electron-hole scattering. Published scattering rates for HgCdTe are used and are presented below. Intervalley phonon scattering is the dominant scattering mechanism in most III-V semiconductors [99]. In contrast, the band structure suggests that in HgCdTe, electrons have a very small intervalley phonon scattering rate. This process has thus been neglected in this work. Piezoelectric scattering is found to affect the value of the low-field mobility by 0.2 % at 77 K [29]. At high electric fields, its effect is further reduced due to the enhancement energy of electrons. This scattering process is therefore not included in the calculations.

A.1 Analytical Band Model

The Monte Carlo model presented in this work uses an analytical approximation for the band structure involving one spherical non-parabolic Γ-valley for the conduction

band (CB). The non-parabolicity of the electron dispersion law is a consequence of the conduction band and valence band interaction in narrow band gap semiconductors. That effect has to be taken into account, especially for electrons, because their effective mass is small. As a consequence, they can reach high energy levels for which non-parabolicity is significant. A one-band model is sufficient because $Hg_{1-x}Cd_xTe$ has a very small band gap for the Γ-valley, and very high L and X valleys (1.5 and 2.5 eV respectively) [100].

A general form of the conduction band energy dispersion relation that holds without restriction on the relative magnitude of the energy band gap E_G and the spin-orbit splitting of the valence band Δ has been given by Kane [101]. It has been shown that this relationship may be simplified as an energy-wave vector relation that we use in this work:

$$\gamma(E) = E(1+\alpha E) = \frac{\hbar^2 k^2}{2m_e^*} \tag{10}$$

$$\alpha = \frac{1}{E_G}\left(1 - \frac{m_e^*}{m_0}\right)^2 \tag{10}$$

where E is the electron energy in the conduction band (eV), α the non-parabolicity parameter of the conduction band (eV^{-1}), ħ the reduced Planck constant (eV.s), k the wave vector (cm^{-1}), E_G the band gap of the material (eV), and m_e^* the effective mass of electrons at the bottom of the conduction band (m_0).

This leads to the formula:

$$E_{CB}(k) = \frac{1}{2\alpha}\left[-1 + \sqrt{1 + 2\alpha\frac{\hbar^2 k^2}{m_e^*}}\right] \tag{10}$$

This simplified E-k relation agrees within 3 % with the exact relation [101] for energies up to 0.1 eV. This simplified relation thus causes very little error and has been conveniently used in the present calculations for all values of the Cd alloy fraction x. The spin-orbit splitting of the valence band Δ is found to have only a small effect on mobility [29]. It is therefore put equal to zero in this work for the sake of simplicity. It may be mentioned that a similar effect of Δ on mobility was obtained also in the case of InSb [102].

A.2 Scattering Rates

The formulas of scattering rates and scattering angles are based on Fermi's golden rule, which is derived from the first-order time dependent perturbation theory in quantum mechanics. The scattering angle defines the new direction of the wave vector after scattering.

A.2.1 Ionized Impurity and Electron-Hole Scattering

The ionized impurity scattering rate calculated in this work is for scattering from singly ionized impurities, such as indium which is a donor in HgCdTe. The scattering is elastic, with the initial and final wavevector magnitudes the same. The scattering potential is a screened Coulombic potential, as per the Brooks-Herring theory [103]. The ionized impurity scattering rate (s^{-1}) for a non-parabolic band can be found in the review by Jacoboni and Reggiani [104]:

$$W_{imp}(k) = W_{par}(k) \times D \tag{103}$$

$$W_{par}(k) = 1.039 \times 10^{18} \frac{m_e^{*} N_I}{\varepsilon_s^{\,2} \beta^3} \times \frac{\sqrt{\eta}}{1+\eta} \ln\left|\frac{1+\eta}{\eta}\right| \tag{104}$$

$$D = (1+2\alpha E)\left[1 + \frac{4\alpha E \eta(1+3\alpha E+2\alpha E\eta)}{(1+2\alpha E)^2} - \frac{4\alpha E \eta(1+\eta)(1+2\alpha E+2\alpha E\eta)}{(1+2\alpha E)^2} \times \ln\left|\frac{1+\eta}{\eta}\right|\right] \tag{105}$$

$$\eta = \frac{\beta}{2k} \tag{106}$$

$$\beta = \sqrt{\frac{1.810 \times 10^{-6} N_I}{\varepsilon_s \left(kT/q\right)}} \tag{107}$$

where $W_{par}(k)$ is the ionized impurity scattering rate for a parabolic band (s^{-1}), m_e^{*} is the electron effective mass (m_0), N_I is the density of the ionized impurities (cm^{-3}), ε_s is the static dielectric constant of HgCdTe, β is the inverse of the Debye screening length (cm^{-1}), and k is the wavevector (cm^{-1}).

As the temperature is increased, we have seen that the intrinsic carrier concentration can become larger than the ionized donor concentration in HgCdTe. In these cases, the contribution of electron-hole scattering may become comparable to the one of ionized impurity scattering. Consequently, we include electron-hole scattering in our Monte Carlo calculations. Since $m_h^* >> m_e^*$ for HgCdTe, the electron-hole scattering rate can be approximated as the ionized impurity scattering rate by replacing the ionized impurity concentration N_I with the hole carrier concentration [105].

A.2.2 Polar Optical Phonon Scattering

At room temperature and low electric field strengths, polar optical phonon (POP) scattering (emission and absorption) dominates in the Γ-valley. This process causes a carrier energy variation corresponding to the phonon energy and an anisotropic change of the wave vector direction.

It must be remembered that the $Hg_{1-x}Cd_xTe$ crystal exhibits a "two-mode" behavior. Indeed, the optical phonon modes associated with both the parent components HgTe and CdTe exist. The intensity of both the modes is found to be nearly proportional to the concentration of their parent components [106]. The polar optical phonon scattering rate must therefore be weighted linearly for the two phonon modes, giving the following expression (s^{-1}) [104]:

$$W_{pop}(k) = \frac{q^2\sqrt{m_e^* m_0}\,\omega_0}{4\pi\sqrt{2}\hbar\varepsilon_0}\left(\frac{1}{\varepsilon_\infty}-\frac{1}{\varepsilon_s}\right)\frac{1+2\alpha E'}{\gamma^{1/2}(E)}F_0(E,E')\times\begin{cases} n(\omega_0) & \text{(absorption)} \\ n(\omega_0)+1 & \text{(emission)}\end{cases} \tag{108}$$

$$\omega_0 = (1-x)\omega_{HgTe} + x\omega_{CdTe} \tag{109}$$

$$E' = \begin{cases} E+\hbar\omega_0 & \text{for absorption} \\ E-\hbar\omega_0 & \text{for emission}\end{cases} \tag{110}$$

$$F_0(E,E') = C^{-1}\left(A\ln\left|\frac{\gamma^{1/2}(E)+\gamma^{1/2}(E')}{\gamma^{1/2}(E)-\gamma^{1/2}(E')}\right| + B\right) \tag{111}$$

$$A = \left[2(1+\alpha E)(1+\alpha E') + \alpha\{\gamma(E)+\gamma(E')\}\right]^2 \tag{112}$$

$$B = -2\alpha\gamma^{1/2}(E)\gamma^{1/2}(E')\times\left[4(1+\alpha E)(1+\alpha E')+\alpha\{\gamma(E)+\gamma(E')\}\right] \quad (113$$

$$C = 4(1+\alpha E)(1+\alpha E')(1+2\alpha E)(1+2\alpha E') \quad (114$$

$$n(\omega_0) = \frac{1}{\exp\left(\frac{\hbar\omega_0}{k_B T}\right)} \quad (115$$

where ε_s and ε_∞ are the static and high frequency permittivity correspondingly, ω_0 is the optical phonon frequency (rad.s^{-1}), ω_{HgTe} and ω_{CdTe} are the optical phonon frequency for the HgTe-mode and the CdTe-mode respectively, E' is the carrier energy after POP scattering (eV), and $n(\omega_0)$ is the optical phonon occupation number determined by the Bose-Einstein distribution at the lattice temperature T.

A.2.3 Acoustic Phonon Scattering

Acoustic phonon scattering is an almost elastic scattering process. In the case of acoustic phonons, the electronic energy perturbation is related to the strain in the crystal and is given by the deformation potential theory. Acoustic phonon scattering is expected to play a lesser role than ionized impurity scattering and polar optical phonon scattering for HgCdTe. It is usually the dominant phonon scattering at low temperatures and low fields, since the system does not have enough energy to excite optical phonons. The acoustic phonon scattering rate (s^{-1}) is given by [102]:

$$W_{ac}(k) = \frac{\left(2m_e^* m_0\right)^{3/2} k_B T U_{ac}^{\ 2}}{2\pi\rho s^2\hbar^4}\gamma^{1/2}(E)(1+2\alpha E)F_a(E) \quad (116$$

$$F_a(E) = \frac{(1+\alpha E)^2 + \frac{1}{3}(\alpha E)^2}{(1+2\alpha E)^2} \quad (117$$

where U_{ac} is the acoustic deformation potential (J), ρ is the mass density (kg.cm^{-3}), and s is the velocity of sound in HgCdTe (m/s).

A.2.4 Alloy Disorder Scattering

Due to the inherent disorder present in alloys, electrons and holes suffer scattering as they propagate through the material. We consider this scattering in a perfectly random HgCdTe alloy where the smallest physical size over which the crystal potential fluctuates randomly is the unit cell. For zinc-blende (such as HgCdTe) and diamond lattices, the volume of the unit cell $V_0=a_0^3/4$, where a_0 is the lattice constant. The alloy scattering rate is then given by [105]:

$$W_{all}(k) = 1.5\times10^{13}\left(m_e^*\right)^{3/2} U_{all}^{\ 2} a_0^{\ 3} x(1-x)\gamma^{1/2}(E)(1+2\alpha E) \qquad (118$$

where U_{all} is the alloy potential (eV) and a_0 is the lattice constant (Å). The electron energy in the conduction band $\gamma(E)$ must be given in eV in this expression.

The choice of the alloy potential was the subject of several studies. Makovski et al. [107] utilized an alloy potential given by the difference in the band gaps of the binary constituents whereas Harrison et al. [108] utilized the difference in electron affinity between the binary constituents. Ferry et al. [109] suggested another form for the alloy potential based on the electro-negativity theory of Phillips [110]. Kinch et al. [111] defined U_{all} as the difference between the s atomic term values of the Hg and Cd atoms. In this work, we consider U_{all} to be equal to 1.5 eV [111].

A.3 HgCdTe Monte Carlo Parameters

Some of the HgCdTe material parameters needed for this Monte Carlo model, such as energy band gap E_G and electron effective mass m_e^*, have been defined previously. Other important parameters are defined in Table A.1 below.

Description	Notation	Value/Expression	Unit
Static dielectric constant [1]	ε_s	$20.5 - 15.5x + 5.7x^2$	-
High frequency dielectric constant [1]	ε_∞	$15.2 - 13.7x + 6.4x^2$	-
Longitudinal optical phonon energies [106]*:* HgTe-mode CdTe-mode	 ω_{HgTe} ω_{CdTe}	 $(17.36 - 1.24x)\times 10^{-3}$ $(18.60 + 3.72x)\times 10^{-3}$	 eV eV
Acoustic deformation potential [112]	U_{ac}	9	eV
Mass density [106]	ρ	$8.05 - 2.30x$	$gm.cm^{-3}$
Elastic constant [106]*:* longitudinal transverse	 c_l c_t	 $(6.422 - 0.102x)\times 10^{11}$ $(1.594 - 0.056x)\times 10^{11}$	 $dyne.cm^{-2}$ $dyne.cm^{-2}$
Velocity of sound [106]*:* longitudinal transverse average	 s_l s_t s	 $(c_l/\rho)^{1/2}$ $(c_t/\rho)^{1/2}$ $(s_l^{\,2}/3 + 2s_t^{\,2}/3)^{1/2}$	 $cm.s^{-1}$ $cm.s^{-1}$ $cm.s^{-1}$
Alloy potential [111]	U_{all}	1.5	eV
Lattice constant [113]	a_0	$6.4614 + 0.0084x + 0.0168x^2 - 0.0057x^3$	Å

Table A.1: Material parameters for HgCdTe.

Appendix B

Electrical Characteristics of PEDOT:PSS Organic Contacts to HgCdTe

Electrical contacts are of high importance for HgCdTe infrared detectors, where structural and chemical defects at the metallic/HgCdTe interfaces have been shown to degrade detector performance and reduce operability in detector arrays [114], [115], [116]. The soft properties of HgCdTe and pronounced chemical interactions with metals make HgCdTe devices much more sensitive to electrical contact materials and fabrication processes. The deposition of metallic contacts such as In or Au on HgCdTe-based IR detectors creates additional stress immediately below the contacts. This stress has been observed to getter threading dislocations, which, in turn, creates misfit dislocation segments just below the detector surface and parallel to the surface, in the active area under and close to the contacts. The dangling bonds across these dislocations enhance random generation-recombination processes, thereby reducing quantum efficiencies and detectivities. Because of their location, these misfit dislocations act as efficient trapping and recombination centers and strongly degrade detector performance, especially in the long wavelength and very long wavelength infrared regions. A decrease in zero-bias impedance (R_0A) and increase in dark current are primary results of these defects.

We propose a new contact material to greatly reduce or eliminate such dislocations associated with HgCdTe electrical contacts through the introduction of organic contact materials [117]. The compliant nature of organic contact materials is expected to reduce or eliminate stress induced defects in HgCdTe electrical contacts. PEDOT:PSS is a conducting polymer that is commonly used as an electrical contact for organic electronics and optoelectronics [118]. In this study, the electrical characteristics

of the organic polymer (3,4-polyethylenedioxythiophene) poly(styrenesulfonate) (PEDOT:PSS) contacts are studied on n-type and p-type HgCdTe.

B.1 Experiment

Four HgCdTe epilayers are used for this study. Three HgCdTe samples under study were grown by molecular beam epitaxy (MBE) with HgCdTe alloy composition x=0.21 and N_D=1x10^{15} cm^{-3} for two of the samples, and x=0.272 and N_D=3x10^{15} cm^{-3} for the third sample. One sample (x=0.21) was annealed at 235 °C for 24 hours to remove Hg vacancies and to obtain n-type HgCdTe for study. To examine contacts on p-type material, the other n-type MBE sample (x=0.21) was blanket implanted with arsenic, then activated by annealing the layer for 10 minutes at 425 °C, and then annealed at 235 °C for 24 hrs. Lastly, a n-type doped sample was grown by liquid phase epitaxy (LPE) with x=0.243 and N_D=1x10^{15} cm^{-3}.

A Br:methanol solution is used to remove the CdTe cap and native oxide layers. A PEDOT:PSS layer with a thickness ~120-180 nm is then deposited on n-type and p-type HgCdTe epilayers by spin coating at 3000 rpm for 30 seconds followed by a dry baking at 80 °C for 1 min. Metallic electrodes with a diameter ~500 μm were evaporated on the polymer through a shadow mask. The metallic electrodes consisted of a 20 nm thick adhesion layer of titanium and a 100 nm layer of gold. The metal electrodes serve as a mask used to pattern the PEDOT:PSS contacts by dipping the sample in DI water and to obtain the contact structure as shown in Figure B.9.1.

Temperature dependent current-voltage (I-V) measurements were performed using an HP4145 system and by properly wire-bonding the sample to a chip carrier placed in a cryostat. Since indium gives ohmic behavior when contacted to HgCdTe, the current-voltage characteristic of Indium/HgCdTe contacts on the n-type HgCdTe sample is also measured for comparison.

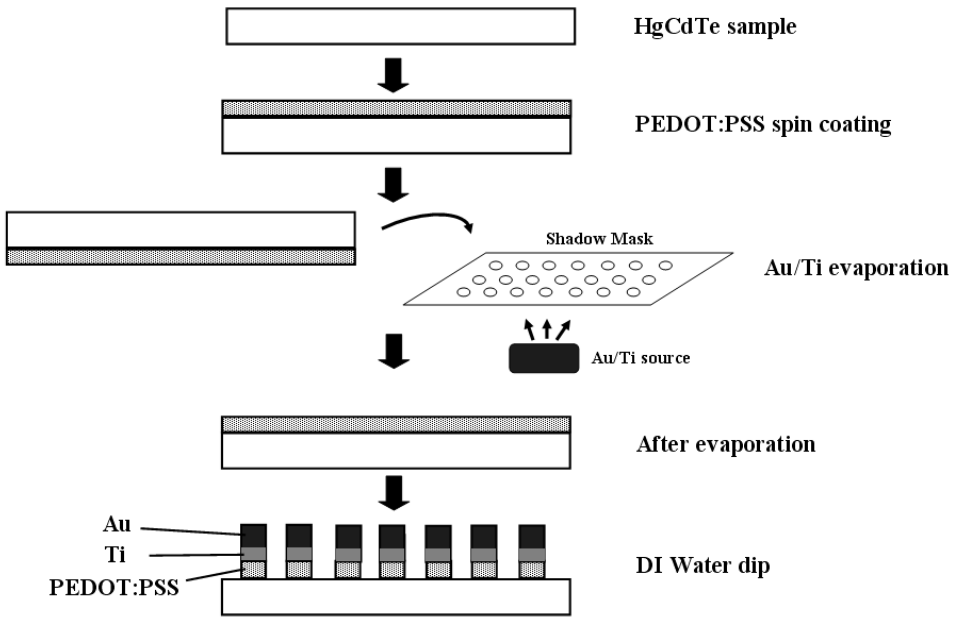

Figure B.9.1: Schematic depicting the process flow.

B.2 Results and Discussion

The current-voltage characteristic for PEDOT:PSS electrical contacts on n-type HgCdTe show a weak rectifying behavior, as shown in Figure B.9.2. The temperature dependence of the I-V characteristic shows an increase in resistance with decreasing temperature. Indium contacts on the same HgCdTe sample show linear ohmic I-V characteristic with similar resistance than the PEDOT:PSS contacts, as compared in Figure B.9.3. The current-voltage characteristic for the second n-type HgCdTe sample grown by MBE and the n-type LPE sample show essentially the same I-V behavior, with somewhat improved ohmic behavior.

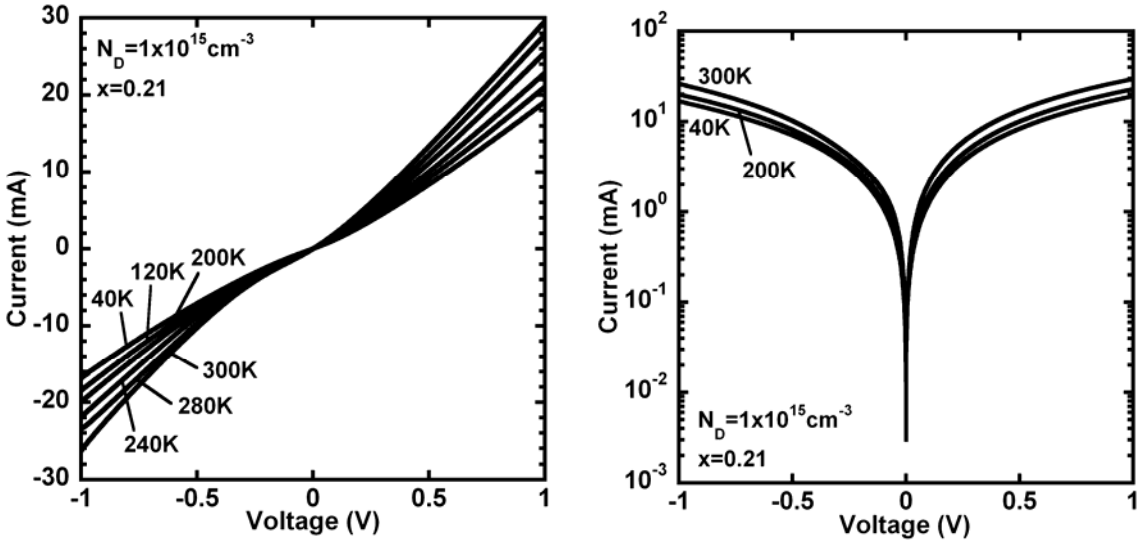

Figure B.9.2: Current-voltage characteristics of PEDOT:PSS electrical contacts to n-HgCdTe (x=0.21, N_D=1x10^{15}cm^{-3}) at varying temperature plotted on a) linear and b) logarithmic scale.

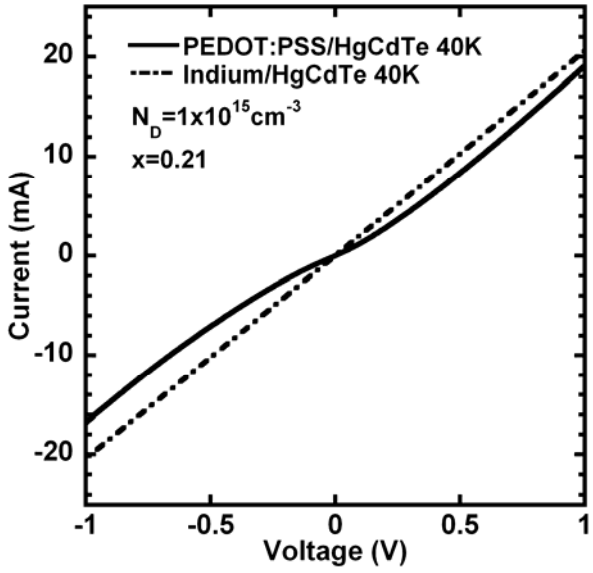

Figure B.9.3: Comparison of current-voltage characteristics for PEDOT:PSS/n-HgCdTe and In/HgCdTe contacts on a HgCdTe sample with x=0.21 at T=40K.

The current-voltage characteristic for PEDOT:PSS contacts to p-type HgCdTe material obtained by MBE growth and ion implantation show nearly linear behavior, as

shown in. The temperature dependence shows a similar increase in resistance with decreasing temperature to the contacts on n-type HgCdTe.

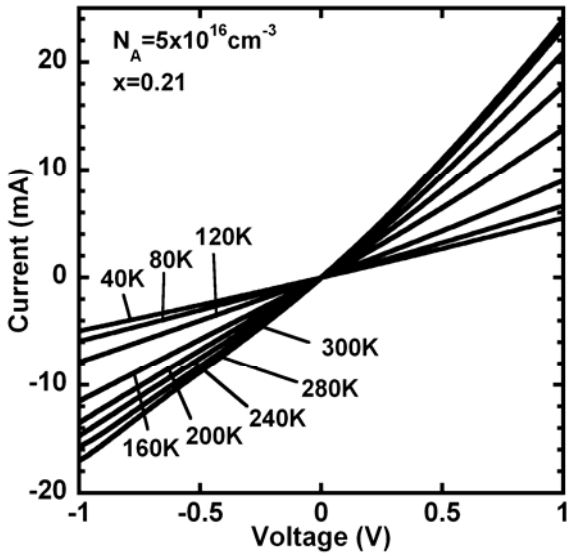

Figure B.9.4: Current-voltage characteristics of PEDOT:PSS electrical contacts to p-HgCdTe (x=0.21, N_A=5x10^{16}cm^{-3}) at varying temperature.

Electron transport in PEDOT:PSS can be described by the Motts Variable-Range Hopping model. The conductivity of PEDOT:PSS is thermally activated so it increases with increasing temperature, and also depends on the particle size in the polymer film. Smaller particles induce more energy barriers and a higher resistivity. The workfunction for PEDOT:PSS is approximately 5.2 eV.

The temperature dependence of I-V characteristic for the PEDOT:PSS/HgCdTe structures all show an increase in resistivity for decreasing temperature. The observed temperature dependence may be due to several factors, including the resistivity of HgCdTe material, resistivity of the PEDOT:PSS, and the interface between HgCdTe and PEDOT:PSS. The resistivity of PEDOT:PSS decreases with temperature due to the thermally activated hopping mechanism defining transport in the material. The temperature dependent resistivity of the material, based on data from the manufacturer, ranges from approximately 200 Ω-cm at T=40 K to approximately 2 Ω-cm at T=300 K. Resistivity measurements at room temperature using the process in our laboratory are consistent with this data. For a 180 nm thick PEDOT:PSS layer as obtained in our

process, the product of resistivity and thickness is a maximum of $3.6x10^{-3}$ Ω-cm^2 at T=40 K, providing an approximate guideline for the minimum detector impedance (RA product) that may be accommodated without significant problems influence from the contact material. The temperature dependence of the HgCdTe resistivity is influenced by both a decrease in carrier density and increase in carrier mobility at decreasing temperature. The net result is an increase in HgCdTe resistivity with decreasing temperature. The PEDOT:PSS/HgCdTe interface may also contribute to the resistance observed in the I-V characteristic. However, the temperature dependence of the I-V characteristic of PEDOT:PSS/n-HgCdTe closely follows the temperature dependence of the In/n-HgCdTe structures (Figure B.9.3), leading us to believe that the behavior is primarily due to the temperature dependent resistivity of the HgCdTe material. In order to better understand the influence of temperature on PEDOT:PSS/HgCdTe contacts, contact resistivity measurements should be performed to separate contact resistance from HgCdTe resistance changes with temperatures.

Then, to understand the difference in I-V characteristic for n-type and p-type samples, we simulate PEDOT:PSS/HgCdTe contacts using our numerical model based on Sentaurus Device [57]. Assuming a work function ~5.2eV for PEDOT:PSS, we observe that a Schottky-like I-V characteristics is expected for n-type samples (Figure B.9.5a) while an ohmic behavior is expected for p-type samples which agrees with our experimental results (Figure B.9.5b).

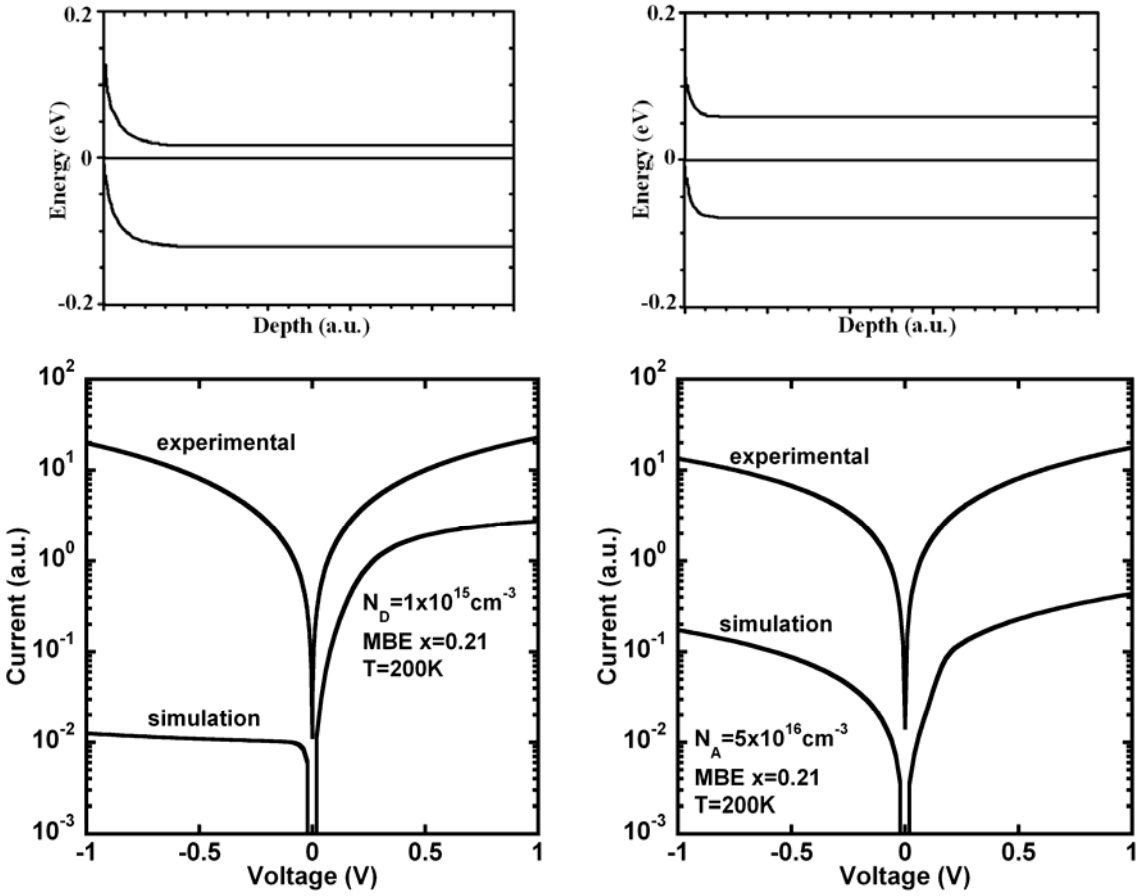

Figure B.9.5: Comparison of experimental and simulated current-voltage characteristics of PEDOT:PSS electrical contacts to a) n-HgCdTe (x=0.21, N_D=1x10^{15}cm^{-3}) and b) p-HgCdTe (x=0.21, N_A=5x10^{16}cm^{-3}) and their corresponding energy band diagrams.

The differences in ohmic behavior for PEDOT:PSS contacts to p-type and n-type HgCdTe may be due to the PEDOT:PSS work function. PEDOT:PSS is often used as a hole injection layer in organic electronics due to the large work function, and we believe that the improved ohmic behavior of PEDOT:PSS contacts to p-type HgCdTe is a direct result of this work function lineup. However, our simulations for PEDOT:PSS contacts to n-type HgCdTe do not agree with our experimental results (Figure B.9.5a). There are numerous potential mechanisms for current flow at the PEDOT:PSS/HgCdTe interface, including thermionic emission, tunneling, trap-assisted tunneling, etc, where thermionic emission will have a strong exponential temperature dependence and tunneling will not have a temperature dependence.

By taking into account Schottky-barrier tunneling (SBT) in our simulations, the I-V characteristic of PEDOT:PSS contacts to n-type HgCdTe is in better agreement with the experimental results (Figure B.9.6), although the rectifying behavior is not exactly similar. From this, we conclude that the rectifying behavior observed for n-type samples is likely to be due to the PEDOT:PSS/HgCdTe interface which induce tunneling effects (SBT, trap-assisted tunneling) at the Schottky junction. Studying the PEDOT:PSS/HgCdTe interface is a subject for future work. Investigating different PEDOT:PSS solutions may help to eliminate the rectifying behavior on n-type HgCdTe. Contact stability can be evaluated by doing thermal fatigue experiments and measuring the I-V characteristics. Interdiffusion of PEDOT:PSS into HgCdTe needs to be studied. These measurements also require further efforts to improve the ability to more accurately define PEDOT:PSS patterns.

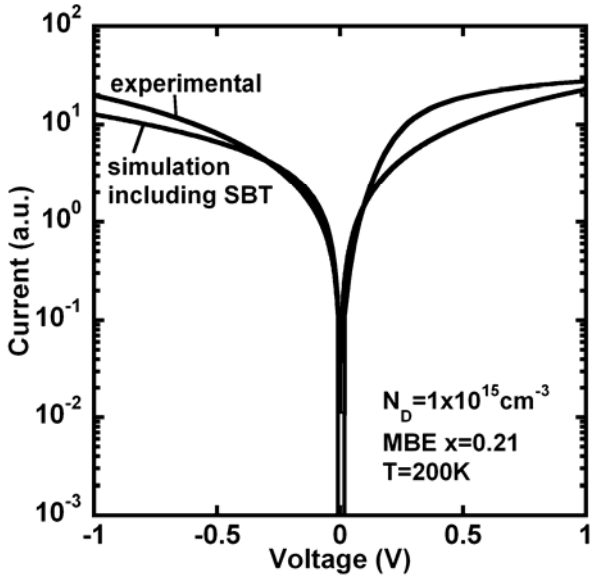

Figure B.9.6: Comparison of experimental and simulated current-voltage characteristics of PEDOT:PSS electrical contacts to n-HgCdTe (x=0.21, N_D=1x10^{15}cm^{-3}) including Schottky-barrier tunneling.

B.3 Summary

We managed to pattern PEDOT:PSS contacts on HgCdTe epilayers using conventional processing techniques. Current-voltage characteristics measurements of

PEDOT:PSS/HgCdTe interface showed nearly ohmic behavior for our p-type sample and a more pronounced rectifying behavior for our n-type sample which is believed to be due to the PEDOT:PSS large work function. The temperature dependence of I-V characteristics for both samples suggests that I-V is primarily dominated by the HgCdTe material. The I-V characteristics for n-type samples is believed to be due to the PEDOT:PSS/HgCdTe interface and induced tunneling effects at reverse bias. These results show good initial prospects in integrating PEDOT:PSS contacts for HgCdTe IR detector arrays and open the possibility for further investigation.

References

[1] A. Rogalski, K. Adamiec, and J. Rutkowski, *Narrow-Gap Semiconductor Photodiodes*. Bellingham, WA: SPIE–The International Society for Optical Engineering (2000).

[2] A. Rogalski, *Rep. Prog. Phys.* **68**, 2267 (2005).

[3] S.M. Sze, *Physics of Semiconductor Devices*. New-York: Wiley (1981).

[4] M.A. Kinch, "Metal-insulator-semiconductor infrared detectors", in *Semiconductors and Semimetals*, Vol. 18, R.K. Willardson and A.C. Beer, Eds. New-York: Academic Press (1981).

[5] P. Norton, *Opto-Electron. Rev.* **10**, 159 (2002).

[6] C.T. Elliott and T. Ashley, *Electron. Lett.* **21**, 451 (1985).

[7] T. Ashley, C.T. Elliott, and A.T. Harker, Infrared Phys. **26**, 303 (1986).

[8] H. Maier and J. Hesse, "Growth, properties and applications of narrow-gap semiconductors", in *Crystal Growth, Properties and Applications*, H.C. Freyhardt, Ed. Berlin: Springer Verlag, pp. 145-219 (1980).

[9] W.F.H. Micklethweite, "The crystal growth of mercury cadmium telluride", in *Semiconductors and Semimetals*, Vol. 18, R.K. Willardson and A.C. Beer, Eds. New-York: Academic Press, pp. 48-119 (1981).

[10] A.B. Chen, Y-M Lai-Hsu, S. Krishnamurthy, M.A. Berding, and A. Sher, *Semicond. Sci. Technol.* **5**, S100 (1990).

[11] G. L. Hansen, J. L. Schmidt, and T. N. Casselman, *J. Appl. Phys.* **53**, 7099 (1982).

[12] J. Wenus, J. Rutkowski, and A. Rogalski, *IEEE Trans. Electron Dev.* **48**, 1326 (2001).

[13] G. L. Hansen and J. L. Schmidt, *J. Appl. Phys.* **54**, 1639 (1983).

[14] M. Weiler, *Semiconduct. Semimet.* **16**, 119 (1981).

[15] R.W. Miles, "Electron and Hole Effective Masses in HgCdTe", in *Properties of Narrow Gap Cadmium-based Compounds*, P. Capper, Ed. London, United Kingdom: INSPEC (1994).

[16] J. Rothman, J. Meilhan, G. Perrais, J.-P. Belle, and O. Gravrand, *J. Electr. Mater.* **35**, 1174 (2006).

[17] W. Scott, *J. Appl. Phys.* **43**, 1055 (1972).

[18] C. Canali, C. Jacobini, F. Nava, G. Ottaviani, and A. Alberigi-Quaranta, *Phys. Rev. B* **12**, 2265 (1975).

[19] N. Sano, T. Aoki, M. Tomizawa, and A. Yoshii, *Phys. Rev. B* **41**, 12122 (1990).

[20] M.V. Fischetti and S.E. Laux, *Phys. Rev. B* **38**, 9721 (1988).

[21] H. Shichijo and K. Hess, *Phys. Rev. B* **23**, 4197 (1981).

[22] G.M. Dunn, G.J. Rees, J.P.R. David, S.A. Plimmer, and D.C. Herbert, *IEEE Trans. Electron Dev.* **43**, 2303 (1996).
[23] G.M. Dunn, G.J. Rees, and J.P.R. David, *Electron. Lett.* **33**, 337 (1997).
[24] D.S. Ong, K.F.Li, G.J. Rees, G.M. Dunn, J.P.R. David, and P.N. Robson, *IEEE Trans. Electron Dev.* **45**, 1804 (1998).
[25] S.A. Plimmer, J.P.R. David, D.S. Ong, and K.F. Li, *IEEE Trans. Electron Dev.* **46**, 769 (1999).
[26] M. Stobbe, R. Redmer, and W. Schattke, *Phys. Rev. B* **49**, 4494 (1994).
[27] K.Y. Choo and D.S. Ong, *J. Appl. Phys.* **96**, 5649 (2004).
[28] C. Groves, J.P.R. David, G.J. Rees, and D.S. Ong, J. Appl. Phys. 95, 6245 (2004).
[29] D. Chattopadhyay, *Phys. Lett.* **81A**, 241 (1981).
[30] B. Gelmont, B. Lund, K-S. Kim, G.U. Jensen, M. Shur, and T.A. Fjeldly, *J. Appl. Phys.* **71**, 4977 (1992).
[31] F. Ma, S. Wang, X. Li, K.A. Anselm, X.G. Zheng, A.L. Holmes, and J.C. Campbell, *J. Appl. Phys.* **92**, 4791 (2002).
[32] F. Ma, X. Li, J.C. Campbell, J.D. Beck, C-F. Wan, and M.A. Kinch, *Appl. Phys. Lett.* **83**, 785 (2003).
[33] R. Granger and C.M. Pelletier, *J. Cryst. Growth* **138**, 486 (1994).
[34] G. Masetti, M. Severi, and S. Solmi, IEEE Trans. Electron Dev. 30, 764 (1983).
[35] C. Canali, G. Majni, R. Minder, and G. Ottaviani, *IEEE Trans. Electron Dev.* **22**, 1045 (1975).
[36] C.A. Hougen, *J. Appl. Phys.* **66**, 3763 (1989).
[37] A.R. Beattie, *J. Phys. Chem. Solids* **24**, 1049 (1962).
[38] J.S. Blakemore, *Semiconductor Statistics*, Oxford, United Kingdom: Pergamon Press (1962).
[39] T.N. Casselman and P.E. Petersen, Solid State Commun. **33**, 615 (1980).
[40] A.R. Beattie and P.T. Landsberg, *Proc. Roy. Soc.* **A249**, 16 (1959).
[41] M.A. Kinch, F. Agariden, D. Chandra, P.-K. Liao, H.F. Schaake, and H.D. Shih, *J. Electron. Mater* **34**, 880 (2005).
[42] S. Krishnamurthy and T.N. Casselman, *J. Electr. Mater.* 29, 828 (2000).
[43] W.van Roosbroeck, and W. Shockley, *Phys Rev*. **94**, 1558 (1954).
[44] W. Shockley and W.T. Read, *Phys. Rev*. **87**, 835 (1952).
[45] R.N. Hall, *Phys Rev*. **87**, 387 (1952).
[46] R. Kiran, "Optimization of the $Hg_{1-x}Cd_xTe$ Surface and its Characterization by Electrical and Optical Techniques", Ph.D. dissertation, University of Illinois at Chicago, Chicago, IL (2008).
[47] P. Capper, "Carrier Lifetimes in n-type HgCdTe", in *Properties of Narrow Gap Cadmium-based Compounds*, P. Capper, Ed. London, United Kingdom: INSPEC (1994).
[48] V. Gopal and S. Gupta, *IEEE Trans. Electron Dev.* **50**, 1220 (2003).
[49] C.D. Maxey, C.L. Jones, N.E. Metcalfe, R.A. Catchpole, N.T. Gordon, A.M. White, and C.T. Elliott, *Proc. SPIE* **3122**, 453 (1997).
[50] T. Skauli, H. Steen, T. Colin, P. Hegelsen, S. Lovold, C.T. Elliott, N.T. Gordon, T.J. Phillips, and A.M. White, *Appl. Phys. Lett.* **68**, 9 (1996).

[51] P.S. Wijewarnasuriya, Y. Chen, G. Brill, N.K. Dhar, C.H. Grein, S. Velicu, P.Y. Emelie, H. Jung, S. Sivananthan, A. D'Souza, M.G. Stapelbroek, and J. Reekstin, *Proc. SPIE* **6542**, 65420G (2007).
[52] C.T. Elliott, N.T. Gordon, R.S. Hall, T.J. Phillips, C.L. Jones, and A. Best, *J. Electr. Mater.* **26**, 643 (1997).
[53] M. Kinch, C.F. Wan, and J.D. Beck, *J. Electr. Mater.* **34**, 928 (2005).
[54] R.J. Westerhout, C.A. Musca, J. Antoszewski, J.M. Dell, and L. Faraone, *J. Electr. Mater.* **36**, 884 (2007).
[55] J. Piotrowski, A. Jozwikowska, K. Jozwikowski, and R. Ciupa, *Infrared Phys.* **34**, 565 (1993).
[56] P.Y. Emelie, J.D. Phillips, S. Velicu, and C.H. Grein, *J. Electr. Mater.* **36**, 846, (2007).
[57] *Sentaurus Device*, Mountain View, CA: Synopsys (2005).
[58] R.E. Bank and D.J. Rose, Numer. Math. **37**, 279 (1981).
[59] R.E. Bank, D.J. Rose, and W. Fichtner, *IEEE T. Electron Dev.* **30**, 1031 (1983).
[60] R.L. Anderson, *Solid State Electron.* **26**, 65 (1983).
[61] V. Ariel and G. Bahir, *J. Electron. Mater.* **26**, 673 (1997).
[62] N.H. Jo, S.D. Yoo, B.G. Ko, S.W. Lee, J. Jang, S.D. Lee, and K.D. Kwack, *Proc. SPIE* **3436**, 50 (1998).
[63] Z.J. Quan, G.B. Chen, L.Z. Sun, Z.H. Ye, Z.F. Li, and W. Lu, *Infrared Phys. Techn.* **50**, 1 (2007).
[64] X. Aymerich-Humet, F. Serra-Mestres, and J. Millan, *J. Appl. Phys.* **54**, 5 (1983).
[65] P. Capper, "Energy Levels due to Donors and Acceptors in HgCdTe", in *Properties of Narrow Gap Cadmium-based Compounds*, P. Capper, Ed. London, United Kingdom: INSPEC (1994).
[66] H.R. Vydyanath, *J. Electrochem. Soc.* **128**, 2619 (1981).
[67] Y. Wu, L. Chen, S.L. Wang, M.F. Yu, Y.M. Qiao, and L. He, *Proc. 6th Int. Conf. Solid-St. Integr. Circ. Technol.* **1**, 286 (2001).
[68] I.K. Sou, "A Experimental Study of Indium-Doped Mercury Cadmium Telluride Grown by Molecular Beam Epitaxy", Ph.D. dissertation, University of Illinois at Chicago, Illinois (1990).
[69] S.M. Johnson, D.R. Rhiger, J.P. Rosbeck, J.M. Peterson, S.M. Taylor, and M.E. Boyd, *J. Vac. Sci. Technol. B* **10**, 1499 (1992).
[70] V. Gopal and S. Gupta, *IEEE Trans. Electron Dev.* **50**, 1220 (2003).
[71] K. Jowikowski and A. Rogalski, *J. Electr. Mater.* **29**, 736 (2000).
[72] A. Jozwikowska, K. Jozwikowski, J. Antoszewski, C.A. Musca, T. Nguyen, R.H. Sewell, J.M. Dell, L. Faraone, and Z. Orman, *J. Appl. Phys.* **98**, 014504 (2005).
[73] D.D. Mooney and R.J. Swift, *A Course in Mathematical Modeling*. Washington, DC: The Mathematical Association of America (1999).
[74] A.I. D'Souza, J. Bajaj, R.E. De Wames, D.D. Edwall, P.S. Wijewarnasuriya, and N. Nayar, *J. Electr. Mater.* **27**, 727 (1998).
[75] P.C. Euthymiou, P.A. Skountzos, C.E. Ravanos, and B.E. Hadjikontis, *Solid State Commun.* **37**, 733 (1981).
[76] P.S. Wijewarnasuriya, M. Zandian, D.D. Edwall, W.V. McLevige, C.A. Chen, J.G. Pasko, G. Hildebrandt, A.C. Chen, J.M. Arias, A.I. D'Souza, S. Rujirawat, and S. Sivananthan, *J. Electr. Mater.* **27**, 546 (1998).

[77] S.M. Johnson, T.J. deLyon, C.A. Cockrum, W.J. Hamilton, T. Tung, F.I. Gesswein, B.A. Baumgratz, L.M. Ruzicka, O.K. Wu, and J.A. Torh, *J. Electr. Mater.* **24**, 467 (1995).
[78] M.A. Kinch, *Proc. SPIE* **168**, 4454 (2001).
[79] R. Zucca, D.D. Edwall, J.S. Chen, S.L. Johnston, and C.R. Younger, J. Electron. Mater. **B9**, 1823 (1991).
[80] S. Velicu, G. Badano, Y. Selamet, C.H. Grein, J.P. Faurie, S. Sivananthan, P. Boeriu, D. Rafol, and R. Ashokan, *J. Electr. Mater.* **30**, 711 (2001).
[81] Y. Chang, C.R. Becker, C.H. Grein, J. Zhao, C. Fulk, T. Casselman, R. Kiran, X.J. Wang, E. Robinson, S.Y. An, S. Mallick, S. Sivananthan, T. Aoki, C.Z. Wang, D.J. Smith, S. Velicu, J. Zhao, J. Crocco, Y. Chen, G. Brill, P.S. Wijewarnasuriya, N. Dhar, R. Sporken, and V. Nathan, *J. Electr. Mater.* **37**, 1171 (2008).
[82] J.D. Benson, L.A. Almeida, M.W. Carmody, D.D. Edwall, J.K. Markunas, R.N. Jacobs, M. Martinka, and U. Lee, *J. Electr. Mater.* **36**, 949 (2007).
[83] G. Badano, J.W. Garland, J. Zhao, and S. Sivananthan, *Proc. SPIE* **4795**, 70 (2002).
[84] S.H. Shin, J.M. Arias, M. Zandian, J.G. Pasko, L.O. Bubulac, and R.E. De Wames, *J. Electr. Mater.* **22**, 1039 (1993).
[85] T.C. Harman, *J. Electr. Mater.* **8**, 191 (1989).
[86] L.O. Bubulac, S.J.C. Irvine, E.R. Gertner, J. Bajaj, W.P. Lin, and R. Zucca, *Semicond. Sci. Technol.* **8**, S270 (1993).
[87] L.O. Bubulac, D.D. Edwall, S.J.C. Irvine, E.R. Gertner, and S.H. Shin, *J. Electr. Mater.* **24**, 617 (1995).
[88] S.H. Shin, J.M. Arias, M. Zandian, J.G. Pasko, L.O. Bubulac, and R.E. De Wames, *J. Electr. Mater.* **24**, 609 (1995).
[89] D. Chandra, M.W. Goodwin, M.C. Chen, and J.A. Dodge, *J. Electr. Mater.* **22**, 1033 (1993).
[90] D. Chandra, M.W. Goodwin, M.C. Chen, and L.K. Magel, *J. Electr. Mater.* **24**, 599 (1995).
[91] D. Shaw, *J. Electr. Mater.* **24**, 587 (1995).
[92] G.R. Nash, J.F.W. Schiz, C.D. Marsh, P. Ashburn, and G.R. Booker, *Appl. Phys. Lett.* **75**, 3671 (1999).
[93] P.S. Wijewarnasuriya, P.Y. Emelie, A. D'Souza, G. Brill, M.G. Stapelbroek, S. Velicu, Y. Chen, C.H. Grein, S. Sivananthan, and N.K. Dhar, *J. Electr. Mater.* **37**, 1283 (2008).
[94] P.Y. Emelie, S. Velicu, C.H. Grein, J.D. Phillips, P.S. Wijewarnasuriya, and N.K. Dhar, *J. Electr. Mater.* **37**, 1362 (2008).
[95] S.P. Tobin, *J. Electr. Mater.* **35**, 1411 (2006).
[96] G.A. Hurkx, D.B. Klassen, and M.P.G. Knuvers, *IEEE Trans. Electron Devices* **39**, 331 (1992).
[97] J. Piotrowski, A. Jozwikowska, K. Jozwikowski, and R. Ciupa, *Infrared Phys.* **34**, 565 (1993).
[98] J. Singh, private communication (2007).
[99] H. Shichijo and K. Hess, *Phys. Rev. B* **23**, 4197 (1981).
[100] A.B. Chen and A. Sher, *J. Vac. Sci. Technol.* **21**, 138 (1982).
[101] E.O. Kane, *J. Phys. Chem. Solids* **1**, 249 (1957).

[102] W. Fawcett and J.G. Ruch, *Appl. Phys. Lett.* **15**, 368 (1969).
[103] H. Brooks and C. Herring, *Phys. Rev.* **83**, 879 (1951).
[104] C. Jacoboni and L. Reggiani, *Rev. Mod. Phys.* **55**, 645 (1983).
[105] J. Singh, *Electronic and Optoelectronic Properties of Semiconductor Structures*. Cambridge, United Kingdom: Cambridge University Press (2003).
[106] R.D.S. Yadava, A.K. Gupta, and A.V.R. Warrier, *J. Electr. Mater.* **23**, 1359 (1994).
[107] L. Makovski and M. Glicksman, *J. Phys. Chem. Solids* **34**, 487 (1973).
[108] J.W. Harrison and J.R. Hauser, *Phys. Rev. B* **13**, 5347 (1976).
[109] D.K. Ferry, *Phys. Rev. B* **17**, 912 (1978).
[110] J.C. Phillips, *Rev. Mod. Phys.* **42**, 317 (1970).
[111] M.A. Kinch, J.D. Beck, C.F. Wan, F.Ma, and J. Campbell, *J. Electr. Mater.* **33**, 630 (2004).
[112] B.R. Nag, *Appl. Phys. A* **29**, 45 (1982).
[113] P. Capper, "Lattice Parameter of HgCdTe", in *Properties of Narrow Gap Cadmium-based Compounds*, P. Capper, Ed. London, United Kingdom: INSPEC (1994).
[114] A.M. Turner, *J. Vac. Sci. Technol. B* **10**, 1534 (1992).
[115] E. Weiss and N. Mainzer, *J. Vac. Sci. Technol. B* **7**, 391 (1989).
[116] O.P. Agnihotri, H.C. Lee, and K. Yang, *Semicond. Sci. Technol.* **17**, R11 (2002).
[117] P.Y. Emelie, E. Cagin, J. Siddiqui, J.D. Phillips, C. Fulk, J. Garland, and S. Sivananthan, *J. Electr. Mater.* **36**, 841 (2007).
[118] S. Kirchmeyer and K. Reuter, *J. Mater. Chem.* **15**, 2077 (2005).
[119] J.Y. Kim, J.H. Jung, D.E. Lee, and J. Joo, *Synthetic Met.* **126**, 311 (2002).